Artificial gauge fields and quantum Hall physics in optical lattices: Control schemes and signatures

vorgelegt von
M. Sc.
Botao Wang
ORCID: 0000-0002-8220-2452

an der Fakultät II – Mathematik und Naturwissenschaften
der Technischen Universität Berlin
zur Erlangung des akademischen Grades

Doktor der Naturwissenschaften
Dr. rer. nat.

genehmigte Dissertation

Promotionsausschuss:

Vorsitzender:	Prof. Dr. Stephan Reitzenstein
Gutachter:	Prof. Dr. André Eckardt
Gutachter:	Prof. Dr. Nathan Goldman (Université Libre de Bruxelles, Belgium)

Tag der wissenschaftlichen Aussprache: 03.03.2022

Berlin 2022

Abstract

The engineering of artificial gauge fields for ultracold atoms in optical lattices opens a new chapter for the quantum simulation of quantum Hall physics. Motivated by recent advances and refined techniques in controlling quantum gases in optical lattices, this thesis explores how the spatio-temporal control of optical lattice systems can be exploited for the engineering of artificial gauge fields, rapid state preparation, and for controlling and probing integer and fractional Chern insulator states and their excitations.

The first example is about the implementation of local magnetic fluxes piercing single lattice plaquettes (analogous to those created by a thin solenoid), which plays an important role in Laughlin's gedankenexperiment of quantum Hall physics. By combining Floquet engineering of artificial magnetic fields with the ability of single-site addressing in quantum gas microscopes, we propose a scheme for the realization of such local solenoid-type magnetic fields in optical lattices. We show that it can be employed to manipulate and probe elementary excitations of a topological Chern insulator, including the quantized charge pumping along tailored paths inside the bulk, as well as the controlled population of edge modes. This possibility is due to the fact that it is the artificial vector potentials (in the form of Peierls phases) that are controlled experimentally, i.e. both the artificial magnetic and electric fields associated with it, rather than the artificial magnetic field alone.

Based on such an observation, then we investigate protocols for adiabatic state preparation via ramping artificial gauge potentials in the form of Peierls phases. Taking an interacting bosonic flux ladder as a minimal model, we find that the time required for adiabatic state preparation dramatically depends on which pattern of Peierls phases is implemented. This can be understood intuitively by noting that different patterns of time-dependent Peierls phases that all give rise to the same magnetic field ramp, generally lead to different artificial electric fields during the ramp. As an intriguing result, we find that an optimal choice allows for preparing the ground state almost instantaneously in the non-interacting system. We show that this effect can be related to the concept of counterdiabatic driving. Remarkably, we find extremely short preparation time also in the strongly-interacting regime. This finding opens new possibilities for robust state preparation in atomic quantum simulators.

The recent progress in engineering topological band structures in optical-lattice systems makes it promising to study fractional Chern insulator states in these systems. In the rest of the thesis, we consider a realistic finite system of a few repulsively interacting bosons on a square lattice with magnetic flux and sharp edges, as it can be realized in quantum-gas microscopes. We investigate under which conditions a fractional Chern insulator state corresponding to the Laughlin-like state at filling $\nu = 1/2$ can be stabilized and its fractional excitations probed. Using numerical simulations, we find an incompressible bulk density at the expected filling for systems, whose linear extent is as small as 6-8 sites. This is a promising result, since such small

systems are favorable with respect to the required adiabatic state preparation. Moreover, we also see very clear signatures of excitations with fractional charge in response both to static pinning potentials and dynamical flux insertion. These observations are robust against changes in various system parameters. Our results suggest that signatures of both a fractional Chern insulator state and its fractional excitations can be found under realistic experimental conditions.

Zusammenfassung

Die Entwicklung künstlicher Eichfelder in optischen Gittern eröffnet ein neues Kapitel der Quantensimulation von Quanten-Hall-Zuständen mit ultrakalten Atomen. Motiviert durch die jüngsten Fortschritte und verfeinerten Techniken bei der Kontrolle von Quantengasen in optischen Gittern, berichtet diese Arbeit darüber, wie die raum-zeitliche Kontrolle optischer Gitter genutzt werden kann, um künstliche Eichender zu kontrollieren, schnelle Zustandspräparationen zu ermöglichen und um (ganz- und gebrochenzahlige) Hall-Zustände und ihre Anregungen zu kontrollieren und zu messen.

Das erste Beispiel betrifft die Implementierung eines lokalen magnetischen Flusses durch eine einzelne Gitterplquette, ähnlich jenem wie er von einem dünnen Solenoid erzeugt wird, welches eine wichtige Rolle im Laughlinschen Gedankenexperiment der Quanten-Hall-Physik spielt. Durch eine Kombination von Floquet-*Engineering* künstlicher Magnetfelder und der Fähigkeit der Einzelplatzadressierung in Quantengasmikroskopen wird ein Schema für die Realisierung solcher lokaler solenoidartiger Magnetfelder in optischen Gittern vorgelegt. Es wird gezeigt, dass damit elementare Anregungen eines topologischen Chern-Isolators manipuliert und untersucht werden können. Dies beinhaltet sowohl quantisiertes Ladungspumpen entlang vorgegebener Pfade im Inneren des Systems, als auch die kontrollierte Population von Randmoden. Diese Möglichkeit ergibt sich aus der Tatsache, dass in Experimenten mit kalten Atomen direkt das künstliche Vektorpotential (in Form von Peierls-Phasen) kontrolliert wird, und damit sowohl die daraus resultierenden künstlichen magnetischen und elektrischen Felder, anstelle von Magnetfeldern allein.

Ausgehend von dieser Beobachtung untersuchen wir im Anschluss Protokolle für die adiabatische zustandspräparation durch das Hochfahren künstlicher Eichpotentiale in Form von Peierls-Phasen. Hierbei dient eine wechselwirkende bosonische Flussleiter als Minimalmodell. Dabei wird festgestellt, dass die für die adiabatische zustandspräparation benötigte Zeit drastisch davon abhängt, welches Muster von Peierls-Phasen verwendet wird. Dies lässt sich intuitiv verstehen, wenn man bedenkt, dass unterschiedliche Protokolle zeitabhängiger Peierls-Phasen, die alle zu derselben Magnetfeldrampe führen, im Allgemeinen unterschiedliche künstliche elektrische Felder während der Rampe induzieren. Ein faszinierendes Ergebnis ist, dass eine optimale Wahl die Präparation des Grundzustands im nicht-wechselwirkenden System fast instantan ermöglicht. Wir zeigen, dass dieser Effekt mit dem Konzept des gegendiabatischen Antriebs in Verbindung gebracht werden kann. Bemerkenswerterweise finden wir extrem kurze Präparationszeiten auch im stark wechselwirkenden System. Diese Erkenntnis eröffnet neue Möglichkeiten für eine robuste Zustandspräparation in atomaren Quantensimulatoren.

Die jüngsten Fortschritte bei der Entwicklung topologischer Bandstrukturen in optischen Gittersystemen sind vielversprechend dafür, auch fraktionale Chern-Isolator-Zustände in diesen Systemen untersuchen zu können. Im weiteren Verlauf der Arbeit wird ein realistisches endliches

System aus einigen repulsiv wechselwirkenden Bosonen in einem quadratischen Gitter mit magnetischem Fluss und scharfen Kanten, wie es in Quantengasmikroskopen realisiert werden kann, betrachtet. Es wird untersucht, unter welchen Bedingungen ein fraktionaler Chern-Isolator Zustand, der dem Laughlin-ähnlichen Zustand bei Füllung $\nu = 1/2$ entspricht, stabilisiert und seine fraktionalen Anregungen untersucht werden können. Mit Hilfe numerischer Simulationen finden wir eine inkompressible Volumendichte bei der erwarteten Füllung für Systeme, für Systeme mit linearen Ausdehnungen von nur 6-8 Gitterplätzen. Dies ist ein vielversprechendes Ergebnis, da solch kleine Systeme für die erforderliche adiabatische Zustandspräparation günstig sind. Darüber hinaus werden auch sehr deutliche Anzeichen von Anregungen mit fraktionaler Ladung als Reaktion sowohl auf statische *Pinning*-Potentiale als auch auf eine dynamische Flusseinführung beobachtet. Diese Beobachtungen sind robust genübel der Änderung gegenüber Änderungen verschiedener Systemparameter. Unsere Ergebnisse deuten darauf hin, dass unter realistischen experimentellen Bedingungen sowohl Signaturen eines fraktionalen Chern-Isolator-Zustands als auch dessen fraktionale Anregungen gefunden werden können.

Publications

- Botao Wang, F. Nur Ünal, and André Eckardt, Floquet Engineering of Optical Solenoids and Quantized Charge Pumping along Tailored Paths in Two-Dimensional Chern Insulators, Phys. Rev. Lett. **120**, 243602 (2018).
- Botao Wang, Xiaoyu Dong, F. Nur Ünal, and André Eckardt, Robust and Ultrafast State Preparation by Ramping Artificial Gauge Potentials, New J. Phys. **23**, 063017 (2021).
- Botao Wang, Xiaoyu Dong, and André Eckardt, Measurable signatures of bosonic fractional Chern insulator states and their fractional excitations in a quantum-gas microscope, SciPost Phys. **12**, 095 (2022).

Contents

1 Introduction

1.1 Topology in condensed matter physics

In the article *More is Different* published in 1972, the late P. W. Anderson emphasized that with increasing complexity of a system (e.g. by adding more and more particles) entirely new properties appear, and the understanding of the new behavior at each level of complexity requires its own fundamental laws [1]. Because of such *emergent* phenomena, it is how the particles are organized, instead of its consisting components, that mainly determines the properties of a material. Different ways of organizing particles are formally called different *order*.

Various phases of matter exhibit different properties because they possess different order. With a deep physical insight, L. D. Landau pointed out that different phases/order are associated with corresponding symmetries in the organization of the constituent particles, and a phase transition is associated by a change of symmetry [2]. For instance, while a liquid has a *continuous* translation symmetry, only *discrete* translation symmetry exists in a crystal. The phase transition from a liquid to a crystal spontaneously reduces the continuous symmetry to the discrete one. Such a change in symmetry is called *spontaneous symmetry breaking*. By introducing order parameters, Ginzburg and Landau developed a standard theory to describe phase transition [3]. The so-called Ginzburg-Landau theory turns out to be a universal description of various states of matter, and has been a cornerstone of condensed matter theory.

However, several great discoveries in the 1980s go beyond the paradigm of Landau's symmetry breaking theory. In the pioneering experiment performed by K. von Klitzing in 1980, based on the sample prepared by G. Dorda and M. Pepper [4], the Hall resistance of a two-dimensional (2D) electronic system became precisely quantized when it was measured under strong magnetic field and at low temperature, i.e.

$$\rho_{xy} = \frac{h}{e^2}\frac{1}{\nu}, \tag{1.1}$$

with ν being integers, h Planck's constant and e the elementary charge. Regardless of various disorder and defects, the extraordinary accuracy of ν (around one part in 10^9) came as a surprise [1]. Even more strikingly, fractional values of ν can also exist, as first discovered in 1982 by D. C. Tsui and H. L. Stormer using samples prepared by A. C. Gossard [5]. Later on, quantized plateaus were observed at different values of ν. Depending on whether they are integer or fractional, the corresponding phenomena are called integer quantum Hall (IQH) and fractional quantum Hall (FQH) effects, respectively. It turns out both the IQH and FQH states cannot be described within the framework of Landau's symmetry breaking theory. Therefore, their understanding calls for new ideas. This is where topology comes to play a role.

[1] This precision is exploited in the new international system of units based on the definition of fundamental constants as introduced in 2019.

In order to understand the IQH effect, within one year after von Klitzing's discovery, R. Laughlin firstly derived the quantized Hall conductance according to the principle of gauge invariance, by performing a *gedankenexperiment* where the two-dimensional (2D) electronic system was bent into a cylinder with a long solenoid placed along its axis [6]. In 1982, D. J. Thouless and co-workers obtained an explicit expression for the integer values of the Hall conductance in the famous TKNN (D. J. Thouless, M. Kohmoto, M. P. Nightingale, and M. den Nijs) paper [7]. The interpretation of these integers as topological invariants (i.e. the Chern number of the first class), was soon made by B. Simon [8], who applied Berry's idea of geometric phase in quantum systems [9]. Thus, Simon not only made a connection between Berry's work with the TKNN paper, but also connected topology and the IQH effect.

When it comes to the FQH effect, the explanation is highly non-trivial because the many-body interaction should be taken into account, which is often notoriously complicated. In his 1983 paper, R. Laughlin explained the fractional quantum Hall (FQH) effect by proposing a many-body wave function ansatz and predicted a sequence of incompressible ground states (now known as Laughlin states) with fractionally-charged excitations [10]. Laughlin's proposal has achieved a big success and has stimulated many new ideas [11]. However, a complete understanding of various FQH states and their origin remains challenging. This may require novel physical concepts and even new theories.

The theory of *topological order* introduced by X. G. Wen opens a new chapter in that direction [12, 13]. Historically, after chiral spin liquids were introduced in an attempt to explain the high-temperature superconductivity [14, 15], Wen realized that many different chiral spin liquids share exactly the same symmetry [16]. Therefore, symmetry alone is not enough and Landau's symmetry breaking theory would fail in characterizing different chiral spin liquids. This indicates the existence of a novel kind of order that is beyond the usual symmetry description. It is called *topological order* [12, 13]. After that, it was proposed that FQH states also contain topological order [17], since there are many different FQH states sharing the same symmetry. In other words, various FQH states are different because they have different topological order.

Topological order can be macroscopically characterized via measurable quantities, which correspond to topological invariants [12]. The early found topological invariants that reveal the essence of FQH states include (i) topological ground-state degeneracies[2] on closed spaces (e.g. a torus) [17, 19], (ii) non-Abelian geometric phases of those degenerate ground states (which determine possible fractional statistics of the topological excitations) [19], and (iii) gapless edge modes [20, 21]. All these properties are robust against local perturbations [13]. Since any symmetry could be broken by local perturbations, the robust properties mentioned above represent a remarkable phenomenon that is beyond symmetry-based descriptions, and thus give rise to a new kind of order – the topological order.

While topological invariants give the macroscopic characteristics of topological order, it has also been attributed to a microscopic origin. It is known that many quantum systems can be described by product states, i.e. the tensor product of individual states belonging to local subspace (e.g. local quantum states on each site). However, the topologically ordered states can

[2]Note that the topological degeneracy is exact when the system size is infinite and small energy splitting appears for finite system [18].

be defined as gapped ground states that cannot be continuously deformed into a product state without gap-closing phase transitions [12, 13]. Such quantum states are said to have long-range entanglement [22–24], and the topological entanglement entropy is another symmetry-irrelevant quantity that is used to characterize topological order. Remark that there is another important class of gapped ground states called symmetry-protected topological (SPT) states. Although the SPT phases do not have ground state degeneracy or fractional statistics, they can have gapless edge excitations that are symmetry-protected. The well-known quantum spin Hall states and the topological insulators (which preserve time-reveral symmetry) [25–29] belong to different SPT phases [12, 13].

Note that the term 'topology' was first introduced in the 19th century by Johann Benedict Listing[3], in order to classify the geometric objects of different shapes. Mathematically, the Gauss-Bonnet theorem states that the integral of the Gaussian curvature over a closed surface gives rise to a quantized topological invariant called Euler characteristic χ, and its value is related to the genus g (which is the number of holes of a surface, $\chi = 2 - 2g$). For instance, a sphere has $g = 0$, but a torus has $g = 1$. This type of topology can be called *classical topology*. By combining the related concepts with the framework of the band theory of solids, gapped band structures can be topologically classified in terms of some topological invariants, which are analogous to genus [28]. The Chern number which determines the quantized Hall conductivity in IQH states, and the Z_2 index in topological insulators and superconductors can all be understood in terms of this type of (classic) topology [12]. However, the topology in topological order mentioned above (e.g. the one associated to the FQH states or chiral spin liquids) has a totally different meaning. The given name topological order was motivated by the theory that has been used – a $U(1)$ Chern-Simons theory – which is a topological quantum field theory [12]. Topological order simply represents long-range entangled order in gapped ground states, and the topology in topological order is referred to as *quantum topology* [12].

Understanding different states of matter is not only of theoretically fundamental interest, the special properties inherent to these states could also have important impacts on practical applications including spintronics and quantum computation. For example, certain topological states with non-Abelian anyonic excitations can be used for topological quantum computation [30, 31]. Even though FQH states are well-known examples that host topological excitations (anyons) satisfying fractional (both Abelian and non-Abelian) statistics [32–35] and carrying fractional charges (for the system with particle-number conservation [12]), clear experimental observations of fractional statistics remains elusive. Therefore, it would be exciting to see further experimental systems allowing for the creation and manipulation of those topological excitations in a highly controllable manner. Among various well-controlled synthetic systems, optical lattices with ultracold atoms provide a promising platform for that purpose [36–41].

[3]Listing also independently discovered the properties of the so-called Möbius strip (a two-dimensional surface with only one side), even a few months earlier than August Ferdinand Möbius.

1.2 Quantum simulation with ultracold atoms

Solving quantum many-body problems in condensed matter physics is usually not easy. The idea of quantum simulation provides a promising approach to circumvent such difficulties. The great vision of quantum simulation given by Richard Feynman[4] can be found in the article published in 1982, which is about *building a computer from quantum mechanical elements which obey quantum mechanical laws* [42]. Such quantum machines in the end could be used to imitate (complex) quantum systems which are difficult simulate with classical computers. Nowadays, the spirit of quantum simulation has been fulfilled in various synthetic platforms, including photonic systems [43–45], superconductor circuits [46], trapped ions [47, 48], as well as ultracold atoms in optical lattices [40, 41].

The interest in ultracold atoms was first motivated by the idea of realizing Bose-Einstein condensation. In 1924, when Albert Einstein firstly saw Satyendra Nath Bose's paper about some novel ideas on photon statistics, he immediately realized the importance of Bose's work (which pioneers the field of quantum statistics) [49]. The extension of Bose's idea makes Einstein predict that cooling particles obeying Bose's statistics to low enough temperatures would cause them to macroscopically occupy one single quantum state, which thus form a new state of matter now known as Bose–Einstein condensates (BECs)[5]. It took 70 years for the first experimental demonstration. In 1995, the team of Eric Cornell and Carl Wieman from Colorado reported the condensate of rubidium-87 atoms [50]; the group lead by Wolfgang Ketterle at MIT produced the BEC of sodium-23 atoms [51]; Randall G. Hulet's group reported evidence for BEC of spin-polarized lithium-7 gases [52]. Their achievements have founded the field of ultracold atoms, and have attracted intense interests of physicists from different areas [53].

Loading BECs into optical lattices opens a new chapter in the quantum simulation of condensed matter physics (especially complex quantum many-body systems) with ultracold atoms [40, 41]. Optical lattices are periodic potentials formed by the interference of superimposing counter-propagating laser beams. Due to the light-induced dipole moment of the atom, its interaction with light field causes a shift in the potential energy (i.e. the ac-Stark shift) which is proportional to the light intensity [54]. Thus the interference pattern with periodic intensity behaves like a periodic lattice potential for atoms [55]. In the influential theoretical proposal given by Jaksch and collaborators in 1998, it was predicted that ultracold atoms in periodic lattice potentials can undergo a quantum phase transition from a superfluid (SF) to a Mott-insulating (MI) state [56]. As discussed in the seminal work by Matthew P. A. Fisher and collaborators in 1989 [57], such a SF-MI quantum phase transition is an important property of the so-called Bose-Hubbard (BH) model that describes interacting bosons on a lattice. Specifically, due to the competition between the tunneling strength J and the repulsive on-site interaction U, the ground state exhibits either a SF phase (with long-range phase coherence but fluctuations of atom number on each site for $J \gg U$) or a MI phase (with equal number of atoms per site but uncertain phase of the matter wave for $U \gg J$). In 2002, the team from Garching led by Immanuel Bloch and Theodor Wolfgang Hänsch put such theoretical prediction and proposal into experimental realization by imposing an optical lattice on ^{87}Rb BECs [58]. With

[4] Feynman's entire interest in simulating physics with computers has been inspired by Edward Fredkin [42].
[5] BEC is also called the fifth state of matter, different from solid, liquid, gas and plasma.

the technique of time-of-flight (TOF) images, the measured matter wave interference patterns clearly reveal the signature of SF-MI phase transition by simply varying lattice potential depth. This was a remarkable result, since it opened the possibility of introducing strong interactions to a system of ultracold atoms. The seminal theoretical proposal together with the beautiful follow-up experimental realization of loading BECs into optical lattices marks a milestone in simulating strongly-correlated phenomena with ultracold atoms, and thus nicely bridges two seemingly different fields of research, namely quantum optics and condensed matter physics [40].

It turns out that optical lattice with ultracold atoms manifest themselves as very flexible platforms with perfect control of system parameters. For instance, the tunneling strength can be precisely tuned by lattice depth (i.e. the intensity of optical standing waves), and the on-site (short-range) interaction can be further controlled by Feshbach resonances [59]. Long-range and anisotropic interaction effects can also be addressed by using atomic species (e.g. Cr, Dy, Er *et al.*) with large magnetic moments [60, 61], polar molecules which exhibit electric dipole moments [62, 63] or Rydberg atoms (atoms of excited states with large principal quantum numbers) [64]. By properly arranging the configuration of laser beams, optical lattices of different dimensions or various geometries can be achieved [41]. While the TOF images reveal the momentum distribution and coherence properties, the advent of quantum gas microscopes allows for imaging and controlling atoms with single lattice site resolution [65–69]. The atoms can be bosons, fermions, or their mixtures. The lattice potentials can be accompanied with harmonic traps, box trapping potentials with sharp edges [70], as well as (quasi-)disordered potentials [41]. Moreover, except for various equilibrium quantum simulations, non-equilibrium situations can also be investigated in a well controllable manner, including sudden parameter changes (quenches), periodical driving [71], and the realization of dissipative Hubbard models [72–75], Because of the high controllability mentioned above, optical lattices with cold atoms not only become a promising platform for quantum simulation (which are especially ideal to simulate various discrete Hamiltonians including Hubbard, Heisenberg models), but also provide a path to regimes which have never been accessed in condensed matter system [41, 55].

In order to simulate quantum Hall physics, however, one important ingredient is the interaction with electromagnetic fields. Due to the charge neutrality of cold atoms, they cannot react like electrons under the effect of magnetic fields. This stimulates the interest of simulating artificial gauge fields (magnetic fields or spin-orbit coupling [76–78]) with charge neutral cold atoms, which can be used to mimic the behaviour of charged electrons [36–41, 71, 79–81]. The early stage of engineering artificial gauge potentials is to use rotating atomic gases, in which case the Coriolis force plays the role of the Lorentz force so that an artificial magnetic field is created in the rotating frame [82, 83]. However, the confining potential usually needs to be rotationally invariant and *strong* magnetic field effects were difficult to be achieved [79]. By coupling atomic internal states with Raman laser beams, strong artificial gauge fields can be created in the laboratory frame [79, 84]. However, one drawback is that spontaneous emission can cause unwanted heating. It was proposed that topological flat bands for ultracold atoms can be realized in the so-called optical flux lattices, where only a few set of laser beams are used to produce a spatially-periodic atom-laser coupling. This would give rise to periodic effective magnetic fields with high flux density in shallow optical lattices [85–87]. Subsequently, it has

been shown that the optical flux lattices can actually be viewed as tight-binding models (which can be engineered to exhibit topologically non-trivial bands) in reciprocal space [88].

Note that while quantum Hall physics was originally observed in 2D spatial space, available dimensions do not have to be the spatial ones. By exploiting internal degrees of freedom, as has been pioneered by the proposal of using Zeeman states [89, 90], synthetic dimension now becomes a well-established routine to imitate topological quantum matter [91]. Because of the sharp boundaries in the synthetic dimensions, topologically protected chiral edge transports have been successfully observed [92–94]. While previous experiments were limited to narrow ribbons (with $2-5$ sites), more recently, a synthetic dimension encoded in 17 magnetic sublevels has been realized by using ultracold dysprosium atoms, where both chiral dynamics along the edge and quantized Hall drift inside the bulk have been clearly observed [95]. Meanwhile, by coupling discrete momentum states, lattices in momentum space have been used to study chiral currents and magnetic reflection [96], or the interplay of disorder and artificial gauge fields [97]. Note that measurements of strong interaction effects (although in the absence of gauge fields) have been performed for the first time in such synthetic lattices [98]. Last but not least, extending 2D space in terms of 1D lattice and time, Thouless (quantized) charge pump has been theoretically proposed [99, 100] and experimentally realized [101–104], which leads to the recent experimental investigation of higher-dimensional (4D) quantum Hall physics [105].

Alternatively, Floquet engineering has established as a powerful tool to create strong artificial magnetic fields for ultracold atoms. A Floquet system is described by a time-periodic Hamiltonian. It can often be well approximated by a time-independent effective Hamiltonian within the framework of Floquet theory [71, 80, 106]. Thus, by properly designing periodic driving protocols, various interesting phenomena and desired models can be engineered in the lab. One type of periodic driving is realized by lattice shaking. It has been shown that non-sinusoidal driving forces can give rise to artificial magnetic fields [107–109]. As originally proposed for graphene [110], circular lattice shaking can also be used to engineer topologically nontrivial band structures. Such a shaking scheme has been successfully implemented in optical lattices with fermions, leading to the realization of the famous Haldane model (a typical topological Chern insulator with vanishing net magnetic flux, corresponding to quantum anomalous Hall effect) [111, 112], as well as the measurement of nontrivial Chern number [113] or quantized circular dichroism [114].

Another type of periodic driving protocol corresponds to applying far-detuned running laser beams, which can be employed to restore tunneling initially suppressed by large on-site energy offsets [115–117]. Such laser/'photon' assisted tunneling would be accompanied by some complex phases (the so-called Peierls phases) for hopping from one site to another. In this case, atoms hopping around one single lattice unit cell would accumulate a net phase, which is analogous to the Aharonov–Bohm phase obtained by electrons moving in magnetic fields along a closed path. Thus the Peierls phases play the role of vector potentials, and the accumulated net phase emulates artificial magnetic fluxes. This approach has been used to create either staggered or uniform artificial magnetic fluxes in a square lattice, the latter corresponding to the paradigmatic Harper-Hofstadter model [118, 119], which has been successfully realized in various experiments [120–125]. Note that (i) the protocols for laser assisted tunneling do not depend

on internal states of atoms, and thus make the heating due to spontaneous emission become negligible; (ii) the engineered artificial magnetic fluxes are extremely strong (in the order of one flux quantum per lattice plaquette), corresponding to magnetic fields with magnitudes of $\sim 10^4$ Tesla for electrons in graphene (due to the small lattice constant therein). This represents one typical advantage of using ultracold atoms to simulate interesting quantum phenomena within/beyond condensed matter physics.

Despite a lot of success in applying Floquet engineering, one big drawback is that a driven many-body system may suffer from the problem of heating in a large time scale [71]. Nevertheless, the time-independent effective Hamiltonian can still describe the driven system to a good approximation on a finite time scale. This becomes realistic provided that the driving frequency is large compared to the typical energy scales in the system (like the tunneling parameter or the Hubbard interaction). As theoretically proposed [126] and experimentally observed [127], a dynamical control of SF-MI phase transition has been realized by lattice shaking, which suggests that it is possible to combine Floquet engineering with the strong interaction required for a strongly-correlated state. More recently, Floquet engineering has also been employed to make progress towards creating dynamical gauge fields (that would include feedback from atoms), which are crucial ingredients in both high energy physics and condensed matter systems [128–132].

It is fascinating to see so many impressive progresses on quantum simulation of quantum Hall physics by using optical lattices with ultracold atoms. Nevertheless, as one of the most exotic phenomena, the counterpart of FQH states in lattices, known as fractional Chern insulators (FCIs) [133, 134], and the corresponding topological excitations (with fractional charges and statistics) have so far been elusive in cold atom experiments. Quantum simulation with cold atoms is thus still a rapidly growing field which keeps drawing intensive attention. Based on recently refined advances and techniques, it would be useful to have more ideas or practical protocols for preparing and probing quantum Hall states and their exotic excitations in optical lattice systems, which is the theme of this thesis.

1.3 Outline

Systems with periodic lattice potentials are known to exhibit Bloch bands. The topological properties encoded in the band structures can be characterized by the topological invariant called Chern number, which has a deep relation to the Berry phase. **Chapter 2** starts with the introduction of all these basic concepts, followed by their application in a paradigmatic topological model – the Harper-Hofstadter (HH) model. After that, a brief overview of the Floquet formalism, together with its direct application for implementing the HH model with cold atoms is presented.

Inserting quanta of magnetic flux by using a thin solenoid, known as the famous Laughlin Gedankenexperiment, plays an important role in quantum Hall physics. Inspired by recent advances in controlling atomic quantum gases in optical lattices, a protocol for Floquet engineering such solenoid-type local fluxes in an optical lattice is presented **Chapter 3**. It is found that it can be employed to create quantized charge pumping along tailored paths in 2D Chern

insulators. This effect can be exploited, e.g. for the controlled population of the topologically protected chiral edge modes. Its extension to a bosonic system is also discussed.

It is interesting to observe that the tailored paths for the above-mentioned charge pumping are determined by the way of arranging the time-dependent artificial vector potentials (in the form of Peierls phases), which induce artificial electric fields during the ramp. It is discussed in **Chapter 4** that such artificial electric fields can also be exploited to optimize adiabatic state preparation. Taking an interacting bosonic flux ladder as a minimal model, we will see that the time required for adiabatic state preparation dramatically depends on the chosen pattern of Peierls phases. It may open a new path for the robust state preparation in interacting quantum systems with artificial gauge fields.

All the discussions mentioned above would contribute to the ultimate goal of realizing and probing fractional Chern insulator states, as well as their anyonic excitations with ultracold atoms in optical lattices. In **Chapter 5**, a systematic investigation of the stability of fractional Chern insulators in finite lattices is presented. It will be shown that the fractional Chern insulator ground states can be stabilized in a wide parameter regime, which will be of particular interest for future experimental implementations. Moreover, clear signatures of excitations with fractional charge in response to both static pinning potentials and dynamical flux insertion will also be presented.

A conclusion and future directions are presented in **Chapter 6**.

2 Preliminaries

Lying at the heart of quantum Hall physics, Berry phase is perhaps the simplest demonstration of how geometry and topology can emerge from quantum mechanics. We start with several basic concepts including Berry phase, Chern number etc., and then apply them to the paradigmatic Harper-Hofstadter (HH) model that describes charged particles moving in a lattice with strong magnetic fields. Last but not least, we discuss the framework of Floquet engineering that has been demonstrated as a powerful tool in cold atom experiments, and see how it can be employed to realize the desired HH model in optical lattices.

2.1 Berry phase

Generally speaking, any parallel-transported vector[6] may acquire an angle with respect to its original orientation after completing a closed path on a surface. Such a rotation angle is called a geometric phase as it is of geometrical origin [135]. In classical mechanics, the Foucault pendulum, which was conceived to demonstrate the rotation of the Earth, is one of the earliest examples that can be used to illustrate the geometric phase. In quantum mechanics, one typical geometric phase was formulated by Michael Berry in 1984, and now is known as Berry phase [9]. Berry's elementary yet profound observation provides a unified description of a wide range of phenomena in quantum physics [136]. Here, we start with deriving the general formula of Berry phase based on his seminal paper [9].

Consider a quantum system whose Hamiltonian $\hat{H}(\boldsymbol{R})$ depends on parameters $\boldsymbol{R} = (R_1, R_2, ...)$. The eigenstates $\left|n(\boldsymbol{R})\right\rangle$ and eigenvalues $E(\boldsymbol{R})$ satisfy

$$\hat{H}(\boldsymbol{R})\left|n(\boldsymbol{R})\right\rangle = E(\boldsymbol{R})\left|n(\boldsymbol{R})\right\rangle. \tag{2.1}$$

Here, the eigenstates are assumed to be non-degenerate.

Now let the Hamiltonian $H(\hat{\boldsymbol{R}}(t))$ be changed by varying parameters $\boldsymbol{R}(t)$ from time $t = 0$ until $t = T$. The state of the system $\left|\psi(t)\right\rangle$ evolves according to the Schrödinger equation

$$i\hbar|\dot{\psi}(t)\rangle = \hat{H}(R(t))\left|\psi(t)\right\rangle, \tag{2.2}$$

with i the imaginary unit, $\hbar$ the reduced Planck constant and the dot $\dot{x}$ denotes time derivative of x.

If the system is initially placed in a non-degenerate eigenstate $\left|n(\boldsymbol{R}(0))\right\rangle$ and $\hat{H}(\boldsymbol{R}(t))$ is varied infinitely slow along a path $\mathcal{P}$ in parameter space, the adiabatic theorem states that at

[6] For a vector moving on a surface, the parallel transport means that the vector moves without a change in its magnitude, and without rotation about the instantaneous normal to the surface as well.

any instant t, the system will essentially stay in the eigenstate $\big|n(\boldsymbol{R}(t))\big\rangle$. The evolved state can be written as

$$\big|\psi(t)\big\rangle = \exp\left\{\frac{-i}{\hbar}\int_0^t dt' E_n(\boldsymbol{R}(t'))\right\}\exp(i\gamma_n(t))\,\big|n(\boldsymbol{R}(t))\big\rangle\,. \tag{2.3}$$

Apart from the well-known dynamical phase shown in the first exponential, it can also be assigned an additional term $\exp(i\gamma_n(t))$. The function $\gamma_n(t)$ is determined by the fact that Eq. (2.3) satisfies the Schrödinger equation. Thus plugging Eq. (2.3) into Eq. (2.2) gives

$$\dot{\gamma}_n(t) = i\langle n|\dot{n}\rangle = i\langle n(\boldsymbol{R}(t))|\nabla_{\boldsymbol{R}} n(\boldsymbol{R}(t))\rangle\dot{\boldsymbol{R}}(t). \tag{2.4}$$

Here $\nabla_{\boldsymbol{R}}$ represents the gradient with respect to the parameters $\boldsymbol{R}$, and the second equality in Eq. (2.4) is due to

$$\dot{f} = \frac{df(\boldsymbol{R}(t))}{dt} = \frac{\partial f}{\partial R_1(t)}\frac{dR_1(t)}{dt} + \frac{\partial f}{\partial R_2(t)}\frac{dR_2(t)}{dt} + \cdots = (\nabla_{\boldsymbol{R}} f)\,\frac{d\boldsymbol{R}(t)}{dt}, \tag{2.5}$$

with $f = f(\boldsymbol{R}(t))$ being a general function of parameters $\boldsymbol{R} = (R_1, R_2, \cdots)$.

It is indicated in Eq. (2.4) that γ_n can be expressed as a line integral in the parameter space

$$\gamma_n = \int_{\mathcal{P}} \boldsymbol{\mathcal{A}}_n \cdot d\boldsymbol{R}, \tag{2.6}$$

$$\boldsymbol{\mathcal{A}}_n(\boldsymbol{R}) = i\left\langle n(\boldsymbol{R})\,\middle|\nabla_{\boldsymbol{R}} n(\boldsymbol{R})\right\rangle, \tag{2.7}$$

where the vector-valued function $\boldsymbol{\mathcal{A}}_n$ has been introduced and is called the *Berry connection*[7].

For an *open* path, i.e. $\boldsymbol{R}(0) \neq \boldsymbol{R}(T)$, it can be shown that the phase γ_n is trivial as it can be easily gauged out. To be specific, by making a gauge transformation

$$|n(\boldsymbol{R})\rangle \to e^{i\xi(\boldsymbol{R})}|n(\boldsymbol{R})\rangle, \tag{2.8}$$

where $\xi(\boldsymbol{R})$ is an arbitrary smooth function, the Berry connection is modified as

$$\boldsymbol{\mathcal{A}}_n \to \boldsymbol{\mathcal{A}}_n - \nabla_{\boldsymbol{R}}\xi(\boldsymbol{R}). \tag{2.9}$$

Consequently, combining Eqs. (2.6) with (2.9) gives that the phase γ_n will be changed by $\Delta\gamma_n = \xi(\boldsymbol{R}(0)) - \xi(\boldsymbol{R}(T))$ after the gauge transformation. In this case, one can always choose a suitable $\xi(\boldsymbol{R})$ such that γ_n accumulated along the path is cancelled out and only the dynamical phase is left. Due to this, the phase γ_n has been considered as unimportant for many years and was usually neglected [137].

This situation has not been challenged until Berry reconsidered the cyclic evolution along a *closed* path in the parameter space i.e. $\boldsymbol{R}(0) = \boldsymbol{R}(T)$. The path is henceforth called a circuit and is denoted by $\mathcal{C}$. Since the phase factor $e^{i\xi(\boldsymbol{R})}$ in the gauge transformation is single-valued, it implies that the phase difference $\Delta\gamma_n$ reads

$$\Delta\gamma_n = 2\pi \times \text{integer}. \tag{2.10}$$

[7] The j-th component of $\boldsymbol{\mathcal{A}}_n$ is written as $\boldsymbol{\mathcal{A}}_n^j = i\langle n(\boldsymbol{R})\frac{\partial}{\partial \boldsymbol{R}_j}|n(\boldsymbol{R})\rangle$.

Namely, γ_n can only be changed by an integer multiple of 2π under the gauge transformation and it cannot be removed. Thus for a closed path, γ_n becomes a gauge-invariant physical quantity (modulo 2π). Note that all gauge-invariant quantities are – at least in principle – measurable [138].

To keep the information of such an unusual phase difference, after completing the circuit $\mathcal{C}$, i.e. when the Hamiltonian returned to its original form $\hat{H}(\boldsymbol{R}(T)) = \hat{H}(\boldsymbol{R}(0))$, the system will return to its original state with additional phase factors according to Eq. (2.3),

$$\left|\psi(T)\right\rangle = \exp\left\{\frac{-i}{\hbar}\int_0^T dt E_n(\boldsymbol{R}(t))\right\}\exp(i\gamma_n(\mathcal{C}))\left|n(0)\right\rangle, \tag{2.11}$$

where the net geometrical phase $\gamma_n(\mathcal{C})$ is

$$\gamma_n(\mathcal{C}) = \oint_{\mathcal{C}} \boldsymbol{\mathcal{A}}_n \cdot d\boldsymbol{R}. \tag{2.12}$$

The phase $\gamma_n(\mathcal{C})$ was first obtained by Berry in 1984 and is now called *Berry phase*. This line integral around the closed path $\mathcal{C}$ in parameter space shows its geometrical origin, and $\gamma_n(\mathcal{C})$ does not depend on the rate at which the path is travelled (as long as the adiabatic approximation holds). Note that the normalization of $|n(\boldsymbol{R})\rangle$ indicates that $\langle n(\boldsymbol{R})|\nabla_{\boldsymbol{R}} n(\boldsymbol{R})\rangle$ is imaginary, i.e. $\nabla_{\boldsymbol{R}} \cdot 1 = \nabla_{\boldsymbol{R}}\left(\langle n(\boldsymbol{R})|n(\boldsymbol{R})\rangle\right) = \langle \nabla_{\boldsymbol{R}} n(\boldsymbol{R})|n(\boldsymbol{R})\rangle + \langle n(\boldsymbol{R})|\nabla_{\boldsymbol{R}} n(\boldsymbol{R})\rangle = 0$, and thus $\gamma_n(\mathcal{C})$ is real (i.e. the Berry connection $\boldsymbol{\mathcal{A}}_n(\boldsymbol{R}) = i\left\langle n(\boldsymbol{R})\right|\left.\nabla_{\boldsymbol{R}} n(\boldsymbol{R})\right\rangle$ is real).

Sometimes it can be awkward to directly evaluate $|\nabla_{\boldsymbol{R}} n(\boldsymbol{R})\rangle$ because it requires a locally single-valued basis for $|n(\boldsymbol{R})\rangle$. Such difficulties are avoided by transforming the circuit integral in Eq. (2.12) into a surface integral over any surface $\mathcal{S}$ with boundary $\mathcal{C}$ in parameter space. By applying Stoke's theorem[8], the Berry phase can be rewritten as

$$\gamma_n(\mathcal{C}) = \iint_{\mathcal{S}} \boldsymbol{\Omega}_n \cdot d\boldsymbol{S}, \qquad \boldsymbol{\Omega}_n = \nabla_{\boldsymbol{R}} \times \boldsymbol{\mathcal{A}}_n, \tag{2.13}$$

where $d\boldsymbol{S}$ is the surface element and Ω_n is called the *Berry curvature*. Although Eq. (2.9) shows that $\boldsymbol{\mathcal{A}}_n$ is not unique and it depends on the choice of the phase of the eigenstate $|n(\boldsymbol{R})\rangle$, the Berry curvature Ω_n is independent on this gauge choice as $\nabla \times \nabla_{\boldsymbol{R}}\xi(\boldsymbol{R}) = 0$. The Berry curvature Ω_n is analogous to a 'magnetic field' (in parameter space), whose 'vector potential' is the Berry connection $\boldsymbol{\mathcal{A}}_n$, and the Berry phase can be interpreted as the 'magnetic flux' piercing the surface with boundary $\mathcal{C}$.

More generally (and more usefully in many cases), the gauge-field tensor form of the Berry

[8] To apply vector calculus, the parameter space has been considered as three-dimension where Stoke's theorem applies. However, the results can also be generalized to higher dimensions [9, 137].

curvature can be written as [137]

$$\begin{aligned}
\boldsymbol{\Omega}^n_{\mu\nu}(\boldsymbol{R}) &= \partial_{R^\mu}\boldsymbol{\mathcal{A}}^\nu_n(\boldsymbol{R}) - \partial_{R^\nu}\boldsymbol{\mathcal{A}}^\mu_n(\boldsymbol{R}) \\
&= i\left[\partial_{R^\mu}\langle n|\partial_{R^\nu}n\rangle - \partial_{R^\nu}\langle n|\partial_{R^\mu}n\rangle\right] \\
&= i\left[\langle\partial_{R^\mu}n|\partial_{R^\nu}n\rangle \cancel{+\langle n|\partial_{R^\mu}\partial_{R^\nu}n\rangle} - \langle\partial_{R^\nu}n|\partial_{R^\mu}n\rangle \cancel{-\langle n|\partial_{R^\nu}\partial_{R^\mu}n\rangle}\right] \\
&= i\left[\langle\partial_{R^\mu}n|\partial_{R^\nu}n\rangle - \langle\partial_{R^\nu}n|\partial_{R^\mu}n\rangle\right] \qquad (2.14) \\
&= i\sum_{n'}\left[\langle\partial_{R^\mu}n|n'\rangle\langle n'|\partial_{R^\nu}n\rangle - (\nu\leftrightarrow\mu)\right],\ \sum_{n'}|n'\rangle\langle n'| = 1 \\
&= i\sum_{n'\neq n}\left[\frac{\langle n|\partial_{R^\mu}\hat{H}|n'\rangle\langle n'|\partial_{R^\nu}\hat{H}|n\rangle}{(E_n - E_{n'})^2} - (\nu\leftrightarrow\mu)\right], \qquad (2.15)
\end{aligned}$$

where we have used $\frac{\partial}{\partial\boldsymbol{R}^\mu} = \partial_{R^\mu}, |n(\boldsymbol{R})\rangle = |n\rangle$ for short, and $\nu\leftrightarrow\mu$ means exchanging ν and μ in the expression before. To arrive at Eq. (2.15) in the last step, (i) For $n' = n$, one can use $\partial_R(\langle n|n\rangle) = \langle\partial_R n|n\rangle + \langle n|\partial_R n\rangle = 0$, such that

$$\langle\partial_{R^\mu}n|n\rangle\langle n|\partial_{R^\nu}n\rangle - (\nu\leftrightarrow\mu) = \left[-\langle n|\partial_{R^\mu}n\rangle\right]\cdot\left[-\langle\partial_{R^\nu}n|n\rangle\right] - \langle\partial_{R^\nu}n|n\rangle\langle n|\partial_{R^\mu}n\rangle = 0. \quad (2.16)$$

(ii) For $n' \neq n$, we have employed $\langle n|\partial_R\hat{H}|n'\rangle = (E_n - E_{n'})\langle\partial_R n|n'\rangle$, which can be derived as below,

$$\begin{aligned}
\partial_R\langle n|\hat{H}|n'\rangle &= \partial_R E_n \underbrace{\langle n|n'\rangle}_{=0} = 0 \\
\partial_R\langle n|\hat{H}|n'\rangle &= \langle\partial_R n|\hat{H}|n'\rangle + \langle n|\partial_R\hat{H}|n'\rangle + \langle n|H|\partial_R n'\rangle \\
&= E_{n'}\langle\partial_R n|n'\rangle + \langle n|\partial_R\hat{H}|n'\rangle + E_n\langle n|\partial_R n'\rangle \\
&\downarrow 0 = \partial_R\langle n|n'\rangle = \langle\partial_R n|n'\rangle + \langle n|\partial_R n'\rangle \\
&= (E_{n'} - E_n)\langle\partial_R n|n'\rangle + \langle n|\partial_R\hat{H}|n'\rangle \\
\Rightarrow \langle n|\partial_R\hat{H}|n'\rangle &= (E_n - E_{n'})\langle\partial_R n|n'\rangle. \qquad (2.17)
\end{aligned}$$

Note that this alternative form Eq. (2.15) has the advantage that no differentiation on the eigenstate is involved, therefore it will be particularly useful for numerical calculations (e.g. in Section 2.4.3), where a smooth phase choice of the eigenstates is not usually guaranteed [137]. Also, no assumption about the dimensionality of the state space is made.

For a physical interpretation, one can see that the dynamical phase factor represents that the system's internal clock will register the passage of time, and the Berry phase means that the system also records its history in a deeply geometrical way [9]. Especially, Eq. (2.15) shows that the Berry curvature, and thus the Berry phase, involves the contributions hidden in parameter-space regions which the system has not visited (i.e. the contributions from all the other states $|n'\rangle \neq |n\rangle$). While the adiabatic approximation is essentially a projection operation which restricts the dynamics of the system to the n-th energy level, the Berry curvature can be regarded as the result of the 'residual' interaction of those projected-out energy levels [137]. To include the contributions from all the energy levels, Eq. (2.15) implies that for each value of $\boldsymbol{R}$,

the summation of $\boldsymbol{\Omega}^n_{\mu\nu}(\boldsymbol{R})$ over n vanishes, i.e.

$$\sum_n \boldsymbol{\Omega}^n_{\mu\nu}(\boldsymbol{R}) = 0, \tag{2.18}$$

which represents the local conservation law for the Berry curvature.

Note that the above deduction is based on the assumption of a separated single energy level. When the state becomes N-fold degenerate over the full course of its evolution, the accumulated 'phase' actually becomes non-Abelian and can be described by a $U(N)$ matrix [136, 139]. Moreover, the concept of geometric phase can also be extended to the case of non-adiabatic evolution, which thus underlines its purely geometrical nature [140, 141].

An alternative geometrical view

While the mathematical interpretation of the Berry phase can be made in terms of holonomy [8], another intuitive picture to view the geometrical nature of Berry phase is to directly consider the phase difference between two states [138]. For any two eigenstates with parameters, say $\boldsymbol{R}_1$ and $\boldsymbol{R}_2$ respectively, their phase difference $\Delta\varphi_{12}$ is naturally defined as

$$e^{-i\Delta\varphi_{12}} = \frac{\langle n(\boldsymbol{R}_1)|n(\boldsymbol{R}_2)\rangle}{\big|\langle n(\boldsymbol{R}_1)|n(\boldsymbol{R}_2)\rangle\big|}, \tag{2.19}$$

$$\begin{aligned}\Delta\varphi_{12} &= -\mathrm{Im}\left(\log\langle n(R_1)|n(R_2)\rangle - \underbrace{\log\big|\langle n(R_1)|n(R_2)\rangle\big|}_{\text{Real number}}\right)\\ &= -\mathrm{Im}\log\langle n(\boldsymbol{R}_1)|n(\boldsymbol{R}_2)\rangle.\end{aligned} \tag{2.20}$$

Note that only the imaginary part on the r.h.s. of the above equations contributes to the phase.

Obviously, by choosing an arbitrary phase of a quantum state (which is referred to as the choice of the gauge), the phase difference between two states is gauge-dependent and cannot have, by itself, any physical meaning. However, when it comes to a closed path in the parameter space, all these gauge-arbitrary phases cancel with each other and thus a gauge-independent quantity can be obtained. To see this specifically, we take four states as an example. By using Eq. (2.20), we get the total phase differences

$$\begin{aligned}\gamma &= \Delta\varphi_{12} + \Delta\varphi_{23} + \Delta\varphi_{34} + \Delta\varphi_{41}\\ &= -\mathrm{Im}\log\langle n(\boldsymbol{R}_1)|n(\boldsymbol{R}_2)\rangle\langle n(\boldsymbol{R}_2)|n(\boldsymbol{R}_3)\rangle\langle n(\boldsymbol{R}_3)|n(\boldsymbol{R}_4)\rangle\langle n(\boldsymbol{R}_4)|n(\boldsymbol{R}_1)\rangle.\end{aligned} \tag{2.21}$$

It is clear that the arbitrary phase in the bra vector cancels with its conjugate in the ket vector, so that the overall phase γ is gauge-invariant.

Now, consider a smooth circuit $\mathcal{C}$ in the parameter space and discretize it with a set of points on it. According to Eq. (2.20), the phase difference between any two contiguous points is

$$e^{-i\Delta\varphi} = \frac{\langle n(\boldsymbol{R})|n(\boldsymbol{R}+\Delta\boldsymbol{R})\rangle}{\big|\langle n(\boldsymbol{R})|n(\boldsymbol{R}+\Delta\boldsymbol{R})\rangle\big|}. \tag{2.22}$$

Assume the arbitrarily chosen phase varies in a differentiable way along the path, and to the leading order in $\Delta\boldsymbol{R}$ in Eq. (2.22), one can have [138]

$$-i\Delta\varphi = \langle n(\boldsymbol{R})|\nabla_{\boldsymbol{R}} n(\boldsymbol{R})\rangle \cdot \Delta\boldsymbol{R}, \tag{2.23}$$

where $e^{-i\Delta\varphi} \simeq 1 - i\Delta\varphi$ and $|n(\boldsymbol{R}+\Delta\boldsymbol{R})\rangle = |n(\boldsymbol{R})\rangle + |\nabla_{\boldsymbol{R}} n(\boldsymbol{R})\rangle \cdot \Delta\boldsymbol{R}$ have been used. In the limit where the discretized points become dense on the continuous path, the summation of the phase difference converge to a circuit integral,

$$\gamma = \sum_{l=1}^{L} \Delta\varphi_{l,l+1} \longrightarrow \oint_{\mathcal{C}} \underbrace{i\langle n(\boldsymbol{R})|\nabla_{\boldsymbol{R}} n(\boldsymbol{R})\rangle}_{\boldsymbol{\mathcal{A}}_n} \cdot d\boldsymbol{R}. \tag{2.24}$$

Thus the expression of Berry phase Eq. (2.12) is reproduced.

One can also gain more intuitive understanding of the geometrical nature of Berry phase from the concept of classical parallel transport in differential geometry (see Fig. 2.1). If a vector is parallel transported around a closed curve on the plane, it comes back unchanged. However, if it is parallel-transported around a closed path on a curved surface, the vector gets rotated by an angle α [135]

$$\alpha = \iint_{\mathcal{S}} \mathcal{K} \cdot d\boldsymbol{S}. \tag{2.25}$$

Here $\mathcal{K} = d\alpha/d\boldsymbol{S}$ is the Gaussian curvature, $d\alpha$ is the angle by which the vector rotates, when it is parallel-transported around an infinitesimal closed curve with area $d\boldsymbol{S}$. As a simple example, consider a vector moving along a closed curve on a sphere with radius r [Fig. 2.1(a)]. After completing the closed path, the vector obtains a rotated angle equal to the solid angle subtended by the loop at the sphere's centre, namely, $\alpha = S/r^2$, where S is the area enclosed by the loop and the Gaussian curvature of a sphere is $\mathcal{K} = 1/r^2$.

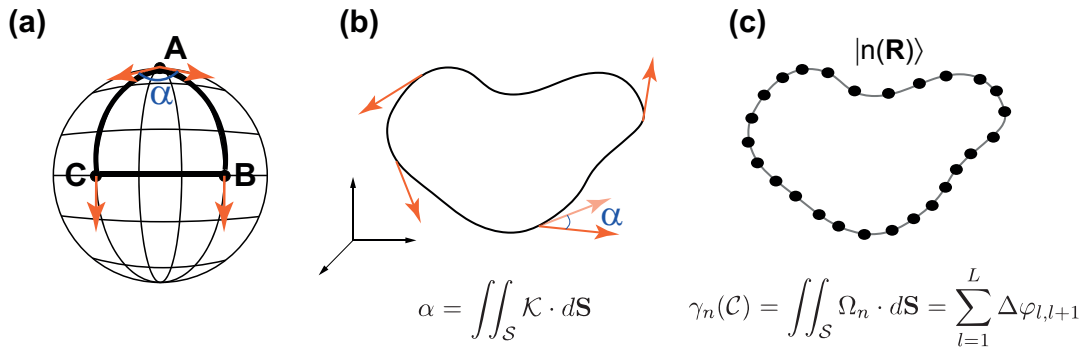

Figure 2.1: Illustration of geometrical phases generated along a closed curve. **(a)** The geometric phase of a vector moving on a sphere. Initially at the north pole, the vector is parallel-transported along the longitude $AB \rightarrow$ the equator $BC \rightarrow$ the longitude CA. Even though the vector has not been rotated relative to the surface of the sphere at any point along its route, it gets rotated by an angle α after returning the north pole. The angle α is given by the solid angle $\alpha = S/r^2$ with S being the area of the enclosed surface, and r is the radius of the shpere. **(b)** The geometric phase of a vector parallel transported on an arbitrary curved surface. After completing a closed path on the surface, a vector is rotated by an angle $\alpha = \iint_S \mathcal{K} \cdot d\boldsymbol{S}$, where $\mathcal{K}$ is the Guassian curvature. **(c)** The adiabatic evolution of a quantum state $|n(\boldsymbol{R}\rangle)$ along a smooth circuit in the parameter space. The quantum parallel transport of a state $|n\rangle$ means that $\langle n|\frac{d}{dt}|n\rangle = 0$. Namely, the change of a state cannot be along its own direction. After returning to the starting point, the state's phase is 'rotated' by the Berry phase $\gamma_n(\mathcal{C}) = \iint_S \boldsymbol{\Omega}_n \cdot d\boldsymbol{S}$, with Ω_n being the Berry curvature. The Berry phase can also be interpreted as the accumulation of the phase difference between the nearest neighbouring quantum states, as is defined in Eq. (2.20).

Manifestation in the Aharonov-Bohm effect

As a modern cornerstone of quantum mechanics, the Aharonov-Bohm (AB) effect, describes a phenomenon where a charged particle is affected by the vector potential $\boldsymbol{A}$, even though the particle is confined to a region in which both the electric field $\boldsymbol{E}$ and magnetic field $\boldsymbol{B}$ vanish [142]. One of the most common examples is to consider a double-slit experiment, in which a beam of electrons is split into two and then the two beams are made to interfere after passing along two different paths [see Fig. 2.2(a)]. The interference fringes can be observed in the intensity of the combined beams, and thus it demonstrates the fundamentally probabilistic nature of quantum mechanical phenomena. Now, what if an infinitely long thin solenoid (with magnetic field $\boldsymbol{B}$ only inside) is placed between the two paths? One might expect that the electron is unaffected, since outside the solenoid, both the electric field $\boldsymbol{E}$ and magnetic field $\boldsymbol{B}$ are zero and thus the Lorentz force also vanishes. However, in their original paper published in 1959, Aharonov and Bohm predicted that[9] the interference fringes will be shifted by altering

[9]Historically, Werner Ehrenberg and Raymond E. Siday first predicted the AB effect in a semi-classical way in 1949 [143]. After the publication of the 1959 paper, Bohm was informed of Ehrenberg and Siday's work,

the magnetic flux inside the long solenoid [145]. Such an effect was soon observed in laboratory by Chambers in 1960 [146], and further excellently confirmed[10] in an experiment by the group led by Tonomura in 1986 [147].

It turns out that the AB effect can be interpreted as a special case of the geometrical phase factor [9]. While the magnetic fields vanish outside the solenoid, the vector potentials $\boldsymbol{A}$ do not. According to the Stokes's theorem, the line integral of $\boldsymbol{A}$ around any loop $\mathcal{C}$ enclosing the solenoid equals to the magnetic flux Φ inside, i.e. $\oint_{\mathcal{C}} \boldsymbol{A} \cdot d\boldsymbol{R} = \Phi$, which also indicates that $\boldsymbol{A}$ falls off like $1/r$ with distance r from centre of the solenoid. Consider two electrons respectively travelling around the solenoid along two paths forming a closed loop, as shown in Fig. 2.2. The electron will interact with the solenoid in the way that its wavefunction accumulates a phase shift $\varphi = -e/\hbar \int \boldsymbol{A} \cdot d\boldsymbol{R}$. Thus, when the two electrons meet on the screen, they have accumulated a phase difference

$$\Delta\varphi = -\frac{e}{\hbar} \oint\!\!\!\!\!\!\int_{\mathcal{C}} \boldsymbol{A} \cdot d\boldsymbol{R} = -\frac{e}{\hbar}\Phi = \gamma_n(\mathcal{C}). \tag{2.26}$$

This phase difference equals to the Berry phase shown in Eq. (2.12), which also implies the analogy between the Berry connection and the vector potentials.

To have an intuitive picture, the AB effect can be made analogous to the classical parallel transport on a cone [135]. A cone may be formed by joining two straight edges at angle θ of a flat piece of paper [see Fig 2.2(b)]. As the paper is not stretched or compressed during this process, the cone has vanishing curvature except at the tip. Thus, away from the tip, a vector will move on the cone just like that on the flat paper. However, if the vector moves around a closed path that encloses the tip, it will accumulate a net rotation by the angle θ. Connecting to the AB effect, the curvature at the tip can be regarded as the magnetic field in the solenoid. The zero intrinsic curvature everywhere else corresponds to the vanishing $\boldsymbol{B}$ outside the solenoid. Thus, the rotated angle θ is analogous to the phase difference between the two wavefunctions of electrons, i.e. the Berry phase.

which was acknowledged in Bohm and Aharonov's subsequent paper in 1961 [144].

[10] Because of its non-obvious nature, the AB effect initially endured considerable scrutiny. By using a tiny toroidal magnet, the 1986 experiment showed excellent agreement with the theoretical prediction and answered all objections about stray fields and unphysical geometries [142].

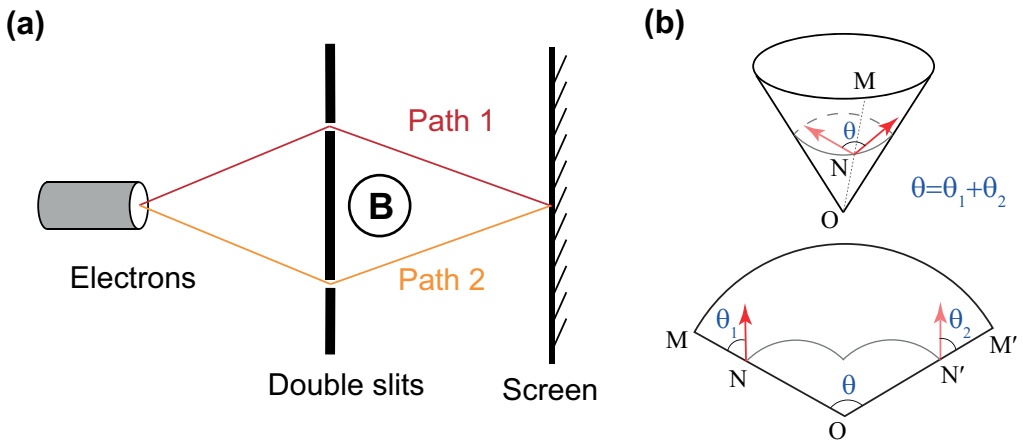

Figure 2.2: **(a)** Schematic illustration of the Aharonov-Bohm effect in a double-slit experiment. The electron beams are coherently split into two beams, which take path 1 and 2 respectively. These two paths form a closed circuit which encloses a solenoid with magnetic field **B** only inside. After meeting on the screen, the electrons accumulate a phase difference which equals to the geometrical phase. The magnetic flux enclosed by the closed circuit determines the phase difference and thus shifts the interference pattern on the screen. **(b)** The parallel transport of a vector on a cone as a classical analogy of the AB effect. The cone is formed by joining two edges OM and OM′ of a flat sheet of paper. After completing the closed path, the parallel transported vector is rotated by the angle θ on the cone. This angle is analogous to the Aharonov-Bohm phase shift and the apex of the cone corresponds to the magnetic filed (the Berry curvature) inside the solenoid.

2.2 Chern number

As shown in Eq. (2.13), the Berry phase can be expressed as the surface integral of the Berry curvature, namely the 'flux' of the Berry curvature. It turns out that such a flux remains meaningful even on a closed surface, such as a sphere or a torus. Importantly, the integral over a closed surface gives a quantized value, i.e.

$$\oiint_{\mathcal{S}} \Omega \cdot d\boldsymbol{S} = 2\pi C. \tag{2.27}$$

Here the integer C is called Chern number of the first class, or the first Chern number. As the Berry curvature is analogous to the magnetic field, the Chern number corresponds to the number of magnetic monopoles enclosed by the surface $\mathcal{S}$.

The proof of Eq. (2.27) is similar to that in Dirac's theory of the quantized magnetic monopole [148]. Assume the Berry curvature $\Omega(\boldsymbol{R})$ is regular and divergence-free on the closed surface $\mathcal{S}$. For simplicity, suppose $\mathcal{S}$ is a spherical surface centred at the origin and $\Omega(\boldsymbol{R})$ is singular at $\boldsymbol{R} = 0$. By cutting the surface along the equator, the integral over the whole closed surface in Eq. (2.27) is now divided into the fluxes through two open surfaces. These two

surfaces $\mathcal{S}_+$ and $\mathcal{S}_-$ share the same boundary $\mathcal{C}$, but have opposite normals $\vec{\mathbf{n}}$. Using Stokes theorem, one gets

$$\begin{aligned}\oiint_{\mathcal{S}} \Omega \cdot d\boldsymbol{S} &= \iint_{\mathcal{S}_+} \Omega \cdot \vec{\mathbf{n}} dS + \iint_{\mathcal{S}_-} \Omega \cdot \vec{\mathbf{n}} dS \\ &= \oint_{\mathcal{C}} \mathcal{A}_+ \cdot d\boldsymbol{R} - \oint_{\mathcal{C}} \mathcal{A}_- \cdot d\boldsymbol{R} \\ &= \gamma_+(\mathcal{C}) - \gamma_-(\mathcal{C}) = 2\pi \times \text{integer}. \end{aligned} \tag{2.28}$$

Here, $\mathcal{A}_\pm$ are the Berry connections on the same circuit and they may differ by a gauge transformation. The above equations prove that the surface integral in Eq. (2.27) are expressed as the difference between two Berry phases on the same closed path, which necessarily give rise to an integer multiple of 2π, as has also been shown in Eq. (2.10).

As a robust topological invariant, the first Chern number turns out to lay behind the the quantized Hall conductance in the integer quantum Hall effect. Historically, before Berry's publication in 1984, D. J. Thouless and co-workers have published the famous TKNN paper in 1982, where they obtained the explicit expressions for the quantized Hall conductance in integer quantum Hall effect [7]. It was B. Simon who applied Berry's idea to interpret the integers in the TKNN paper and made a connection between these two works [8]. Nowadays, the geometric and topological ideas laying behind the quantum Hall effect have drawn intensive attention and have had a significant impact on modern condensed-matter physics [137]. In the following sections we will see how topology enters into a crystalline system with periodic potentials.

2.3 Berry phase in Bloch bands

It is well know from solid state physics that a band structure of a periodic potential is specified by its energy. Nevertheless, sometimes the bands can also exhibit geometrical and topological features, which are related to how the wave functions change with the quasi-momentum across the Brillouin zone (BZ).

Consider the following Hamiltonian that describes a single particle moving in d-dimensional lattice potentials $V(\boldsymbol{r}) = V(\boldsymbol{r} + \boldsymbol{a}_i)$, with $\boldsymbol{a}_i$ being primitive lattice vectors ($i = 1, 2, \cdots, d$),

$$\hat{H} = -\frac{\hbar^2}{2m}\nabla^2 + V(\boldsymbol{r}), \tag{2.29}$$

where the momentum operator has been expressed in the position representation as $\hat{\boldsymbol{p}} = -i\hbar\nabla$. While in free space the energy of an atom is $p^2/2m$ with p the magnitude of momentum and atom mass m, this quadratic dispersion relation is fundamentally modified as forbidden energy regions appear as a consequence of the diffraction of the quantum mechanical waves in the periodic potentials. This gives rise to energy bands called Bloch bands. Due to the translational symmetry, the band structure can be derived from Bloch's theorem, which states that the eigenstates taking the form of a plane wave multiplied by a periodic function, i.e.

$$\psi_{n\boldsymbol{q}}(\boldsymbol{r}) = e^{i\boldsymbol{q}\cdot\boldsymbol{r}} u_{n\boldsymbol{q}}(\boldsymbol{r}). \tag{2.30}$$

They satisfy the following boundary condition,

$$\psi_{n\boldsymbol{q}}(\boldsymbol{r}+\boldsymbol{a}_i) = e^{i\boldsymbol{q}\cdot\boldsymbol{a}_i}\psi_{n\boldsymbol{q}}(\boldsymbol{r}), \tag{2.31}$$

for all the primitive lattice vectors $\boldsymbol{a}_i$, where n is the band index and the wave vector $\boldsymbol{q}$ is associated with the translational symmetry of the periodic potential. As $\hbar\boldsymbol{q}$ plays a role similar to momentum in free space, it is called the quasi-momentum (or crystal momentum). The periodic functions

$$u_{n\boldsymbol{q}}(\boldsymbol{r}+\boldsymbol{a}_i) = u_{n\boldsymbol{q}}(\boldsymbol{r}) \tag{2.32}$$

have the same periodicity as the lattice.

Plugging Eq. (2.30) into the Schrödinger equation $\hat{H}\psi_{n\boldsymbol{q}}(\boldsymbol{r}) = E_{n\boldsymbol{q}}\psi_{n\boldsymbol{q}}(\boldsymbol{r})$, one can straightforwardly find that $u_{n\boldsymbol{q}}(\boldsymbol{r})$ satisfies

$$\underbrace{\left[-\frac{\hbar^2}{2m}\left(\nabla+i\boldsymbol{q}\right)^2 + V(\boldsymbol{r})\right]}_{\hat{H}_{\boldsymbol{q}}} u_{n\boldsymbol{q}}(\boldsymbol{r}) = E_{n\boldsymbol{q}}u_{n\boldsymbol{q}}(\boldsymbol{r}). \tag{2.33}$$

This is equivalent to perform the unitary transformation $u_{n\boldsymbol{q}}(\boldsymbol{r}) = e^{-i\boldsymbol{q}\cdot\boldsymbol{r}}\psi_{n\boldsymbol{q}}(\boldsymbol{r})$, so that $u_{n\boldsymbol{q}}(\boldsymbol{r})$ become the eigenstates of the $\boldsymbol{q}$-dependent Hamiltonian $\hat{H}_{\boldsymbol{q}} = e^{-i\boldsymbol{q}\cdot\boldsymbol{r}}\hat{H}e^{i\boldsymbol{q}\cdot\boldsymbol{r}}$. Different from the original Hamiltonian Eq. (2.29), which is $\boldsymbol{q}$-independent, now both the transformed Hamiltonian $\hat{H}_{\boldsymbol{q}}$ and functions $u_{n\boldsymbol{q}}(\boldsymbol{r})$ are explicitly $\boldsymbol{q}$-dependent. What has been achieved here is that, different from $\psi_{n\boldsymbol{q}}(\boldsymbol{r})$ which live in different state spaces defined by the $\boldsymbol{q}$-dependent twisted boundary condition (2.31) in each unit cell of the lattice, all functions $u_{n\boldsymbol{q}}(\boldsymbol{r})$ obey the same boundary condition (2.32) and can thus be viewed as elements of the same state space.

Now, by identifying the $\boldsymbol{q}$-space (i.e. the Brillouin zone) as the parameter space of the Hamiltonian $\hat{H}_{\boldsymbol{q}}$ with the eigenstates denoted by $|u_{n\boldsymbol{q}}\rangle$, the formalism of the Berry phase can be applied. Namely, if $\boldsymbol{q}$ is forced to vary along a closed path in the quasi-momentum space, the Bloch state $|u_{n\boldsymbol{q}}\rangle$ will pick up a geometric phase

$$\gamma_n = i\oint_{\mathcal{C}} d\boldsymbol{q}\cdot\langle u_{n\boldsymbol{q}}|\nabla_{\boldsymbol{q}}u_{n\boldsymbol{q}}\rangle. \tag{2.34}$$

This phase γ_n is called the Berry phase in the n-th Bloch band.

To generate a closed path in momentum space, generally there are two ways. One way is to apply a magnetic field, that is able to induce a cyclotron motion along a closed path in $\boldsymbol{q}$-space [137]. Note that such a closed path is only possible in two- and three-dimensional (2D and 3D) systems. The other way is to apply an electric field (or a time-dependent vector potential), which can cause a linear variation in $\boldsymbol{q}$. Due to the periodicity of the Brillouin zone under the addition of the reciprocal lattice vector $\boldsymbol{G}$, a trajectory from $\boldsymbol{q}$ to $\boldsymbol{q}+\boldsymbol{G}$ thus forms a closed loop. Recall that the reciprocal lattice is constructed from the basis vectors $\{\boldsymbol{G}_i\}$ defined by $\boldsymbol{G}_i\cdot\boldsymbol{a}_j = 2\pi\delta_{ij}$. Usually, $\boldsymbol{q}$ is chosen to be restricted to the first Brillouin zone which is a defined primitive cell in reciprocal space.

The geometrical phase along a trajectory connecting points $\boldsymbol{q}$ and $\boldsymbol{q}+\boldsymbol{G}$ across the Brillouin zone, was obtained by Zak in 1989 as a way to characterize the energy bands and is now known as the *Zak phase* [149]:

$$\gamma_n^{\mathrm{Zak}} = i\int_{\boldsymbol{q}}^{\boldsymbol{q}+\boldsymbol{G}} d\boldsymbol{q}\cdot\langle u_{n\boldsymbol{q}}|\nabla_{\boldsymbol{q}}u_{n\boldsymbol{q}}\rangle. \tag{2.35}$$

The Zak phase can only be defined because of the torus topology of the Brillouin zone (i.e. the two points $\boldsymbol{q}$ and $\boldsymbol{q}+\boldsymbol{G}$ are identical), otherwise it would not be possible to complete a closed path. Due to the same reason, a non-trivial Zak phase can appear even in a one-dimensional (1D) parameter space. Especially, as a consequence of some symmetry, the Zak phase can be quantized. For example, γ_n^{Zak} is 0 or π in 1D crystals with inversion symmetry [149]. Generally, a non-trivial Zak phase characterizes various topological properties in 1D solids [137]. More recently, the Zak phase has also been measured by using ultracold atoms in a 1D optical lattice [122].

In dimensions higher than one, generally a rich structure of Berry phases appear [149]. In order to characterize the topological property of a given (non-degenerate) Bloch band with index n in 2D, the topological invariant, i.e. the first Chern number C_n (often and henceforth just called Chern number) is commonly employed. It is given by the integral of the Berry curvature $\boldsymbol{\Omega}_{n\boldsymbol{q}}$ over the closed surface of the first Brillouin zone (being a torus)

$$2\pi C_n = \iint_{BZ}\boldsymbol{\Omega}_{n\boldsymbol{q}}\cdot d^2q, \tag{2.36}$$

where the Berry curvature can be calculated according to Eq.(2.15). As argued before (see Eq. (2.27)), the Chern number in Eq. (2.36) is a gauge-invariant integer and represents the number of flux quanta of Berry curvature through the Brillouin zone. A Bloch band with non-vanishing Chern number is usually called a *Chern band*. It follows from the conservation law for the Berry curvature Eq. (2.18) that the total Chern number of all the Bloch bands vanish, i.e.

$$\sum_n C_n = 0. \tag{2.37}$$

Notice that for systems with time-reversal symmetry[11], the Chern number of each Bloch band always vanishes because under time reversal transformation, the eigenstates $u_{n,\boldsymbol{q}}(\boldsymbol{r}) \mapsto u^*_{n,-\boldsymbol{q}}(\boldsymbol{r})$ lead to the Berry curvatures $\Omega_{n,\boldsymbol{q}} = -\Omega_{n,-\boldsymbol{q}}$ as indicated in Eq. (2.14). Therefore, the realization of Chern bands requires a time-reversal symmetry breaking. In the following section 2.4, we introduce one paradigmatic topological model, namely the Harper-Hofstadter model, which breaks the TR symmetry via complex tunnelling matrix elements and thus host non-zero Chern numbers.

[11] The time reversal transformation indicates that time $t \mapsto -t$, momentum $k \mapsto -k$, magnetic fields $B \mapsto -B$, position wavefunctions $\psi(x) \mapsto \psi^*(x)$, while position $x \mapsto x$ and electric fields $E \mapsto E$ remain unchanged [150]. To justify the conjugate of wavefunction, one can see that while the wavefunction $\psi(t) = e^{-it\hat{H}/\hbar}\psi(t=0)$ satisfies the Schrödinger equation $i\hbar\partial_t\psi(t) = \hat{H}\psi(t)$, the transformed one $\psi^*(-t)$ also does.

2.4 Harper-Hofstadter model and its topology

The Harper-Hofstadter Hamiltonian is an iconic topological model from condensed matter theory, which describes charged particles moving in a 2D lattice with the presence of strong magnetic fields [118, 119]. The interplay between the underlying periodic potential and a uniform magnetic field $\boldsymbol{B}$ (which defines a magnetic length $\ell_B \propto B^{-1/2}$ that breaks the lattice symmetry) gives rise to a complex fractal energy spectrum known as Hofstadter's butterfly [119]. Of particular interest is the case where the magnetic field splits the original Bloch bands into topologically nontrivial ones characterized by finite Chern numbers. These are directly related to quantized Hall conductivity in IQH effect.

To arrive at the Harper-Hosftadter model, one can start with the following tight-binding Hamiltonian that describes a single particle in a 2D square lattice,

$$\hat{H}_0 = -\sum_{\langle \ell,\ell' \rangle} J \hat{a}^\dagger_{\ell'} \hat{a}_\ell, \tag{2.38}$$

where $\hat{a}_\ell$ ($\hat{a}^\dagger_\ell$) are the annihilation (creation) operators on site ℓ. The positive J is the tunnelling strength. Here the sum runs over all ordered pairs of nearest-neighbouring sites, so that the Hamiltonian is hermitian.

As has been discussed in section 2.3, the single particle eigenstates in the presence of a lattice potential are Bloch waves Eq. (2.30). It turns out that the periodic part $u_{n\boldsymbol{q}}(\boldsymbol{r})$ of low-energy bands possess pronounced maxima at the lattice potential minima. For *deep* lattices, the confinement on each single site is approximately harmonic and particles are *tightly* confined at lattice sites with separated vibrational energy levels. At low temperatures, particles are restricted to the lowest vibrational level and their kinetic energy is then frozen, except for tunnelling with small amplitudes to neighbouring sites [55]. The tunnelling matrix elements in Eq. (2.38) can be derived from Eq. (2.29) by expressing the Bloch functions in an alternative basis formed by orthonormal Wannier orbitals, which are exponentially localized at the lattice sites [151].

By assigning phases to the tunnelling matrix elements, the single-particle Hamiltonian with complex tunnelling parameters can be expressed as

$$\hat{H}'_0 = -\sum_{\langle \ell,\ell' \rangle} J e^{i\theta_{\ell'\ell}} \hat{a}^\dagger_{\ell'} \hat{a}_\ell, \tag{2.39}$$

where the phases $\theta_{\ell'\ell}$ are known as Peierls phases [152, 153]. In this case, a particle will accumulate the phases after hopping around the borders of each lattice plaquette denoted by P, as depicted in Fig. 2.3(a),

$$\Phi_P = \sum_P \theta_{\ell'\ell} \equiv 2\pi\alpha. \tag{2.40}$$

The accumulated phase Φ_P is analogous to the Aharonov-Bohm phase experienced by an electron moving in a magnetic field, as has been shown in Eq. (2.26),

$$\Phi_{AB} = -\frac{e}{\hbar} \oint_{\mathcal{C}} \mathbf{A} \cdot d\boldsymbol{R} \equiv -2\pi\Phi_B/\Phi_0, \tag{2.41}$$

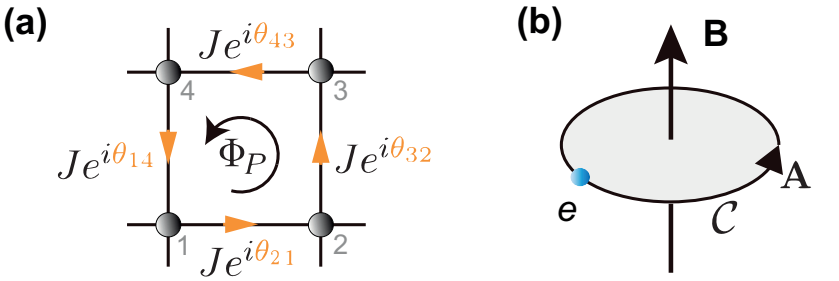

$\Phi_P = \theta_{21} + \theta_{32} + \theta_{43} + \theta_{14}$ $\quad$ $\Phi_{AB} = -\frac{e}{\hbar}\oint_{\mathcal{C}} \mathbf{A} \cdot d\mathbf{R}$

Figure 2.3: **(a)** Schematic illustration of the effective magnetic flux obtained from complex tunnelling amplitudes . **(b)** Illustration of the Aharonov-Bohm phase obtained by an electron moving along a closed path $\mathcal{C}$ with the presence of magnetic field $\mathbf{B} = \nabla \times \mathbf{A}$. This comparison shows that the Peierls phases $\theta_{\ell'\ell}$ play the role of vector potentials and Φ_P represents the effective magnetic flux per plaquette.

where Φ_B is the flux of applied magnetic field $\boldsymbol{B}$ and $\Phi_0 = h/e$ is the magnetic flux quantum, with h being the Planck constant, e the electron charge. Therefore, the Peierls phases $\theta_{\ell'\ell}$ play the role of vector potentials, and the flux Φ_P in Eq. (2.40) represents the effective magnetic flux per plaquette. Accordingly, $\alpha = \Phi_P/2\pi$ is the effective flux in units of the magnetic flux quantum. Note that for electrons in real magnetic fields, the Peierls phases can be expressed as the line integral of the vector potentials $\boldsymbol{A}$ between neighbouring sites, i.e. $\theta_{\ell'\ell} = -\frac{e}{\hbar}\int_{\boldsymbol{r}_\ell}^{\boldsymbol{r}_{\ell'}} \mathbf{A}(\boldsymbol{r}) \cdot d\boldsymbol{r}$. However, for charge neutral atoms, they are engineered differently, as will be shown below (see section 2.5.2).

Of particular interest, a 2D lattice with homogenous magnetic flux $\Phi_P \equiv \phi$ per plaquette is described by the famous Harper-Hofstadter Hamiltonian [118, 119]

$$\hat{H} = -J\sum_{m,n}\left(e^{i\theta^x_{m,n}}\hat{a}^\dagger_{m+1,n}\hat{a}_{m,n} + e^{i\theta^y_{m,n}}\hat{a}^\dagger_{m,n+1}\hat{a}_{m,n} + h.c.\right) \tag{2.42}$$

$$= -J\sum_{m,n}\left(e^{-i\phi n}\hat{a}^\dagger_{m+1,n}\hat{a}_{m,n} + \hat{a}^\dagger_{m,n+1}\hat{a}_{m,n} + h.c.\right), \tag{2.43}$$

where $\hat{a}_{m,n}$ are the annihilation operators on the sites labelled by (m,n), with m and n being the site indices along x and y, respectively. The uniform flux ϕ, defined modulo 2π, is determined by the Peierls phases $\theta^i_{m,n}$, $i = x, y$. While different choices of Peierls phase pattern (which reflects a gauge choice) affect the form of Hamiltonian and eigenstates, all physical observables (e.g. energy spectrum, density distribution *et al.*) are gauge-independent. The above Hamiltonian Eq. (2.43) has been written in the so-called Landau gauge $(\theta^x_{m,n}, \theta^y_{m,n}) = (-\phi n, 0)$ for simplicity. One can easily check that after hopping around each single plaquette, the particle picks up the phase ϕ corresponding to the magnetic flux, as can be seen in Fig. 2.4(a).

2.4.1 Magnetic translation symmetry

The existence of Bloch states, whose energies form Bloch bands, is a consequence of the discrete translational symmetry of the lattice. In a lattice with the presence of magnetic flux, however, the incommensurate magnetic length scale changes the symmetry of the system. The new symmetry can be revealed by the so-called magnetic translation operators (MTOs) denoted by $\hat{T}_x^M,\ \hat{T}_y^M$, which can be defined as [154, 155]

$$\hat{T}_x^M = \sum_{m,n} e^{i\chi^x_{m,n}} |m+1,n\rangle\langle m,n|, \quad \hat{T}_y^M = \sum_{m,n} e^{i\chi^y_{m,n}} |m,n+1\rangle\langle m,n|, \tag{2.44}$$

where we employ the lattice basis $\{|m,n\rangle\}$ with $|m,n\rangle = \hat{a}^\dagger_{m,n}|0\rangle$ and $|0\rangle$ being the vacuum state. The phases $\chi^{x,y}_{m,n}$ are determined by imposing the commutation $[\hat{T}^M_{x,y}, \hat{H}] = 0$ and take the following form,

$$\chi^x_{m,n} = \theta^x_{m,n} + \phi n, \quad \chi^y_{m,n} = \theta^y_{m,n} - \phi m, \tag{2.45}$$

with $\phi = \theta^x_{m,n} + \theta^y_{m+1,n} - \theta^x_{m,n+1} - \theta^y_{m,n}$ being the flux per plaquette.

It interesting to note that the magnetic translation operators satisfy

$$\hat{T}_x^M \hat{T}_y^M = e^{i\phi} \hat{T}_y^M \hat{T}_x^M. \tag{2.46}$$

The above equation indicates that the action of magnetic translation operators around the borders of one lattice unit cell simply picks up the pierced flux, see Fig. 2.4(b). This suggests a way to construct commuting operators by successive application of $\hat{T}_x,\ \hat{T}_y$, so that a super-cell with integer multiples of 2π can be enclosed. From Eq. (2.46) one immediately gets

$$\left(\hat{T}_x^M\right)^k \left(\hat{T}_y^M\right)^l = \left(\hat{T}_x^M\right)^{k-1} e^{i\phi\cdot l} \left(\hat{T}_y^M\right)^l \hat{T}_x^M = e^{i\phi\cdot kl} \left(\hat{T}_y^M\right)^l \left(\hat{T}_x^M\right)^k, \tag{2.47}$$

where $(\hat{T}_x^M)^k$ represents a translation by k lattice constants along x and $(\hat{T}_y^M)^l$ corresponds to a translation by l lattice constants along y. Therefore, in the case of rational values of flux per plaquette $\alpha = \phi/2\pi \equiv p/q$, where p, q are relatively prime, the commutation $[(\hat{T}_x^M)^k, (\hat{T}_y^M)^l] = 0$ is achieved for $kl = q \times$ integers, and the smallest super-cell given by $kl = q$ is called *magnetic unit cell*, that is q times larger than the lattice unit cell, see Fig. 2.4(c).

Now, the new operators $(\hat{T}_x^M)^k,\ (\hat{T}_y^M)^l$ and the Hamiltonian $\hat{H}$ (2.43) form a complete set of commuting operators and they share the simultaneous eigenstates. Based on these new magnetic translation symmetries, the eigenstate wave-functions $\Psi_{m,n}$ can be found by formulating the following generalized Bloch theorem,

$$\begin{aligned} (\hat{T}_x^M)^k \Psi_{m,n} &= \Psi_{m+k,n} = e^{ik_x ka} \Psi_{m,n} \\ (\hat{T}_y^M)^l \Psi_{m,n} &= \Psi_{m,n+l} = e^{ik_y la} \Psi_{m,n} \end{aligned} \tag{2.48}$$

where a denotes the lattice constant and $k_x,\ k_y$ are defined within the first *magnetic Brillouin zone*, $-\pi/(ka) \le k_x < \pi/(ka), -\pi/(la) \le k_y < \pi/(la)$.

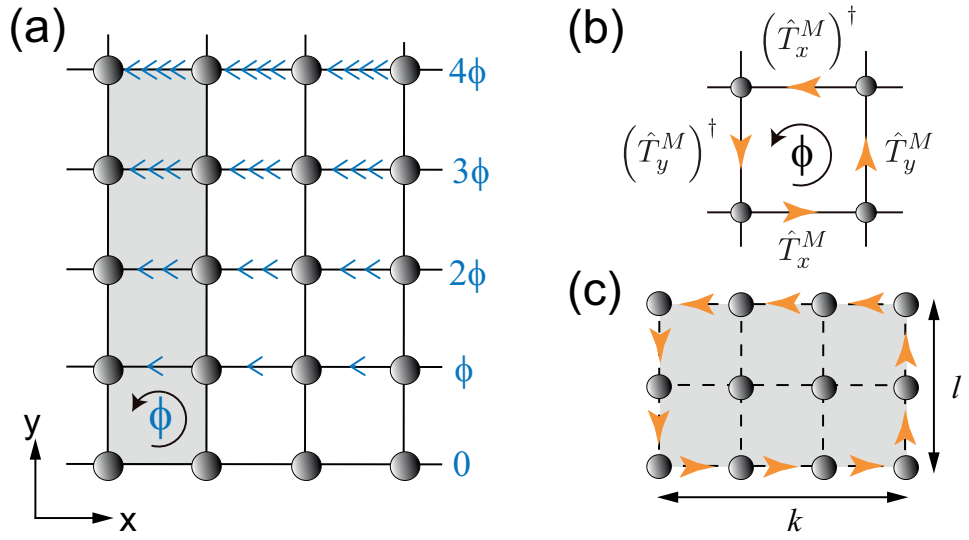

Figure 2.4: **(a)** Sketch of the Harper-Hofstadter model in Landau gauge. Each arrow represents the Peierls phase of one ϕ. For $\alpha = 1/4$, the magnetic unit cell oriented along y is indicated by the shadow region, which is four times larger than the usual lattice unit cell. **(b)** Applications of magnetic translation operators around one lattice unit cell. After completing one the unit cell, the ground state accumulate a phase of ϕ, i.e. $\left(\hat{T}_y^M\right)^\dagger \left(\hat{T}_x^M\right)^\dagger \hat{T}_y^M \hat{T}_x^M |\psi_{m,n}\rangle = e^{i\phi}|\psi_{m,n}\rangle$. **(c)** Successive applications of magnetic translation operators around one super-cell of size kl. The accumulated phases after completing this super-cell becomes $kl\phi$.

2.4.2 Energy spectrum

To solve the Schrödinger equation, we first apply th expressions of magnetic translation operators shown in Eqs. (2.44) and (2.45) for the Hamiltonian (2.43) written in Landau gauge $(\theta^x_{m,n}, \theta^y_{m,n}) = (-\phi n, 0)$,

$$\hat{T}^M_x = \sum_{m,n} |m+1,n\rangle\langle m,n|, \quad \hat{T}^M_y = \sum_{m,n} e^{-i\phi m}|m,n+1\rangle\langle m,n|. \tag{2.49}$$

For flux $\alpha = p/q$, the magnetic unit cell of size $kl = q$ can be chosen to be oriented along the y-direction with dimensions $(1 \times q)$. The corresponding commuting magnetic translation operators are given by

$$\begin{aligned} \hat{T}^M_x &= \sum_{m,n} |m+1,n\rangle\langle m,n|, \\ \left(\hat{T}^M_y\right)^q &= \sum_{m,n} e^{-i\phi mq}|m,n+q\rangle\langle m,n| = \sum_{m,n} |m,n+q\rangle\langle m,n|, \end{aligned} \tag{2.50}$$

where $\phi = 2\pi p/q$ indicates the phases $\phi mq = 2\pi mp$.

To fulfill the generalized Bloch theorem (2.48),

$$\begin{aligned} \hat{T}^M_x \Psi_{m,n} &= \Psi_{m+1,n} = e^{ik_x a}\Psi_{m,n}, \\ (\hat{T}^M_y)^q \Psi_{m,n} &= \Psi_{m,n+q} = e^{ik_y qa}\Psi_{m,n}, \end{aligned} \tag{2.51}$$

one can make the following ansatz for the wave-functions

$$\Psi_{m,n} = e^{ik_x ma}e^{ik_y na}\psi_n, \quad \psi_{n+q} = \psi_n, \tag{2.52}$$

where $k_x,\ k_y$ are defined in the first magnetic Brillouin zone as $-\pi/a \leq k_x < \pi/a, -\pi/(qa) \leq k_y < \pi/(qa)$.

The eigenstates can be expressed in the lattice basis as

$$|\Psi\rangle = \sum_{m,n} \Psi_{m,n}|m,n\rangle. \tag{2.53}$$

Thus $|\Psi_{m,n}|^2$ represents the probability density of a particle occupying site (m,n). Inserting the above expression into the time-independent Schrödinger equation $\hat{H}|\Psi\rangle = E|\Psi\rangle$ associated with Hamiltonian (2.43), one gets

$$\hat{H}|\Psi\rangle = -J\sum_{m,n}\left(e^{-i\phi n}\Psi_{m,n}|m+1,n\rangle + e^{i\phi n}\Psi_{m+1,n}|m,n\rangle + \Psi_{m,n}|m,n+1\rangle + \Psi_{m,n+1}|m,n\rangle\right). \tag{2.54}$$

Multiplying the above equation with a bra $\langle m,n|$ gives

$$\begin{aligned} E\Psi_{m,n} &= \langle m,n|E|\Psi\rangle \\ &= \langle m,n|\hat{H}|\Psi\rangle = -J\left(e^{-i\phi n}\Psi_{m-1,n} + e^{i\phi n}\Psi_{m+1,n} + \Psi_{m,n-1} + \Psi_{m,n+1}\right) \end{aligned} \tag{2.55}$$

By applying the ansatz Eq. (2.52) one arrives at

$$E\psi_n = -J\left(2\cos(\phi n + k_x a)\psi_n + e^{-ik_y a}\psi_{n-1} + e^{ik_y a}\psi_{n+1}\right). \tag{2.56}$$

Due to the magnetic translational invariance, considering only one magnetic unit cell (with size $1 \times q$) is enough. Therefore, the problem reduces to solve the eigenvalue equation of a $q \times q$ matrix,

$$E(\boldsymbol{k}) \begin{pmatrix} \psi_0 \\ \psi_1 \\ \vdots \\ \psi_{q-1} \end{pmatrix} = \hat{H}(\boldsymbol{k}) \begin{pmatrix} \psi_0 \\ \psi_1 \\ \vdots \\ \psi_{q-1} \end{pmatrix}, \tag{2.57}$$

with the matrix expressed as

$$\hat{H}(\boldsymbol{k}) = -J \begin{pmatrix} h_0 & e^{ik_y a} & 0 & \cdots & 0 & e^{-ik_y a} \\ e^{-ik_y a} & h_1 & e^{ik_y a} & 0 & \cdots & 0 \\ 0 & e^{-ik_y a} & h_2 & e^{ik_y a} & \cdots & 0 \\ 0 & 0 & e^{-ik_y a} & h_3 & \cdots & 0 \\ \vdots & \vdots & \vdots & \vdots & \ddots & \vdots \\ e^{ik_y a} & 0 & \cdots & 0 & e^{-ik_y a} & h_{q-1} \end{pmatrix}, \tag{2.58}$$

where $h_n = 2\cos(\phi n + k_x a)$ has been introduced for simplicity, and the two terms $e^{\pm ik_y a}$ at the corners are due to the periodic boundary condition $\psi_{-1} = \psi_{q-1}, \psi_q = \psi_0$ according to Eq. (2.52).

For vanishing magnetic fields (thus $\psi_{n-1} = \psi_n = \psi_{n+1}$), as indicated in Eq. (2.56), the system shows a single energy band with dispersion relation $E(\boldsymbol{k}) = -2J(\cos(k_x a) + \cos(k_y a))$. In the presence of a rational flux $\phi = 2\pi\alpha = 2\pi p/q$ per plaquette, the single band fragments into q bands, with the dispersion relations $E_\mu(\boldsymbol{k})$ ($\mu = 1, \cdots, q$) determined from solving the eigenvalues of Eq. (2.58). By plotting the energy versus rational values of α, one obtains the fractal structure of the so-called Hofstadter butterfly [12], as shown in Fig. 2.5(a). Taking $\alpha = 1/4$ as an example, the complete energy bands are plotted in Fig. 2.5(b), which shows $q = 4$ sub-bands.

[12] Interesting self-repeated structures also appear in other lattice geometries with magnetic fields, including hexagonal lattice, kagome lattice, Penrose tiling lattice *et al.* [156].

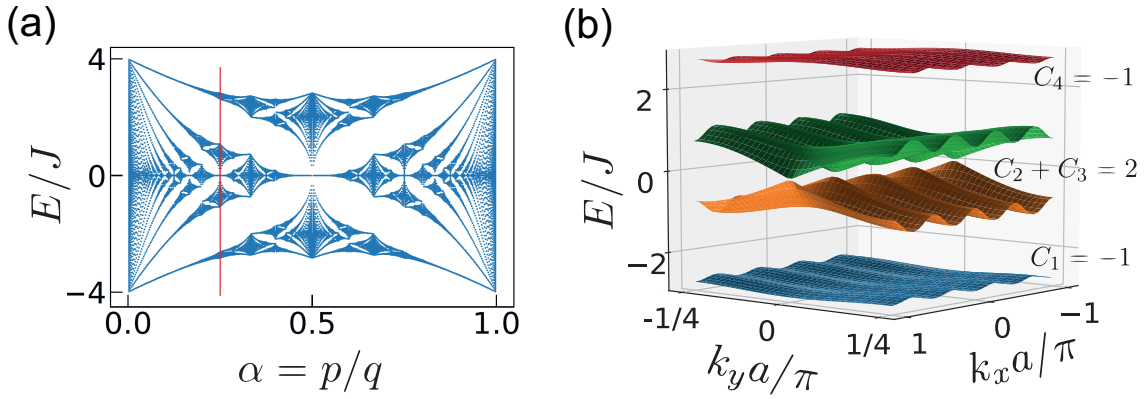

Figure 2.5: (a) Hofstadter butterfly. The vertical red line indicate $\alpha = 1/4$. The plot is obtained by numerically solving Eq. (2.58) with $q = 400$ and $p = 1, 2, \cdots, q-1$. Note that the values of k_x and k_y do not change the fractal structure. (b) The single-particle energy spectrum at $\alpha = 1/4$. The lowest band and the top band share the same Chern number -1 and the sum of Chern numbers of the middle two bands is 2.

2.4.3 Chern number of Hofstadter bands

The topological properties of the energy bands can be characterized by the Chern number. After solving the eigenvalue equation (2.57), the Chern number of j-th band is determined by applying Eq. (2.36),

$$2\pi C_j = \iint_{BZ} \Omega_{j\boldsymbol{k}} \cdot dk_x dk_y, \tag{2.59}$$

$$\Omega_{j\boldsymbol{k}} \equiv \boldsymbol{\Omega}_j(k_x, k_y) = i\left[\langle \partial_{k_x} j | \partial_{k_y} j\rangle - \langle \partial_{k_y} j | \partial_{k_x} j\rangle\right] \tag{2.60}$$

$$= i\left[\sum_{j' \neq j} \frac{\langle j|\partial_{k_x}\hat{H}|j'\rangle\langle j'|\partial_{k_y}\hat{H}|j\rangle}{\left(E_j - E_{j'}\right)^2} - (k_x \leftrightarrow k_y)\right], \tag{2.61}$$

where we have used $|j\rangle \equiv |j(k_x, k_y)\rangle$ to denote the eigenstates and $|\partial_k j\rangle \equiv \partial|j\rangle/\partial k$ for short. Note that as it can not be guaranteed to define the phase of eigenstates smoothly over the entire Brillouin zone. Instead of calculating the differentiation on the eigenstates in Eq. (2.60), applying Eq. (2.61) with $\partial_k \hat{H} \equiv \hat{H}(k + dk) - \hat{H}(k)$ is thus particularly useful for numerical calculations. The derivation of Eq. (2.61) can be found in Eq. (2.15).

After the following discretization,

$$\begin{aligned} k_x &= 2\pi \frac{n_x}{N_x}, \quad n_x = 0, 1, \cdots, N_x - 1, \\ k_y &= \frac{2\pi}{q}\frac{n_y}{N_y}, \quad n_y = 0, 1, \cdots, N_y - 1, \end{aligned} \tag{2.62}$$

the Chern number can be obtained from summing over the discretized quasi-momenta for

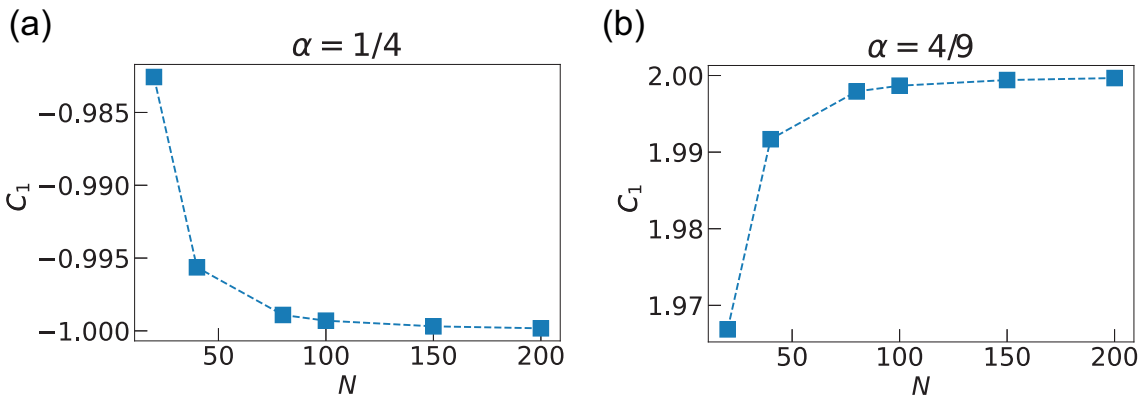

Figure 2.6: Chern number of the lowest band C_1 of the system with (a) $\alpha = 1/4$, (b) $\alpha = 4/9$. We have used the same number $N_x = N_y = N$ for discretization.

sufficiently large values of N_x, N_y. As shown in Fig. 2.6, taking $\alpha = 1/4, 4/9$ for example, the corresponding Chern number of the lowest band are found to saturate at $C_1 = -1, 2$ respectively.

The same procedure can be applied for each band separately. However, for the two middle bands with touching points, e.g. as shown in Fig. 2.5(b), the above formula cannot be directly applied. According to the conservation of Chern number mentioned in Eq. (2.37), the sum of Chern numbers of the two middle bands can be estimated as $C_{mid} = C_2 + C_3 = -C_1 - C_4 = 2$, with the Chern number of top band $C_4 = C_1 = -1$. This result can be further confirmed by either analytical solutions [13] based on a Diophantine equation [155, 157], or numerical calculation according to Ref. [158].

2.4.4 Symmetry consideration

We have shown that the broken time-reversal symmetry allows for non-zero Chern numbers; the magnetic translational symmetry guarantees a generalized Bloch theorem. As another important property of the HH model, the particle-hole symmetry gives rise to both an energy spectrum and Chern numbers that are symmetric with respect to zero energy $E = 0$.

Consider the transformation $\Psi_{m,n} \to \tilde{\Psi}_{m,n} = (-1)^{m+n}\Psi_{m,n}$ and apply it in Eq. (2.55), one gets [155]

$$-E\tilde{\Psi}_{m,n} = -J\left(e^{-i\phi n}\tilde{\Psi}_{m-1,n} + e^{i\phi n}\tilde{\Psi}_{m+1,n} + \tilde{\Psi}_{m,n-1} + \tilde{\Psi}_{m,n+1}\right). \tag{2.63}$$

Comparing the above equation with Eq. (2.55), one can find that it simply modifies the energy as $E \to -E$. Therefore, the existence of a state $\Psi_{m,n}$ with energy E indicates that there also exists a state $\tilde{\Psi}_{m,n}$ with opposite energy $-E$.

According to the generalized Bloch theorem (2.48), one can make a similar ansatz as Eq. (2.52)

[13] The total Chern number of bands with touching points read $C_{\text{mid}} = q - 2$ for r even and $C_{\text{mid}} = q - 1$ for r odd, where r denotes the r-th energy gap of the Hofstadter spectrum [155, 157]. Thus, the sum of Chern numbers of the two middle bands corresponding to $\alpha = 1/4$ is $C_{mid} = C_2 + C_3 = q - 2 = 2$.

for the new state $\tilde{\Psi}_{m,n} = e^{ik_x ma} e^{ik_y na} \tilde{\psi}_n$, $\tilde{\psi}_{n+q} = \tilde{\psi}_n$. After applying it to Eq. (2.63), one finds

$$E\tilde{\psi}_n = -J\left(2\cos(\phi n + k_x a + \pi)\tilde{\psi}_n + e^{-i(k_y a+\pi)}\tilde{\psi}_{n-1} + e^{i(k_y a+\pi)}\tilde{\psi}_{n+1}\right), \tag{2.64}$$

where the minus sign in energy has been absorbed in the coefficients on the right-hand side of the equation by a π shift in the quasi-momenta. Therefore, the similarity between Eqs. (2.56) and (2.64) implies that the eigenstates associated with positive energies are related to corresponding states with negative ones according to

$$\psi_n(k_x, k_y) = \tilde{\psi}_n(k_x + \pi/a, k_y + \pi/a). \tag{2.65}$$

Consequently, the Berry curvature of the n-th band with positive energies is related to the Berry curvature of the $\tilde{n}$-th band with negative energies via

$$\mathbf{\Omega}_n(k_x, k_y) = \Omega_{\tilde{n}}(k_x + \pi/a, k_y + \pi/a). \tag{2.66}$$

Therefore, after integrating the Berry curvatures over first BZ, the resulting Chern number of the bands with opposite energies are identical. That is, the Chern numbers have a symmetric distribution with respect to $E = 0$, as has been exemplified for $\alpha = 1/4$ with $C_1 = C_4 = -1$.

2.5 Floquet engineering

In order to measure the topological properties in the HH model, a prerequisite is to realize the model in a real experiment, which has been a challenging task. This is mainly because extremely strong magnetic fields are needed for electrons in solid-state lattices. Namely, to achieve the order of one flux quantum per plaquette in real solid state systems, where the lattice constants are rather small (on the order of a few angstroms), the magnetic fields need to be up to 10^4 Tesla which are unfeasible in present-day laboratory. Considering, in turn, ultracold atoms in optical lattices, extremely strong artificial magnetic fields can be achieved by using Floquet engineering. After the first realization of the HH model by using ultracold atoms [120, 121], the Chern number of the lowest band has also been measured recently [124]. In this section, we shall briefly review the formalism of Floquet engineering by following Refs. [71, 159], after which we will see how it can be applied to engineer the desired HH model[14].

2.5.1 General properties

Consider a Floquet system, namely a periodically driven quantum system that is described by a time-periodic Hamiltonian

$$\hat{H}(t) = \hat{H}(t + T), \tag{2.67}$$

with $T = 2\pi/\omega$ being the driving period.

[14]Note that the Floquet engineering has also been employed to realize the Haldane model [112–114].

Floquet states

Similar to the existence of Bloch states (2.30) in spatially periodic systems, there exist generalized stationary states in a time-periodic system, which are called Floquet states $|\psi_n(t)\rangle$. They have the following form

$$|\psi_n(t)\rangle = e^{-i\varepsilon_n t/\hbar}|u_n(t)\rangle,\ |u_n(t)\rangle = |u_n(t+T)\rangle \tag{2.68}$$

with real quasienergy ε_n that determines the linear phase evolution and the time-periodic Floquet mode $|u_n(t)\rangle$ that represents the so-called micromotion. The Floquet states are solutions of the time-dependent Schrödinger equation

$$i\hbar d_t|\psi(t)\rangle = \hat{H}(t)|\psi(t)\rangle, \tag{2.69}$$

where d_t denotes the time derivative.

Using $\hat{U}(t_2,t_1)$ to denote the time evolution operator from time t_1 to t_2, it turns out that the Floquet states are eigenstates of the time-evolution operator over one driving period,

$$\hat{U}(t+T,t)|\psi_n(t)\rangle = |\psi_n(t+T)\rangle = e^{-i\varepsilon_n T/\hbar}|\psi_n(t)\rangle, \tag{2.70}$$

with $e^{-i\varepsilon_n T/\hbar}$ being the eigenvalues. Thus at any fix time t, the Floquet states can be chosen to form a complete orthonormal basis. The time evolution operator can thus be written as

$$\hat{U}(t_2,t_1) = \sum_n |\psi_n(t_2)\rangle\langle\psi_n(t_1)| = \sum_n e^{-i\varepsilon_n(t_2-t_1)/\hbar}|u_n(t_2)\rangle\langle u_n(t_1)|. \tag{2.71}$$

Accordingly, the time evolution of a state $|\psi(t)\rangle$ can be expressed as

$$|\psi(t)\rangle = \hat{U}(t,t_0)|\psi(t_0)\rangle = \sum_n c_n e^{-i\varepsilon_n t/\hbar}|u_n(t)\rangle, \tag{2.72}$$

where we have applied Eq. (2.71) in the second equation and $c_n = e^{i\varepsilon_n t_0/\hbar}\langle u_n(t_0)|\psi(t_0)\rangle$ are time-independent coefficients. The above equation implies that (i) if the system is initially prepared in a single Floquet state $n = n_0$, its time evolution will be periodic and be dermined by the single Floquet mode $|u_{n_0}(t)\rangle$ (apart from an irrelevant overall phase factor $e^{-i\varepsilon_{n_0}t/\hbar}$); (ii) if the system is prepared in a coherent superposition of several Floquet states, the evolution will not be periodic any more. Besides the contribution from the (periodic) time dependence of Floquet modes $|u_n(t)\rangle$, namely the micromotion, the evolution will also be affected by the dephasing factors $e^{-i\varepsilon_n t/\hbar}$. Thus the deviations from a periodic evolution are governed by the quasienergies ε_n, in a fashion like the time evolution of an autonomous system (with time-independent Hamiltonian) is governed by the energies of the stationary states.

Floquet Hamiltonian and micromotion operator

A nice property of the Floquet formalism is that the behaviour of a periodically driven system can be effectively captured by a time-independent Hamiltonian. By treating the dynamics in a stroboscopic fashion, i.e. in steps of the driving period T, the time evolution can be described

by the so-called Floquet Hamiltonian $\hat{H}^F_{t_0}$, which is defined to generate the time evolution over one period,

$$\hat{U}(t_0+T,t_0)=\exp\left(-\frac{i}{\hbar}T\hat{H}^F_{t_0}\right), \tag{2.73}$$

where t_0 denotes initial time. Comparing the above definition with Eq. (2.70), one can immediately see that the Floquet modes $|u_n(t_0)\rangle$ and quasienergies ε_n are respectively the eigenstates and eigenvalues of the Floquet Hamiltonian, i.e.

$$\hat{H}^F_{t_0}|u_n(t_0)\rangle=\varepsilon_n|u_n(t_0)\rangle. \tag{2.74}$$

Thus the Floquet Hamiltonian can also be expressed as

$$\hat{H}^F_{t_0}=\sum_n \varepsilon_n|u_n(t_0)\rangle\langle u_n(t_0)|. \tag{2.75}$$

While the Floquet modes $|u_n(t_0)\rangle$ at initial time t_0 can be obtained from the diagonalization of $\hat{H}^F_{t_0}$ via Eq. (2.74), the (periodic) time dependence of the Floquet modes, i.e. the micromotion, can be conveniently described by defining a two-point micromotion operator

$$\hat{U}_F(t_2,t_1)=\sum_n |u_n(t_2)\rangle\langle u_n(t_1)|. \tag{2.76}$$

Apparently, it evolves the Floquet modes in time,

$$|u_n(t_2)\rangle=\hat{U}_F(t_2,t_1)|u_n(t_1)\rangle, \tag{2.77}$$

and it is periodic in both arguments $\hat{U}_F(t_2,t_1)=\hat{U}_F(t_2,t_1+T)=\hat{U}_F(t_2+T,t_1)$ individually.

Note that in terms of the Floquet Hamiltonian and the micromotion operator, the time evolution operator can be expressed as

$$\hat{U}(t_2,t_1)=e^{-i(t_2-t_1)\hat{H}^F_{t_2}/\hbar}\hat{U}_F(t_2,t_1)=\hat{U}_F(t_2,t_1)e^{-i(t_2-t_1)\hat{H}^F_{t_1}/\hbar}. \tag{2.78}$$

This can be easily checked. For instance, one has

$$\begin{aligned}\hat{U}_F(t_2,t_1)e^{-i(t_2-t_1)\hat{H}^F_{t_1}/\hbar}|\psi(t_1)\rangle&=\hat{U}_F(t_2,t_1)e^{-i(t_2-t_1)\hat{H}^F_{t_1}/\hbar}e^{-i\varepsilon t_1/\hbar}|u(t_1)\rangle\\&=\underbrace{e^{-i(t_2-t_1)\varepsilon/\hbar}e^{-i\varepsilon t_1/\hbar}}_{e^{-i\varepsilon t_2/\hbar}}\underbrace{\hat{U}_F(t_2,t_1)|u(t_1)\rangle}_{|u(t_2)\rangle}\\&=|\psi(t_2)\rangle=\hat{U}(t_2,t_1)|\psi(t_1)\rangle.\end{aligned} \tag{2.79}$$

Extended Hilbert space

According to Eq. (2.70), the Floquet states and their quasienergies could be obtained by solving the eigenvalue problem of the time evolution operator over one period. However, what is uniquely determined from this calculation are the Flqouet states $|\psi_n(t)\rangle$ and the phase factors $e^{-i\varepsilon_n T/\hbar}$, rather than the quasienergies ε_n. Note that the phase factors remain unchanged after

adding integer multiples of $\hbar\omega$ to the quasienergy. Thus, starting from a possible value ε_n one can denote all choices for the quasienergies as

$$\varepsilon_{nm} = \varepsilon_n + m\hbar\omega. \tag{2.80}$$

Due to this, the corresponding Floquet modes $|u_n(t)\rangle = e^{i\varepsilon_n t/\hbar}|\psi_n(t)\rangle$ and the Floquet Hamiltonian (2.75) are not uniquely defined as well. Since the Floquet states are unique,

$$|\psi_n(t)\rangle = e^{-i\varepsilon_n t/\hbar}|u_n(t)\rangle = e^{-i\varepsilon_{nm} t/\hbar}\underbrace{e^{im\omega t}|u_n(t)\rangle}_{|u_{nm}(t)\rangle}, \tag{2.81}$$

the Floquet modes are accordingly modified as

$$|u_n(t)\rangle \to |u_{nm}(t)\rangle = e^{im\omega t}|u_n(t)\rangle. \tag{2.82}$$

Applying the modified form of Floquet states Eq. (2.81) into the Schrödinger equation Eq. (2.69), one has

$$\left[\hat{H}(t) - i\hbar d_t\right]|u_{nm}(t)\rangle = \varepsilon_{nm}|u_{nm}(t)\rangle. \tag{2.83}$$

This equation can now be interpreted as an eigenvalue problem in an extended Hilbert space $\mathcal{F} = \mathcal{H} \otimes \mathcal{L}_T$, where $\mathcal{H}$ is the Hilbert space of a quantum system (with the quasienergies lying within the interval of width $\hbar\omega$), and $\mathcal{L}_T$ represents the space of T-periodically time-dependent functions. A complete set of orthonormal basis states of $\mathcal{F}$ thus can be chosen as

$$|\alpha m(t)\rangle = |\alpha\rangle e^{im\omega t}, \tag{2.84}$$

where $\{|\alpha\rangle\}$ is an orthonormal basis of $\mathcal{H}$ and the indices m label the complete set of time-periodic functions $e^{im\omega t}$.

To make a distinction, for states $|u(t)\rangle$ at time t in $\mathcal{H}$, a double ket notation $|u\rangle\!\rangle$ is used for elements in $\mathcal{F}$, where time t is treated as another intrinsic coordinate. Accordingly, the scalar product in $\mathcal{F}$ is defined as

$$\langle\!\langle u|v\rangle\!\rangle = \frac{1}{T}\int_0^T dt\langle u(t)|v(t)\rangle, \tag{2.85}$$

which combines the scalar product in $\mathcal{H}$ with time average over driving period T.

Meanwhile, an operator acting in $\mathcal{F}$ will be marked by an overbar. For instance, in $\mathcal{H}$ the operator $\hat{Q}$ introduced as

$$\hat{Q} = \hat{H}(t) - i\hbar d_t, \tag{2.86}$$

is correspondingly denoted as $\bar{Q}$ in $\mathcal{F}$. Now Eq. (2.83) becomes an eigenvalue problem of $\bar{Q}$,

$$\bar{Q}|u_{nm}\rangle\!\rangle = \varepsilon_{nm}|u_{nm}\rangle\!\rangle. \tag{2.87}$$

The operator $\bar{Q}$ is called quasienergy operator and is hermitian in $\mathcal{F}$.

The above equation (2.87) actually represents one of the advantages of going to the extended space $\mathcal{F}$ (via treating time t as an intrinsic coordinate), since the time-dependent Schrödinger equation (2.83) is now converted to a 'time-independent' one. In this case, methods or intuition

from the physics of systems described by time-independent Hamiltonian can be employed to diagonalize the quasienergy operator $\bar{Q}$, from which the Floquet modes and quasienergies can be straightforwardly computed. However, the cost is that the Hilbert space is drastically increased. To see this, one can now write down the matrix elements of the quasienergy operator $\bar{Q}$ in the basis $|\alpha m\rangle\!\rangle$ of $\mathcal{F}$,

$$\begin{aligned}
\langle\!\langle \alpha' m'|\bar{Q}|\alpha m\rangle\!\rangle &= \frac{1}{T}\int_0^T dt e^{-im'\omega t}\langle\alpha'|\left(\hat{H}(t)-i\hbar d_t\right)|\alpha\rangle e^{im\omega t} \\
&= \frac{1}{T}\int_0^T dt\left[e^{-im'\omega t}\langle\alpha'|\hat{H}(t)|\alpha\rangle e^{im\omega t} - e^{-im'\omega t}\langle\alpha'|\alpha\rangle\left(i\hbar d_t e^{im\omega t}\right)\right] \\
&= \langle\alpha'|\underbrace{\frac{1}{T}\int_0^T dt e^{-i(m'-m)\omega t}\hat{H}(t)}_{\hat{H}_{m'-m}}|\alpha\rangle - \delta_{\alpha'\alpha}i\hbar(im\omega)\underbrace{\frac{1}{T}\int_0^T dt e^{i(m-m')\omega t}}_{\delta_{m'm}} \\
&= \langle\alpha'|\hat{H}_{m'-m}|\alpha\rangle + m\hbar\omega\delta_{\alpha'\alpha}\delta_{m'm},
\end{aligned} \tag{2.88}$$

where the Fourier transform of the Hamiltonian $\hat{H}(t)$ has been introduced as

$$\hat{H}_m = \frac{1}{T}\int_0^T dt e^{-im\omega t}\hat{H}(t) = \hat{H}_{-m}^\dagger, \tag{2.89}$$

$$\hat{H}(t) = \hat{H}(t+T) = \sum_{m=-\infty}^{\infty} e^{im\omega t}\hat{H}_m. \tag{2.90}$$

According to Eq. (2.88), the matrix form of the quasienergy operator $\bar{Q}$ with respect to m can be depicted as in Fig. 2.7(a), where each block corresponds to an operator $\hat{Q}_{m'm} = \hat{H}_{m'-m} + m\hbar\omega\delta_{m'm}$ acting in $\mathcal{H}$. Solutions of such a matrix of 'infinite' dimension contain a lot of redundant information, since different solutions with $m' \neq m$ are related to each other via Eqs. (2.80), (2.82), but the corresponding Floquet states (2.81) are unique. It is thus possible to construct all Floquet states from the solutions with the quasienergies lying within the same interval of width $\hbar\omega$. Each interval is often called a single Brillouin zone of the quasienergy spectrum, which is analogous to Bloch's theory of spatially periodic system.

To diagonalize the quasienergy operator $\bar{Q}$, one can construct a unitary operator $\bar{U}_D$ which transform the Floquet modes to be a new basis $|\alpha m\rangle\!\rangle = \bar{U}_D^\dagger|u_{\alpha m}\rangle\!\rangle$, such that

$$\begin{aligned}
&\langle\!\langle u_{\alpha m}|\bar{Q}|u_{\alpha m}\rangle\!\rangle = \varepsilon_{\alpha m} = \varepsilon_\alpha + m\hbar\omega \\
\Leftrightarrow &\langle\!\langle \alpha' m'|\underbrace{\bar{U}_D^\dagger\bar{Q}\bar{U}_D}_{\bar{Q}'}|\alpha m\rangle\!\rangle = \delta_{m'm}\delta_{\alpha'\alpha}\left(\langle\alpha|\hat{H}_D|\alpha\rangle + m\hbar\omega\right),
\end{aligned} \tag{2.91}$$

where $\hat{H}_D$ is a time-independent gauge-transformed Hamiltonian,

$$\hat{H}_D = \hat{U}_D^\dagger(t)\left(\hat{H}(t)-i\hbar d_t\right)\hat{U}_D(t), \tag{2.92}$$

which is diagonal in the basis $|\alpha\rangle$,

$$\langle\alpha'|\hat{H}_D|\alpha\rangle = \delta_{\alpha'\alpha}\varepsilon_\alpha. \tag{2.93}$$

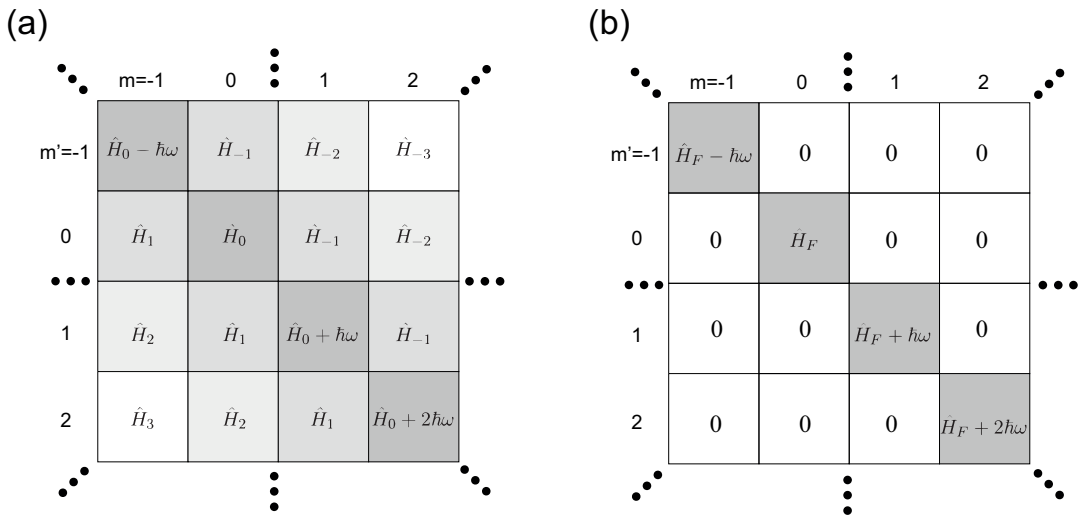

Figure 2.7: (a) Matrix form of the quasienergy operator $\bar{Q}$ with respect to indices m. Each block represents the matrix form of operator $\hat{Q}_{m'm} = \hat{H}_{m'-m} + m\hbar\omega\delta_{m'm}$ acting in the $\mathcal{H}$ space (i.e. with respect to indices α). (b) Block diagonalization of the quasienergy operator $\bar{Q}$ with respect to indices m. Each diagonal block corresponds to the matrix form of the effective Hamiltonian $\hat{H}_F$ represented in $\mathcal{H}$, which does not have to be diagonal. Cited from Ref. [159].

By applying the transformation $|u_{\alpha m}(t)\rangle = \hat{U}_D(t)|\alpha\rangle e^{im\omega t}$ (which corresponds to $|u_{\alpha m}\rangle\!\rangle = \bar{U}_D|\alpha m\rangle\!\rangle$) with $m = 0$ in Eq. (2.75), the Floquet Hamiltonian $\hat{H}^F_{t_0}$ can be expressed as

$$\begin{aligned}\hat{H}^F_{t_0} &= \sum_\alpha \varepsilon_\alpha |u_{\alpha 0}(t_0)\rangle\langle u_{\alpha 0}(t_0)| \\ &= \sum_\alpha \varepsilon_\alpha \hat{U}_D(t_0)|\alpha\rangle\langle\alpha|\hat{U}^\dagger_D(t_0) = \hat{U}_D(t_0)\underbrace{\sum_\alpha \varepsilon_\alpha |\alpha\rangle\langle\alpha|}_{\hat{H}_D}\hat{U}^\dagger_D(t_0) \\ &= \hat{U}_D(t_0)\hat{H}_D\hat{U}^\dagger_D(t_0). \end{aligned} \tag{2.94}$$

Namely, the Floquet Hamiltonian $\hat{H}^F_{t_0}$ is a unitary transformation of $\hat{H}_D$. Similarly, the micromotion operator $\hat{U}_F(t_2, t_1)$ defined in Eq. (2.76) becomes

$$\begin{aligned}\hat{U}_F(t_2, t_1) &= \sum_\alpha |u_{\alpha 0}(t_2)\rangle\langle u_{\alpha 0}(t_1)| \\ &= \sum_\alpha \hat{U}_D(t_2)|\alpha\rangle\langle\alpha|\hat{U}^\dagger_D(t_1) = \hat{U}_D(t_2)\hat{U}^\dagger_D(t_1). \end{aligned} \tag{2.95}$$

Effective Hamiltonian

The above equations (2.94) and (2.95) provides a different approach to calculate the Floquet Hamiltonian and the micromotion operator, alternative to using Eqs. (2.75) and (2.76) that

require the calculation of the Floquet states and the quasienergies from diagonalizing the time evolution operator over one driving period. Actually, for this purpose one does not have to fully diagonalize the quasienergy operator $\bar{Q}$. It would be sufficient to find a unitary operator $\bar{U}_F$ so that it *block diagonalizes* $\bar{Q}$ with respect to indices m,

$$\langle\!\langle \alpha' m' | \bar{U}_F^\dagger \bar{Q} \bar{U}_F | \alpha m \rangle\!\rangle = \delta_{m'm} \left(\langle \alpha' | \hat{H}_F | \alpha \rangle + \delta_{\alpha'\alpha} m\hbar\omega \right), \tag{2.96}$$

with $\hat{H}_F$ being a time-independent gauge transformed Hamiltonian,

$$\hat{H}_F = \hat{U}_F^\dagger(t) \left(\hat{H}(t) - i\hbar d_t \right) \hat{U}_F(t). \tag{2.97}$$

Such a time-independent Hamiltonian $\hat{H}_F$ is called *effective Hamiltonian*. The block diagonalization of $\bar{Q}$ is illustrated in Fig. 2.7(b). Note that $\bar{U}_F$ is not unique, as multiplying $\bar{U}_F$ with any time-independent unitary operator from the right only modifies the matrix form of each block (by causing a mixing of states within each block), leaving the overall block diagonal structure unchanged.

Each of the diagonal blocks of $\bar{U}_F^\dagger \bar{Q} \bar{U}_F$ offers a possible choice for the Floquet Hamiltonian. Applying $\delta_{\alpha\alpha'}\varepsilon_{\alpha m} = \langle\!\langle u_{\alpha' m} | \bar{Q} | u_{\alpha m} \rangle\!\rangle$ according to Eq. (2.87) and taking the $m = m' = 0$ block as an example, the Floquet Hamiltonian in Eq. (2.75) can be expressed as

$$\begin{aligned}
\hat{H}_{t_0}^F &= \sum_\alpha \varepsilon_\alpha |u_{\alpha 0}(t_0)\rangle\langle u_{\alpha 0}(t_0)| \\
&= \sum_{\alpha\alpha'} |u_{\alpha' 0}(t_0)\rangle \delta_{\alpha\alpha'} \varepsilon_\alpha \langle u_{\alpha 0}(t_0)| \\
&= \sum_{\alpha\alpha'} |u_{\alpha' 0}(t_0)\rangle \langle\!\langle u_{\alpha' 0} | \bar{Q} | u_{\alpha 0} \rangle\!\rangle \langle u_{\alpha 0}(t_0)| \\
&= \sum_{\alpha\alpha'} \hat{U}_F(t_0)|\alpha'\rangle \underline{\langle\!\langle \alpha' 0 | \bar{U}_F^\dagger \bar{Q} \bar{U}_F | \alpha 0 \rangle\!\rangle} \langle\alpha | \hat{U}_F^\dagger(t_0) \qquad (2.98) \\
&= \sum_{\alpha\alpha'} \hat{U}_F(t_0)|\alpha'\rangle \underline{\langle \alpha' | \hat{H}_F | \alpha \rangle} \langle\alpha | \hat{U}_F^\dagger(t_0) \qquad (2.99) \\
&= \hat{U}_F(t_0) \hat{H}_F \hat{U}_F^\dagger(t_0), \qquad (2.100)
\end{aligned}$$

where the transformation $|u_{\alpha m}\rangle\!\rangle = \bar{U}_F |\alpha m\rangle\!\rangle$ (corresponding to $|u_{\alpha m}(t)\rangle = \hat{U}_F(t)|\alpha\rangle e^{im\omega t}$) has been used to arrive at Eq. (2.98), and Eq. (2.96) has been applied for Eq. (2.99). It is clear that the effective Hamiltonian $\hat{H}_F$ is related to the Floquet Hamiltonian $\hat{H}_{t_0}^F$ via a unitary transformation.

Similar to Eq. (2.95), the two-point micromotion operator can also be written as

$$\hat{U}_F(t_2, t_1) = \hat{U}_F(t_2) \hat{U}_F^\dagger(t_1), \tag{2.101}$$

where $\hat{U}_F(t)$ are usually called one-point micromotion operator. Now, with Eqs. (2.100) and (2.101), the time-evolution operator $\hat{U}(t_2, t_1)$ in Eq. (2.78) can be directly expressed in terms of

$\hat{H}_F$ and $\hat{U}_F(t)$, without calculating $\hat{H}^F_{t_0}$ and $\hat{U}_F(t_2,t_1)$ beforehand, i.e.

$$\begin{aligned}
\hat{U}(t_2,t_1) =&\hat{U}_F(t_2,t_1)e^{-i(t_2-t_1)\hat{H}^F_{t_1}/\hbar}\\
=&\hat{U}_F(t_2,t_1)\sum_n \frac{1}{n!}\left(\frac{-i(t_2-t_1)}{\hbar}\hat{H}^F_{t_1}\right)^n\\
=&\hat{U}_F(t_2)\hat{U}^\dagger_F(t_1)\sum_n \frac{1}{n!}\left(\frac{-i(t_2-t_1)}{\hbar}\right)^n\left(\hat{U}_F(t_1)\hat{H}_F\hat{U}^\dagger_F(t_1)\right)^n\\
=&\hat{U}_F(t_2)\hat{U}^\dagger_F(t_1)\left[1+\left(\frac{-i(t_2,t_1)}{\hbar}\right)\hat{U}_F(t_1)\hat{H}_F\hat{U}^\dagger_F(t_1)\right.\\
&\left.+\frac{1}{2!}\left(\frac{-i(t_2-t_1)}{\hbar}\right)^2\hat{U}_F(t_1)\hat{H}_F\hat{H}_F\hat{U}^\dagger_F(t_1)+\cdots\right]\\
=&\hat{U}_F(t_2)\hat{U}^\dagger_F(t_1)\hat{U}_F(t_1)\sum_n \frac{1}{n!}\left(\frac{-i(t_2-t_1)}{\hbar}\right)^n\left(\hat{H}_F\right)^n\hat{U}^\dagger_F(t_1)\\
=&\hat{U}_F(t_2)e^{-i(t_2-t_1)\hat{H}_F/\hbar}\hat{U}^\dagger_F(t_1).
\end{aligned}\tag{2.102}$$

As the micromotion operator $\hat{U}_F$ is not unique and it can be multiplied by any time-independent unitary operator from the right, choosing $\hat{U}_F(t_0+T)=\hat{U}_F(t_0)=1$ is allowed[15]. In this case, for $t_1=t_0, t_2=t_0+T$, both Eqs. (2.100) and (2.102) confirm that $\hat{H}_F$ goes back to the $\hat{H}^F_{t_0}$. This implies that the Floquet Hamiltonian is a special choice of the effective Hamiltonian, which generates the stroboscopic time evolution in steps of driving period T. Therefore, directly computing the effective Hamiltonian offers an efficient way to study the long-time dynamics when the detailed dynamics within each driving period can be neglected.

Nevertheless, the effective Hamiltonian $\hat{H}_F$ can also be used to address the short-time dynamics within one driving period. By diagonalizing $\hat{H}_F$,

$$\hat{H}_F|\tilde{u}_n\rangle=\varepsilon_n|\tilde{u}_n\rangle,\tag{2.103}$$

the Floquet modes and the quasienergies can be expressed as

$$|u_{nm}(t)\rangle=\hat{U}_F(t)|\tilde{u}_n\rangle e^{im\omega t},\ \varepsilon_{nm}=\varepsilon_n+m\hbar\omega.\tag{2.104}$$

Now the short-time dynamics within one driving period, i.e. the micromotion, can be described by the Floquet mode $|u_n(t)\rangle\equiv|u_{n0}(t)\rangle$ in the following way,

$$|u_n(t)\rangle=\hat{U}_F(t)|\tilde{u}_n\rangle=\sum_\alpha \underbrace{\hat{U}_F(t)|\alpha\rangle}\underbrace{\langle\alpha|\tilde{u}_n\rangle}=\sum_\alpha\gamma_{\alpha n}|\alpha(t)\rangle_F,\tag{2.105}$$

where we have introduced the coefficients $\gamma_{\alpha n}=\langle\alpha|\tilde{u}_n\rangle$ and the time-dependent basis states $|\alpha(t)\rangle_F=\hat{U}_F(t)|\alpha\rangle$. Note that the micromotion operator $\hat{U}_F$ can also be expressed as

$$\hat{U}_F(t)=e^{\hat{G}(t)},\ \hat{G}(t)=-i\hat{K}(t),\tag{2.106}$$

[15]For example, for a given $\hat{U}_F(t)$, it can be replaced by $\hat{U}'_F(t)=\hat{U}_F(t)\hat{U}^\dagger_F(t_0)$ such that $\hat{U}'_F(t_0)=1$.

where the Hermitian $\hat{K}(t)$ is called a kick operator [160], which describes an abrupt switch-on of the periodic forcing.

One crucial part of Floquet theory is to compute the effective Hamiltonian and the micromotion operator. For the driving frequency large compared to other system parameters like tunnelling matrix elements of $\hat{H}(t)$, one can treat $-i\hbar d_t$ as an unperturbed part with $\langle\langle \alpha' m'| - i\hbar d_t |\alpha m\rangle\rangle = \delta_{m'm}\delta_{\alpha'\alpha} m\hbar\omega$, and $\hat{V} = \hat{H}(t)$ as a perturbation. In this case, degenerate perturbation theory can be used to systematically block diagonalize the quasienergy operator [159], which leads to a high-frequency expansion of the effective Hamiltonian and the micromotion operator,

$$\hat{H}_F \approx \sum_{\mu=1}^{\mu_{\text{cut}}} \hat{H}_F^{(\mu)}, \hat{U}_F \approx \exp\left(\sum_{\mu=1}^{\mu_{\text{cut}}} \hat{G}^{(\mu)}(t)\right), \tag{2.107}$$

with $\hat{H}_F^{(\mu)} = \hat{H}_F^{(\mu)\dagger}, [\hat{G}^{(\mu)}(t)]^\dagger = -\hat{G}^{(\mu)}(t)$. The integer μ_{cut} determines the cut-off of the considered orders. The leading terms read,

$$\hat{H}_F^{(1)} = \hat{H}_0, \tag{2.108}$$

$$\hat{H}_F^{(2)} = \sum_{m\neq 0} \frac{\hat{H}_m \hat{H}_{-m}}{m\hbar\omega}, \tag{2.109}$$

$$\hat{H}_F^{(3)} = \sum_{m\neq 0} \frac{[\hat{H}_{-m}, [\hat{H}_0, \hat{H}_m]]}{2(m\hbar\omega)^2} + \sum_{m'\neq 0,m} \frac{[\hat{H}_{-m'}, [\hat{H}_{m'-m}, \hat{H}_m]]}{3mm'(\hbar\omega)^2}, \tag{2.110}$$

and

$$\hat{G}^{(1)}(t) = -\sum_{m\neq 0} \frac{e^{im\omega t}\hat{H}_m}{m\hbar\omega}, \tag{2.111}$$

$$\hat{G}^{(2)}(t) = -\sum_{m\neq 0} \frac{e^{im\omega t}[\hat{H}_0, \hat{H}_m]}{(m\hbar\omega)^2} + \sum_{m'\neq 0,m} \frac{e^{i(m-m')\omega t}[\hat{H}_{-m'}, \hat{H}_m]}{2m(m-m')(\hbar\omega)^2}. \tag{2.112}$$

where $\hat{H}_m$ is the Fourier transform of $\hat{H}(t)$ defined in Eq. (2.89).

Note that the high-frequency expansion of the effective Hamiltonian $\hat{H}_F$ can be related to the frequently-employed Floquet-Magnus expansion of the Floquet Hamiltonian $\hat{H}_{t_0}^F$ [159]. By plugging $\hat{H}_F = \hat{H}_F^{(1)} + \hat{H}_F^{(2)} + \cdots$, $\hat{U}_F(t_0) = 1 + \hat{U}_F^{(1)}(t_0) + \hat{U}_F^{(2)}(t_0) + \cdots$ into Eq. (2.100), one arrives at $\hat{H}_{t_0}^F = \sum_\mu \hat{H}_{t_0}^{F(\mu)}$ with the leading order,

$$\hat{H}_{t_0}^{F(1)} = \hat{H}_F^{(1)} = \hat{H}_0, \tag{2.113}$$

$$\begin{aligned}\hat{H}_{t_0}^{F(2)} &= \hat{H}_F^{(2)} + \hat{H}_F^{(1)}\hat{U}_F^{(1)\dagger}(t_0) + \hat{U}_F^{(1)}(t_0)\hat{H}_F^{(1)} \\ &= \sum_{m\neq 0} \frac{\hat{H}_m\hat{H}_{-m} + e^{im\omega t_0}[\hat{H}_0, \hat{H}_m]}{m\hbar\omega},\end{aligned} \tag{2.114}$$

where $\hat{U}_F^{(1)}(t_0) = \hat{G}^{(1)}(t) = -[\hat{G}^{(1)}(t)]^\dagger$ has been used. Nevertheless, for order $\mu \geq 2$, the t_0-dependence of the second term in the above equation indicates that the spectrum of the

approximated Floquet Hamiltonian will possess an artifactual dependence on the initial time t_0, and thus equivalently on the driving phase. This is inconsistent with the exact Floquet Hamiltonian whose spectrum is independent of driving phase. Even though the high-order terms with t_0-dependence is small in high-frequency regime, they could induce a spurious breaking of the rotational symmetry of the quasienergy dispersion relation, which thus changes the system properties [159]. This indicates that the Floquet-Magnus approximation should be used with care. Note that such a t_0-dependence issue can be avoided by using the high-frequency expansion of the effective Hamiltonian Eq. (2.107).

At first glance, it seems that the Floquet formalism is only about finding some effective time-independent Hamiltonians to describe a periodically driven quantum system. However, in many situations one tries to engineer a target model as the effective Hamiltonian in a certain low order ($\mu_{\text{cut}} = 1$ or 2) by designing time-periodic driving properly [71]. This approach is called *Floquet engineering* and has been successfully applied in synthetic platforms by using ultracold atoms [38, 39] or photons [91]. Topics include dynamic localization, 'photon'/laser-assisted tunneling, dynamical control of superfluid to Mott insulator phase transition, kinetic frustration, coherent resonant band coupling and so on (see Ref.[71] and references therein). Of our particular interest, the artificial gauge fields have been widely engineered in synthetic platforms [81]. In the following section, we will see how to apply the Floquet engineering in a tight-binding model, such that the artificial gauge fields and the HH model can be engineered in the laboratory.

2.5.2 Application to tight-binding models

Optical lattices with ultracold atoms have been a promising candidate for quantum simulation. At first glance, an important ingredient – the effect of magnetic fields – is missing since the particles in the system are charge-neutral atoms. However, with the help of the Floquet engineering technique (among other schemes like relying on laser dressing of internal degrees of freedom in atoms [79, 80]), complex tunneling matrix elements can be achieved by, e.g. by moving-secondary-lattice or asymmetric-shaking schemes. Here, effective tunneling phases (Peierls phases) play the role of vector potentials [71, 81]. Particularly, after hopping around a single plaquette, the accumulated Peierls phase describes an effective magnetic flux.

A general consideration

Consider non-interacting particles in deep lattices described by the following tight-binding Hamiltonian

$$\hat{H}(t) = -\sum_{\langle \ell\ell' \rangle} J_{\ell'\ell} \hat{a}^\dagger_{\ell'} \hat{a}_\ell + \sum_\ell w_\ell(t) \hat{n}_\ell, \tag{2.115}$$

where $\hat{a}_\ell$, $\hat{a}^\dagger_\ell$ denote the annihilation and creation operators on lattice site ℓ, and $\hat{n}_\ell = \hat{a}^\dagger_\ell \hat{a}_\ell$ is the number operator. $J_{\ell'\ell}$ is the strength of the bare tunneling between two nearest-neighbour sites denoted by $\langle \ell\ell' \rangle$. The periodic driving is represented by a time-periodic on-site modulation $w_\ell(t) = w_\ell(t+T)$.

By performing a gauge transformation

$$|\psi'(t)\rangle = \hat{U}^\dagger(t)|\psi(t)\rangle, \tag{2.116}$$

the Schrödinger equation $i\hbar d_t|\psi(t)\rangle = \hat{H}(t)|\psi(t)\rangle$ becomes

$$i\hbar d_t|\psi'(t)\rangle = \hat{H}'(t)|\psi'(t)\rangle, \tag{2.117}$$

with

$$\hat{H}'(t) = \hat{U}^\dagger(t)\hat{H}(t)\hat{U}(t) - i\hbar\hat{U}^\dagger(t)[d_t\hat{U}(t)]. \tag{2.118}$$

Namely the dynamics of $|\psi'(t)\rangle$ is governed by a gauge-transformed Hamiltonian $\hat{H}'(t)$. The time-periodic unitary operator can be defined as

$$\hat{U}(t) = \exp\left(i\sum_\ell \chi_\ell(t)\hat{n}_\ell\right) \tag{2.119}$$

with

$$\chi_\ell(t) = -\int_{t_0}^{t} dt' \frac{w_\ell(t')}{\hbar} - \chi_{0\ell}. \tag{2.120}$$

Here the free gauge parameter $\chi_{0\ell}$ is chosen to remove t_0-dependent terms, which corresponds to $\int_0^T dt\chi_\ell(t) = 0$.

Now, by employing $\hat{a}_\ell\hat{n}_\ell = (\hat{n}_\ell + 1)\hat{a}_\ell$ one can straightforwardly arrive at

$$\hat{a}_\ell\hat{U}(t) = \exp\left[i\sum_\ell \chi_\ell(t)\left(\hat{n}_\ell + 1\right)\right]\hat{a}_\ell = \hat{U}(t)e^{i\chi_\ell(t)}\hat{a}_\ell. \tag{2.121}$$

Plugging Eq. (2.115) and the above equation (2.121) into the transformed Hamiltonian Eq. (2.118), one gets

$$\begin{aligned}
\hat{H}'(t) &= -\sum_{\langle\ell\ell'\rangle} J_{\ell'\ell}\underbrace{\hat{U}^\dagger\hat{a}_{\ell'}^\dagger}\underbrace{\hat{a}_\ell\hat{U}} + \hat{U}^\dagger\sum_\ell w_\ell(t)\hat{n}_\ell\hat{U} - i\hbar\hat{U}^\dagger[d_t\hat{U}] \\
&= -\sum_{\langle\ell\ell'\rangle} J_{\ell'\ell}\hat{a}_{\ell'}^\dagger e^{-i\chi_{\ell'}(t)}\cancel{\hat{U}^\dagger\hat{U}}e^{i\chi_\ell(t)}\hat{a}_\ell + \sum_\ell w_\ell(t)\hat{n}_\ell\cancel{\hat{U}^\dagger\hat{U}} \\
&- \cancel{i\hbar\hat{U}^\dagger\hat{U}}\sum_\ell i\hat{n}_\ell\left(d_t\chi_\ell(t)\right) \\
&= -\sum_{\langle\ell\ell'\rangle} J_{\ell'\ell}e^{-i\chi_{\ell'}(t)}e^{i\chi_\ell(t)}\hat{a}_{\ell'}^\dagger\hat{a}_\ell + \cancel{\sum_\ell w_\ell(t)\hat{n}_\ell + i\hbar\sum_\ell i\hat{n}_\ell w_\ell(t)/\hbar} \\
&= -\sum_{\langle\ell\ell'\rangle} J_{\ell'\ell}e^{i\theta_{\ell'\ell}(t)}\hat{a}_{\ell'}^\dagger\hat{a}_\ell,
\end{aligned} \tag{2.122}$$

where the time-dependent Peierls phases $\theta_{\ell'\ell}(t)$ have been introduced as

$$\theta_{\ell'\ell}(t) = \chi_\ell(t) - \chi_{\ell'}(t). \tag{2.123}$$

In the high-frequency regime, i.e. $\hbar\omega$ is large compared to the system's characteristic energy scales ($\hbar\omega \gg J_{\ell'\ell}$), the above Hamiltonian can be approximated by its cycle average,

$$\hat{H}(t) \to \hat{H}_{\text{eff}} = \frac{1}{T}\int_0^T dt\hat{H}'(t) = -\sum_{\langle\ell\ell'\rangle} J_{\ell'\ell}^{\text{eff}}\hat{a}_{\ell'}^\dagger\hat{a}_\ell, \tag{2.124}$$

$$J_{\ell'\ell} \to J_{\ell'\ell}^{\text{eff}} = J_{\ell'\ell}\frac{1}{T}\int_0^T dte^{i\theta_{\ell'\ell}(t)}, \tag{2.125}$$

where $J^{\text{eff}}_{\ell'\ell}$ is the modified effective tunneling matrix element. As the rapidly oscillating terms are absorbed into the tunneling matrix elements, it can be treated as a rotating-wave-type approximation. This corresponds to the leading order of the high-frequency expansion in the rotating frame. The time-independent Hamiltonian $\hat{H}_{\text{eff}}$ approximates the effective Hamiltonian $\hat{H}_F$, and the unitary operator $\hat{U}(t)$ defined in Eq. (2.119) is an approximation of the micromotion operator $\hat{U}_F(t)$, i.e.

$$\hat{H}_F \approx \hat{H}_{\text{eff}},\ \hat{U}_F(t) \approx \hat{U}(t). \tag{2.126}$$

This can be seen clearly by noticing that the Hamiltonian $\hat{H}_{\text{eff}}$ defined in Eq. (2.124) is the $m = 0$ component in the Fourier transformation of $\hat{H}'(t)$ [see Eq. (2.89)], and thus it corresponds to the lowest-order of the high-frequency expansion (2.107) applied to $\hat{H}'(t)$, i.e.

$$\hat{H}_{\text{eff}} = \frac{1}{T}\int_0^T dt\hat{H}'(t) = \hat{H}'_{m=0} = \hat{H}'^{(1)}_F. \tag{2.127}$$

Note that the time-average has been performed for the gauge-transformed Hamiltonian $\hat{H}'(t)$, instead of the original one $\hat{H}(t)$. This is because a desired modification of the tunneling usually requires strong driving with amplitudes of the order of $\hbar\omega$, which would spoil the high-frequency approximation.

Engineering artificial gauge fields and the HH model

Regarding experimental implementations, the periodic driving potentials $w_\ell(t)$ have been widely realized by lattice shaking, which gives rise to periodic linear, circular, elliptical, and even non-sinusoidal forcing etc [71]. Alternatively, $w_\ell(t)$ can also be given by on-site modulations induced by a secondary lattice moving with respect to the host lattice.

To be general, suppose the on-site modulations take the form,

$$w_\ell(t) = w^{\text{dr}}_\ell(t) + \nu_\ell\Delta, \tag{2.128}$$

where $w^{\text{dr}}_\ell(t) = w^{\text{dr}}_\ell(t+T)$ represents time-periodic driving of zero average $\int_0^T dt w^{\text{dr}}_\ell(t) = 0$, and Δ corresponds to a static potential with integers ν_ℓ. In the case, where driving is absent but the potential difference between two neighbouring sites is large enough compared to the bandwidth ($\Delta \geq J$), tunneling process between these two sites will be significantly suppressed. However, coherent tunneling can be induced by periodic driving under the resonance condition $\Delta = \text{integer}\times\hbar\omega$. This phenomenon is known as 'photon'-assisted, or laser-assisted tunneling [71]. In the following, we will focus on sinusoidal forcing and adopt $\Delta = \hbar\omega$.

Since a tunneling process depends on the potentials of both neighbouring sites, it is convenient to write down the relative modulations $w_{\ell'\ell}(t) \equiv w_{\ell'}(t) - w_\ell(t)$ between two neighbouring sites as

$$w_{\ell'\ell}(t) = -K_{\ell'\ell}\cos(\omega t - \varphi_{\ell'\ell}) + \nu_{\ell'\ell}\hbar\omega, \tag{2.129}$$

with $\nu_{\ell'\ell} = \nu'_\ell - \nu_\ell$, leaving $K_{\ell'\ell}$ and $\varphi_{\ell'\ell}$ determined from the specific form of $w^{\text{dr}}_\ell(t)$. For

instance, a sinusoidal forcing $w_\ell^{\rm dr}(t) = K\sin(\omega t - \varphi_\ell)$ gives

$$\begin{aligned} w_{\ell'}^{\rm dr}(t) - w_\ell^{\rm dr}(t) &= K\sin(\omega t - \varphi_{\ell'}) - K\sin(\omega t - \varphi_\ell) \\ &= K\sin\left(\omega t - \frac{\varphi_\ell + \varphi_{\ell'}}{2} + \frac{\varphi_\ell - \varphi_{\ell'}}{2}\right) - K\sin\left(\omega t - \frac{\varphi_\ell + \varphi_{\ell'}}{2} - \frac{\varphi_\ell - \varphi_{\ell'}}{2}\right) \\ &= 2K\sin\frac{\varphi_\ell - \varphi_{\ell'}}{2}\cos\left(\omega t - \frac{\varphi_{\ell'} + \varphi_\ell}{2}\right). \end{aligned} \tag{2.130}$$

Thus one gets

$$K_{\ell'\ell} = 2K\sin\left(\frac{\varphi_{\ell'} - \varphi_\ell}{2}\right),\ \varphi_{\ell'\ell} = \frac{\varphi_{\ell'} + \varphi_\ell}{2}. \tag{2.131}$$

With the form of $w_{\ell'\ell}(t)$ in (2.129), the time-dependent Peierls phases $\theta_{\ell'\ell}(t)$ can be now expressed as

$$\begin{aligned} \theta_{\ell'\ell}(t) &= \chi_\ell(t) - \chi_{\ell'}(t) \\ &= \int_{t_0}^t dt' \frac{w_{\ell'\ell}(t')}{\hbar} + \chi_{0\ell'} - \chi_{0\ell} \\ &= \frac{1}{\hbar}\int_{t_0}^t dt' \left[-K_{\ell'\ell}\cos\left(\omega t' - \varphi_{\ell'\ell}\right) + \nu_{\ell'\ell}\hbar\omega\right] + \chi_{0\ell'} - \chi_{0\ell} \\ &= \frac{-K_{\ell'\ell}}{\hbar\omega}\sin\left(\omega t - \varphi_{\ell'\ell}\right) + \nu_{\ell'\ell}\omega t. \end{aligned} \tag{2.132}$$

Accordingly, the effective tunneling matrix element now becomes,

$$\begin{aligned} J_{\ell'\ell}^{\rm eff} =& J_{\ell'\ell}\frac{1}{T}\int_0^T dt e^{i\theta_{\ell'\ell}(t)} \\ =& J_{\ell'\ell}\frac{1}{T}\int_0^T dt \exp\left[i\frac{-K_{\ell'\ell}}{\hbar\omega}\sin\left(\omega t - \varphi_{\ell'\ell}\right)\right]\exp\left(i\nu_{\ell'\ell}\omega t\right) \\ &\Downarrow \underline{-\tau \equiv \omega t - \varphi_{\ell'\ell}, -d\tau = \omega dt} \\ =& J_{\ell'\ell}\frac{1}{T}\int_{-2\pi+\varphi_{\ell'\ell}}^{\varphi_{\ell'\ell}} \frac{d\tau}{\omega}\exp\left(i\frac{K_{\ell'\ell}}{\hbar\omega}\sin\tau\right)\exp\left[i\nu_{\ell'\ell}(-\tau + \varphi_{\ell'\ell})\right] \\ =& J_{\ell'\ell}\underline{\frac{1}{2\pi}\int_{-2\pi+\varphi_{\ell'\ell}}^{\varphi_{\ell'\ell}} d\tau \exp\left[i\left(\frac{K_{\ell'\ell}}{\hbar\omega}\sin\tau - \nu_{\ell'\ell}\tau\right)\right]}\exp(i\nu_{\ell'\ell}\varphi_{\ell'\ell}) \\ =& J_{\ell'\ell}\underline{\mathcal{J}_{\nu_{\ell'\ell}}\left(\frac{K_{\ell'\ell}}{\hbar\omega}\right)}e^{i\nu_{\ell'\ell}\varphi_{\ell'\ell}}, \end{aligned} \tag{2.133}$$

where the Bessel function of the first kind $\mathcal{J}_n(x) = \frac{1}{2\pi}\int_{-\pi}^{\pi} d\tau e^{i(x\sin\tau - n\tau)}$ has been used for the equation with underline. It is interesting to notice the correspondence between the relative modulations (2.129) and the effective tunneling matrix element (2.133). Namely the amplitude of the effective tunneling is a function of the relative modulation strength, while the effective tunneling phase can be controlled by the relative driving phase along with the static potential offsets.

By properly tuning laser beams, for instance, a pair of far-detuned running waves $\propto \exp(i\boldsymbol{k}_{1,2}\cdot \boldsymbol{r}-\omega_{1,2}t)$ can be used to create a secondary moving lattice, which gives rise to the sinusoidal on-site potentials

$$w_\ell^{\mathrm{dr}}(t)=V_0\cos(\omega t+\boldsymbol{q}\cdot\boldsymbol{r}_\ell+\varphi_0), \tag{2.134}$$

where we have introduced $\boldsymbol{q}=\boldsymbol{k}_1-\boldsymbol{k}_2=k_1\boldsymbol{e}_x-k_2\boldsymbol{e}_y$, $\omega=\omega_1-\omega_2$, and $\boldsymbol{r}_\ell=ma\boldsymbol{e}_x+na\boldsymbol{e}_y$ with $(m,\ n)$ being the lattice indices along x and y-direction to label site ℓ. φ_0 is a possible phase difference between these two running waves. For a two-dimensional square lattice with a strong static potential gradient along x direction, i.e. $\nu_\ell\Delta=m\hbar\omega$, the driven system is described by the following time-periodic Hamiltonian

$$\begin{aligned}\hat{H}(t)=&\sum_{m,n}\left(-J_x\hat{a}^\dagger_{m+1,n}\hat{a}_{m,n}-J_y\hat{a}^\dagger_{m,n+1}\hat{a}_{m,n}+h.c.\right)\\&+\sum_{m,n}\left(V_0\sin(\omega t-\varphi_{m,n})+m\hbar\omega\right)\hat{n}_{m,n},\end{aligned} \tag{2.135}$$

with

$$\varphi_{m,n}=-(\boldsymbol{q}\cdot\boldsymbol{r}_\ell+\varphi_0+\pi/2)=-\left(k_1am-k_2an+\varphi_0+\pi/2\right). \tag{2.136}$$

In this case, the above equations (2.131) and (2.133) can be directly applied, leading to the following time-independent Hamiltonian,

$$\hat{H}_{\mathrm{eff}}=\sum_{m,n}\left(-J_x^{\mathrm{eff}}\hat{a}^\dagger_{m+1,n}\hat{a}_{m,n}-J_y^{\mathrm{eff}}\hat{a}^\dagger_{m,n+1}\hat{a}_{m,n}+h.c.\right), \tag{2.137}$$

with

$$J_x^{\mathrm{eff}}=J_x\mathcal{J}_1\left(\frac{K_x}{\hbar\omega}\right)e^{i\phi_{m,n}},\quad K_x=2V_0\sin\left(\frac{k_1a}{2}\right),\quad \phi_{m,n}=k_2an+\eta_m, \tag{2.138}$$

$$J_y^{\mathrm{eff}}=J_y\mathcal{J}_0\left(\frac{K_y}{\hbar\omega}\right),\quad K_y=2V_0\sin\left(\frac{k_2a}{2}\right). \tag{2.139}$$

Note that $\mathcal{J}_n(-x)=\mathcal{J}_{-n}(x)=(-1)^n\mathcal{J}_n(x)$ has been applied and η_m contains all the constant and m-dependent terms, which have no contribution to the flux per plaquette. It is easy to check that, after hopping around each plaquette, the accumulated phase reads

$$\phi=ak_2\equiv\frac{\pi\lambda}{\lambda_R}. \tag{2.140}$$

By using $k_1=k_2\equiv k_R$ and choosing the wavelength of the running waves to be twice as large as that of the host lattice, i.e. $\lambda_R=2\pi/k_R=2\lambda$, the HH model with uniform flux of $\phi=\pi/2$ becomes realized, leaving the tunneling amplitude modified by $J_x^{\mathrm{eff}}\propto J_x\mathcal{J}_1\left(\frac{\sqrt{2}V_0}{\hbar\omega}\right)e^{i\phi n}$, $J_y^{\mathrm{eff}}=J_y\mathcal{J}_0\left(\frac{\sqrt{2}V_0}{\hbar\omega}\right)$. Note that the horizontal running laser beam, i.e. $k_1\neq 0$ is also required. Otherwise, K_x and thus the effective tunnelling amplitude J_x^{eff} would vanish, as indicated in Eq. (2.138).

Historically, using laser-assisted tunneling to create artificial magnetic fields was first theoretically proposed based on Raman transitions between internal atomic states [115, 116, 161, 162].

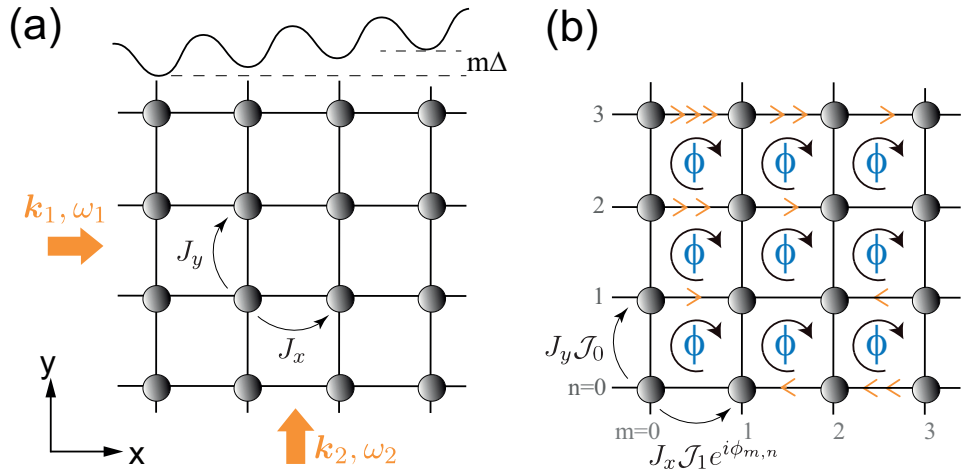

Figure 2.8: (a) Sketch of the lattices described by the full time dependent Hamiltonian (2.135). The tunneling process along x-direction is initially inhibited because of the strong potential gradient $\Delta \gg J_x$ in that direction. It is restored by applying a pair of far-detuned ($\omega = \omega_1 - \omega_2$) running wave laser beams (orange arrows) under the resonant condition $\Delta = \hbar\omega$. (b) Sketch of the lattice model described by the time independent effective Hamiltonian (2.137). The restored tunneling along the direction with static potential offsets is modified by complex tunneling matrix elements $J_x \to J_x\mathcal{J}_1\left(\frac{\sqrt{2}V_0}{\hbar\omega}\right)e^{i\phi_{m,n}}$, while the y-tunneling matrix element remains to be real. The arrow pattern corresponds to $\phi_{m,n} = \phi(n-m)$ with each arrow to the right and left representing tunneling phase of ϕ and $-\phi$ respectively. After hopping around each plaquette, a uniform flux of ϕ is obtained and thus the HH model is realized.

Alternatively, the scheme of combining periodic driving with static potential offsets described above was later on proposed for cold atoms [117, 163] and trapped ions [164]. Inspired by these ideas, the first experimental realization of large uniform artificial magnetic fields has been achieved in both I. Bloch's group in Munich [121] and W. Ketterle's group at MIT [120]. Apart from the observation of cyclotron-type dynamics of a single charge-neutral cold atom [121, 165], the Munich group has also performed the measurement of chiral current in a two-leg optical ladder with uniform flux of $\pi/2$, which is analogous to the Meissner effect in type-II superconductors [122]. Remarkably, by combining two pair of running laser beams with static superlattice staggered potentials, the same group has been able to populate the Hofstadter bands homogeneously with incoherent bosons, which enables the first determination of the Chern number of two-dimensional Bloch bands using ultracold atoms [124]. Meanwhile, the MIT group reports the first observation of Bose–Einstein condensation in the optical lattice system with uniform artificial magnetic flux, and an adiabatic many-body state preparation of superfluid ground state via the Mott insulating phase has also been explored. More recently, the interacting HH model has also been realized and the chiral motion of two interacting bosons studied in M. Greiner's group at Harvard [125]. All these advances provide promising steps toward the realization of strongly-correlated fractional quantum Hall states in optical lattices with cold atoms in the near future.

3 Floquet engineering of solenoid-type fluxes

As has been introduced in Chapter 1, the quantum Hall effect (QHE) – one of the most significant discoveries in the last century – opens up a whole new world of topological quantum effects. However, before using topology terminologies like geometric phase or Chern number, R. Laughlin has explained the quantized Hall conductance by performing a *Gedankenexperiment*, where the flux insertion created by a thin solenoid constitutes an important ingredient [6]. Nowadays, insertion of flux quanta has been a hallmark to characterize quantum Hall states. It thus becomes interesting to see whether it is possible to realize such a local flux insertion scenario in highly-controllable synthetic systems, such as optical lattices. To insert flux quanta through one single lattice plaquette has not been easy. Inspired by the recent experimental progress in controlling atomic quantum gases, here we propose and simulate a realistic scheme for the Floquet engineering of such strong solenoid-type local fluxes, for the first time, in a two-dimensional (2D) optical lattice. By combining with the ability of single-site addressing enabled by quantum gas microscopes, we show that it can be employed to manipulate and probe elementary excitations of a Chern insulator. This includes quantized adiabatic charge pumping along tailored paths inside the bulk, as well as the controlled population of edge modes [166].

Most results of Section 3.2 – 3.4 have been published in Ref. [166]. The rest parts in this chapter are unpublished, which serve as supplementary materials for an extension and better understanding.

3.1 Laughlin's Gedankenexperiment

In order to explain the quantization of the quantum Hall conductivity, in his seminal paper published in 1981, Laughlin considered a 2D electronic system which is bent into a cylinder [6]. As shown in Fig. 3.1, we consider a cylinder with radius R and length L, and choose the coordinates with x-axis parallel to the cylinder axis, y-axis having periodic boundary condition along the circumstance, and z pointing in radial direction, i.e. $\boldsymbol{e}_x = \boldsymbol{e}_x, \boldsymbol{e}_y = \boldsymbol{e}_\varphi, \boldsymbol{e}_z = \boldsymbol{e}_r$. Apart form the uniform magnetic field $\mathbf{B}$ piercing through the cylinder surface, an additional flux Φ generated by a thin solenoid is placed along the cylinder axis. Suppose the solenoid is long enough so that its magnetic field exist only within the solenoid, and the corresponding vector potential on the cylinder surface read

$$\boldsymbol{A}_\Phi = \big(0, -\Phi/(2\pi R), 0\big)\,. \tag{3.1}$$

Meanwhile, the vector potentials of the radial magnetic field $\mathbf{B}$ can be written as,

$$\boldsymbol{A} = (0, Bx, 0), \tag{3.2}$$

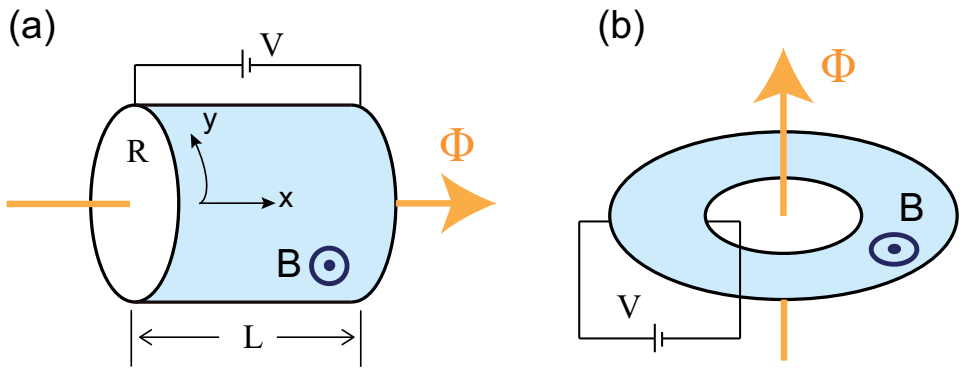

Figure 3.1: (a) Laughlin's *Gedankenexperiment* on a cylinder. The surface is pierced by a uniform magnetic field $\mathbf{B}$, and a long solenoid carrying a flux Φ is placed inside. Two electrodes with an electric potential difference V are connected to the two ends. (b) Flux insertion in a Corbino ring structure. This geometry is topologically equivalent to the cylinder shown in (a).

thus the total vector potentials are

$$\boldsymbol{A} + \boldsymbol{A}_\Phi = \left(0, B\left(x - \Phi/(2\pi RB)\right), 0\right). \tag{3.3}$$

Now, consider the solenoid flux which is changed by $\Delta\Phi$, i.e.

$$\Phi \to \Phi + \Delta\Phi. \tag{3.4}$$

As the change of flux in the solenoid affects the vector potentials on the cylinder surface (where the magnetic field $\mathbf{B}$ is independent of Φ), it leads to a gauge transformation of the electron wavefunction $\psi(x, y)$,

$$\psi(x, y) \to \psi(x, y)e^{ie\chi(x,y)/\hbar}, \quad \chi(x, y) = \frac{\Delta\Phi}{2\pi R}y. \tag{3.5}$$

For localized states, the above gauge transformation applies for arbitrary values of Φ and thus a continuous gauge transformation is allowed. However, when the electron states are extended/delocalized along the y direction, due to the periodic boundary condition along y, a continuous gauge transformation is 'illegal' [6, 167]. Specifically, for the states that are extended along y, the wavefunctions satisfy

$$\psi(x, y) = \psi(x, y + 2\pi R). \tag{3.6}$$

Applying the gauge transformation (3.5) on the above equation, one gets

$$\begin{aligned}\psi(x, y + 2\pi R) &\to \psi(x, y + 2\pi R)e^{ie\chi(x,y+2\pi R)/\hbar} \\ &= \psi(x, y)e^{ie\chi(x,y)/\hbar}e^{ie\Delta\Phi/\hbar}.\end{aligned} \tag{3.7}$$

Due to the periodic boundary condition (3.6), comparing Eq. (3.5) and (3.7) immediately gives

$$e^{ie\Delta\Phi/\hbar} = 1 \Rightarrow \Delta\Phi = \frac{h}{e} \times \text{integer}, \tag{3.8}$$

i.e., a 'legal' gauge transformations corresponds to a quantized change of flux in units of the flux quantum $\Phi_0 = h/e$.

Now we discuss the effects of this quantized flux insertion on the charge transport in the cylinder with two electrodes placed at the edges. From Eq. (3.3), one can see that the change of $\Delta\Phi$ is equivalent to a translation in the wave functions by $\Delta x = \Delta\Phi/(2\pi RB)$ in x direction. Recall that the IQHE is observed when the Fermi level lies above the occupied Landau levels, and extended states always exist at the center of each Landau level. Hence, with the increase of flux $\Delta\Phi$, electrons in the extended states below the Fermi energy will move adiabatically along x, and the number N of the transported electrons are determined by the number of Landau levels below the Fermi energy [167]. For a electric potential difference V between two electrodes, the electron transport costs an energy of $\Delta E = NeV$, which is the same as that required to change the solenoid flux. This energy cost originates from the fact that the magnetic field induced by the current along the y-direction interacts with the magnetic field inside the solenoid. In this case, the insertion of one flux quantum, $\Delta\Phi = h/e$, the density of currents along y can be expressed as

$$i_y = \frac{1}{L}\frac{\Delta E}{\Delta\Phi} = \frac{1}{L}\frac{NeV}{\frac{h}{e}} = N\frac{e^2}{h}\frac{V}{L} = N\frac{e^2}{h}E_x. \tag{3.9}$$

Therefore, the quantized Hall conductance $\sigma_{xy} = -Ne^2/h$ is obtained.

Note that while this cylinder scenario is difficult to realize in real experiments, its topological equivalence, namely a Corbino ring geometry [see Fig. 3.1(b)] offers the opportunity to perform this Gedankenexperiment in the laboratory. Indeed, such a ring geometry has been realized, for example, in a 2D electronic system where well-quantized Hall resistances have been measured [168]. However, when it comes to a 2D lattice, it is a nontrivial task to do a local flux insertion experiment. In the following, we will discuss how to insert a local flux though a single plaquette of the lattice, so that the insertion of integer quanta of flux gives rise to the creation of a quantized charge (corresponding to a localized quasiparticle or quasihole).

3.2 Flux insertion in 2D lattices

In the previous chapter we have seen that the HH model with uniform flux of $\alpha = 1/4$ possesses a lowest band with Chern number $C = -1$. Such a topologically nontrivial band structure can be used to mimic the physics of IQHE. For instance, by occupying the lowest Hofstadter band with free fermions, a quantum of flux insertion is expected to create quasiparticle/quasihole with charge ± 1. Namely, the flux insertion would give rise to quantized charge pumping. For this purpose, the basic idea is to modify the HH model with background flux $\phi = 2\pi\alpha$ by putting additional tunneling phases $\delta\phi$ in a selective manner, such that the fluxes of only two plaquettes are modified to be $\phi \pm \delta\phi$. As shown in Fig. 3.2, for instance, by putting identical additional

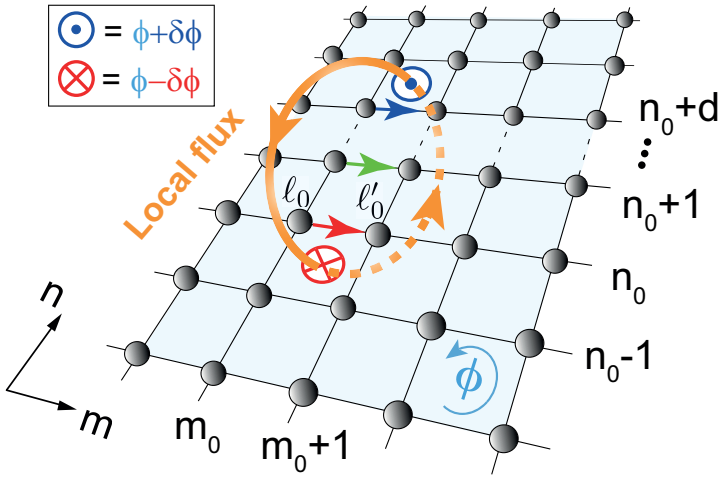

Figure 3.2: Sketch of a 2D lattice with uniform background flux ϕ as well as a solenoid-type local flux $\delta\phi$. Identical additional phases are accompanied by the hopping on the links labelled by horizontal arrows. The fluxes of plaquettes denoted by $\odot$ and $\otimes$ becomes $\phi \pm \delta\phi$. d represents the distance of these two modified plaquettes.

phases on the links labelled by arrows, the flux of plaquette denoted by $\otimes$ ($\odot$) becomes $\phi - \delta\phi$ ($\phi + \delta\phi$). For the plaquettes with two modified links the identical additional phases cancel each other, leaving the flux of those plaquettes unchanged. Therefore, by implementing and varying $\delta\phi$, a solenoid-type local flux insertion in a 2D lattice could be simulated. To check whether a quantized charge pumping will be induced, we start with an introduction to the numerical simulation of the HH model, and then study its time evolution.

3.2.1 Eigenvalue problem

Consider the following HH model,

$$\hat{H} = \sum_{m,n} \left(-Je^{-i\phi n} \hat{a}^\dagger_{m+1,n} \hat{a}_{m,n} - J_y \hat{a}^\dagger_{m,n+1} \hat{a}_{m,n} + h.c. \right), \tag{3.10}$$

where the Peierls phases have been chosen to be along the x direction. As discussed in Section 2.4.2, after expressing a single-particle state $|\Psi\rangle$ in the lattice basis $\{|m,n\rangle\}$ with $|m,n\rangle \equiv \hat{a}^\dagger_{m,n}|\text{vac}\rangle$ and $|\text{vac}\rangle$ being the vacuum state, i.e. $|\Psi\rangle = \sum_{m,n} \Psi_{m,n}|m,n\rangle$, the eigenvalue problem of the Hamiltonian in the single-particle subspace reads

$$E\Psi_{m,n} = -\left(J_x e^{-i\phi n} \Psi_{m-1,n} + J_x e^{i\phi n} \Psi_{m+1,n} + J_y \Psi_{m,n-1} + J_y \Psi_{m,n+1} \right). \tag{3.11}$$

Apparently, the r.h.s. of the above equation corresponds to the hopping process from the nearest-neighbouring sites of site (m,n).

For a system of $M \times N$ sites, in order to solve the problem numerically, we map the double indices (m,n) with $m \in \{0,1,\cdots,M-1\}$, $n \in \{0,1,\cdots,N-1\}$ to a single one $\ell = m + Mn \in \{0,1,\cdots,MN-1\}$, i.e. $|\ell\rangle = |m,n\rangle$. As an example, we present the Hamiltonian

matrix with elements $H_{\ell'\ell} = \langle \ell' | \hat{H} | \ell \rangle$ of a 3×3 lattice in Fig. 3.3. The meaning of the matrix elements $H_{\ell+k,\ell} = \langle \ell + k | \hat{H} | \ell \rangle$ is presented in Table 3.1. In the following, we set $J_x = 1$ so that all the energies will be in the unit of J_x and the Hamiltonian becomes dimensionless. We will focus on the case with $J_y = J_x$ and $\alpha = 1/4$.

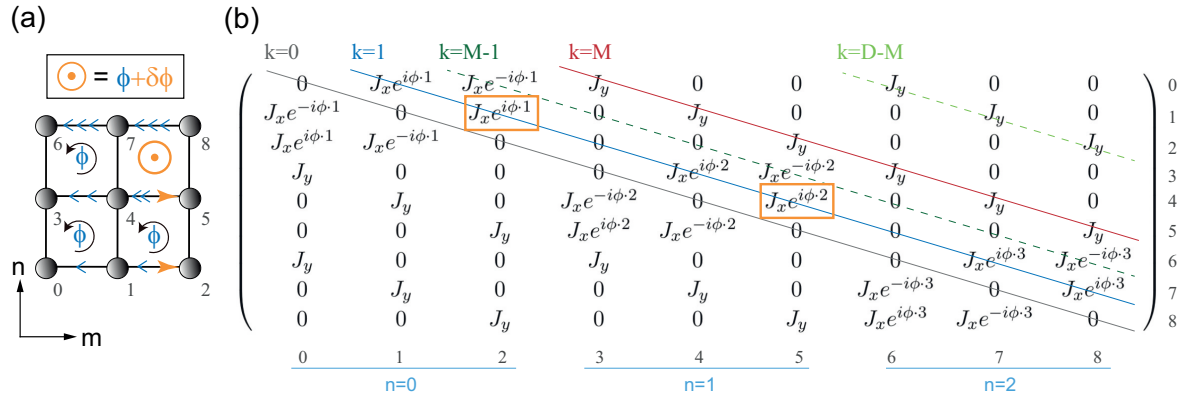

Figure 3.3: (a) Sketch of a lattice with size 3×3. Each blue thin arrow represents a tunneling phase of ϕ, and each orange thick arrow denotes the additional phase of $\delta\phi$. Overall, only the flux of the plaquette denoted by $\odot$ is modified to be $\phi + \delta\phi$, leaving the fluxes of all other plaquettes unchanged. (b) The matrix form of $-\hat{H}$ describing a 3×3 lattice with uniform flux ϕ. The k-values label the (off-)diagonals in the matrix. The lower triangular part corresponds to the hermitian conjugate of the upper one.

Table 3.1: Illustration of the Hamiltonian matrix elements

k	$H_{\ell+k,\ell}$	Meaning
0	0	on-site potentials
± 1	$-J_x e^{\pm i\phi \cdot n}$	x-tunneling
$\pm M$	$-J_y$	y-tunneling
$\pm(M-1)$	$-J_x e^{\mp i\phi \cdot n}$	periodic boundary condition along x
$\pm(D-M)$	$-J_y$	periodic boundary condition along y

After having the matrix form of the Hamiltonian according to the above-mentioned procedure, the ground state properties can be investigated by diagonalizing the matrix, e.g. via Numpy library in Python. For a system of size $M \times N$ with open boundary condition (OBC), identical additional phases $\delta\phi$ are assigned from the link labelled by the left sites (m_0, n_0) until (m_0, n_0+d), with d being the distance of two modified plaquettes, as depicted in Fig. 3.2. The Hamiltonian then takes the form

$$\hat{H}_{\text{ideal}} = \sum_{m,n} \left(-J e^{-i(\phi n - \mu_{m,n}\delta\phi)} \hat{a}^\dagger_{m+1,n} \hat{a}_{m,n} - J_y \hat{a}^\dagger_{m,n+1} \hat{a}_{m,n} + h.c. \right), \tag{3.12}$$

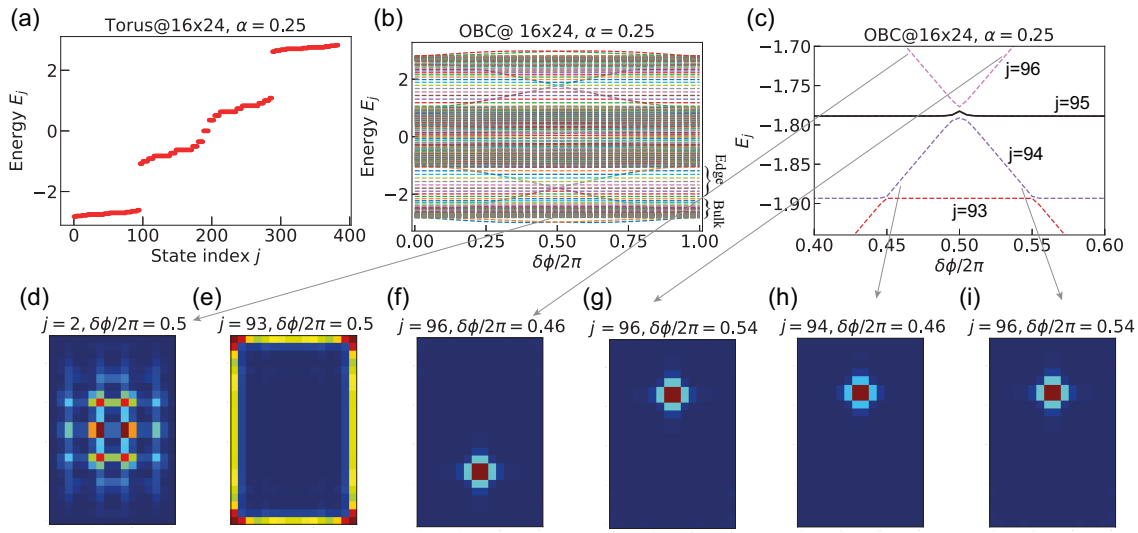

Figure 3.4: (a) Energy spectrum as a function of state index n for a torus of size 16×24 at $\delta\phi = 0$. (b) Energy spectrum as a function of $\delta\phi$ in a lattice of size 16×24 with open boundary condition. The spectrum is symmetric with respect to zero energy due to the particle-hole symmetry. (c) Zoom-in region near $\delta\phi = \pi$ in the spectrum shown in (b). n is the eigenstate index counted from 0. (d-i) Snapshots of the spatial density distributions of different eigenstates at different values of $\delta\phi$. The state indices and values of $\delta\phi$ are written in the title of each plot. Other parameters are $J_y = J_x$ and $\alpha = 1/4$.

where $\mu_{m,n} = 1$ for $m = m_0,\ n = \{n_0, n_0 + 1, \cdots, n_0 + d\}$, which label the links with arrows in Fig. 3.2, otherwise $\mu_{m,n} = 0$. Taking $M = 16, N = 24$ for example, we choose $m_0 = 7, d = 10$. The energy spectrum as a function of $\delta\phi$ is plotted in Fig. 3.4(b). Note that the positive spectrum is symmetric with respect to zero energy $E = 0$ due to the particle-hole symmetry of the HH model. Clearly, a spectral flow appears, which indicates an adiabatic charge pumping could be induced by ramping $\delta\phi$.

As a reference, we first plot the eigenvalues of the Hamiltonian describing a torus (i.e. with periodic boundary conditions along both directions) at $\delta\phi = 0$ in Fig. 3.4(a). Clearly, there is a large energy gap above the lowest band, which indicates the topological robustness as will be discussed below. For the system with open boundary condition, we plot the eigenvalues as a function of $\delta\phi$ in Fig. 3.4(b). While the (extended) bulk states exist within the lowest band, the larger level spacing, inverse to the density of states, indicates edge states in the gap. Typical spatial density distributions of the bulk and edge states are plotted in Figs. 3.4(d) and (e) respectively. Meanwhile, it is also interesting to notice that the slope in the spectrum (which enables the spectral flow) corresponds to the states localized around the modified plaquettes. Specifically, the eigenstates in the positive (negative) slope have a localized density distribution around the upper (lower) plaquette with modified flux $\phi + \delta\phi$ ($\phi - \delta\phi$). It is because of this type of spectrum, that ramping $\delta\phi$ from 0 to 2π corresponding to the insertion of one flux quantum,

that would lead to quantized charge pump from one modified plaquette to the other, as will be shown in the following.

3.2.2 Time evolution

For the time-dependent Hamiltonian $\hat{H}(t) = \hat{H}[\delta\phi(t)]$, the dynamics of the system is governed by the time-dependent Schrödinger equation,

$$i\hbar d_t|\psi(t)\rangle = \hat{H}(t)|\psi(t)\rangle. \tag{3.13}$$

The time evolution operator $\hat{U}(t, t_0)$ defined by $|\psi(t)\rangle = \hat{U}(t, t_0)|\psi(t_0)\rangle$ is generally expressed as

$$\hat{U}(t, t_0) = \mathcal{T} \exp\left(\frac{1}{i\hbar}\int_{t_0}^{t} \hat{H}(t')dt'\right), \tag{3.14}$$

with $\mathcal{T}$ indicating time ordering operator. While there are many integrated algorithms (for example in Python) for solving the evolution problem, in the following we adopt an alternative approach. The idea is based on that for small enough time interval $dt \ll 1$, $\hat{U}(t + dt, t)$ can be approximated by its Tylor expansion up to the leading order,

$$\hat{U}(t + dt, t) = e^{-i\hat{H}(t)dt} \approx 1 - i\hat{H}(t)dt, \tag{3.15}$$

where we have used dimensionless quantities by doing the replacement

$$\hat{H} \longleftrightarrow \hat{H}/J_x, t \longleftrightarrow tJ_x/\hbar. \tag{3.16}$$

However, the problem is that the approximated time evolution operator (3.15) is not unitary any more. This issue can be circumvented by the following trick,

$$\begin{aligned} |\psi(t + dt/2)\rangle &= \left[1 - i\hat{H}(t)dt/2\right]|\psi(t)\rangle \\ |\psi(t + dt/2)\rangle &= \left[1 - i\hat{H}(t)(-dt)/2\right]|\psi(t + dt)\rangle \\ \Rightarrow |\psi(t + dt)\rangle &= \underbrace{\left[1 + i\hat{H}(t)dt/2\right]^{-1}\left[1 - i\hat{H}(t)dt/2\right]}_{\hat{U}'(t+dt,t)}|\psi(t)\rangle. \end{aligned} \tag{3.17}$$

One can easily check the newly constructed evolution operator $\hat{U}'(t + dt, t)$ is unitary, and for small enough dt, the simulation of time evolution can be efficiently performed.

Along this line, we numerically solve the time-dependent Schrödinger equation by linearly increasing $\delta\phi$ from 0 to 2π within total ramping time τ, i.e. $\delta\phi\,(t) = (2\pi/\tau)t$. In the following, we focus on a square lattice of size 16×25 with uniform background flux ϕ; the two plaquettes with modified fluxes $\phi \pm \delta\phi$ are separated by $d = 10$ lattice constants in the center.

To mimic the IQH-type physics in our HH model, for now we consider non-interacting spinless (namely spin-polarized) fermions. Putting the Fermi energy above the lowest Landau level is equivalent to occupy all the states belonging to the lowest Hofstadter band. Due to the non-trivial Chern number $C = -1$ for the lowest band at $\alpha = 1/4$, a quasiparticle (quasihole) of 'charge' +1 (-1) is expected to be created after one quantum of flux insertion.

Results

Each eigenstate $|\Psi_j\rangle$ can be expressed in the lattice basis as $|\Psi_j\rangle = \sum_\ell \psi_\ell^j |\ell\rangle$ with the state index j and the coefficient $\psi_\ell^j \equiv \langle \ell|\Psi_j\rangle$. For non-interacting fermions occupying the lowest Hofstadter band, the initial state reads

$$|\Psi_F(t=0)\rangle = \prod_{j=0}^{N_F-1} \hat{a}_j^\dagger |\text{vac}\rangle, \text{ with } \hat{a}_j^\dagger = \sum_\ell \psi_\ell^j \hat{a}_\ell^\dagger, \tag{3.18}$$

where $N_F = MN/4$ is the number of occupied states below the Fermi energy. During the time evolution, the evolved state becomes

$$|\Psi_F(t)\rangle = \prod_{j=0}^{N_F-1} \hat{a}_j^\dagger(t) |\text{vac}\rangle, \text{ with } \hat{a}_j^\dagger(t) = \sum_\ell \psi_\ell^j(t) \hat{a}_\ell^\dagger, \tag{3.19}$$

where the time-dependent coefficients are determined according to

$$\psi_\ell^j(t) = \langle \ell|\hat{U}(t,0)|\Psi_j\rangle. \tag{3.20}$$

In this case, the particle density on site ℓ can be expressed as

$$n_\ell(t) = \langle \Psi_F(t)|\hat{n}_\ell|\Psi_F(t)\rangle = \sum_{j=0}^{N_F-1} \left|\psi_\ell^j(t)\right|^2. \tag{3.21}$$

Thus the total particle number in a specific region $R \in \{A, B, C\}$ in the lattice is

$$N_R(t) = \sum_{\ell \in R} n_\ell(t). \tag{3.22}$$

We define that the region A (B) is a square-shaped region of size 10×10, centered at the plaquette with additional flux $\delta\phi$ ($-\delta\phi$), and C is the area between A and B, as depicted in Fig. 3.5(b). To observe a possible signature of quantized charge pumping, we track the particle number differences (or 'charges') at time t

$$\Delta N_R(t) = N_R(t) - N_R(t=0). \tag{3.23}$$

As shown in Fig. 3.5(a), the values $\Delta N_{A,B}$ near ± 1 at $\delta\phi(\tau) = 2\pi$ suggest the creation of a quasiparticle (quasihole) around the plaquette where the additional flux $\delta\phi(-\delta\phi)$ is inserted. This charge pumping result can also be clearly visualized in Fig. 3.5(b), which shows the charge distribution $N_\ell(t) - N_\ell(0)$ at the end of flux insertion.

In order to prevent the created excitations from dispersing, static pinning potentials $V/J_x = \pm 1$ can be applied [169] on each of the four sites around the plaquette with additional flux $\mp\delta\phi$. As demonstrated in Figs. 3.5(c,d), the presence of pinning potentials $\mp V$ efficiently localizes the quasi-particle/hole. The origin of this dispersing behaviour can be attributed to the fact that, unlike the Landau levels of a continuous system, the energy bands of the Harper-Hofstadter model are not perfectly flat. Note that as a result of the incompressibility in the bulk of the

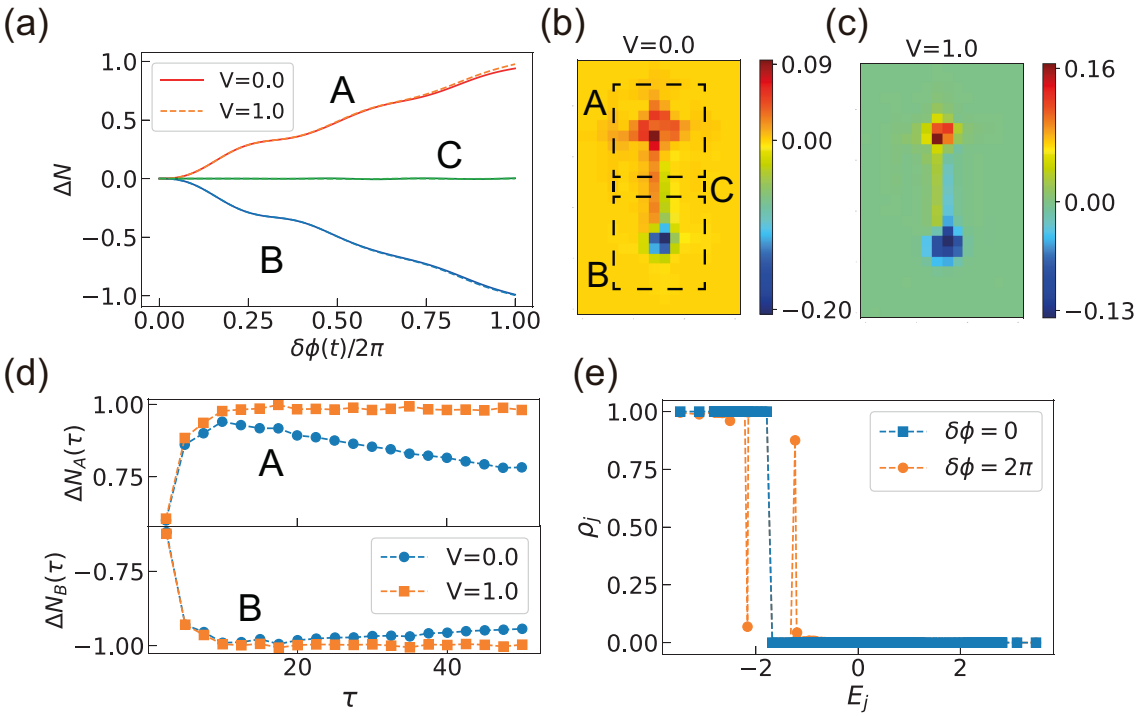

Figure 3.5: (a) The particle number difference $\Delta N_R = N_R(t) - N_R(t = 0)$ in regions $R = \{A, B, C\}$ [defined in (b)] as a function of $\delta\phi(t)$. The solid and dashed lines corresponds to the situation without and with pinning potential $V = \pm 1$, respectively. (b, c) Snapshots of the charge distribution at $t/\tau = 1$ for $V = 0$ and $V = 1$. (d) The final charge values in region A (upper panel) and B (lower panel) as a function of the total ramping time τ. While too short ramping times are not sufficient for adiabatic charge pumping, for too long times the pumped charge will disperse. The latter can be efficiently suppressed by introducing on-site pinning potentials. (e) Population of single-particle energy eigenstates before and after the flux insertion with $V = 1$. In (a-c) and (e), $\delta\phi$ is linearly ramped from 0 to 2π within time $\tau = 10$. We use $M = 16, N = 25, \alpha = 1/4, J_y = 1$. The energy and time are in the unit of J_x and $\hbar/J_x$ respectively.

Chern insualtr, small V will cause only tiny local density disturbances in the ground state. Since the pinning potentials are present before the flux insertion, they do not contribute to the relative density change.

Last but not least, one can also locate the quasiparticle and quasihole in the energy spectrum E_j by calculating the mean occupation ρ_j of the state with index j. For an initial eigenstate $|\Psi_{j'}\rangle$, at the end of ramping, the evolved state can be expressed in the eigenstate basis as $|\Psi_{j'}(\tau)\rangle = \sum_j \langle\Psi_j|\Psi_{j'}(\tau)\rangle|\Psi_j\rangle$. With this, the mean occupation ρ_j of state $|\Psi_j\rangle$ is defined as

$$\rho_j = \sum_{j'=0}^{N_F-1} \left|\langle\Psi_j|\Psi_{j'}(\tau)\rangle\right|^2. \tag{3.24}$$

In Fig. 3.5(e), we plot ρ_j at the beginning ($\delta\phi = 0$) and the end ($\delta\phi = 2\pi$) of the flux insertion in the case with $V/J_x = \pm 1$. Clearly, the states below the Fermi energy E_F are completely filled initially. At the end of flux insertion, while a quasihole appears in the occupied lowest band, a quasiparticle is created in the first excited band, which is broader than the lowest band. Note that without pinning potentials, the quasiparticle and quasihole excitations are distributed over several states. The presence of pinning potentials helps to pick certain dominant states, as shown by the sharp peak/dip in Fig. 3.5(e), so that the quasi-particle/hole can be well localized.

3.3 Engineering a tunable local flux

After the demonstration of quantized charge pumping by using the ideal modified HH model, in the following, we will see how to engineer this kind of solenoid-type local flux insertion by applying periodic driving in optical lattice with cold atoms.

3.3.1 Uniform flux in staggered potentials

As has been mentioned, the HH model with homogeneous artificial magnetic flux based on photon-assisted tunneling in a 2D optical square lattice has been realized in several experimental groups [120, 121, 123–125]. Here, we focus on the scheme used in the Munich group, who reported the first measurement of Chern number in optical lattices with cold atoms [124]. The experiment considers a sinusoidally driven superlattice with staggered potential offsets in x-direction, which can be described by the following time-periodic Hamiltonian,

$$\hat{H}(t) = \sum_{m,n}\left(-J_x\hat{a}^\dagger_{m+1,n}\hat{a}_{m,n} - J_y\hat{a}^\dagger_{m,n+1}\hat{a}_{m,n} + h.c.\right) + \sum_{m,n} w_{m,n}(t)\hat{n}_{m,n}, \tag{3.25}$$

$$\begin{aligned} w_{m,n}(t) = {} & V_s\cos\left(m\frac{\pi}{2} - \frac{\pi}{4}\right)\cos\left(\omega t - n\frac{\pi}{2} + \varphi_r\right) \\ & + V_s\cos\left(m\frac{\pi}{2} + \frac{\pi}{4}\right)\cos\left(\omega t + n\frac{\pi}{2} - \varphi_b\right) + \frac{1+(-1)^m}{2}\Delta. \end{aligned} \tag{3.26}$$

Here, $w_{m,n}(t)$ represent the on-site modulation potentials. The superlattice staggered potentials with offset $\Delta \gg J_x$ suppress the bare hopping along x. Resonant tunneling are restored by

two pairs of running-wave beams with amplitude V_s and frequency $\omega \equiv \omega_r = -\omega_b = \Delta/\hbar$. Note that each pair of running-wave beams consists of a standing wave along x and a running wave along y [155]. In the high-frequency limit $\hbar\omega \gg J_x, J_y$, using the formalism introduced in Section 2.5.2, a uniform artificial magnetic flux can be realized, and the effective Hamiltonian is expressed as

$$\begin{aligned}\hat{H}_{\text{eff}} = &-\sum_{m,n} J_x \mathcal{J}_1\left(\frac{\sqrt{2}V_s}{\hbar\omega}\right) e^{i\phi_{m,n}} \hat{a}^\dagger_{m+1,n}\hat{a}_{m,n} \\ &-\sum_{m,n} J_y \mathcal{J}_0\left(\frac{\sqrt{2}V_s}{\hbar\omega}\right) \hat{a}^\dagger_{m,n+1}\hat{a}_{m,n} + h.c.,\end{aligned} \tag{3.27}$$

where the tunneling strength is modified by the Bessel functions of the first kind $\mathcal{J}_\nu$ with $\nu = 0, 1$. In the following we consider isotropic tunneling, i.e.

$$J \equiv J_x \mathcal{J}_1\left(\frac{\sqrt{2}V_s}{\hbar\omega}\right) = J_y \mathcal{J}_0\left(\frac{\sqrt{2}V_s}{\hbar\omega}\right). \tag{3.28}$$

This can be achieved by tuning J_y/J_x via choosing different depth of the primary lattice in x and y directions. The effective tunneling phases read

$$\begin{aligned}\phi_{m,n} &= \frac{1-(-1)^m}{2}\left[n\frac{\pi}{2} \pm (m-1)\frac{\pi}{2} - \varphi_r\right] + \frac{1+(-1)^m}{2}\left[n\frac{\pi}{2} \pm (m+2)\frac{\pi}{2} - \varphi_b\right] \\ &\equiv n\frac{\pi}{2} + \eta_m.\end{aligned} \tag{3.29}$$

Here we introduce η_m to describe the m-dependent terms, which have no contribution in the value of flux per plaquette and thus represent a gauge freedom. It is the n-dependent phases that determine the uniform background flux of $\phi = \pi/2$ in the system, which is determined by the wavelength of the running wave along y. In the following, we give a detailed derivation of the above effective Hamiltonian by employing the formalism developed in Section 2.5.2.

Effective tunneling along x

From the on-site modulations $w_{m,n} \equiv w_\ell$ in Eq. (3.26), the relative modulations along x can be expressed as

$$\begin{aligned}w^x_{\ell'\ell}(t) =& w_{m+1,n}(t) - w_{m,n}(t) \\ =& V_s\left(-\sqrt{2}\sin\frac{m\pi}{2}\right)\cos\left(\omega t - n\frac{\pi}{2} + \varphi_r\right) \\ &+ V_s\left(-\sqrt{2}\cos\frac{m\pi}{2}\right)\cos\left(\omega t + n\frac{\pi}{2} - \varphi_b\right) + (-1)^{m+1}\hbar\omega \qquad (3.30) \\ =& \begin{cases} -\sqrt{2}V_s\cos\left[\omega t - \left(n\frac{\pi}{2} - \varphi_r \pm (m-1)\frac{\pi}{2}\right)\right] + \hbar\omega, & \text{odd } m \\ -\sqrt{2}V_s\cos\left[\omega t + \left(n\frac{\pi}{2} - \varphi_b \pm m\frac{\pi}{2}\right)\right] - \hbar\omega, & \text{even } m \end{cases}. \qquad (3.31)\end{aligned}$$

Based on the correspondence between the relative modulations Eq. (2.129) and the effective tunneling matrix element Eq. (2.133), one can thus immediately write down the effective tunneling parameters as

$$J_x^{\text{eff}} = \begin{cases} J_x \mathcal{J}_1\left(\frac{\sqrt{2}V_s}{\hbar\omega}\right) e^{i\left[\left(n\pi/2-\varphi_r\pm(m-1)\pi/2\right)\right]}, & \text{odd } m \\ J_x \mathcal{J}_{-1}\left(\frac{\sqrt{2}V_s}{\hbar\omega}\right) e^{i\left(n\pi/2-\varphi_b\pm m\pi/2\right)}, & \text{even } m \end{cases}. \tag{3.32}$$

By using the relation $\mathcal{J}_{-n}(x) = (-1)^n \mathcal{J}_n(x)$ the effective tunneling amplitude in Eq. (3.27) and phase (3.29) are obtained.

Effective tunneling along y

The relative modulations along y can be written as

$$\begin{aligned} w^y_{\ell'\ell}(t) =& w_{m,n+1}(t) - w_{m,n}(t) \\ =& \sqrt{2}V_s \cos\left(m\frac{\pi}{2} - \frac{\pi}{4}\right) \sin\left(\omega t - n\frac{\pi}{2} + \varphi_r - \frac{\pi}{4}\right) \\ &+ \sqrt{2}V_s \cos\left(m\frac{\pi}{2} + \frac{\pi}{4}\right) \sin\left(-\omega t - n\frac{\pi}{2} + \varphi_b - \frac{\pi}{4}\right) \qquad (3.33) \\ =& \frac{V_s}{\sqrt{2}}\left[-\cos\left(\frac{m+n}{2}\pi + \omega t - \varphi_b\right) - \cos\left(\frac{m+n}{2}\pi + \omega t + \varphi_r - n\pi\right)\right] \\ &+ \frac{V_s}{\sqrt{2}}\left[\sin\left(\frac{m+n}{2}\pi - \omega t + \varphi_b - n\pi\right) - \sin\left(\frac{m+n}{2}\pi - \omega t - \varphi_r\right)\right] \qquad (3.34) \\ \equiv& \begin{cases} \frac{V_s}{\sqrt{2}}\cos\left(\frac{m+n}{2}\pi\right) \times A, & \text{even } (m+n) \\ \frac{V_s}{\sqrt{2}}\sin\left(\frac{m+n}{2}\pi\right) \times B, & \text{odd } (m+n) \end{cases}. \qquad (3.35) \end{aligned}$$

For convenience, in the last equation we introduce A and B to denote the terms related to even or odd $(m+n)$. Specifically, for even $(m+n)$, the A-terms read

$$\begin{aligned} A =& -\cos(\omega t - \varphi_b) - \cos(\omega t + \varphi_r - n\pi) + \sin(-\omega t + \varphi_b - n\pi) + \sin(\omega t + \varphi_r) \\ =& \begin{cases} \sqrt{2}\left[\sin(\omega t + \varphi_r - \pi/4) - \sin(\omega t - \varphi_b + \pi/4)\right], & \text{even } n \\ \sqrt{2}\left[\sin(\omega t + \varphi_r + \pi/4) + \sin(\omega t - \varphi_b - \pi/4)\right], & \text{odd } n \end{cases} \\ =& \begin{cases} -2\sqrt{2}\cos\left(\omega t + \frac{\varphi_r - \varphi_b}{2}\right)\sin\left(\frac{\pi}{4} - \frac{\varphi_r + \varphi_b}{2}\right), & \text{even } n \\ 2\sqrt{2}\sin\left(\omega t + \frac{\varphi_r - \varphi_b}{2}\right)\cos\left(\frac{\pi}{4} + \frac{\varphi_r + \varphi_b}{2}\right), & \text{odd } n \end{cases} \\ =& 2\sqrt{2}\sin\left(\frac{\varphi_r + \varphi_b}{2} - \frac{\pi}{4}\right)\cos\left(\omega t + \frac{\varphi_r - \varphi_b}{2} + \frac{\pi}{2}\frac{1-(-1)^n}{2}\right). \end{aligned} \tag{3.36}$$

After a similar calculation for the B-terms, the relative modulations can be expressed as

$$w^{y}_{\ell'\ell}(t) = \begin{cases} 2V_s \cos\frac{(m+n)\pi}{2} \sin\left(\frac{\varphi_r+\varphi_b}{2} - \frac{\pi}{4}\right) \cos\left(\omega t + \frac{\varphi_r-\varphi_b}{2} + \frac{\pi}{2}\frac{1-(-1)^n}{2}\right), & \text{even } (m+n) \\ -2V_s \sin\frac{(m+n)\pi}{2} \cos\left(\frac{\varphi_r+\varphi_b}{2} - \frac{\pi}{4}\right) \cos\left(\omega t + \frac{\varphi_r-\varphi_b}{2} + \frac{\pi}{2}\frac{1+(-1)^n}{2}\right), & \text{odd } (m+n) \end{cases}. \tag{3.37}$$

As there is no static offset along the y-direction, i.e. $v_{\ell'\ell} = 0$, the y-tunneling parameter is modified by the 0th order Bessel function which satisfies $\mathcal{J}_0(-x) = \mathcal{J}_0(x)$. Based on this observation, requiring that

$$\left|\sin\left(\frac{\varphi_r+\varphi_b}{2} - \frac{\pi}{4}\right)\right| = \left|\cos\left(\frac{\varphi_r+\varphi_b}{2} - \frac{\pi}{4}\right)\right| = \frac{\sqrt{2}}{2}, \tag{3.38}$$

i.e. $\varphi_r + \varphi_b = \pi \times$ integer, the effective tunneling matrix element Eq. (2.133) becomes

$$J^{\text{eff}}_y = J_y \mathcal{J}_0\left(\frac{K^y_{\ell'\ell}}{\hbar\omega}\right) = J_y \mathcal{J}_0\left(\frac{\sqrt{2}V_s}{\hbar\omega}\right). \tag{3.39}$$

Note that while the relative phase difference $\varphi_r - \varphi_b$ can be controlled experimentally, the value of a single φ_r or φ_b could take a different value for each experimental realization [155]. This would thus induce inhomogeneous tunneling along the y direction. Taking $\varphi_r - \varphi_b = -\pi/2$ for example, the y-tunneling amplitude is modified as

$$J^{\text{eff}}_y = \begin{cases} J_y \mathcal{J}_0\left(\frac{2V_s}{\hbar\omega}\sin\varphi_r\right), & \text{even } (m+n) \\ J_y \mathcal{J}_0\left(\frac{2V_s}{\hbar\omega}\cos\varphi_r\right), & \text{odd } (m+n) \end{cases}. \tag{3.40}$$

Nevertheless, due to the fact that $\mathcal{J}_0(x) \approx 1 - x^2/4$ changes slowly with small arguments ($V_s/\hbar\omega \ll 1$), the effective coupling is well approximated by $J^y_{\text{eff}} \approx J_y$ in high-frequency regime.

3.3.2 Tunable local flux via additional driving

We now describe how to engineer additional solenoid-type fluxes piercing two lattice plaquettes, as depicted in Fig. 3.6(a). For this purpose, we consider additional sinusoidal driving potentials (which can be induced by digital mirror devices) in the shaded subregion R_s of Fig. 3.6(a). Thus the Hamiltonian consists of the original one $\hat{H}(t)$ (3.25) and the additional driving terms on some sites ℓ,

$$\hat{H}'(t) = \hat{H}(t) + \sum_{\ell\in R_s} K_\ell \sin(\omega t - \varphi_\ell)\,\hat{n}_\ell. \tag{3.41}$$

The driven system is described by the modified effective time-independent Hamiltonian

$$\hat{H}'_{\text{eff}} = -\sum_{m,n} J'^{x}_{\text{eff}} \hat{a}^\dagger_{m+1,n}\hat{a}_{m,n} - \sum_{m,n} J'^{y}_{\text{eff}} \hat{a}^\dagger_{m,n+1}\hat{a}_{m,n} + h.c., \tag{3.42}$$

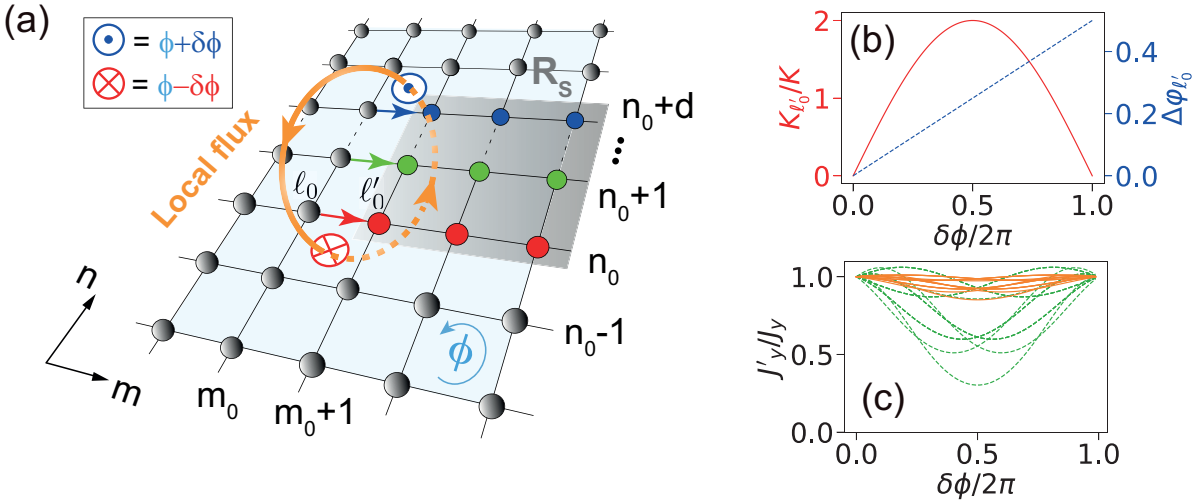

Figure 3.6: (a) Scheme for realizing solenoid-type local plaquette fluxes in a 2D optical lattice. The bonds labeled by colored arrows acquire an additional Peierls phase $\delta\phi$ as a result of the modification of the driving potentials on the colored rows. The integer d represents the distance between the plaquettes labeled by $\otimes, \odot$ whose flux become $\phi \pm \delta\phi$, with homogeneous background flux ϕ. (b) Amplitude $K_{\ell_0'}/K$ and phase $\Delta\varphi_{\ell_0'} \equiv (\varphi_{\ell_0'} - \varphi_{\ell_0'\ell_0})/2\pi$ of the additional driving versus the phase shift $\delta\phi$ according to Eq. (3.44). (c) Modification of tunneling parameters transverse to the colored rows at the background flux $\phi = \pi/2$, for $K = 0.15\hbar\omega$ (orange/solid) and $K = 0.35\hbar\omega$ (green/dashed).

which shall approximate the ideal Hamiltonian (3.12). In the following, we first summarize the basic idea of how to engineer the additional driving to obtain the desired properties of the effective tunneling parameters, before a detailed derivation is given.

We first discuss the x-tunneling process. Within the rows labelled by the same color, identical driving is imposed on every site. Thus the relative energies of the neighbouring sites of the same color in Fig. 3.6(a) are not changed, so that between theses sites the effective tunneling matrix elements are not modified. However, for hopping on the link connected by an unmodified site and a modified one [denoted by arrows in Fig. 3.6(a)], their relative modulation is changed and thus affects the hopping process. We choose the additional driving so that the strength of tunneling remains the same, while the tunneling phase obtains a shift of $\delta\phi$. The parameter for hopping leftward along that link shall be modified to

$$J_x'^{\text{eff}} = J_x^{\text{eff}} e^{i\delta\phi} = J_x \mathcal{J}_1\left(\frac{\sqrt{2}V_s}{\hbar\omega}\right) e^{i\left(\phi_{m,n}+\delta\phi\right)}. \tag{3.43}$$

In the n_0-th row, e.g., this can be achieved by applying additional driving potential $K_{\ell_0'}\sin(\omega t - \varphi_{\ell_0'})$ on site $\ell_0' = (m_0+1, n_0)$ (and all other red sites), with

$$K_{\ell_0'} = 2K\sin\left(\delta\phi/2\right) \text{ and } \varphi_{\ell_0'} = \varphi^x_{\ell_0'\ell_0} + \delta\phi/2, \tag{3.44}$$

where $\varphi^x_{\ell_0'\ell_0}$ are determined according to the expression of $w^x_{\ell'\ell}(t) = K\cos\left(\omega t - \varphi^x_{\ell'\ell}\right) + v_{\ell'\ell}\hbar\omega$ with $K \equiv -\sqrt{2}V_s$ in Eq. (3.31). In the case of odd m_0, for example, one has $\varphi^x_{\ell_0'\ell_0} = (n_0 \pm m_0)\,\pi/2 - \varphi_r$. The values of $\delta\phi$ can be varied continuously from 0 to 2π by simultaneously tuning both the strength $K_{\ell_0'}$ and the phase $\varphi_{\ell_0'}$ of the additional driving as depicted in Fig. 3.6(b). For the other rows in the shadowed area, the same strategy is applied and the same $\delta\phi$ is implemented on each of the modified links [labeled by arrows in Fig. 3.6(a)]. This results in solenoid-type local fluxes $\phi \pm \delta\phi$ for the plaquettes at the end of the modified links [denoted by $\otimes, \odot$ in Fig. 3.6(a)], while the other plaquettes remain to have the uniform background flux ϕ.

According to Eq. (3.44), the additional driving phase $\varphi_{\ell'}$ in the nth row depends on the phase $\varphi_{\ell'\ell}$ of the relative modulation on the modified bond in that row. Such row-dependent additional driving will modify the y-tunneling matrix elements involving coloured sites with additional driving,

$$J_y'^{\text{eff}} = J_y \mathcal{J}_0\left(\frac{K'^y_{\ell'\ell}}{\hbar\omega}\right), \tag{3.45}$$

where $K'^y_{\ell'\ell}$ is the amplitude of the relative modulation on the vertical links, which will be modified by the additional driving on different rows. In the case of a background flux $\phi = \pi/2$, the tunneling matrix elements are modified in eight different ways (depending on their position) that are plotted in Fig. 3.6(c) for two different values of $K/(\hbar\omega)$. Notice that the so-induced tunneling inhomogeneities can be efficiently reduced for small $K/\hbar\omega$ due to $\mathcal{J}_0(x) \simeq 1 - x^2/4$. Moreover, since we are interested in (topologically non-trivial) insulating states, which are protected by a bulk gap, the system will be robust against small inhomogeneities. In the following, we provide more details about the deviation of the above effective tunneling matrix elements.

Modified tunneling along x

Consider the modified link connected by the sites $\ell = (m_0, n)$, $\ell' = (m_0 + 1, n)$. Without additional driving potential, the relative modulation (3.31) can be reformed as,

$$w^x_{\ell'\ell}(t) = K\cos\left(\omega t - \varphi^x_{\ell'\ell}\right) + v_{\ell'\ell}\hbar\omega, \tag{3.46}$$

with

$$\varphi^x_{\ell'\ell} = n\frac{\pi}{2} + \tilde{\eta}_{m_0}, \tag{3.47}$$

$$\tilde{\eta}_{m_0} \equiv \frac{1-(-1)^{m_0}}{2}\left(\pm(m_0-1)\frac{\pi}{2} - \varphi_r\right) + \frac{1+(-1)^{m_0}}{2}\left(\pm m_0\frac{\pi}{2} - \varphi_b\right), \tag{3.48}$$

$$v_{\ell'\ell} = \frac{1-(-1)^{m_0}}{2} - \frac{1+(-1)^{m_0}}{2} = \begin{cases} 1, & \text{odd } m_0 \\ -1, & \text{even } m_0 \end{cases}. \tag{3.49}$$

Due to the additional driving on site ℓ', the relative modulation is modified as

$$\begin{aligned} w'^x_{\ell'\ell}(t) &= w^x_{\ell'\ell}(t) + K_{\ell'}\sin\left(\omega t - \varphi_{\ell'}\right) \\ &= K\cos\left(\omega t - \varphi^x_{\ell'\ell}\right) + v_{\ell'\ell}\hbar\omega + K_{\ell'}\sin\left(\omega t - \varphi_{\ell'}\right). \end{aligned} \tag{3.50}$$

Again, based on the correspondence between Eq. (2.129) and Eq. (2.133), in order to fix the hopping strength while giving a shift of $\delta\phi$ in the tunneling phase, i.e.

$$J'^x_{\text{eff}} = J_x\mathcal{J}_{v_{\ell'\ell}}\left(\frac{-K}{\hbar\omega}\right)e^{iv_{\ell'\ell}\left(\varphi_{\ell'\ell}+\delta\phi\right)} = J_x\mathcal{J}_1\left(\frac{-K}{\hbar\omega}\right)e^{i\left(\phi_{m,n}+\delta\phi\right)}, \tag{3.51}$$

the modified relative modulation should take the form of

$$w'^x_{\ell'\ell}(t) = K\cos\left[\omega t - \left(\varphi^x_{\ell'\ell} + \delta\phi\right)\right] + v_{\ell'\ell}\hbar\omega. \tag{3.52}$$

Combining Eq. (3.50) with Eq. (3.52), one gets

$$\begin{aligned} K_{\ell'}\sin\left(\omega t - \varphi_{\ell'}\right) &= K\cos\left[\omega t - \left(\varphi^x_{\ell'\ell} + \delta\phi\right)\right] - K\cos\left(\omega t - \varphi^x_{\ell'\ell}\right) \\ &\equiv K\cos A - K\cos B \\ &= K\cos\left(\frac{A+B}{2} + \frac{A-B}{2}\right) - K\cos\left(\frac{A+B}{2} - \frac{A-B}{2}\right) \\ &= -2K\sin\left(\frac{A-B}{2}\right)\sin\left(\frac{A+B}{2}\right) \\ &= 2K\sin\frac{\delta\phi}{2}\sin\left(\omega t - \frac{2\varphi^x_{\ell'\ell} + \delta\phi}{2}\right), \end{aligned} \tag{3.53}$$

where we have introduced $A = \omega t - \left(\varphi^x_{\ell'\ell} + \delta\phi\right)$, $B = \omega t - \varphi^x_{\ell'\ell}$ for short. From the two sides of the above equation (3.53), one immediately has

$$K_{\ell'} = 2K\sin\frac{\delta\phi}{2}, \varphi_{\ell'} = \varphi^x_{\ell'\ell} + \frac{\delta\phi}{2}. \tag{3.54}$$

Thus Eq. (3.44) is reproduced. Combing the above equation with Eq. (3.47), the value of $\delta\phi$ can be varied continuously from 0 to 2π by simultaneously tuning the additional driving amplitude K'_ℓ and phase φ'_ℓ, as shown in Fig. 3.6(b).

Modified tunneling along y

The y-tunneling parameters will suffer even more complicated modifications, as the additional driving generally varies for different rows. Consider a vertical hopping from site $\ell = (m, n)$ to site $\ell' = (m, n+1)$. In the case without additional driving, the relative modulation (3.37) can be rewritten as

$$w^y_{\ell'\ell}(t) = K^y_{\ell'\ell} \cos\left(\omega t - \varphi^y_{\ell'\ell}\right), \tag{3.55}$$

with

$$K^y_{\ell'\ell} = K \sin\frac{(m+n)\pi}{2} - K\cos\frac{(m+n)\pi}{2}, \tag{3.56}$$

$$\varphi^y_{\ell'\ell} = -\frac{1+(-1)^m}{2}\frac{\varphi_r - \varphi_b}{2} - \frac{1-(-1)^m}{2}\frac{\varphi_r - \varphi_b + \pi}{2}, \tag{3.57}$$

where we have chosen $\varphi_r + \varphi_b = \pi$ in Eq. (3.37) for simplicity and $\varphi_r - \varphi_b$ is a free parameter that can be tuned experimentally.

In the presence of additional driving on both sites, according to Eqs. (3.47) and (3.54), the amplitude of an additional driving is independent on any site index, and the phase φ_ℓ only depends on indices n. Thus in the following we use the notation $K' \equiv K_\ell$ and $\varphi_n \equiv \varphi_\ell$. Now the relative modulations are modified as

$$\begin{aligned} w'^y_{\ell'\ell}(t) =& w^y_{\ell'\ell}(t) + K'\sin(\omega t - \varphi_{n+1}) - K'\sin(\omega t - \varphi_n) \\ =& \cos\omega t\left(K^y_{\ell'\ell}\cos\varphi^y_{\ell'\ell} - K'\sin\varphi_{n+1} + K'\sin\varphi_n\right) \\ &+ \sin\omega t\left(K^y_{\ell'\ell}\sin\varphi^y_{\ell'\ell} + K'\cos\varphi_{n+1} - K'\cos\varphi_n\right). \end{aligned} \tag{3.58}$$

The modified y-tunneling matrix element (3.45) can be obtained by directly applying the relation between Eq. (2.129) and Eq. (2.133), in which case it is convenient to generally write $w'^y_{\ell'\ell}(t)$ as

$$w'^y_{\ell'\ell}(t) = K'^y_{\ell'\ell}\cos\left(\omega t - \varphi'^y_{\ell'\ell}\right) = K'^y_{\ell'\ell}\cos\omega t\cos\varphi'^y_{\ell'\ell} + K'^y_{\ell'\ell}\sin\omega t\sin\varphi'^y_{\ell'\ell}. \tag{3.59}$$

Comparing the above two equations (3.58) and (3.59), one has

$$\begin{cases} K'^y_{\ell'\ell}\cos\varphi'^y_{\ell'\ell} = K^y_{\ell'\ell}\cos\varphi^y_{\ell'\ell} - K'\sin\varphi_{n+1} + K'\sin\varphi_n \\ K'^y_{\ell'\ell}\sin\varphi'^y_{\ell'\ell} = K^y_{\ell'\ell}\sin\varphi^y_{\ell'\ell} + K'\cos\varphi_{n+1} - K'\cos\varphi_n \end{cases}. \tag{3.60}$$

Summing the square of both sides of the above equations leads to

$$\begin{aligned} \left(K'^y_{\ell'\ell}\right)^2 =& \left(K^y_{\ell'\ell}\right)^2 + 2K'^2 + 2K^y_{\ell'\ell}K'\sin\left(\varphi^y_{\ell'\ell} - \varphi_{n+1}\right) \\ &- 2K^y_{\ell'\ell}K'\sin\left(\varphi^y_{\ell'\ell} - \varphi_n\right) - 2K'^2\cos\left(\varphi_{n+1} - \varphi_n\right). \end{aligned} \tag{3.61}$$

With this, the modified y-tunneling matrix element (3.45) can be determined.

As a summary, for both sites with additional driving, the effective y-tunneling parameter is

$$J'^{\text{eff}}_y = J_y \mathcal{J}_0\left(\frac{K'_{\ell'\ell}}{\hbar\omega}\right), \tag{3.62}$$

with

$$\begin{cases} K'^{y}_{\ell'\ell} = \sqrt{\left(K^{y}_{\ell'\ell}\right)^2 + 2K'^2 + 2K^{y}_{\ell'\ell}K'\left(\sin\left(\varphi^{y}_{\ell'\ell} - \varphi_{n+1}\right) - \sin\left(\varphi^{y}_{\ell'\ell} - \varphi_n\right)\right) - 2K'^2\cos\left(\varphi_{n+1} - \varphi_n\right)}, \\ K^{y}_{\ell'\ell} = K\sin\frac{(m+n)\pi}{2} - K\cos\frac{(m+n)\pi}{2}, \\ K' = 2K\sin\frac{\delta\phi}{2}, \\ \varphi_n = \varphi^{x}_{\ell'\ell} + \frac{\delta\phi}{2} = n\frac{\pi}{2} + \tilde{\eta}_{m_0} + \frac{\delta\phi}{2}, \\ \tilde{\eta}_{m_0} = \frac{1-(-1)^{m_0}}{2}\left(\pm(m_0-1)\frac{\pi}{2} - \varphi_r\right) + \frac{1+(-1)^{m_0}}{2}\left(\pm m_0\frac{\pi}{2} - \varphi_b\right), \\ \varphi^{y}_{\ell'\ell} = -\frac{1+(-1)^{m}}{2}\frac{\varphi_r-\varphi_b}{2} - \frac{1-(-1)^{m}}{2}\frac{\varphi_r-\varphi_b+\pi}{2}. \end{cases} \tag{3.63}$$

Similarly, for the vertical hopping on the links connected by a unmodified site and a modified one (which corresponds to region $R_{\text{upper}}, R_{\text{lower}}$ in Fig. 3.9), the effective tunneling matrix elements can be obtained by slightly modifying the above $K'^{y}_{\ell'\ell}$. Depending on hopping from or towards the modified site, one has

$$\begin{cases} w'^{y}_{\ell'\ell}(t) = w^{y}_{\ell'\ell}(t) + K'\sin(\omega t - \varphi_{n+1}), & \ell \in R_{\text{lower}} \\ \Rightarrow K'^{y}_{\ell'\ell} = \sqrt{\left(K^{y}_{\ell'\ell}\right)^2 + K'^2 + 2K^{y}_{\ell'\ell}K'\sin\left(\varphi^{y}_{\ell'\ell} - \varphi_{n+1}\right)}, & \\ w'^{y}_{\ell'\ell}(t) = w^{y}_{\ell'\ell}(t) - K'\sin(\omega t - \varphi_n), & \ell \in R_{\text{upper}} \\ \Rightarrow K'^{y}_{\ell'\ell} = \sqrt{\left(K^{y}_{\ell'\ell}\right)^2 + K'^2 - 2K^{y}_{\ell'\ell}K'\sin\left(\varphi^{y}_{\ell'\ell} - \varphi_n\right)}. & \end{cases} \tag{3.64}$$

Taking into account all these possibilities, the inhomogeneous y-tunneling matrix elements (3.45) are plotted in Fig. 3.6(c).

3.3.3 Dynamics from effective Hamiltonian

To investigate the effect of the inhomogeneous tunneling induced by the additional driving, we now follow the procedure shown in Section 3.2.2 and numerically solve the time-dependent Schrödinger equation for the effective Hamiltonian (3.42). The corresponding results of accumulated charges as a function of $\delta\phi$ are shown by the dotted line in Fig. 3.7(a). After comparing with the results obtained for the ideal Hamiltonian (3.12), good agreement is observed. This demonstrates the topological property of quantized charge pumping, which is robust against finite y-tunneling inhomogeneities.

This observation is further confirmed by the snapshots of the evolution of the spatial density distributions, as shown in Fig. 3.7(c). It shows that the tunneling inhomogeneity mainly induces extra excitations at the edge. This is related to the fact that the edge modes are gapless and thus not protected. However, it does not affect the creation of quasiparticles and quasiholes in the bulk, which is protected by an energy gap.

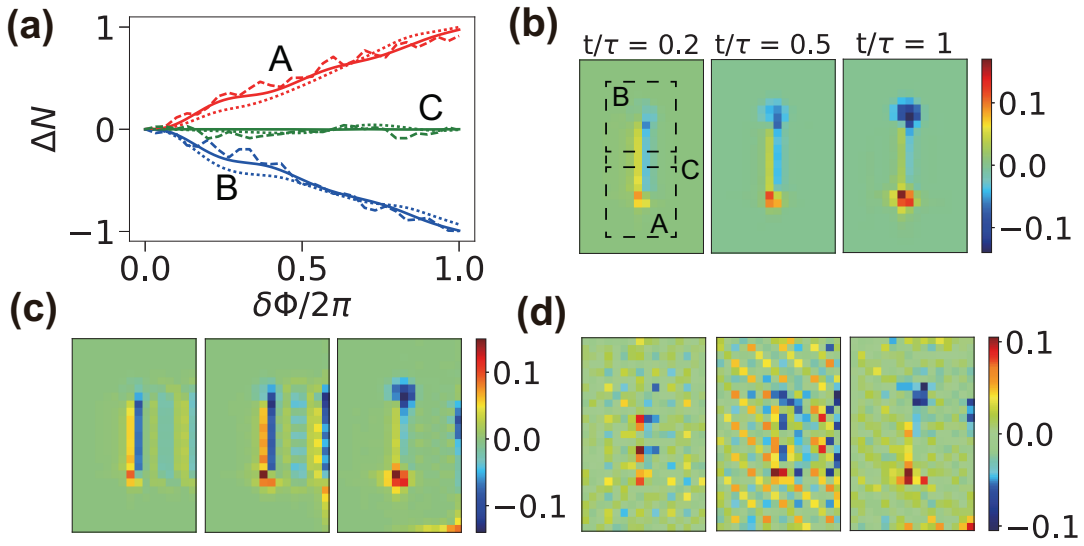

Figure 3.7: (a) The particle number difference $\Delta N_i = N_i(t) - N_i(t=0)$ in regions $i =$ A, B and C [defined in (b)] as a function of $\delta\phi(t)$, which is ramped linearly from 0 to 2π within the time $\tau = 10\hbar/J$, for $K/\hbar\omega = 0.35$. The solid, dotted, and dashed lines are obtained by solving the time-dependent Schrödinger equation for the ideal Hamiltonian (3.12), the effective Hamiltonian (3.42), and the time-dependent Hamiltonian (3.66) respectively. Snapshots of the respective changes in spatial densities are depicted in (b), (c) and (d). The simulation of Hamiltonian (3.66) includes the preparation of the Chern insulator before the ramp (see Fig. 3.8), and also imperfections as they would arise from a limited spatial resolution of the additional driving potentials. Note that in order to adapt to the previous experimental realization of the uniform background flux, different from the discussion in Section 3.2.2, the flux per plaquette is $\phi = -\pi/2$ when defined via counter-clockwise hopping around one lattice unit cell.

3.3.4 Full time dynamics

For the implementation of the above-mentioned local flux scheme, we consider the following experimental protocol, which includes also the preparation of the Chern insulator state from the ground state of the undriven lattice [Fig. 3.8(a)]. We start with a trivial band insulator in a staggered potential with energy offsets $\Delta + \delta$ along x and δ along y direction [124]. Then the driving amplitude K is ramped up linearly to its final value within time τ_1. Subsequently the detuning δ/J is ramped down between τ_1 and τ_2. During this ramp, the system undergoes a topological phase transition into a Chern insulator state [124]. This topologically non-trivial regime should be reached adiabatically by relying on the finite extent of the system. At the same time, the pinning potentials ($|V|/J = 1$) are also switched on at the modified plaquettes. In the last stage ($\tau_2 \to \tau_3$), the additional flux $\delta\phi$ is ramped from 0 to 2π by tuning the amplitudes K'_ℓ and the phases φ'_ℓ according to Eq. (3.44). Overall, the full-time dependent Hamiltonian

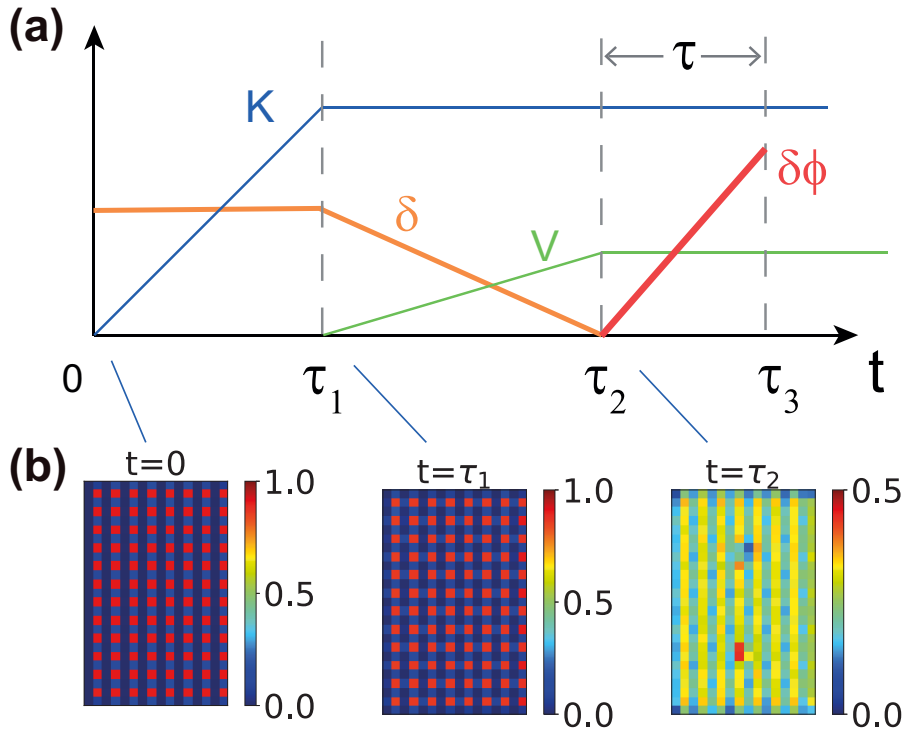

Figure 3.8: (a) Experimental protocol for the preparation of the Chern insulator starting from the ground state of the undriven lattice and the subsequent flux insertion (see main text). (b) Spatial density distribution at different stages of the protocol from the simulation of the time evolution of Eq. (3.66), for driving frequency of $\hbar\omega = 70J$, initial superlattice strength $\delta = 4J$, final driving amplitude $K/\hbar\omega = 0.35$, as well as ramping times $\tau_1 = 200\hbar/J, \tau_2 - \tau_1 = 400\hbar/J, \tau = \tau_3 - \tau_2 = 10\hbar/J$. The effect of the flux insertion ($\tau_2 \to \tau_3$) is shown in Fig. 3.7(d).

takes the following form,

$$\begin{aligned}\hat{H}_{\text{full}}(t) =& \sum_{m,n}\left(-J_x\hat{a}^\dagger_{m+1,n}\hat{a}_{m,n} - J_y\hat{a}^\dagger_{m,n+1}\hat{a}_{m,n} + h.c.\right) + \sum_{m,n} w_{m,n}(t)\hat{n}_{m,n} \\ &+ \sum_{m,n\in R_s} K'\sin\left(\omega t - \varphi_n\right)\hat{n}_{m,n} + \sum_{m,n}\left[(-1)^m\,\delta/2 + (-1)^n\,\delta/2\right]\hat{n}_{m,n},\end{aligned} \tag{3.65}$$

where $w_{m,n}$ (3.26) represent the sinusoidally driven staggered superlattice potentials; the additional driving terms are applied in the shadow region defined in Fig. 3.6(a); the additional staggered potentials δ are used for adiabatic preparation from an insulator that hosts four topologically trivial bands.

As discussed in Section 2.5.2, by going to a rotating frame via a gauge transformation (2.118), the above Hamiltonian can be rewritten as

$$\begin{aligned}\hat{H}'_{\text{full}}(t) =& \sum_{m,n}\left(-J_x e^{i\theta'^x_{\ell'\ell}(t)}\hat{a}^\dagger_{m+1,n}\hat{a}_{m,n} - J_y e^{i\theta'^y_{\ell'\ell}(t)}\hat{a}^\dagger_{m,n+1}\hat{a}_{m,n} + h.c.\right) \\ &+ \sum_{m,n}\left[(-1)^m\,\delta/2 + (-1)^n\,\delta/2\right]\hat{n}_{m,n}.\end{aligned} \tag{3.66}$$

According to Eqs. (2.120)(2.123), the tunneling phases are expressed as,

$$\theta'_{\ell'\ell}(t) = \int_{t_0}^{t} dt' w'_{\ell'\ell}(t')/\hbar + \chi_\ell(t_0) - \chi_{\ell'}(t_0), \tag{3.67}$$

where $w'_{\ell'\ell}(t')$ is the relative modulation between two nearest neighbouring sites and $\chi(t_0)$ are gauge free parameter to get rid of the initial time dependence. Specifically, regarding the leftward tunneling along the x-direction, for two sites without additional driving, the relative modulation (3.30) leads to the following tunneling phase

$$\begin{aligned}w^x_{\ell'\ell}(t') \Rightarrow \theta^x_{\ell'\ell}(t) =& \int_{t_0}^{t} dt' w^x_{\ell'\ell}(t')/\hbar + \chi_\ell(t_0) - \chi_{\ell'}(t_0) \\ =& \frac{K}{\hbar\omega}\sin\frac{m\pi}{2}\sin\left(\omega t - n\frac{\pi}{2} + \varphi_r\right) \\ &+ \frac{K}{\hbar\omega}\cos\frac{m\pi}{2}\sin\left(\omega t + n\frac{\pi}{2} - \varphi_b\right) + (-1)^{m+1}\omega t.\end{aligned} \tag{3.68}$$

It is then straightforward to get the modified tunneling phase due to the presence of additional driving on the right site ℓ', i.e. $w'^x_{\ell'\ell}(t') = w^x_{\ell'\ell}(t') + K'\sin\left(\omega t - \varphi_{\ell'}\right)$. In this case, one obtains

$$\theta'^x_{\ell'\ell}(t) = \begin{cases}\theta^x_{\ell'\ell}(t) - \frac{K'}{\hbar\omega}\cos\left(\omega t - \varphi_{\ell'}\right), & \ell \in R_{\text{arrow}}, \\ \theta^x_{\ell'\ell}(t), & \text{otherwise.}\end{cases} \tag{3.69}$$

Here, R_{arrow} denotes the region of sites that label the links with arrows, as depicted in Fig. 3.9.

For the upward hopping process, the bare relative modulation (3.33) gives rise to

$$\begin{aligned} w^y_{\ell'\ell}(t') \Rightarrow \theta^y_{\ell'\ell}(t) =& \int_{t_0}^{t} dt' w^y_{\ell'\ell}(t')/\hbar + \chi_\ell(t_0) - \chi_{\ell'}(t_0) \\ =& \frac{K}{\hbar\omega} \cos\left(m\frac{\pi}{2} - \frac{\pi}{4}\right) \cos\left(\omega t - n\frac{\pi}{2} + \varphi_r - \frac{\pi}{4}\right) \\ & - \frac{K}{\hbar\omega} \cos\left(m\frac{\pi}{2} + \frac{\pi}{4}\right) \cos\left(-\omega t - n\frac{\pi}{2} + \varphi_b - \frac{\pi}{4}\right). \end{aligned} \tag{3.70}$$

Due to the additional driving, the tunneling phases are accordingly modified as

$$\theta'^y_{\ell'\ell}(t) = \begin{cases} \theta^y_{\ell'\ell}(t) - \frac{K'}{\hbar\omega} \cos\left(\omega t - \varphi_{\ell'}\right), & \ell \in R_{\text{lower}} \\ \theta^y_{\ell'\ell}(t) + \frac{K'}{\hbar\omega} \cos\left(\omega t - \varphi_{\ell}\right), & \ell \in R_{\text{upper}} \\ \theta^y_{\ell'\ell}(t) - \frac{K'}{\hbar\omega} \cos\left(\omega t - \varphi_{\ell'}\right) + \frac{K'}{\hbar\omega} \cos\left(\omega t - \varphi_{\ell}\right), & \ell \in R_{\text{mid}} \\ \theta^y_{\ell'\ell}(t), & \text{otherwise} \end{cases} \tag{3.71}$$

where R denote the regions defined in Fig. 3.9, where the y-tunneling matrix elements are modified in an inhomogeneous fashion.

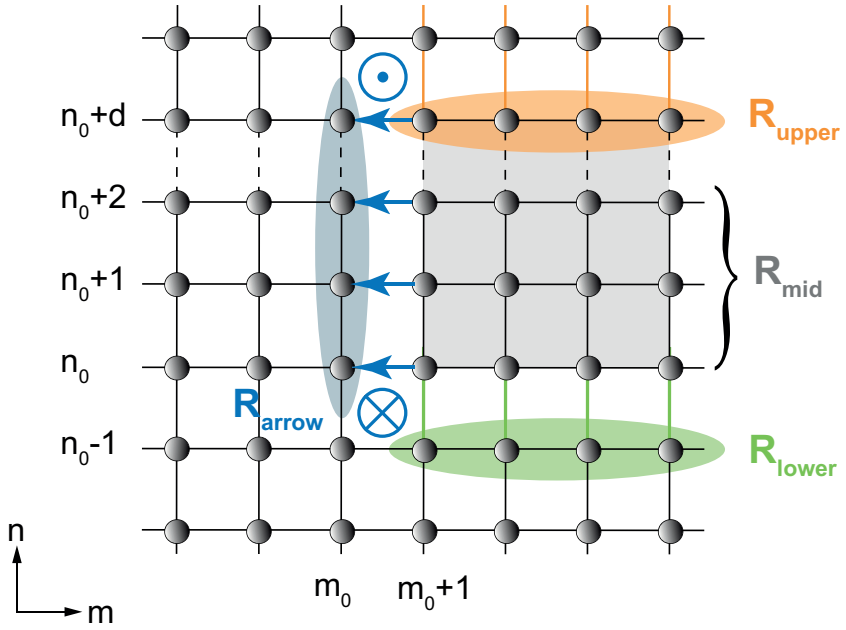

Figure 3.9: Sketch of modified regions due to the presence of additional driving. $R_{\text{arrow}} = \{(m_0, n)\}$ with $n \in \{n_0, n_0{+}1, \cdots, n_0{+}d\}$ locates the links with modified x-tunneling parameters. The other regions $R_{\text{lower}} = \{(m, n_0 - 1)\}$ and $R_{\text{lower}} = \{(m, n_0 + d)\}$ with $m \in \{m_0 + 1, m_0 + 2, \cdots, M - 1\}$ represent the link with additional driving only on one site. M is the total number of sites along the horizontal direction. The middle region $R_{\text{mid}} = \{(m, n)\}$ with $m \in \{m_0 + 1, m_0 + 2, \cdots, M - 1\}$ and $n \in \{n_0, n_0 + 1, \cdots, n_0 + d - 1\}$ corresponds to the links with both sites are modified with additional driving. Note that the shadow area defined in Fig. 3.6(a) is $R_s = R_{\text{mid}} + R_{\text{upper}}$.

In order to demonstrate the validity of our driving protocol, we have taken several practical issues into account. First, we start from the ground state of the initial un-driven Hamiltonian, i.e. a trivial band insulator. Thus possible driving induced interband transitions (i.e. Floquet heating) [71, 170] are included. Second, to address any concern regarding the impact of a possible limited optical resolution when creating additional light-shift potentials with the help of digital mirror devices, we assume that the light field is spatially smeared out. Namely, we consider only 80% of the proposed ideal additional driving on site ℓ to act on this site and the remaining 20% to be distributed evenly among the four neighboring sites. The results obtained from integrating the time evolution for this protocol using the time-dependent Hamiltonian (3.66) are presented in Fig. 3.7(a) (dashed lines) and (d). We observe that the quantized charge transport is spoiled neither by such interband excitations nor by the imperfect spatial resolution [Fig. 3.8(a), (d)]. The accumulated pumped charge shows excellent agreement with the ideal case [Fig. 3.7(a)], despite noticeable density modulations [Fig. 3.7(d)]. Note that not taking into account interactions is well justified in systems of spin-polarized fermionic atoms, and that the heating in Floquet systems has not been a major problem in experiments with such

spin-polarized fermions [112].

3.4 Controlled charge pumping

While the quantized charge pumping induced by the local flux insertion can be expected and is not surprising, we find an interesting unexpected effect. Namely, the path for a quantized charge pumping can created in a controllable fashion. It is related to the fact that in our approach, we directly engineer the vector potential rather than the magnetic field, so that during the pump cycle artificial electric fields $E \propto d(\delta\phi)/dt$ are present as well.

3.4.1 Tailored charge pumping in the bulk

One can observe in Fig. 3.7(b) that the path along which a quantum of charge is transported corresponds to the sequence of bonds with the additional Peierls phase $\delta\phi$. This phenomenon can be understood by noting that artificial electric fields are created by the time-dependent artificial vector potentials in the form of additional Peierls phases $\delta\phi(t)$. Let us investigate whether this scenario holds also for more complicated choices of Peierls phases that lead to the same time dependent magnetic fluxes, but different electric fields.

As shown in Figs. 3.10 (a,c), one can arrange the links with additional phases $\delta\phi$ in different ways, but guarantee that there are only two plaquettes with modified fluxes $\phi \pm \delta\phi$. In this case, after a quantum of flux insertion, as shown in Figs. 3.10(b,d) where we plot the snapshots of charge distributions at different time instant, one can clearly see that the charge is pumped along the tailored path.

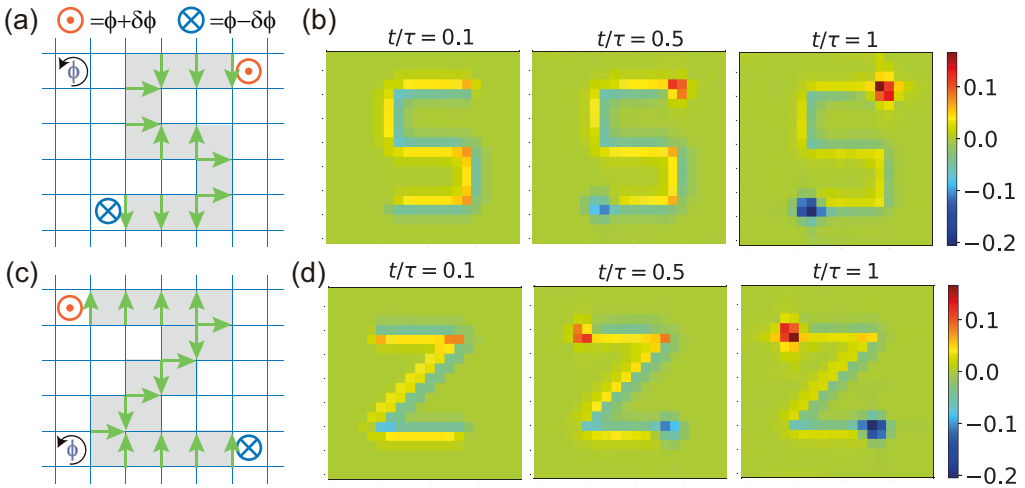

Figure 3.10: (a) Sketch of putting the additional phases $\delta\phi$ (denoted by green arrows) along a given path. Overall, only the fluxes of the plaquettes denoted by $\odot$ and $\otimes$ are modified to be $\phi \pm \delta\phi$, leaving the fluxes of all other plaquettes unchanged. (b) Snapshots of the charge distribution at different time instant during the ramp. (c, d) Same plots as (a,b) but using a different pattern for the path. All the simulations are performed for a system of size 20×20, with $J_y = 1, \alpha = 1/4$. $\delta\phi$ is linearly ramped from 0 to 2π within time $\tau = 10$. To prevent the quasi-particle from dispersing, small pinning potentials $V = -1$ have been placed on each of the four sites around the plaquette ($\odot$) with flux $\phi + \delta\phi$. The energy and time are in the unit of J_x and $\hbar/J_x$ respectively.

3.4.2 Edge mode population

As an interesting application, the paths can be tailored so as to populate edge mode coherently. As shown in Fig. 3.11(a), by adding phases $\delta\phi$ on the bonds starting from the target plaquettes to the edge instead of between them, a different particle transport is induced. Apart from the bulk excitations [as has been shown in Fig. 3.7(b)], a quasiparticle and a quasihole appear at the edges, see Fig. 3.11(b). Again quanta of charge are transported along the path defined by the modified Peierls phases. After being created, such edge excitations follow a chiral motion, until their densities annihilate each other after some time.

Alternatively, by introducing the additional flux through one single plaquette [Fig. 3.11(c)], a long-lived edge mode can also be populated. The time-evolving density distributions are shown in Fig. 3.11(d). In order to see the robustness against external perturbations, we have put strong impurity potentials of strength $10J_x$ in the edge during the time evolution. The absence of scattering at both the corners and the impurity indicates the topologically-protected property of the edge mode. Thus this mechanism can be a useful tool to probe robust chiral edge transport.

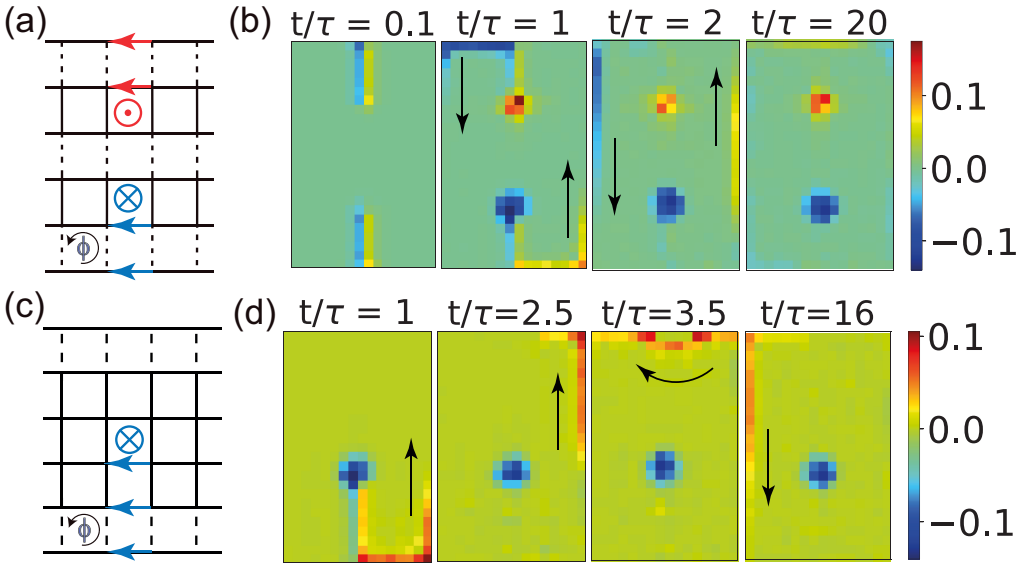

Figure 3.11: (a) Local flux configuration by modifying the links between the modified plaquette and the edge. (b) Snapshots of corresponding spatial density distributions during ramp. (c) and (d) for additional flux in a single plaquette. The chiral edge transport visible in (d) is robust at the corners and against an impurity potential of $10J_x$ at the lower edge. The results are obtained from time evolution with $\delta\phi(t) = 2\pi t/\tau$ for $t < \tau$ and $\delta\phi(t) = 2\pi$ for $t \geq \tau$, where $\tau = 10\hbar/J_x$.

3.5 Application in bosonic systems

So far we have been considering fermionic systems with the Fermi energy set above the lowest band. However, in the cold atom experiment where the Chern number was measured, it was a bosonic system that was implemented [124]. It is thus interesting to see a possible application of the local-flux insertion protocol also in such bosonic systems.

As has been validated experimentally, an incoherent distribution of bosons with homogeneous population within each band can be achieved by using a band-mapping technique [124]. To include the effects of populations in all Hofstadter bands, one firstly define the filling of particles in each band as

$$\eta_\mu = N_\mu / N_{tot}, \tag{3.72}$$

with N_μ being the particle number in the band labelled by $\mu \in \{1, 2, 3\}$ and $N_{tot} = \sum_\mu N_\mu$ being the total atom number. Note that for the HH model with a quarter flux $\alpha = 1/4$, the system exhibit only three well separated bands with the middle two touching sub-bands forming a 'super' band (labelled by $\mu = 2$), as indicated in Fig. 3.12(a). Assuming all bands being populated homogeneously and considering negligible inter-band transitions (which is justified at least within short time [124]), the charges that are pumped after one quantum of flux insertion can be expressed as

$$\Delta N = \sum_{\mu=1} \eta_\mu C_\mu, \tag{3.73}$$

where C_μ are the Chern numbers of the μ-th band and read $-1, 2, -1$ for $\mu = 1, 2, 3$ respectively.

To confirm the above prediction, one can now perform the simulation of flux insertion again, but calculate the charges (3.23) according to a slightly-modified form

$$\Delta N_R(t) = \sum_{\ell \in R} \sum_{j=0}^{N_{\text{count}}-1} \eta_{\mu,j} (|\psi_\ell^j(t)|^2 - |\psi_\ell^j(0)|^2), \tag{3.74}$$

where the number N_F of states below the Fermi energy in Eq. (3.21) is now replaced by N_{count}, which counts the states that have been populated by bosons. $\eta_{\mu,j} = \eta_\mu$ for the states labelled by j belonging to the band μ. Meanwhile, to better quantify the values of pumped charges, we define the relative differences of charges in region B and A, i.e.

$$\Delta N(t) = [\Delta N_B(t) - \Delta N_A(t)]/2. \tag{3.75}$$

Focusing on the local flux configuration with middle links modified, as described in Section 3.2, we consider three examples with different band populations. (i) Only the lowest band is populated, i.e. $\eta_\mu = \{1, 0, 0\}$ and $N_{\text{count}} = MN/4$. At the end of flux insertion $t = \tau$, the pumped charge reads $\Delta N(\tau) = -0.97 \simeq C_1 = -1$, which, as expected, has no difference with the fermionic case with the Fermi energy above the lowest band. (ii) When the bands $\mu = 1, 2$ are both homogeneously populated, as the middle band $\mu = 2$ contains twice as many states as that in the lowest band, one has $\eta_\mu = \{1/3, 2/3, 0\}$ and $N_{\text{count}} = 3MN/4$. Now the pumped charge calculated from Eq. (3.75) becomes $\Delta N(\tau) = 0.97$ which is in agreement with the prediction $\Delta N = -1 \cdot 1/3 + 2 \cdot 2/3 = 1$ given by Eq. (3.73). The reverse charge

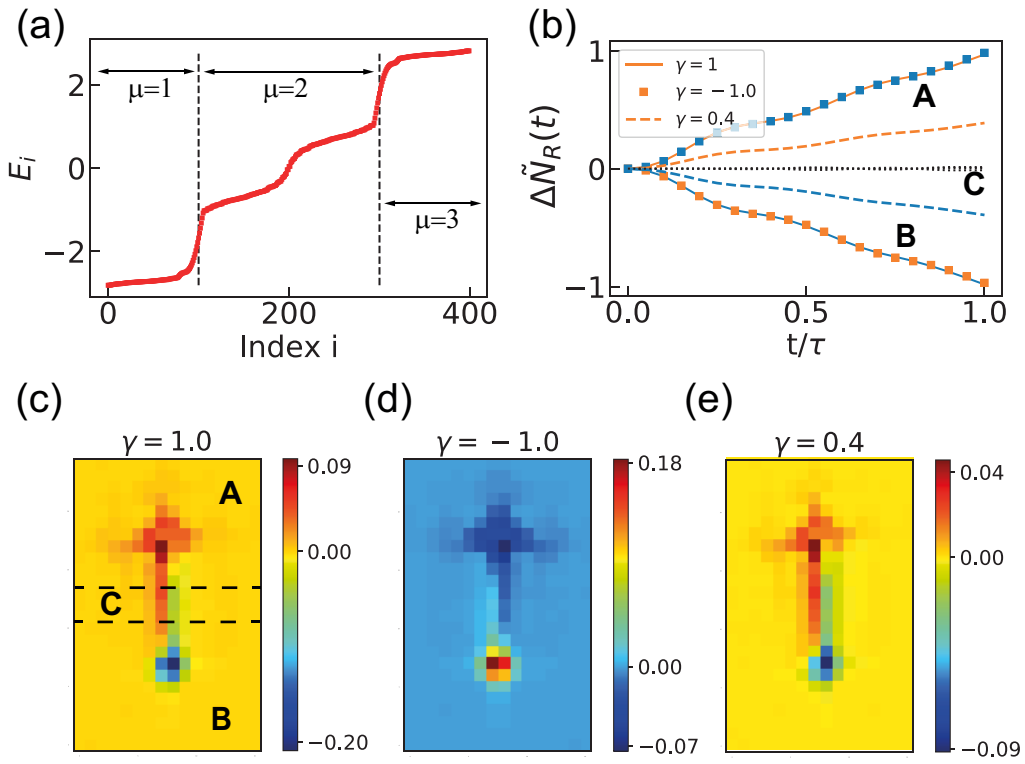

Figure 3.12: (a) Eigenvalues as function of state indices for a system of size 16×25 at $\alpha = 1/4$. The vertical dashed lines distinguish states belonging to three well-separated bands. (b) The particle number difference $\Delta N_R = N_R(t) - N_R(0)$ in regions $R = \{A, B, C\}$ as a function of ramping time for different band populations $\eta_\mu = \{1, 0, 0\}, \{1/3, 2/3, 0\}, \{0.7, 0.2, 0.1\}$, corresponding to $\gamma = 1, -1, 0.4$ respectively. While the orange colours illustrate the charges in Region A, the blue lines/dots represent charges in B. The black dotted lines are the results in Region C (the undisturbed background). (c-e) Snapshots of charge distributions at the end of flux insertion for $\gamma = 1, -1, 0.4$, respectively. The regions A, B, C are defined in (c). In all cases, we have used the total ramping time $\tau = 10\hbar/J_x$.

pumping can be visualized in Fig. 3.12(d). (iii) For a typical population that close to the experimental realization, i.e. $\eta_\mu = \{0.7, 0.2, 0.1\}$, the pumped charges include contributions from all the populated bands and one has to consider all the states $N_{\text{count}} = MN$. The numerical calculation gives the value of $\Delta N(\tau) = -0.39$, which also agrees with the expected value $\Delta N = -1 \cdot 0.7 + 2 \cdot 0.2 - 1 \cdot 0.1 = -0.4$.

Based on the above observation, one can see that the protocol of local flux insertion provides an alternative way of measuring Chern number even in bosonic system. To be specific, now making use of the relation of the Chern numbers $C_1 = C_3 = -C_2/2$ in the specific case of $\alpha = 1/4$, Eq. (3.73) indicates that the Chern number C_1 can be expressed as

$$C_1 = \Delta N/\gamma, \ \gamma \equiv \eta_1 - 2\eta_2 + \eta_3, \tag{3.76}$$

where the filling factor γ has been introduced for convenience. In case (iii) with $\gamma = 0.4$, for instance, the Chern number of the lowest band is found to be $C_1 = \Delta N(\tau)/\gamma = -0.39/0.4 = -0.975$. A better result can be obtained by considering larger system sizes or by introducing tiny on-site pinning potentials to prevent the created charges from dispersing. For example, the Chern number is found to be $C_1 = -0.989$ for the system size 16×37 with $V = 0$, and $C_1 = -0.996$ for 16×25 with $V/J_x = 1$.

To sum up, we have seen that the Chern number can be extracted from the pumped charges (which can be measured from *in-situ* images of atomic clouds) combined with the band populations (which can be determined from a band-mapping technique). It would thus complement the measurement of Chern number from transverse displacement in the previous cold atom experiment [124]. Meanwhile, such a robust way of quantized charge pumping via local flux insertion in bosonic systems would also be of interest for future experimental realization by using photons [43].

4 State preparation via ramping artificial gauge potentials

The engineering of artificial magnetic fields for charge-neutral atoms in optical lattices has been a powerful tool to simulate lattice models with exotic phases including quantum Hall states and topological insulators [36, 38, 71, 76, 79, 80]. More precisely, in these experiments a *static* artificial gauge potential (in the form of Peierls phases) is engineered in a particular choice of gauge (relative to the plain lattice without magnetic field). Typically, this choice is made based on experimental convenience. For a *dynamic* process, however, where these artificial gauge potentials are varied in time, this choice does not simply correspond to a gauge freedom anymore. This is because their temporal change generates an artificial electric field. After initial confirmation in a trapped quantum gas [171], such artificial electric forces were observed also in optical lattices [108, 172] and predicted to lead to 'gauge-dependent' time-of-flight images of Bose Einstein condensates [123, 173, 174]. In the previous chapter, we have shown that the engineering of time-dependent artificial gauge potentials can be employed for quantized charge pumping along tailored paths in two dimensional Chern insulators [166]. This effect can also be generalized to fractionalized charge pumping in fractional Chern insulators [175, 176] (see Chapter 5). Other applications include the control of the dynamics of a wave packet in synthetic dimensions [177] and nonlinear systems [178]. With the recent advances in quantum gas microscope techniques [65, 68, 69, 125, 179–182], it becomes more and more important to explore the possibilities of controlling artificial gauge potentials in both space and time. Since robust adiabatic state preparation is a prerequisite for the experimental investigation (quantum simulation) of interesting states of matter with atomic quantum gases, in this chapter, we will see how this technique can be exploited for the optimization of a state preparation.

As minimal lattice systems with artificial magnetic fields, flux ladders have recently drawn tremendous attention, including the experimental observation of chiral edge currents [92, 93, 96, 122, 125, 183], the theoretical exploration of rich phase diagrams [184–207], the investigation of Laughlin-like states [208–213], the study of the Hall effect [214–218] and other aspects [219–225]. In this chapter, we investigate the adiabatic preparation of the ground state in such ladder systems via continuously ramping up the corresponding Peierls phases. Comparing results for different patterns of Peierls phases, all giving rise to the same magnetic flux but to different synthetic electric fields during the ramp, we find that the degree of adiabaticity dramatically depends on this choice. As an intriguing result, the optimal choice of Peierls phases allows for an almost instantaneous preparation of the ground state. We show that for vanishing interactions, this effect can be related to counterdiabatic driving [24, 226–230]. Remarkably, our approach works also for very strong interactions, where a simple explanation in terms of counterdiabatic driving is not possible.

The results of Section 4.2 – 4.5 have been published in Ref. [231]. Section 4.1 is added as a preliminary introduction of the two-leg ladder system.

4.1 Two-leg flux ladder

We consider interacting bosons in a two-leg ladder described by the Bose-Hubbard model

$$\hat{H} = -\sum_{\langle \ell,\ell' \rangle} J_{\ell'\ell} e^{i\theta_{\ell'\ell}} \hat{a}^\dagger_{\ell'} \hat{a}_\ell + \frac{U}{2} \sum_\ell \hat{n}_\ell (\hat{n}_\ell - 1), \tag{4.1}$$

with bosonic creation operator $\hat{a}^\dagger_\ell$ and number operator $\hat{n}_\ell = \hat{a}^\dagger_\ell \hat{a}_\ell$ on site ℓ. The nearest-neighbor tunneling amplitude $J_{\ell'\ell}$ equals J along legs and $J_\perp$ along rungs, and it is accompanied by the Peierls phase $\theta_{\ell'\ell}$. U is the on-site repulsive interaction energy. In the following, we use J, $\hbar/J$ and lattice constant a as units for energy, time and lengths, respectively.

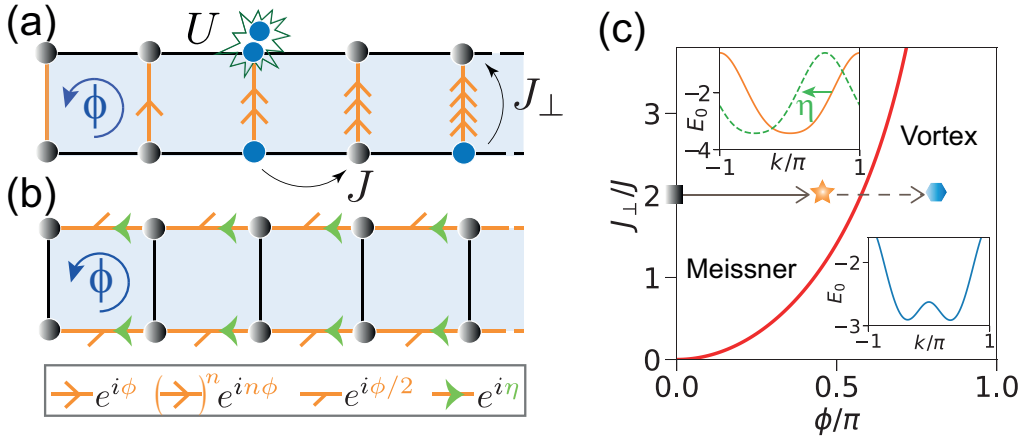

Figure 4.1: Bose-Hubbard ladder, with interaction parameter U, tunneling amplitudes J ($J_\perp$) along the legs (rungs) as well as Peierls phases $\theta_{\ell\ell'}$ either along rungs (a) or legs (b). $\theta_{\ell\ell'}$ are symbolized by arrows and describe a uniform plaquette flux ϕ. (c) Phase diagram for non-interacting system. Upper inset shows the lowest Bloch band with single minimum in the Meissner phase, for $J_\perp = 2$ and Peierls phases $\theta^{\parallel}_{\ell'\ell}(\phi = \pi/2, \eta)$ with $\eta = 0$ (solid orange line) and $\eta = \pi/2$ (dashed green line). Lower inset shows double minima of the lowest band in the vortex phase with $\phi = 4\pi/5$ and $\eta = 0$. The horizontal arrows indicate the paths for our state preparation via ramping artificial magnetic flux.

As has mentioned in the chapter 2, the accumulated net phase around one lattice plaquette is analogous to the Aharonov-Bohm phase experienced by a charged particle in a real magnetic field, and the Peierls phase $\theta_{\ell'\ell}$ plays the role of a vector potential. Each set of time-independent Peierls phases $\{\theta_{\ell'\ell}\}$ that gives the same plaquette flux reflects a gauge choice. A uniform flux ϕ can be realized by using gauge potentials along rungs, $\theta^{\perp}_{\ell'\ell}(\phi)$ [Fig. 4.1(a)], or along

legs, $\theta^{\parallel}_{\ell'\ell}(\phi,\eta)$ [Fig. 4.1(b)], with the phase η describing a continuous family of Peierls phases. However, when ϕ and η vary in time, the time-dependent artificial gauge potentials $\theta^{\perp}_{\ell'\ell}(\phi)$ and $\theta^{\parallel}_{\ell'\ell}(\phi,\eta)$ no longer describe gauge choices, but different artificial electric fields. This difference lies at the heart of the discussion of this chapter.

4.1.1 Phase diagram in the non-interacting ladder

Let us start with the non-interacting limit ($U = 0$). To analytically obtain the ground state properties, we rewrite the Hamiltonian in the following form,

$$\hat{H} = \sum_m \left(-Je^{i\theta_0}\hat{a}^\dagger_{m+1,0}\hat{a}_{m,0} - Je^{i\theta_1}\hat{a}^\dagger_{m+1,1}\hat{a}_{m,1} - J_\perp \hat{a}^\dagger_{m,1}\hat{a}_{m,0} + h.c \right), \tag{4.2}$$

where $m = 0, 1, \cdots, M-1$ are the site indices along the legs (specified by the second index, 0 or 1) and M is the total number of rungs. We use $\theta_0 = \phi/2 - \eta, \theta_1 = -\phi/2 - \eta$ to generalize different ways of arranging Peierls phases $\theta^{\parallel}_{\ell'\ell}(\phi,\eta)$ along the legs.

As the system possesses translational invariance along the leg, one can use the following ansatz for the wavefunctions

$$\Psi_{m,n} = e^{ikam}\psi_n, \tag{4.3}$$

where $n = 0, 1$ denotes the lower and upper leg respectively. The quasimomentum k is within the first Brillouin zone $-\pi \leq ka < \pi$ and we set the lattice constant $a = 1$ in the following. Similar to the calculation in Section 2.4.2, for a general state $|\Psi\rangle = \sum_{m,n}\Psi_{m,n}|m,n\rangle$, one has

$$E\Psi_{m,n} = \langle m,n|\hat{H}|\Psi\rangle = -Je^{i\theta_n}\Psi_{m-1,n} - Je^{-i\theta_n}\Psi_{m+1,n} - J_\perp\Psi_{m,n-1} - J_\perp\Psi_{m,n+1}. \tag{4.4}$$

Combining Eqs. (4.3) and (4.4), one has

$$E\psi_n = -2J\cos(\theta_n - k)\psi_n - J_\perp\psi_{n+1} - J_\perp\psi_{n-1}. \tag{4.5}$$

The above equation gives rise to the following matrix form of the Hamiltonian,

$$\hat{H} = \begin{pmatrix} -2J\cos(\phi/2 - \eta - k) & -J_\perp \\ -J_\perp & -2J\cos(\phi/2 + \eta + k) \end{pmatrix} \equiv h_0(k) + \boldsymbol{h}(k)\cdot\boldsymbol{\sigma}, \tag{4.6}$$

with

$$\begin{cases} h_0(k) = -2J\cos(\phi/2)\cos(k+\eta), \\ h_z(k) = -2J\sin(\phi/2)\sin(k+\eta), \\ h_x(k) = -J_\perp, \\ h_y(k) = 0, \end{cases} \tag{4.7}$$

where the vector of Pauli matrices $\boldsymbol{\sigma}$ acts on the sublattice degree of freedom given by the upper and lower leg. Now the eigenstates and energy spectrum can be straightforwardly expressed as

$$|\psi_\pm(k)\rangle = N_\pm \begin{pmatrix} h_x \\ E_\pm - h_0 - h_z \end{pmatrix}, \tag{4.8}$$

$$\begin{aligned} E_\pm &= h_0(k) \pm |\boldsymbol{h}(k)| \\ &= -2J\cos(\phi/2)\cos(k+\eta) \pm \sqrt{J_\perp^2 + 4J^2\sin^2(\phi/2)\sin^2(k+\eta)}, \end{aligned} \tag{4.9}$$

with $N_\pm$ being the normalization factors.

For weak magnetic flux, the dispersion relation of the lowest band possesses a unique minimum for $k = 0$ and the ground state exhibits currents along the leg (see the following section), resembling the screening currents of the Meissner phase (MP) of a superconductor. With the increase of ϕ, the minimum of the dispersion relation eventually splits into two minima and rung-currents appear in the ground state, allowing the formation of vortices, analoguous to the vortex phase (VP) of a type-II superconductor [122, 189]. The phase boundary between the MP and the VP, as shown in Fig. 4.1(c), can be determined by

$$\frac{\partial E_-}{\partial k} = 2J\sin(k+\eta)\left[\cos\frac{\phi}{2} - \frac{2J\sin^2(\phi/2)\cos(k+\eta)}{\sqrt{J_\perp^2 + 4J^2\sin^2(\phi/2)\sin^2(k+\eta)}}\right] = 0,$$

$$\Rightarrow \begin{cases} k+\eta = 0, \\ \cos^2(k+\eta) = \frac{J_\perp^2}{4J^2}\cot^2\frac{\phi}{2} + \cos^2\frac{\phi}{2}, \end{cases} \tag{4.10}$$

$$\Rightarrow (J_\perp)_c = 2J\sin\frac{\phi_c}{2}\tan\frac{\phi_c}{2}. \tag{4.11}$$

Namely, for $J_\perp > (J_\perp)_c$, the spectrum has a single minimum at $k+\eta = 0$ [upper inset in Fig. 4.1(c)]. If $J_\perp < (J_\perp)_c$, however, as shown in the lower inset in Fig. 4.1(c), the spectrum has double minima at $k = -\eta \pm k_0$, with

$$k_0 = \arccos\sqrt{\frac{J_\perp^2}{4J^2}\cot^2\frac{\phi}{2} + \cos^2\frac{\phi}{2}}. \tag{4.12}$$

4.1.2 Chiral currents

The ground state chiral current plays a key role in charactering different phases in a ladder system [122, 189, 192, 232]. Based on the continuity relation, the local current operators on legs and rungs are respectively defined as [122, 189, 192, 232],

$$\hat{j}^{\parallel}_{m,n} = -i\frac{a}{\hbar}\left(Je^{i\theta_n}\hat{a}^\dagger_{m+1,n}\hat{a}_{m,n} - h.c.\right) \tag{4.13}$$

$$\hat{j}^{\perp}_{m} = -i\frac{a}{\hbar}\left(J_\perp\hat{a}^\dagger_{m,1}\hat{a}_{m,0} - h.c.\right), \tag{4.14}$$

with $\theta_n = \phi\left(1/2 - n\right) - \eta, n = 0, 1$. In this case, the global chiral current is defined as

$$j_c = \frac{1}{M}\sum_m \left\langle \hat{j}^{\parallel}_{m,0} - \hat{j}^{\parallel}_{m,1}\right\rangle. \tag{4.15}$$

For a single particle state $|\Psi\rangle = \sum_{m,n}\Psi_{m,n}\hat{a}^\dagger_{m,n}|0\rangle$, the currents expectation values can be expressed as

$$j^{\parallel}_{m,n} = \left\langle \hat{j}^{\parallel}_{m,n}\right\rangle = 2\mathrm{Im}\left(e^{i\theta_n}\langle\Psi|\hat{a}^\dagger_{m+1,n}\hat{a}_{m,n}|\Psi\rangle\right) = 2\mathrm{Im}\left(e^{i\theta_n}\Psi^*_{m+1,n}\Psi_{m,n}\right), \tag{4.16}$$

$$j^{\perp}_{m} = \left\langle \hat{j}^{\perp}_{m}\right\rangle = 2\mathrm{Im}\left(J_\perp\langle\Psi|\hat{a}^\dagger_{m,1}\hat{a}_{m,0}|\Psi\rangle\right) = 2\mathrm{Im}\left(J_\perp\Psi^*_{m,1}\Psi_{m,0}\right), \tag{4.17}$$

where Im denotes the imaginary part, $J_\perp$ is in the unit of J and the currents are calculated in the units of $aJ/\hbar$.

Now we apply the above formulas in the Meissner and vortex regimes respectively. To be brief, we firstly rewrite the ground state (4.8) for the unit cell labelled by $m = 0$ as

$$|\psi_-(k)\rangle \equiv \begin{pmatrix}\psi_0(k)\\ \psi_1(k)\end{pmatrix} = \psi_0(k)\hat{a}^\dagger_{0,0}|0\rangle + \psi_1(k)\hat{a}^\dagger_{0,1}|0\rangle. \tag{4.18}$$

By using the condition (4.3), the ground state for the whole ladder can be constructed as

$$\begin{aligned}|\Psi_-(k)\rangle &= \sum_m \left(\Psi_{m,0}\hat{a}^\dagger_{m,0}|0\rangle + \Psi_{m,1}\hat{a}^\dagger_{m,1}|0\rangle\right)\\ &= \sum_m \left(e^{ikam}\psi_0(k)\hat{a}^\dagger_{m,0}|0\rangle + e^{ikam}\psi_1(k)\hat{a}^\dagger_{m,1}|0\rangle\right).\end{aligned} \tag{4.19}$$

For $\phi < \phi_c$, the single ground state exhibiting a Meissner phase reads

$$|\Psi\rangle_M = |\Psi_-(k=0)\rangle = \sum_m \left(\psi_0\hat{a}^\dagger_{m,0}|0\rangle + \psi_1\hat{a}^\dagger_{m,1}|0\rangle\right). \tag{4.20}$$

By applying Eqs. (4.16)(4.17), the currents along legs and rungs are respectively expressed as

$$j^\parallel_{m,n} = 2\mathrm{Im}\left(e^{i\theta_n}|\psi_n|^2\right) = 2|\psi_n|^2\sin\left(\phi/2 - n\phi\right), \tag{4.21}$$

$$j^\perp_m = 0. \tag{4.22}$$

Therefore the chiral current (4.15) in the Meissner phase is

$$j^M_c = j^\parallel_{m,0} - j^\parallel_{m,1} = 2\sin\frac{\phi}{2}, \tag{4.23}$$

where the normalization condition $|\psi_0|^2 + |\psi_1|^2 = 1$ has been applied. The above equations (4.21) and (4.22) indicate that within the Meissner phase (i.e. $k = 0$), ramping up the flux from zero to a finite value will induce currents along the legs.

For $\phi > \phi_c$, the system enters into the vortex phase. For convenience, here we consider $\eta = 0$ so that the spectrum has double minima at $k = \pm k_0$ [see Eq. (4.12)], giving rise to two degenerate ground states $|\Psi_-(\pm k_0)\rangle$. Due to the inversion symmetry between these two legs (i.e. same population on both legs of the ladder) , the vortex ground state can be written as the superposition of the components $|\Psi_-(\pm k_0)\rangle$ with the same weight [122, 194],

$$|\Psi\rangle_V = \left(|\Psi_-(k_0)\rangle + e^{i\xi}|\Psi_-(-k_0)\rangle\right)/\sqrt{2} \equiv \sum_m \left(\Psi'_{m,0}\hat{a}^\dagger_{m,0}|0\rangle + \Psi'_{m,1}\hat{a}^\dagger_{m,1}|0\rangle\right), \tag{4.24}$$

with

$$\begin{cases}\Psi'_{m,0} = \left(e^{ik_0am}\psi_0(k_0) + e^{i(\xi-k_0am)}\psi_0(-k_0)\right)/\sqrt{2},\\ \Psi'_{m,1} = \left(e^{ik_0am}\psi_1(k_0) + e^{i(\xi-k_0am)}\psi_1(-k_0)\right)/\sqrt{2}.\end{cases} \tag{4.25}$$

Here ξ is a possible relative phase. In this case, the expectation values of currents (4.16) and (4.17) become

$$\begin{aligned} j^{\parallel}_{m,n} =& 2\mathrm{Im}\left(e^{i\theta_n}\Psi'^{*}_{m+1,n}\Psi'_{m,n}\right) \\ =& |\psi_n(k_0)|^2\sin(\theta_n - k_0 a) + |\psi_n(-k_0)|^2\sin(\theta_n + k_0 a), \\ &+ 2\psi_n(k_0)\psi_n(-k_0)\cos\left[k_0 a(2m+1) - \xi\right]\sin\theta_n \end{aligned} \tag{4.26}$$

$$\begin{aligned} j^{\perp}_{m} =& 2\mathrm{Im}\left(J_\perp \Psi'^{*}_{m,1}\Psi'_{m,0}\right) \\ =& 2J_\perp\left[\psi_1(k_0)\psi_0(-k_0) - \psi_1(-k_0)\psi_0(k_0)\right]\sin(\xi - 2k_0 a m). \end{aligned} \tag{4.27}$$

Therefore, by combining with the above equations, the chiral current (4.15) in the vortex phase becomes

$$j^V_c = j^{\parallel}_{m,0} - j^{\parallel}_{m,1} = 2\left[|\psi_0(k_0)|^2\sin(\frac{\phi}{2} - k_0 a) + |\psi_0(-k_0)|^2\sin(\frac{\phi}{2} + k_0 a)\right], \tag{4.28}$$

where the terms proportional to $\cos\left[k_0 a(2m+1) - \xi\right]$ are neglected because they vanish when averaging the whole system, and we have used the relations $|\psi_0(k_0)| = |\psi_1(-k_0)|, |\psi_0(-k_0)| = |\psi_1(k_0)|$. It is indicated in the above formula that the phase ξ simply shifts the positions of currents globally, leaving the chiral current (4.28) unaffected.

The dependence of chiral currents (4.23) and (4.28) on flux ϕ is plotted in Fig. 4.2(a), and the current and particle density distributions are exemplified in Fig. 4.2(b). At small fluxes, probability currents exist only along the legs and behave like screening currents, and the low-flux phase is thus identified as a Meissner phase, in analogy to that in a type-II superconductor. For large values of the flux, the system enters into a vortex phase, where finite rung currents emerge and form vortex structures. Such a MP-VP phase transition has been confirmed in cold atom experiments by measuring the chiral currents of the system [122].

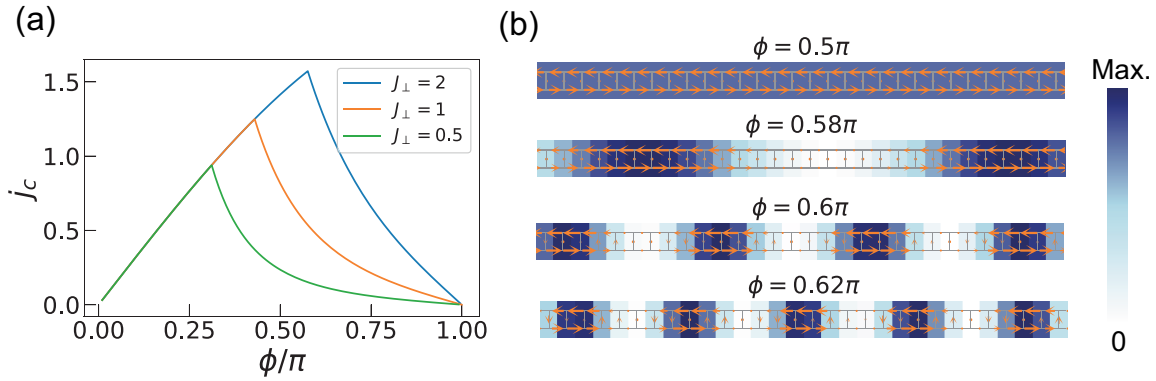

Figure 4.2: (a) Chiral currents as a function of flux ϕ for different values of tunneling parameter $J_\perp$. (b) Current and particle density distributions at $J_\perp = 2$ for different values of ϕ. Note that the MP-VP transition occurs at $\phi_c/\pi = 0.576$ for $J_\perp = 2$ according to Eq. (4.11). The arrows denote the currents, which are normalized by the maximum values in each case.

4.2 State preparation in non-interacting system

In order to study adiabatic state preparation, we take our initial state and target state as the ground states of the Hamiltonian with flux $\phi = 0$ and $\phi = \pi/2$, denoted as $|\psi_0\rangle$ and $\left|\psi_{\pi/2}\right\rangle$, respectively. The tunneling amplitude along rungs is fixed at $J_\perp = 2$ so that the target state lies in the MP, as is marked by the star in Fig. 4.1(c). By linearly ramping the Peierls phases from zero to final values given by either $\theta^{\perp}_{\ell'\ell}(\phi)$ or $\theta^{\parallel}_{\ell'\ell}(\phi,\eta)$, the flux is continuously increased from 0 to $\pi/2$ within the ramping time τ. The evolved state $\left|\psi(\tau)\right\rangle$ is obtained by numerically solving the Schrödinger equation of the Hamiltonian for a finite system with $M = 24$ rungs under open boundary condition.

To quantify the degree of adiabaticity, we define the fidelity as the squared overlap between the evolved state and the target state,

$$\mathcal{F} = \left|\left\langle \psi_{\pi/2}|\psi(\tau)\right\rangle\right|^2 . \tag{4.29}$$

Fig. 4.3(a) shows the fidelities calculated by choosing artificial gauge potentials $\theta^{\perp}_{\ell'\ell}(\phi)$ and $\theta^{\parallel}_{\ell'\ell}(\phi,\eta)$ with $\eta = \{0, \pi/4, 3\pi/4\}$ [cf. legend in Fig. 4.3(c)]. For gauge potentials on the rungs, we find fidelities close to 1 for ramping times on the order of $\tau = 300$. For gauge potentials on the legs, this time scale strongly depends on η. Remarkably, it vanishes in the limit of $\eta = 0$, so that the ground state can be prepared by switching on the gauge potentials abruptly. This picture is confirmed also by looking at two other quantities characterizing the evolved state. One is the chiral current $j_c(\tau)$ defined in Eq. (4.15) scaled by its target value j_c^{target} [Fig. 4.3(b)], which can be readily measured in experiment [92, 93, 122]. The other quantity is the excitation energy ΔE [Fig. 4.3(c)], defined as

$$\Delta E = \langle\psi(\tau)|\hat{H}|\psi(\tau)\rangle - E_g, \tag{4.30}$$

where E_g is the ground state energy for the final Hamiltonian. Both measures reflect the degree of adiabaticity observed in the fidelity.

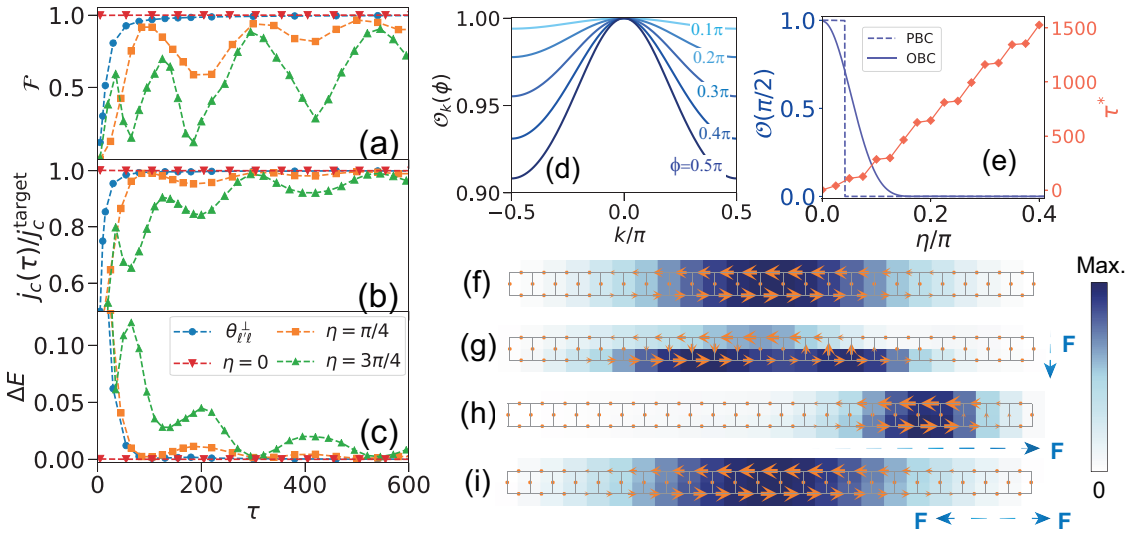

Figure 4.3: (a) Fidelity, (b) scaled chiral current and (c) excitation energy as functions of total ramping time τ for different choices of Peierls phase configurations. The legends in (a) and (b) are the same as those in (c). (d) The overlap $\mathcal{O}_k(\phi)$ for different values of ϕ for $\eta = 0$. (e) Ground state overlap $\mathcal{O}(\pi/2)$ and minimal ramping time τ^* required to reach $\mathcal{F} = 0.9$ as a function of η for open (solid) and periodic (dashed) boundary conditions. Distributions of spatial density and local currents of (f) the target state, and the evolved states for (g) $\theta^{\perp}_{\ell'\ell}(\phi)$, $\tau = 15$, (h) $\theta^{\parallel}_{\ell'\ell}(\phi, \eta = \pi/4)$, $\tau = 200$ and (i) $\theta^{\parallel}_{\ell'\ell}(\phi, \eta = 0)$, $\tau = 1$. The darker color indicate higher densities and the size of the orange arrows along the bonds is proportional to the amplitude of probability currents. The dashed arrows F indicate directions of the average artificial electric forces.

The ultrafast adiabatic state preparation can be explained by the fact that the ground state does not depend on the flux for the choice $\theta^{\parallel}_{\ell'\ell}(\phi, \eta = 0)$. For the translationally invariant ladder, the Bloch states $|\psi_{\pm}(k; \eta, \phi)\rangle$ in Eq. (4.8) of both bands $E_{\pm}(k)$ are described by k dependent vectors $\pm\boldsymbol{h}(k)/|\boldsymbol{h}(k)|$ on the Bloch sphere. In the MP the ground state lies at $k = -\eta/a$ with $h_z = 0$. We define the overlap $\mathcal{O}_k(\phi)$ to quantify the similarity between lowest-band eigenstates with and without magnetic flux ϕ, i.e.

$$\mathcal{O}_k(\phi) = |\langle\psi_-(k; 0, 0)|\psi_-(k; \eta, \phi)\rangle|^2. \tag{4.31}$$

Remarkably, in the case of $\eta = 0$, the ground state wave function ($k = 0$) does not depend on the magnetic flux ϕ, as $h_z = h_y = 0$ for all ϕ so that $\mathcal{O}_{k=0}(\phi) = 1$ [Fig. 4.3(d)]. For a system of M rungs with periodic boundary condition, the quasimomentum k takes discrete values given by integer multiples of $2\pi/M$. As the spectrum is shifted by η, the squared overlap $\mathcal{O}(\pi/2) = \left|\left\langle\psi_{\pi/2}|\psi_0\right\rangle\right|^2$ between the initial and the target states drops suddenly from 1 to 0 when the shift η becomes larger than π/M, as shown by the dashed line in Fig. 4.3(e). Since k is not a good quantum number anymore in the finite system with open boundary conditions, we

observe a smooth decay of $\mathcal{O}(\pi/2)$ as a function of η, starting from a value close to 1 for $\eta = 0$ [$\mathcal{O}(\pi/2)|_{\eta=0} = 0.995$ for $M = 24$ rungs, and $\mathcal{O}(\pi/2)|_{\eta=0}$ gets closer to 1 for larger M.]. This behaviour explains that the minimal ramping time τ^* required to reach $\mathcal{F} = 0.9$ approaches zero when η drops to zero.

Note that each point in Fig. 4.3(a-c) corresponds to the result at the end of a parameter ramp. To interpret the oscillation behavior, we plot the fidelity $\mathcal{F} = \left|\langle\psi_\phi|\psi(t)\rangle\right|^2$ and center of mass $\langle X\rangle$ during a single ramping process in Fig. 4.4. It shows that when the center of mass gets closer to the middle of the ladder, the fidelity always has a large value. It turns out that the oscillation of $\mathcal{F}$ is related to the Bloch oscillations of the atomic cloud, which are triggered by the finite synthetic electric fields that are generated during the ramp for non-zero η.

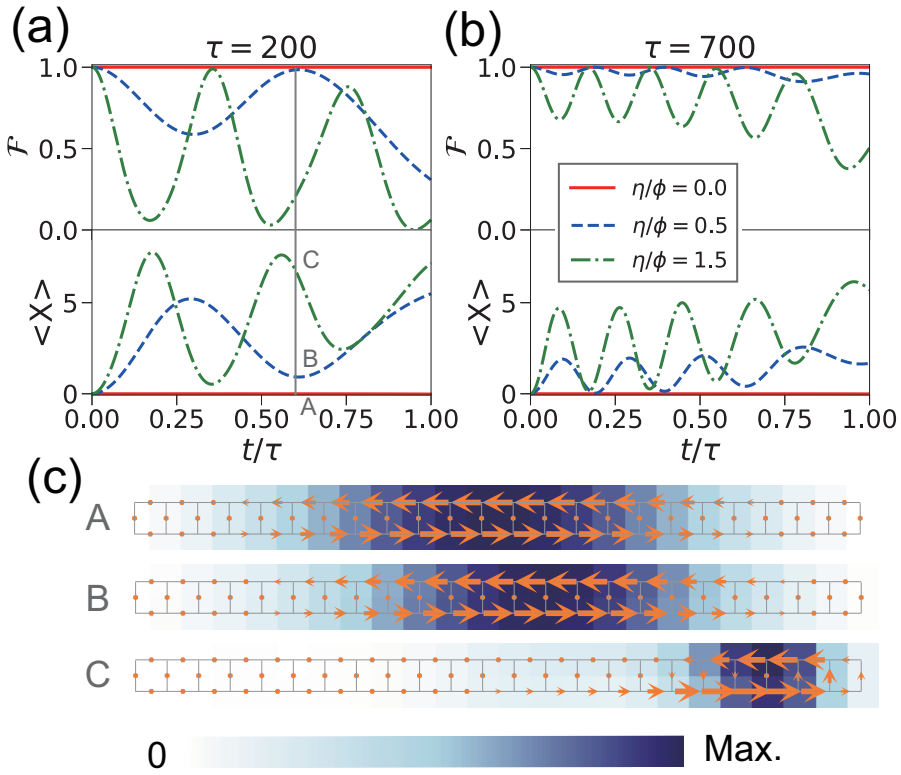

Figure 4.4: Fidelity $\mathcal{F}$ (upper panel) and center of mass $\langle X\rangle$ (lower panel) as a function of time within (a) $\tau = 200$ and (b) $\tau = 700$. The origin $\langle X\rangle = 0$ is defined to lie at the middle of the ladder. (c) Spatial density and probability current distributions at $t/\tau = 0.6$ with $\tau = 200$. A-C correspond to $\eta/\phi = 0, 0.5, 1.5$ respectively. It shows that the closer is the center-of-mass to the middle of ladder, the larger fidelity is obtained. Other parameters are chosen as $U = 0$, $J_\perp = 2$, $\phi(t) = (\pi/2)t/\tau$ and $M = 24$.

4.3 Counterdiabatic driving

Counterdiabatic (CD) driving has been an important protocol to realize shortcuts to adiabaticity (STA), i.e. to speed up adiabatic processes which are usually very slow [230]. The basic idea is to apply auxiliary terms to the original system described by $\hat{H}_0$, so that the evolved state of the system follows exactly the eigenstates of $\hat{H}_0$ within arbitrarily short time. The counterdiabatic driving formalism dates back to Demirplak and Rice [226, 227], and was then rediscovered by Berry in a different but equivalent way [228]. After it was employed to cool down atoms in a harmonic trap [24], where the so-called shortcuts to adiabaticity was coined, the past decade has witnessed rapid development in the applications of shortcuts to adiabaticity [230]. In this section, we will briefly review the original formulation, followed by a comparison with our protocol.

4.3.1 Previous formalism

Berry's formulation

Considering its simplicity, we firstly recap the Berry's formulation [228, 230]. We start with a reference Hamiltonian $\hat{H}_0(t)$ with instantaneous eigenstates $|n(t)\rangle$ and eigenenergies $E_n(t)$,

$$\hat{H}_0(t) = \sum_n E_n(t)|n(t)\rangle\langle n(t)|. \tag{4.32}$$

By designing a proper scheme, one requires that the evolved state $|\psi_n(t)\rangle$ of the system exactly follows the eigenstate of $\hat{H}_0$, except for a global phase $\xi_n(t)$, i.e.

$$|\psi_n(t)\rangle = e^{i\xi_n(t)}|n(t)\rangle = \hat{U}(t)|n(0)\rangle, \tag{4.33}$$

with the time evolution operator $\hat{U}(t)$ expressed as

$$\hat{U}(t) = \sum_n e^{i\xi_n(t)}|n(t)\rangle\langle n(0)|. \tag{4.34}$$

For this purpose, we need to construct a new Hamiltonian $\hat{H}(t)$ which governs the dynamics according to the Schrödinger equation,

$$i\hbar\partial_t|\psi_n(t)\rangle = \hat{H}(t)|\psi_n(t)\rangle. \tag{4.35}$$

By plugging Eq (4.33) into Eq. (4.35) one has

$$\hat{H}(t) = i\hbar\left[\partial_t\hat{U}(t)\right]\hat{U}^\dagger(t) \equiv \hat{H}_0(t) + \hat{H}_{CD}(t), \tag{4.36}$$

where the additional term $\hat{H}_{CD}(t)$ represents the CD driving and is determined by inserting Eq. (4.34) into the above equation,

$$\hat{H}_{CD}(t) = i\hbar\sum_n \left[|\partial_t n(t)\rangle\langle n(t)| - \langle n(t)|\partial_t n(t)\rangle|n(t)\rangle\langle n(t)|\right]. \tag{4.37}$$

Therefore, by introducing the auxiliary term $\hat{H}_{CD}(t)$ into the original system, the dynamics is expected to follows the adiabatic evolution driven by $\hat{H}_0$.

Demirplak and Rice's formulation

Historically, Demirplak and Rice have formulated the counterdiabatic driving protocol already earlier than Berry. The idea is to consider two frames. In the laboratory frame (denoted by lower index 0), the system Hamiltonian $\hat{H}_0$ and the dynamical solution $|\psi_0(t)\rangle$ satisfy the Schrödinger equation,

$$i\hbar\partial_t|\psi_0(t)\rangle = \hat{H}_0(t)|\psi_0(t)\rangle. \tag{4.38}$$

Note that the phases of the eigenstates $|n_0(t)\rangle$ of $\hat{H}_0$ can be chosen to satisfy the parallel transport condition [230], i.e.

$$\langle n_0(t)|\partial_t n_0(t)\rangle = 0. \tag{4.39}$$

To find the counterdiabatic driving term, one express the dynamics in an adiabatic frame (denoted by lower index 1) via the following transformation,

$$|\psi_1(t)\rangle = \hat{A}_0^\dagger(t)|\psi_0(t)\rangle, \tag{4.40}$$

with

$$\hat{A}_0(t) = \sum_n |n_0(t)\rangle\langle n_0(0)|. \tag{4.41}$$

Plugging the transformation (4.40) into the Schrödinger equation (4.38), one obtains

$$\begin{aligned} i\hbar\partial_t|\psi_0(t)\rangle &= i\hbar\left(\partial_t\hat{A}_0(t)\right)|\psi_1(t)\rangle + i\hbar\hat{A}_0(t)\partial_t|\psi_1(t)\rangle, \\ \Rightarrow i\hbar\partial_t|\psi_1(t)\rangle &= \hat{A}_0^\dagger(t)\left[i\hbar\partial_t|\psi_0(t)\rangle - i\hbar\left(\partial_t\hat{A}_0(t)\right)|\psi_1(t)\rangle\right] \\ &= \left[\hat{A}_0^\dagger(t)\hat{H}_0\hat{A}_0(t) - i\hbar\hat{A}_0^\dagger(t)\left(\partial_t\hat{A}_0(t)\right)\right]|\psi_1(t)\rangle \\ &\equiv \hat{A}_0^\dagger(t)(\hat{H}_0 - \hat{K}_0)\hat{A}_0(t)|\psi_1(t)\rangle, \end{aligned} \tag{4.42}$$

with $\hat{K}_0 = i\hbar\left(\partial_t\hat{A}_0(t)\right)\hat{A}_0^\dagger(t)$. Since the first term $\hat{A}_0^\dagger(t)\hat{H}_0\hat{A}_0(t)$ is, by construction, time-independent, it represents an adiabatic evolution. The presence of the second term $-i\hbar\hat{A}_0^\dagger(t)(\partial_t\hat{A}_0(t))$ spoils the adiabaticity and thus it represents the 'diabatic' contribution. In order to counterbalance this diabatic term, one can apply additional term $\hat{A}_0^\dagger(t)\hat{K}_0\hat{A}_0$ in the adiabatic frame, which is equivalent to use $\hat{H}_0 + \hat{K}_0$ in the laboratory frame.

The above $\hat{K}_0$ can be alternatively written as

$$\hat{K}_0 = i\hbar\sum_n \frac{d\hat{P}(t)}{dt}\hat{P}(t), \tag{4.43}$$

with $\hat{P}(t) = |n_0(t)\rangle\langle n_0(t)|$. Nevertheless, $\hat{K}_0$ can also be expressed in arbitrary basis of time evolved basis states $|n(t)\rangle$. By applying $\hat{P}(t) = |n(t)\rangle\langle n(t)|$ in the above equation, one has

$$\hat{K}_0 = i\hbar\sum_n \left[|\dot{n}(t)\rangle\langle n(t| - \langle n(t)|\dot{n}(t)\rangle|n(t)\rangle\langle n(t)|\right], \tag{4.44}$$

where the dot $\dot{x}$ represents time derivative of x. Thus $\hat{K}_0$ exactly corresponds to the counterdiabatic driving term expressed in Eq. (4.37), which demonstrates the equivalence of Berry's formulation and that of Demirplak and Rice.

4.3.2 Comparison with our protocol

Now we will show that the idea of choosing an optimal vector potential for adiabatic state preparation can be related to the above-mentioned counterdiabatic driving. To make the discussion more general, let H_p be a Hamiltonian depending on a parameter p and $|\psi_p\rangle$ the corresponding ground state. Starting from the ground state at $p = 0$, we wish to rapidly prepare the ground state of the target Hamiltonian $H_{p=f}$. The idea of counterdiabatic driving is to consider a family of unitaries $U_{p(t)}$ labelled by $p(t)$, so that the evolved state exactly follows $|\psi_{p(t)}\rangle$ when being driven by the new Hamiltonian $H(t) = H_{p(t)} + i\hbar(d_t U_{p(t)})U^\dagger_{p(t)}$. Our approach, in turn, corresponds to directly working in the rotating frame of reference with instantaneous eigenstate $|\psi'_p\rangle = U_p^\dagger|\psi_p\rangle$ governed by the Hamiltonian $H'_p = U_p^\dagger H_p U_p$. For an ideal choice of U_p (e.g. the optimal choice of Peierls phases with $\eta = 0$), one can find a p-independent ground state $|\psi'_p\rangle = |\psi_0\rangle$, and thus it allows for the parameter ramp within arbitrarily short time. Note that the preparation protocol we have considered here works only for the ground state but not for excited states, which is different from the typical counterdiabatic driving protocol described in Section 4.3.1 that work for all the eigenstates. Nevertheless, the advantage of our approach is that there will be no need for applying external terms to the system. Meanwhile, our protocol can be easily extended to the many-body system, as will be shown in Sections 4.4 and 4.5.

The optimal choice ($\eta = 0$) of Peierls phases can also be understood intuitively by noting that the artificial electric fields generated during the ramp correspond to those dictated by Faraday's law of induction [see also Fig. 4.3(i)]. In turn, for non-optimal choices with $\eta \neq 0$, additional electric fields are created as well during the ramp [causing the drift shown in Figs. 4.3(g,h)] that are not related to the time-dependence of the magnetic field via Faraday's law of induction. These non-Faraday electric fields could be compensated by a time-dependent scalar potential. The freedom of choosing η is a consequence of the fact that the experimentalist directly engineers the artificial gauge potential (via Peierls phases) rather than the artificial magnetic field. The counterdiabatic driving terms required for rapid state preparation for the non-optimal choices of Peierls phases would simply correspond to time-dependent scalar potentials subtracting the non-Faraday forces generated by $\eta(t) \neq 0$. Note, however, that the choice of $\eta = 0$ and the absence of non-Faraday forces is not always optimal, as will be seen in Section 4.5 when discussing parameter ramps leaving the Meissner phase.

4.4 Role of interactions

4.4.1 Ground state properties

Let us now investigate the interacting system at filling $n = 1/2$ per site by using the TeNPy library [233–236] and a matrix product operator based time evolution method [237, 238]. The squared overlap $\mathcal{O}\left(\pi/2\right) = \left|\left\langle \psi_{\pi/2}|\psi_0\right\rangle\right|^2$ between the initial and the target states as a function of interaction strength U is plotted in Fig. 4.5(a). In the case of $\eta = 0$, the overlap $\mathcal{O}(\pi/2)$ exhibits non-monotonic behavior, reflecting a complex competition between many-body interactions and artificial magnetic fluxes, as will be specified in the following.

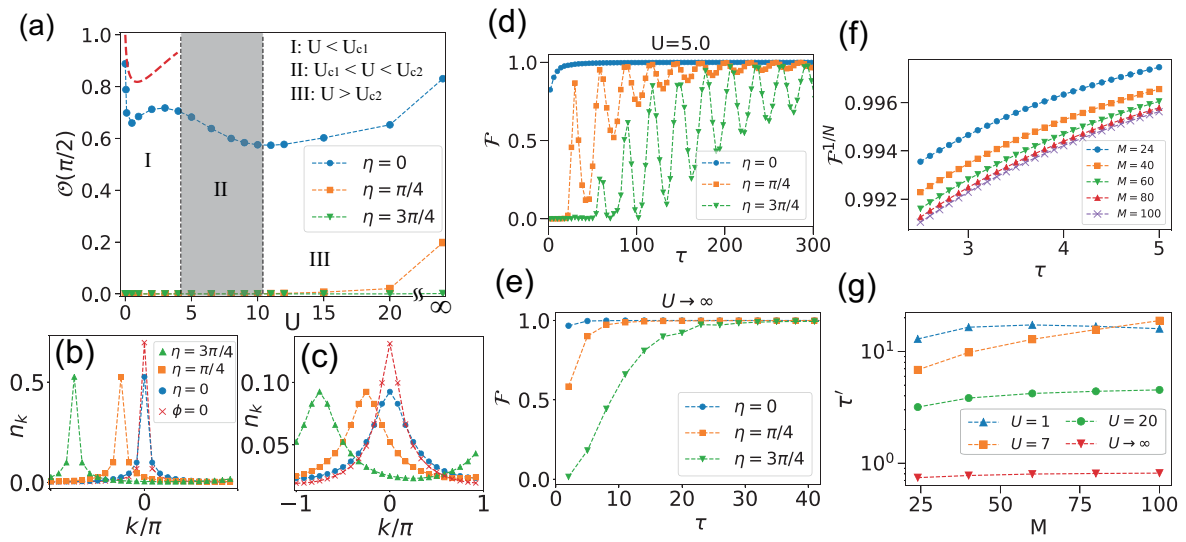

Figure 4.5: (a) Squared overlap of initial state $|\psi_0\rangle$ and target state $\left|\psi_{\pi/2}\right\rangle$ as a function of U for different values of η. The two vertical dashed lines $U_{c1} = 4.2$ and $U_{c2} = 10.4$ locate the BKT-transition points for $\phi = \pi/2$ and $\phi = 0$ respectively. Quasimomentum distribution for (b) $U = 1$ and (c) $U = 10$. In the legend different η refer to $\phi = \pi/2$. Fidelity as a function of total ramping time τ with interaction (d) $U/J = 5$ and (e) hard-core limit.The simulations in (a-e) are performed in the system with the number of rungs $M = 24$. (f) Single-particle fidelity $\mathcal{F}^{1/N}$ as a function of total ramping time τ for different numbers of rungs M at $\eta = 0$ and $U = 20$. (g) Minimal ramping time τ' required to reach $\mathcal{F}^{1/N} = 0.995$ as a function of M at $\eta = 0$. For all cases we use $J_\perp = 2$ at 1/2 filling. (Dashed lines are guides to the eye.)

While the system features a Meissner-like superfluid (SF) ground state for weak interactions, (in the thermodynamic limit) it undergoes a Berezinskii-Kosterlitz-Thouless (BKT) transition to a Mott-insulator (MI) state with single particles localised on the rungs as U is increased [186, 192, 239]. This picture can be confirmed by extracting from the finite-size scaling of peaks in quasimomentum distribution $n_k^{\max} M^{-3/4}$ [186, 192, 239], where n_k is defined as

$$n_k = \frac{1}{M} \sum_{n=0,1} \sum_{m,m'} e^{ik(m-m')} \langle \hat{a}^\dagger_{m',n} \hat{a}_{m,n} \rangle. \tag{4.45}$$

As plotted in Fig. 4.6, the crossing determines the BKT-transition points at $U_{c1} \approx 10.4$ for $\phi = 0$ and $U_{c2} \approx 4.2$ for $\phi = \pi/2$. Accordingly, they defined three regions (I: $U < U_{c1}$, II: $U_{c1} < U < U_{c2}$, and III: $U_{c2} < U$) shown in Fig. 4.5(a).

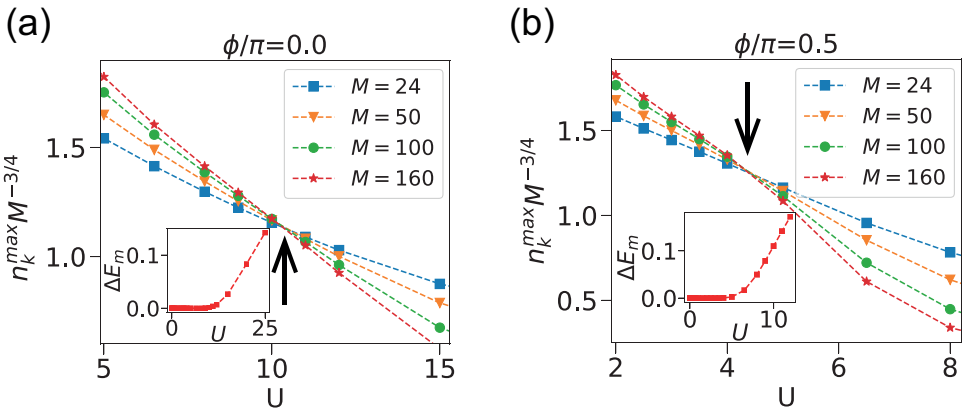

Figure 4.6: Scaling quasimomentum peak $n_k^{\max} M^{-3/4}$ as a function of U for different M at (a) $\phi = 0$ and (b) $\phi = \pi/2$. The crossing corresponds to BKT-transition points, which can be further confirmed by the mass gap shown in the inset.

Regardless of whether the system is non-interacting, superfluid, or in a Mott insulator phase, the system always possesses the 'screening' currents, just like in the Meissner phase (see Fig. 4.7). Thus to be more precise, the ground states can be called the Meissner superfluid (M-SF) phase for weak interaction and the Meissner-Mott insulator (M-MI) phase in strongly interacting regime [192].

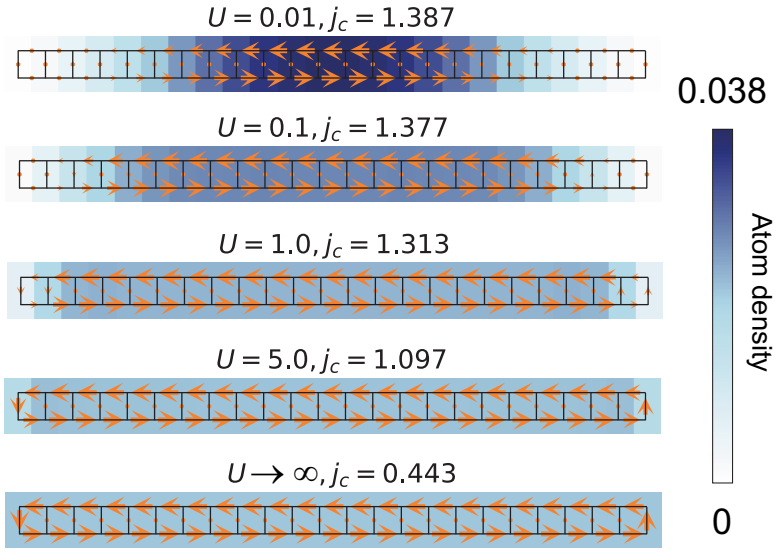

Figure 4.7: Probability current patterns for different U at $J_\perp = 2, \phi = \pi/2, n = 1/2, M = 24$. The arrow size is proportional to the expectations values of the local currents.

In the weakly interacting region I, the overlap in Fig. 4.5(a) first decreases rapidly, before it slightly increases again. This behaviour is qualitatively reproduced by Bogoliubov theory (red dashed line) [see Appendix A]. It can be related to the fact that the interaction-induced

population of finite momentum modes initially occurs much faster in the presence of magnetic flux (giving rise to an enlarged effective mass due to a frustration of the kinetics). However, for a bit stronger interactions the resulting momentum mismatch becomes smaller again [see Appendix A]. For $U_{c1} < U < U_{c2}$, while the ground state with zero flux remains superfluid, the ground state with flux $\phi = \pi/2$ already becomes a Mott insulator, and therefore the overlap decreases once more. After $U > U_{c2}$, the fact that both ground states present Mott-insulating phases gives rise to an increase again.

4.4.2 State preparation

Despite this non-monotonic behavior, $\mathcal{O}(\pi/2)$ takes comparably large values for $\eta = 0$ in a finite system. This leads to rather short adiabatic preparation times also in the strongly interacting regime. In Figs. 4.5(d) and (e), we plot the fidelity $\mathcal{F}$ versus the ramping time for $U = 5$ and the hard-core limit $U \to \infty$, respectively. Remarkably, for hard-core bosons (and $\eta = 0$), we find fidelities close to one already for very short ramping times on the order of 1 (in units of the tunnelling time). The fact that such rapid state preparation is found for the strongly interacting system cannot be fully explained by the single-particle analysis presented in the previous sections. This short ramping time may be related to the fact that the larger overlap of quasimomentum distribution occurs for stronger interaction, as indicated in Figs 4.5(b) and (c).

In Figs. 4.5(f) and (g), we investigate the finite size effect for the optimal choice of $\eta = 0$. The fact that a many-body fidelity drops with the system size can be attributed to two effects. On the one hand, a finite-size gap (as present in the superfluid regime) separating the ground state from the first excited state decreases with ladder length M, leading to a reduction of adiabaticity. On the other hand, a decrease of the many-body fidelity with system size is expected already from the very fact that (at least for product states) the N-particle fidelity is given by the Nth power of the single-particle fidelity. In order to compensate for the latter effect, when comparing results for different system sizes, we use the single-particle fidelity $\mathcal{F}^{1/N}$. In Fig. 3(f), we plot $\mathcal{F}^{1/N}$ versus the ramping time τ for $\eta = 0$ and $U = 20$ for different ladder length M. In Fig. 3(g), we extract the ramping time τ' above which a fidelity $\mathcal{F}^{1/N} \geq 0.995$ is achieved and plot it versus M for various interaction strengths U. Remarkably, we find that the ramping time increases very slowly both in the superfluid and the Mott-insulating regions (i.e. I and III). A noticeable increase is only visible in regime II, where the Mott transition occurs during the ramp.

For finite values of η, taking $\eta = \pi/4, 3\pi/4$ as examples shown in Fig. 4.5(a), $\mathcal{O}(\pi/2)$ takes small values until deep in the Mott regime, where the correlations between individual rungs are suppressed by interactions for both $\phi = 0$ and $\phi = \pi/2$. This can also be understood from the quasi-momentum distribution defined in Eq. (4.45). From Fig. 4.5(b,c) we can see that the distribution is centered around $k = 0$ for the initial state ($\phi = 0$), and at $k = -\eta$ for the target state ($\phi = \pi/2$). Although the shift of quasi-momentum (for $\eta \neq 0$) causes difficulties in state preparations, the increase of interaction broadens the quasimomentum distributions, which results in gradually increasing overlap and a shorter adiabatic ramping time as indicated in Fig. 4.5(d,e).

4.5 Leaving the Meissner regime

So far, we have considered parameter ramps within the Meissner-type phase. Increasing ϕ further gives rise to various phases [190, 192, 193, 197], including the biased ladder phase (BLP) in the weakly and intermediately interacting regime [190, 192–196], which is characterized by vanishing rung currents and the spontaneous $\mathbb{Z}_2$ reflection symmetry breaking in the form of a density imbalance between both legs. In the following, we show that the biased ladder phase can also be efficiently prepared by choosing proper Peierls phase patterns (determined by η).

Let us start with the non-interaction limit, where beyond a critical flux ϕ_c, the system enters the vortex phase and the dispersion relation develops two degenerate minima [Fig. 4.8(a)]. Since each minimum predominantly corresponds to the occupation of one of the legs, the degeneracy can be lifted by introducing a small bias potential ($0.01J$) between both legs, so that the ground state resembles that of the biased ladder phase. Despite the fact that the small bias softens the sharp transition at $\phi_c \approx 0.667\pi$ into a narrow crossover, we observe a sudden drop of the fidelity at ϕ_c when linearly ramping up the Peierls phases with $\eta = 0$ [Fig. 4.8(c)]. Here the dashed line represents the fidelity between the evolved state and the instantaneous eigenstate. As a remedy, one can vary η during the ramp in such a fashion that the overlap $\mathcal{O}(\phi)$ remains maximal during the ramp. (For an infinitely large system without bias, this can be achieved by choosing $\tilde{\eta}(t) = \arccos\sqrt{J_\perp^2/4\cot^2(\phi/2) + \cos^2(\phi/2)}$ for $\phi > \phi_c$, so that the right minimum of the dispersion relation always remains at $k = 0$ [Fig. 4.8(b)].) In this case, the evolved state successfully follows the instantaneous eigenstate even after the critical point, as indicated by the horizontal blue line in Fig. 4.8(c). Thus, different from the previously discussed case, now the optimal choice of Peierls phases does not correspond to the situation where all the non-Faraday forces were absent during the ramp. Instead, the forces induced by $\eta \neq 0$ are actively employed for state preparation, as they induce shifts in quasimomentum that keep the system state at the minimum of the dispersion relation.

The scheme can also be applied to the interacting system. For instance, the transition to the biased ladder phase occurs at critical flux $\phi_c' \approx 0.8\pi$ for a 0.8-filling ladder at $U = 2.0, J_\perp = 3$ [192]. As shown by the dashed lines in Fig. 4.8(d), using $\eta = 0$ leads to an essentially vanishing fidelity after the critical point, as the biased ladder phase has imbalanced distribution between positive and negative quasimomenta due to the broken reflection symmetry [193, 194]. To compensate the quasimomentum differences between initial and final states during the ramp, the protocol $\tilde{\eta}'(t)$ [shown in the inset of Fig. 4.8(d)] can be determined by maximizing the ground state overlap, and the corresponding $\mathcal{F}$ assumes rather large values as shown by solid lines in Fig. 4.8(d). Note that the finite value $\mathcal{F} = 0.78$ found for $\tau = 100$ indicates a near unity single-particle fidelity ($0.78 \approx 0.994^N$) for the system with number of particle $N = 40$ considered here. Higher fidelities can be achieved for longer ramping times.

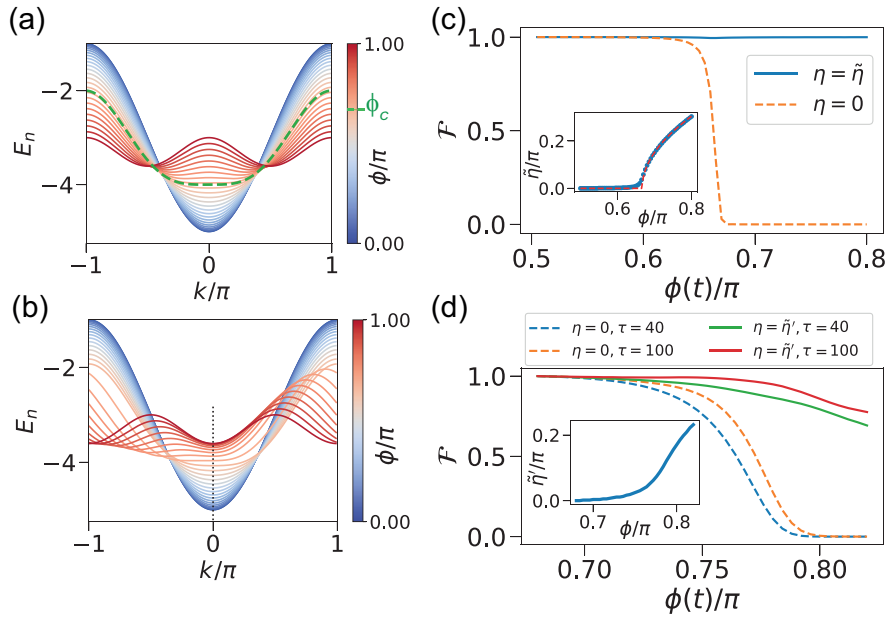

Figure 4.8: (a) Spectrum of the non-interacting ladder with $\theta^{\parallel}_{\ell'\ell}(\eta = 0)$ at $J_\perp = 3$. (b) Spectrum of the non-interacting ladder with $\theta^{\parallel}_{\ell'\ell}(\eta = \tilde{\eta})$, where $\tilde{\eta}$ shifts the spectrum so that the right minimum is always located at $k = 0$. (c) The fidelity as a function of time-dependent flux $\phi(t)$ at $U = 0$. The flux is ramped from $\phi_i = 0.5\pi$ to $\phi_f = 0.8\pi$ within a ramping time $\tau = 30$ in a ladder with $M = 50$ rungs at $J_\perp = 3$. The inset depicts $\tilde{\eta}$ as a function of ϕ, where the blue dots come from maximizing the ground state overlap $\mathcal{O}(\phi)$ and the red dashed line represents the analytical results. (d) The total fidelity as a function of $\phi(t)$ at $U = 2.0, J_\perp = 3$ with particle number of $N = 40$ in the ladder with $M = 25$ rungs. The flux is ramped from $\phi'_i = 0.68\pi$ to $\phi'_f = 0.82\pi$ within time $\tau = 40$ and 100. The inset depicts $\tilde{\eta}'$ as a function of ϕ which maximizes the ground state overlap.

5 Bosonic fractional Chern insulators and their fractional excitations

While we have discussed some topological properties of 2D Chern insulators in Chapters 2 and 3, in this chapter we shall investigate measurable signatures of *fractional* Chern insulators (FCIs, i.e. the lattice analogues of fractional quantum Hall states) in systems of optical lattice with ultracold atoms. Indeed, realizing fractional quantum Hall states [5, 10, 12, 240] and manipulating their anyonic excitations [31, 241, 242] in highly controllable systems is a long-standing interest and challenge. As has been mentioned in chapter 1 and chapter 4, there has been tremendous progress in realizing topologically non-trivial band structures in systems of ultracold atoms [36, 38, 39, 64, 91]. This includes, the realization of artificial magnetic fields [79–81, 243] and spin-orbit coupling [76, 77], the measurement of the quantum anomalous Hall effect [112] and topological invariants [94, 113, 114, 124, 244–247], as well as the observation of chiral edge currents [92, 93, 95, 96, 122, 125, 183, 248, 249]. Since atomic quantum gases in optical lattices are highly controllable, especially allowing for the ability to manipulate and observe the system with single-lattice-site resolution in the so-called quantum-gas microscopes [65, 66, 68, 250], it is an intriguing perspective to combine the realization of topologically non-trivial band structures with strong interactions in these systems, for the purpose of stabilizing fractional Chern insulator states [133, 134], as well as to probe and manipulate individually their anyonic excitations.

The results of this chapter have been published in the preprint Ref. [251]. Small changes have been made in order to fit the style of this thesis. Minor additions (i.e. Section 5.1 and Fig. 5.6) have been given for completeness.

5.1 State of the art

From chapter 2, we already know that the paradigmatic Harper-Hofstadter model exhibits topologically non-trivial bands [38, 118, 119]. In the presence of strong interactions (i.e. the Harper-Hofstadter-Hubbard model), up to the limit of hard-core bosons, this system has been predicted to host Laughlin-type fractional Chern insulator states [252–254]. Theoretically, the fractional Chern insulator state in such a model can be characterized from the overlap with Laughlin wave-function [252], ground state degeneracy [12, 255], many-body Chern number [256–258], topological entanglement entropy [22, 23], and particle entanglement spectra [259, 260]. Moreover, various realistic protocols have been proposed for the detection of their topologically-nontrivial properties, such as edge excitations [261, 262], interferometric measurements [263], adiabatic charge pumps [175, 264, 265], anyonic statistic from time-of-flight images [266] or spatial density depletions [267], as well as many body Chern number from circular dichroism [268, 269] or statistical correlations of randomized measurements [258]. More recently, the Hall drift

has been proposed as a useful tool to detect the fractional Chern insulator states in a finite optical lattice, even with a small atomic ensemble [270, 271]. Of particular interest, excitations in the fractional Chern insulators can be anyons that possess fractional charges and satisfy fractional statistics. It is thus desirable to investigate to which extent such anyoic excitations could also be stabilized and probed in such a small/intermediate setting.

Experimentally, apart from the realization of the non-interacting Harper-Hofstadter model by using ultracold atoms [120, 121, 124], the dynamics of two interacting particles in such a model has recently been investigated in a two-leg ladder geometry [125], without encountering driving induced heating (see e.g. [71]) on the experimental time scale. Considering these achievements, along with various practical schemes for the adiabatic preparation of the fractional Chern insulator states [208, 258, 264, 265, 272–279], it becomes possible soon to stabilize and probe fractional Chern insulator states of (at least a few) interacting bosons on a lattice in a quantum-gas microscope.

In this chapter, we consider realistic system geometries with open boundary conditions with a quarter of a flux quantum per plaquette. We focus on the regime, where a Laughlin-like state at a filling of $\nu = 1/2$ particles per flux quantum is expected. Using numerical simulations based on density matrix renormalization group (DMRG) approach [233, 234, 236–238], we compute experimentally accessible quantities and explore in which parameter regimes they show signatures of a FCI state. In particular, we (i) investigate the minimal system sizes required to show homogeneous bulk behavior at the filling factor expected for the FCI state, (ii) find that the edges serve as a reservoir for particles allowing for variations of the total particle number, (iii) show that both static local pinning potentials and dynamical flux insertion can be employed to probe charge fractionalization, and (iv) point out that FCI behavior is robust against various parameter variations.

5.2 Ground state properties

We consider strongly-interacting/hard-core bosons in a two-dimensional (2D) square lattice, described by the Harper-Hofstadter-Hubbard model in Landau gauge:

$$\begin{aligned}\hat{H} =& \sum_{m,n} \left(-J_x e^{-i\phi n} \hat{a}^\dagger_{m+1,n} \hat{a}_{m,n} - J_y \hat{a}^\dagger_{m,n+1} \hat{a}_{m,n} + \text{h.c.} \right) \\ &+ \frac{U}{2} \sum_{m,n} \hat{n}_{m,n}(\hat{n}_{m,n} - 1) + \sum_{m,n} W_{m,n} \hat{n}_{m,n}. \end{aligned} \tag{5.1}$$

Here $\hat{a}^\dagger_{m,n}(\hat{a}_{m,n})$ are the bosonic creation (annihilation) operators and $\hat{n}_{m,n} = \hat{a}^\dagger_{m,n}\hat{a}_{m,n}$ are the number operators on sites (m, n), with integer site indices $m = 0, 1, \ldots, L_x - 1$ and $n = 0, 1, \ldots, L_y - 1$ along the directions x and y, respectively. They define a rectangular system of $L_x \times L_y$ sites with open boundary conditions, as it can be realized in quantum gas microscopes. The hopping terms between nearest neighbors have the strength J_x (J_y) in the x (y) direction. The Peierls phase factors for the hoppings in x-direction give rise to a magnetic flux of $\phi = 2\pi\alpha$ per plaquette. We mainly focus on $\alpha = 1/4$ since the Harper-Hofstadter model with this value has been readily realized in cold atom experiments [121, 122, 124, 125]. Here h.c. refers to the

Hermtian conjugate. The Hubbard parameter U quantifies the on-site interactions between the particles. In the following we assume hard-core bosons, where an infinitely large positive value of U suppresses doubly occupied lattice sites completely (We have also checked that qualitatively similar results are found for large values of U, as will be exemplified in Section 5.3.3). Finally, we also consider different on-site potentials $W_{m,n}$ that will be specified later. The energies and angular frequencies will be measured in unit of J_x, i.e. $\hbar = 1$ and $J_x = 1$.

While the Harper-Hofstadter model for single particles exhibits topological non-trivial bands characterized by non-zero Chern numbers [38], by introducing strong interactions and partially filling the lowest band, the ground state is predicted to be a fractional Chern insulator state analogous to a Laughlin state [175, 252–255, 257, 258, 262, 264–267, 269–271, 280]. In this section, we explore signatures of $\nu = 1/2$ FCI state which could be the ground state with flux $\alpha = 1/4$ in open boundary conditions and $W_{m,n} = 0$. For this purpose, we employ the DMRG algorithm from the TenPy library [236].

5.2.1 Ground-state density and probability current

As a first experimentally observable quantity, we study the ground-state density

$$n_{m,n} = \langle \hat{n}_{m,n} \rangle. \tag{5.2}$$

We choose the particle number N which satisfies the half filling condition

$$N/N_\phi = \nu = 1/2, \tag{5.3}$$

where N_ϕ is the number of flux quanta piercing the lattice

$$N_\phi = \alpha(L_x - 1)(L_y - 1). \tag{5.4}$$

Note that for a finite system with open boundary conditions, N_ϕ is noticeably different from the value

$$N'_\phi = \alpha L_x L_y, \tag{5.5}$$

which is found for periodic boundary conditions. The corresponding incompressible FCI ground state is expected to feature a uniform density distribution in the bulk, with an average density per site

$$\rho = \alpha\nu = 1/8. \tag{5.6}$$

In Fig. 5.1(a) we plot the density distribution of a system with $N = N_\phi/2 = 14$ particles on 17×8 sites. We can observe that this finite system features already a flat density distribution at the expected bulk density $\rho = 1/8$ in its center. This can be seen more clearly also in the upper panel of Fig. 5.1(b), where we plot the density $n_{m,3}$ along the central row ($n = 3$) versus the x-coordinate m. This is a first indication of the expected incompressible behavior of the FCI state. Further evidence for incompressibility is gathered when plotting the density also for different total particle numbers in Fig. 5.1(b): While the density increases close to the boundary, the bulk remains at $\rho = 1/8$ for up to $N = 16$ particles. Thus, compressible boundaries serve as a reservoir for the incompressible center of the system. For $N \geq 17$ or $N \leq 10$, we find

noticeable density oscillations also in the center, suggesting a break-down of the FCI state. This observation also confirms that we should, indeed, consider particle numbers N that are close to $N_\phi/2 = 14$, rather than ones close to $N'_\phi/2 = 17$.

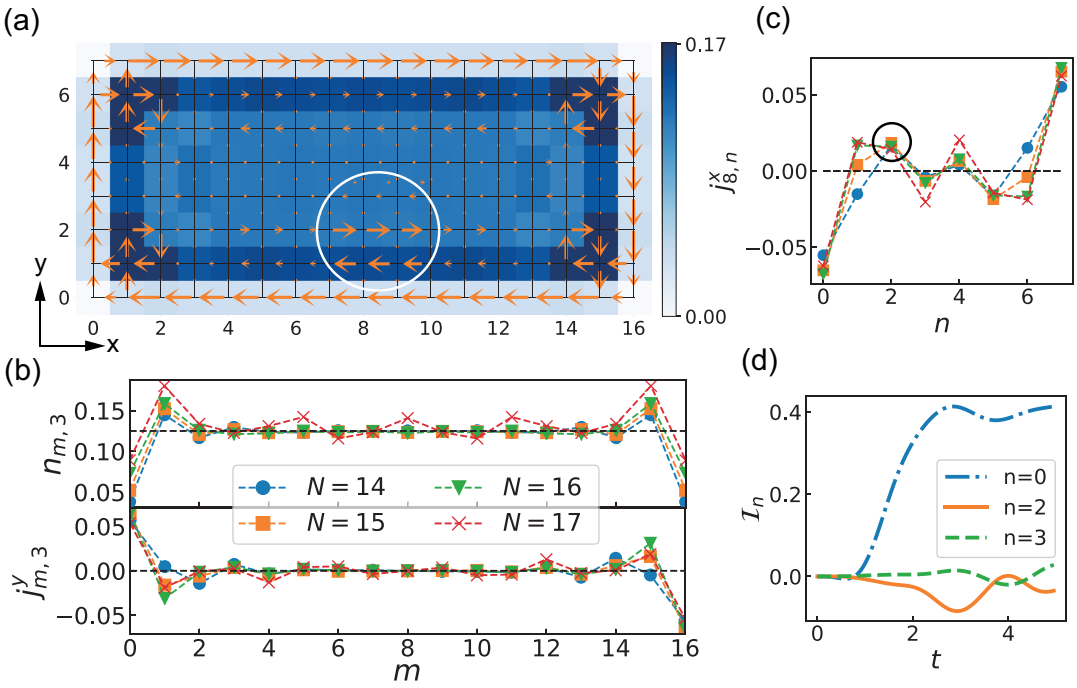

Figure 5.1: (a) Spatial density and current distributions of the ground state of hard-core bosons in a lattice of size 17×8 with $N = 14$, $\alpha = 1/4$ and $J_y = 1$. The magnitudes of current in the white circle are zoomed in by a factor of 3 for a clear visualization. (b) Densities (upper panel) of the middle row $n = 3$ and vertical currents (lower panel) on the middle links connected by $n = 3$ and $n = 4$. The horizontal dashed lines locates the expected $\rho = 1/8$ and $j = 0$. (c) Horizontal currents on the middle bonds connected by $m = 8$ and $m = 9$. The legend is the same as that in (b). The black circle is used to highlight that the currents with opposite chirality are almost independent of N. (d) Imbalance in the n-th row $\mathcal{I}_n$ as a function of evolution time.

A second observable that we study is the particle current between neighboring sites. As has been discussed in Chapter 4, the current leaving site (m, n) in positive x and y direction is given by the operators

$$\hat{j}^x_{m,n} = iJ_x \left(e^{-i\phi n} \hat{a}^\dagger_{m,n} \hat{a}_{m+1,n} - \text{h.c.} \right), \tag{5.7}$$

$$\hat{j}^y_{m,n} = iJ_y \left(\hat{a}^\dagger_{m,n} \hat{a}_{m,n+1} - \text{h.c.} \right). \tag{5.8}$$

respectively, as can be confirmed by writing out the time derivative of $n_{m,n}$ [232]. We denote their mean by

$$j^\eta_{m,n} = \langle \hat{j}^\eta_{m,n} \rangle, \tag{5.9}$$

with $\eta = x, y$. Such currents have been measured recently in systems of ultracold atoms in optical lattices [122]. The $\nu = 1/2$ FCI state is expected to feature chiral edge currents in the presence of open boundary conditions. This behavior is also confirmed in Fig. 5.1(a), where the currents are indicated by orange arrows, whose direction and size indicate direction and magnitude of the current, respectively. In the lower panel of Fig. 5.1(b), we plot the y current in the center ($n = 3$), $j^y_{m,3}$, as a function of the x-coordinate m. We can see that to a good approximation it vanishes in the center of the system, where we also found signatures of incompressibility in the density distribution.

An interesting observation is that when moving inwards from the boundary to the bulk, the chiral current not only decays in magnitude, but also reverses its sign in an oscillatory fashion. In order to make this effect more visible, we have enlarged the size of the current arrows by a factor of 3 inside the white ring in Fig. 5.1(a). It can also be seen in Fig. 5.1(c), where the typical currents $j^x_{8,n}$ in center horizontal links (between the sites $m = 8$ and $m = 9$) are plotted versus the y-coordinate n. For various particle numbers, it is a robust observation that the current at the second row ($n = 2$) away from the boundary ($n = 0$) is opposite to the current at the boundary. Another feature, which seems to be related to these edge current oscillations, is the formation of current vortices around the plaquettes close to the corner.

The current can be measured in various ways [122, 218, 281–287], for example, by suddenly isolating two neighboring sites and subsequently observing the change of the density imbalance in linear order with respect to time. As is shown now, it can also be inferred from the spatial density imbalance $\mathcal{I}_n$ in the n-th row of the system [262],

$$\mathcal{I}_n(t) = \sum_{m<L_x/2} n_{m,n}(t) - \sum_{m>L_x/2} n_{m,n}(t), \tag{5.10}$$

as it builds up with time after releasing a single particle from the center of that row. Such an extra particle can be created by preparing the ground state of the system in the presence of a large potential dip ($V = -20$) at site $(m = 8, n)$, which is then suddenly switched off. The time evolution of $\mathcal{I}_n$ for this scenario is plotted in Fig. 5.1(d). The change of the imbalance that builds up for short times directly after the quench is consistent with the computed ground state currents.

To further confirm the existence of robust counter-propagating probability currents, here we provide more data obtained from simulating a larger system of size 21×10. In Figs. 5.2(a-d), we plot the distributions of both density and currents of the ground states for different particle numbers N. The densities of the middle row $n = 4$ and the vertical currents on the middle links connected by $n = 4$ and $n = 5$ are plotted in Figs. 5.2(e) and (f), respectively, which represent more pronounced signatures of FCI ground states in the larger system considered here. While the currents in row $n = 1$ change their directions with increasing N, the direction of currents in row $n = 2$ remains fixed, and they are always in opposite direction with the currents in the outermost edges. From Fig. 5.2(g), one can see the amplitude of the counter-propagating currents are almost independent of N, which indicate their robustness. By initially trapping extra one [Fig. 5.2(h)] or three [Fig. 5.2(i)] particles in the centre of given row, the density imbalances formed after the quench of on-site trapping present clear negative imbalance on the row $n = 2$ which could be readily measured in experiments.

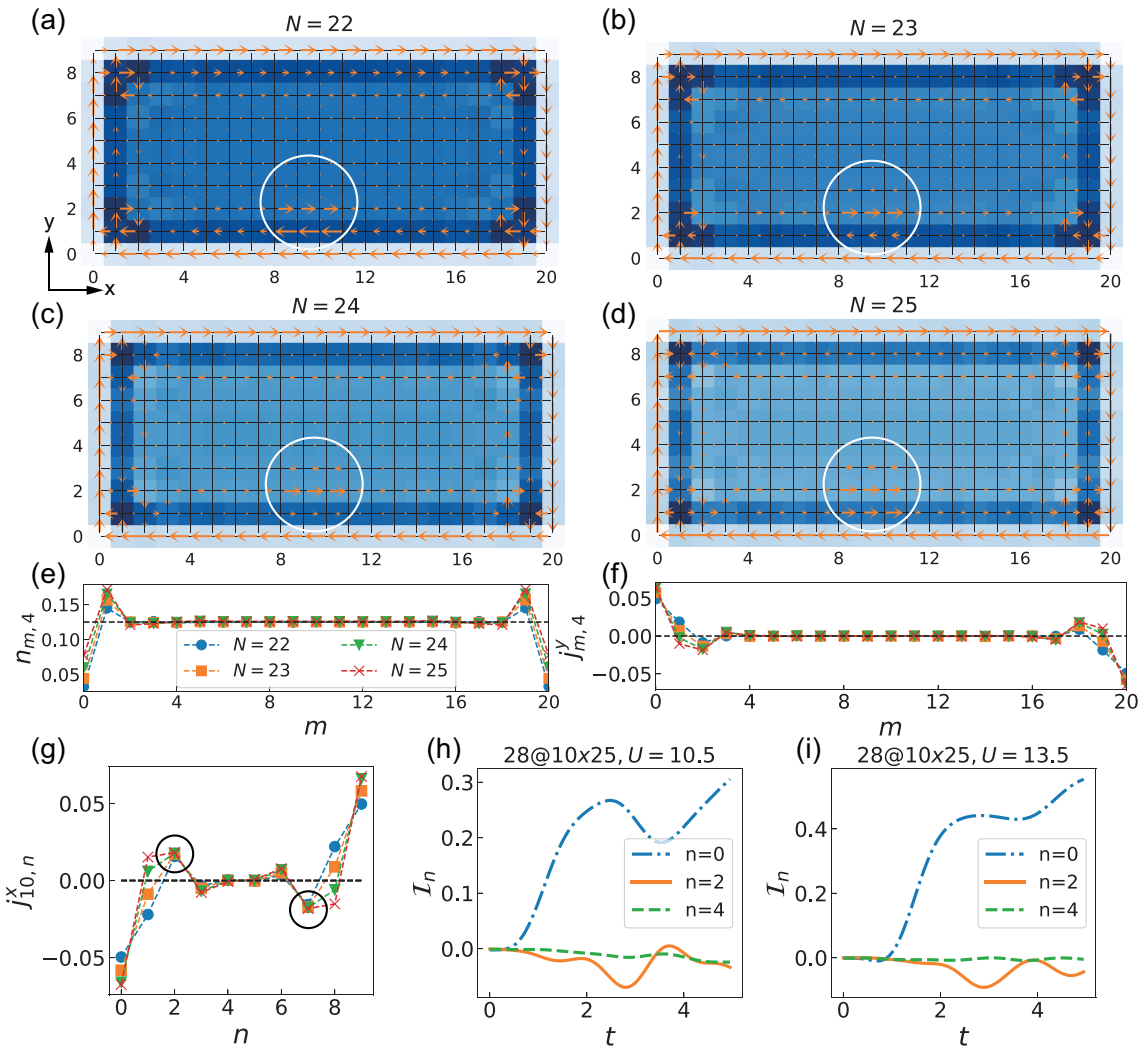

Figure 5.2: (a-d) Spatial density and current distributions of the ground state of hard-core bosons in a lattice of size 21×10 with $N = 22, 23, 24, 25$ respectively. The magnitudes of currents in the white circle are zoomed in for a clear visualization. (e) Density of the middle row $n = 4$ and (f) vertical currents on the middle links connected by $n = 4$ and $n = 5$. The horizontal dashed lines locates the expected $n = 1/8$ and $j = 0$. (g) Horizontal currents on the middle bonds connected by $m = 10$ and $m = 11$. (e-g) share the same legend. The black circles are used to highlight that the currents with opposite chirality are almost independent of N. Imbalance in the n-th row $\mathcal{I}_n$ as a function of evolution time with (h) one and (i) three extra particles initially trapped in the centre of given rows. Consistent negative $\mathcal{I}_2$ appear after roughly three tunneling time. Other parameters are $\alpha = 1/4$ and $J_y = 1$.

5.2.2 Crossover to charge-density waves

For the adiabatic preparation of FCI insulator states, it will be favorable to consider small systems [264, 265, 288]. In order to estimate the minimal linear extent permitting the observations of FCI signatures, we compute the ground state for systems of different widths L_y. Keeping $L_x = 17$ and $\alpha = 1/4$ fixed and targeting the $\nu = 1/2$ state, the particle number is always chosen as

$$N = \nu N_\phi = 2(L_y - 1). \tag{5.11}$$

For small L_y the system can be viewed as a flux ladder, as they were investigated recently in various experiments [92–96, 125, 183, 248, 249]. In this quasi-1D limit the FCI states are predicted to be adiabatically connected to charge density waves (CDW) [208, 288–293].

The spatial density and probability current distributions are plotted in Fig. 5.3(a). One can observe density oscillations are consistent with CDW behavior in the 'bulk' (i.e. the inner sites) for L_y smaller than 5. When $L_y \gtrsim 6$, a homogeneous bulk density is formed at the filling of $\rho = 1/8$ particles per site expected for the FCI state. In order to quantify this statement we plot the mean [Fig. 5.3(b)] and standard deviation [Fig. 5.3(c)] of the density $n_{m,n}$, averaged over the central sites ($m = 4, \ldots 8$) of the middle row (e.g. $n = 2$ for $L_y = 5$). One can clearly see that the filling approaches 1/8 for $L_y \gtrsim 6$ and the standard deviation becomes (very) small for $L_y \gtrsim 6$ (8). This suggests that a linear extent of 6 to 8 lattice sites should be sufficient to observe FCI bulk behaviour.

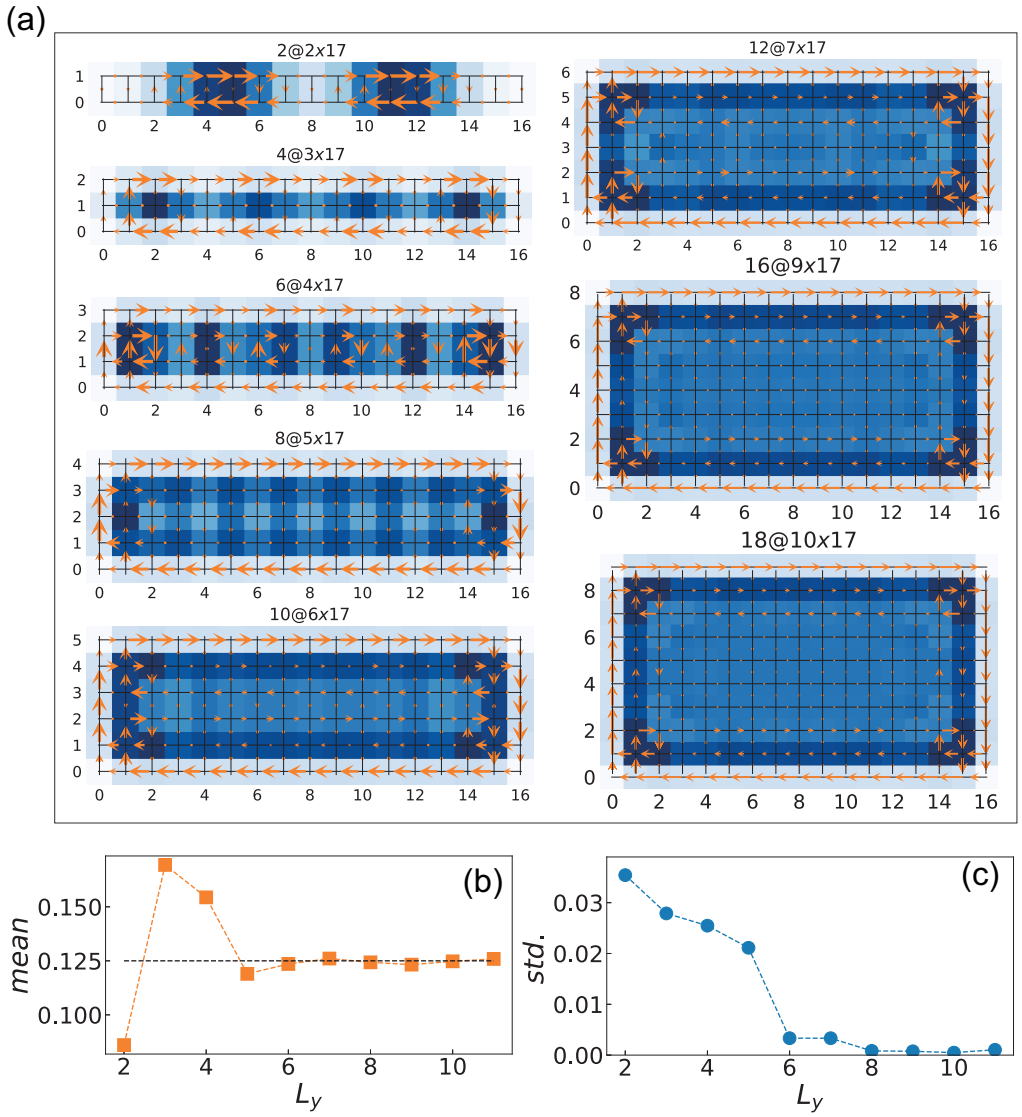

Figure 5.3: (a) Density and current patterns in the ground state for increasing values of the vertical extent L_y show a crossover from CDW to FCI behavior. The mean (b) and the standard deviation (c) of the particle number density on the middle row with m from 4 to 12. Other parameters are $\nu = 1/2$, $\alpha = 1/4$, $J_y = 1$, $L_x = 17$ and $N = 2(L_y - 1)$ in the hard-core limit.

5.3 Probing fractional excitations via pinning potentials

In this section, we investigate signatures of charge fractionalization. In order to probe the fractional 'charge' of $1/2$ and $-1/2$ of the anyonic quasiparticle (QP) and quasihole (QH) excitations of the $\nu = 1/2$ FCI, we compute the ground state of the system in the presence of local potential dips and bumps of strength $-V$ and V (to be specified below) by setting the

corresponding local potential terms $W_{m,n}$. These lower the energy of localized quasiparticle and quasihole excitations, respectively, so that above a threshold value of V, we expect an excited state with such an excitation to become the new ground state of the system. Such pinned excitations have been used to estimate the spatial extent of QHs in various FCI models [169, 294, 295] and also for extracting their anyonic statistics [267, 296–300]. For probing the fractional charge of the excitations, we will compare the ground-state density distribution of the system with and without such pinning potentials. As a signature of the formation of the FCI, we expect the particle number in the vicinity of these local defects to change in steps of the fractional charge 1/2. In fact, such a scenario has been studied in an earlier study based on exact diagonalization [175]. Due to the limited simulation ability, however, rather small systems of only 4 particles were considered, and the signatures of fractional charge were not very clear. The results presented here extend the earlier study to larger systems based on the DMRG approach [236–238], which is able to transform a 2D lattice into a 1D chain, thus allowing for the numerical study of a system with intermediate size. We will see that not only the expected fractional charges can be clearly observed in an intermediate lattice, but also that this behaviour is robust against the variation of various system parameters, like the magnetic flux, the particle number, or a tunneling anisotropy. These results are very promising regarding a possible experimental observation of charge fractionalization in optical lattices with ultracold atoms.

5.3.1 Fractional charges and screening

In the first set of simulations, we consider systems with $\alpha = 1/4$ and a horizontal extent of $L_x = 21$. We vary the vertical extent L_y and the particle number N, so that N takes integer values close to $\alpha\nu(L_x - 1)(L_y - 1) = (L_y - 1)5/2$. In the center of the left and right half of the system, respectively, we place a potential bump and a potential dip [as sketched in Fig. 5.4(c) and (f)]. Namely, on 2×2 or 3×1 neighboring sites, the potential is changed by $\pm V/4$ or $\pm V/3$ In all later plots, we choose the 2×2 configuration. The choice of such a pair of defects is motivated by the desire to keep the average filling away from the defects constant. We will see below, however, that the effect can also be observed for single defects, since the edge can provide/absorb the required charge. For every value of V, we then compute the ground state and compare how the particle number in the vicinity of the pinning potentials changes with respect to the ground state with a homogenous bulk ($V = 0$). We define the accumulated charge as

$$Q_{\pm V} = \sum_{\ell \in D_\pm(r)} \left[\langle n_\ell \rangle_{\pm V} - \langle n_\ell \rangle_{V=0} \right] . \tag{5.12}$$

Here, the region $D_\pm(r)$ includes all the sites $\ell = (m, n)$ within a disc of radius r that is co-centred with the local impurity. The radius r has to be chosen big enough so that the regions $D_+(r)$ and $D_-(r)$ essentially contain the whole pinned QH and QP excitation, respectively. In sufficiently large systems the precise choice of r should not matter, as long as this condition is fulfilled. This is indeed, what we observe [see Figs. 5.4(b) and (e) and the discussion below]. In the following we choose $r = 4$.

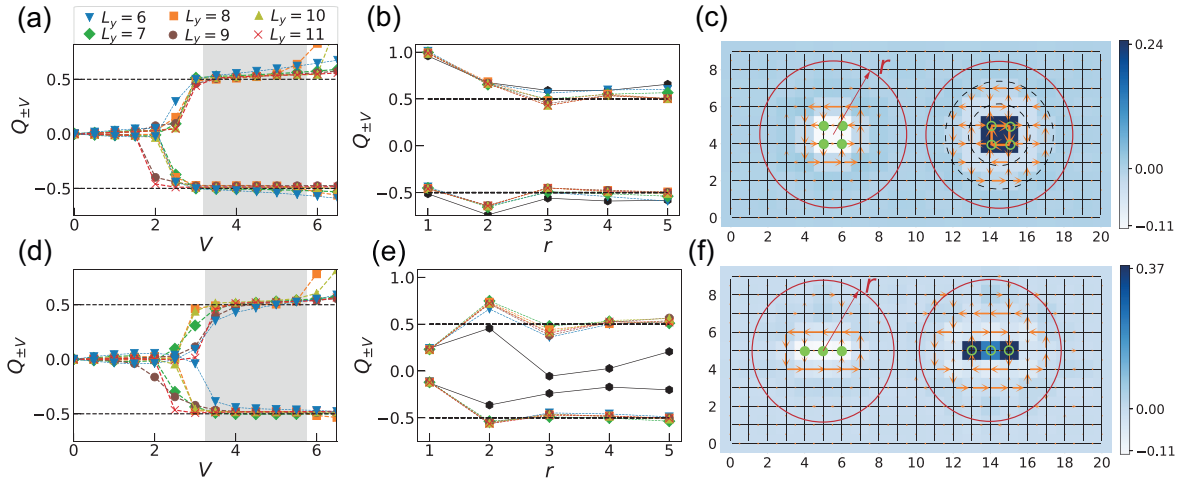

Figure 5.4: (a) Charges of QP/QH induced by negative/positive four-site pinning potentials as a function of pinning strength V. We have fixed $\nu = 1/2$, $L_x = 21$, $\alpha = 1/4$, $J_y = 1$ and adapted $N = (L_x - 1)(L_y - 1)\alpha\nu \approx 13, 15, 18, 20, 23, 25$ for $L_y = 6, 7, 8, 9, 10, 11$ respectively. (b) Integrated charges in the vicinity of negative/positive pinning potentials $|V| = 5$ as a function of the radius r of the counted disc. The black hexagon dots correspond to $L_y = 5$, which shows a small system fails to give expected fractional charges. The legend in (b) is the same as that in (a) and lines are guide for the eye. (c) Distribution of the density and current differences between the ground states with $V = 5$ and $V = 0$ in a system of 21×10 with $N = 23$. The impurities of strength $\pm V/4$ are distributed over four sites of a plaquette, as indicated by the solid and empty green circles respectively. The red circles are used to locate the counting region $D(r)$ with radius r. The dashed circles with $r = 2$ and 3 capture the currents of opposite chirality. (d-f) Same plots as (a-c), but using a three-site pinning. The shaded area in (a) and (c) indicate the regime of pinning strength that is able to pin the expected fractional charges.

In Figs. 5.4(a) and (d) we plot $Q_\pm$ for various $L_y \geq 6$ as a function of V for 2×2 and 3×1 pinning potentials, respectively. We can clearly observe two effects. Firstly, the density is hardly affected by a small pinning potential. This is another confirmation of the bulk incompressibility expected for the FCI state. Secondly, once V is raised above a threshold, the accumulated charge quickly changes to values close to $\pm 1/2$ at which it stays to form an extended plateau with respect to V. This confirms the fractional charges of the elementary QP and QH excitations of the system. Moreover, the results not only show that it is a robust way to create QP and QH excitations by using pinning potentials, but also indicate that the shape of topological excitations could be tailored by designing the pinning potentials. While we can identify plateaus already for $L_y = 6$, $Q_\pm$ remains closer to $\pm 1/2$ for larger system sizes. Choosing $V = 5$ as a value in the middle of the plateau, we compare results for different radii r in Figs. 5.4(b) and (e) and find that they saturate close to $\pm 1/2$ for $r \geq 3$.

A typical density and current distribution, as it is found for $V = 5$ (in the middle of the

plateau) is presented in Figs. 5.4(c) and (f) for $L_y = 10$. The extent of the QP is larger than that of the QH, which can be most clearly seen in the probability currents surrounding these localized excitations. When moving away from the center of the QP or QH, we observe that both the excess density and the chiral currents oscillate and change sign. These oscillations are more prominent for the QP excitation on the right hand side.

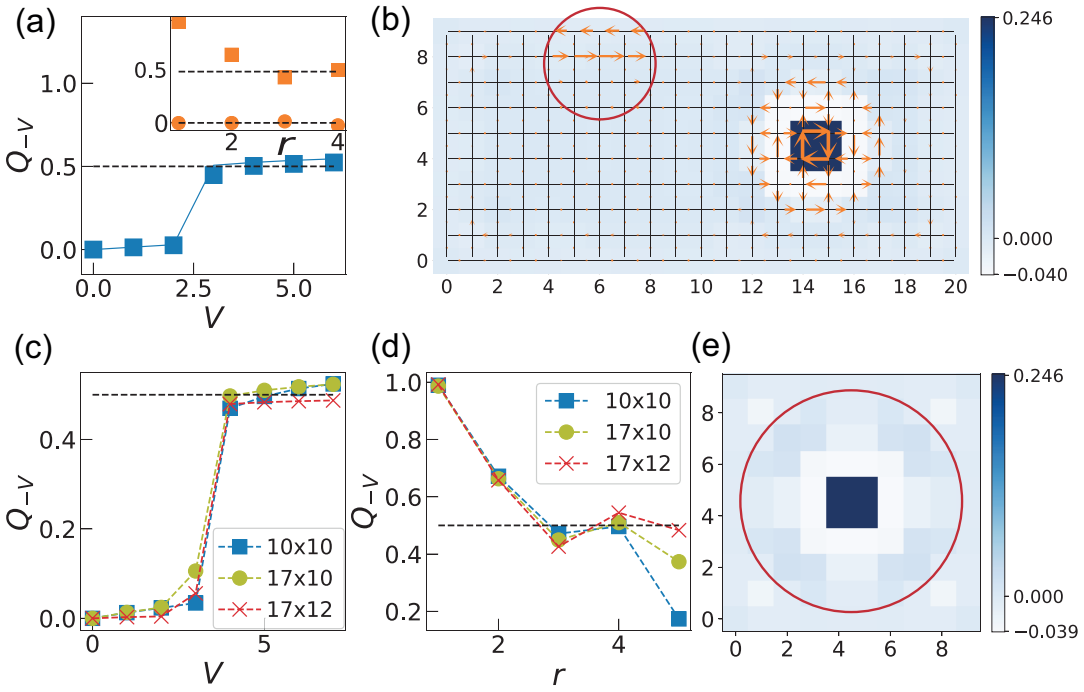

Figure 5.5: (a) Charges integrated in the vicinity of negative four-site pinning potentials at $r = 4$ as a function of V. The discrete points correspond to the case of a single potential dip, while the solid lines are obtained by applying both potential dips and bumps as in Fig. 5.4. The inset shows the charges at $V = 5$ as a function of the radius r, and the circles and squares respectively represent the charges in the left and right regions as defined in Fig. 5.4(a). We have used $N = 23$ in a system of 21×10. (b) A typical charge and current distributions at $V = 5$. The currents within the circle are zoomed in by a factor of 6 for clear visualization. (c) Charges as a function of V for different systems with negative 2×2 pinning potentials. The numbers N are given by 10, 18, 22 for system size 10×10, 17×10, 17×12, respectively, to achieve $\nu = 1/2$ particle per flux quantum. (d) Charges as a function of radius r at $V = 5$. Note that the drop at $r = 5$ for $L_y = 10$ is due to extra excitations appearing in the edge. (e) A typical charge distribution at $V = 5$ in system of size 10×10 with $N = 10$. Other parameters are $\alpha = 1/4, J_y = 1$.

As discussed in the previous section, where we investigated ground-state properties without pinning potential, the edge of the system can serve as a reservoir for excess particles. Thus, we can expect that it is also possible to create not only charge-neutral pairs of QP and QH, but

also individual excitations in the bulk. This scenario is investigated in Fig. 5.5. By applying only one potential dip in a system that otherwise agrees with the one studied in Fig. 5.4(c), we find the same signatures of incompressibility and charge fractionalization in the response of the ground-state density as before. The additional charge required for the creation of a QP by the potential dip is provided by the compressible edges. Note that this implies as well that the reservoir given by the compressible edges can host (and thus exchange with the system) fractional charges in units of $\nu = 1/2$. This would be experimentally favourable, since in this way one might allow for a smaller extent of the system also in x-direction. As shown in Fig. 5.5(c-e), clear signatures of fractional charges can still be observed in a smaller system of 10×10 sites.

Considering a more experimentally-realistic single potential bump, we find similar behavior for the creation of a single quasi-hole excitation within the bulk. In order to benchmark the appearance of a quasi-hole excitation, we firstly consider a large lattice of size 17×12 with particle number $N = 22$. As shown by the black dots in Fig. 5.6(a), the charge nicely saturates at $-1/2$ with the increase of radius of the counted disk [see e.g. Fig. 5.6(f)]. This result shall be used as a reference for the following discussion. By plotting the charges as a function of radius r for different system sizes, one can see that for the size larger than 6×6, the excitations exhibit very similar behaviour near the pinning potentials ($r \leq 2$). For 6×6, the charges at $r = 2$ as a function of impurity V [blue dots in Fig. 5.6(b)] behave similarly as that in the early study of a lattice size 5×9 [175], where a relatively-large deviation from $-1/2$ was also observed. As shown here, in order to observe clearer signatures of quasi-hole excitations, a system larger than 8×8 would be needed. Typical charge distributions of system with different sizes are shown in Fig. 5.6(c-f). Note that the values of charges close to $-1/2$ at $r = 1$ [Fig. 5.6(a)] can be misleading, as the density per site is $1/8$ and the sum of depletions on the four sites with pinning potentials would certainly go to $-1/2$ for large pinning.

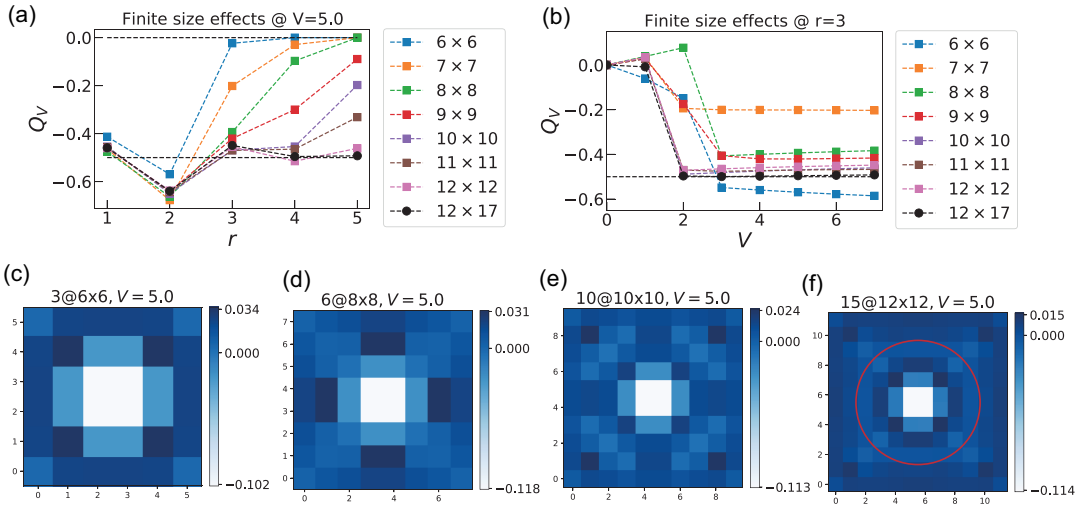

Figure 5.6: (a) Charges as a function of radius r at $V = 5$. (b) Charges integrated in the vicinity of positive four-site pinning potentials at $r = 3$ as a function of pinning strength V. Note that $r = 2$ is taken for the smallest size 6×6. (c-f) Charge distributions at $V = 5$ in a system of size 6×6, 8×8, 10×10 and 12×12, respectively. Other parameters are $\alpha = 1/4, J_y = J_x$. We adapt the total particle number $N = (L_y - 1)^2/8$, so that a Laughlin-like state at $\nu = 1/2$ is expected.

5.3.2 Robustness

We will now investigate the robustness of the fractionalized ground-state response to pinning potentials, when changing various system parameters. Starting from a scenario like the one investigated in Fig. 5.4, with a pair of 2×2 pinning potentials of opposite sign and a system size of 21×10 sites, in Fig. 5.7 we show results for different total particle numbers, plaquette fluxes, and anisotropic tunneling matrix elements. In panel (a), we plot the accumulated charges $Q_{\pm V}$ as a function of V for different particle numbers. Again the precise choice of $r = 4$ does not significantly influence the results, as can be inferred from (b), where r is varied for fixed $V = 5$. Optimal particle numbers are expected to lie close to $\nu\alpha(L_x - 1)(L_y - 1) = 22.5$. And, indeed, we can see very clear signatures of charge fractionalization for a range of particle numbers $N = 21, 22, 23$. However, when the particle number becomes too small (large), the threshold value of V at which a QH (QP) is created shifts to smaller values. Moreover, for the smallest particle number considered, $N = 20$, we even find the creation of a second QH excitation at a second threshold value of V.

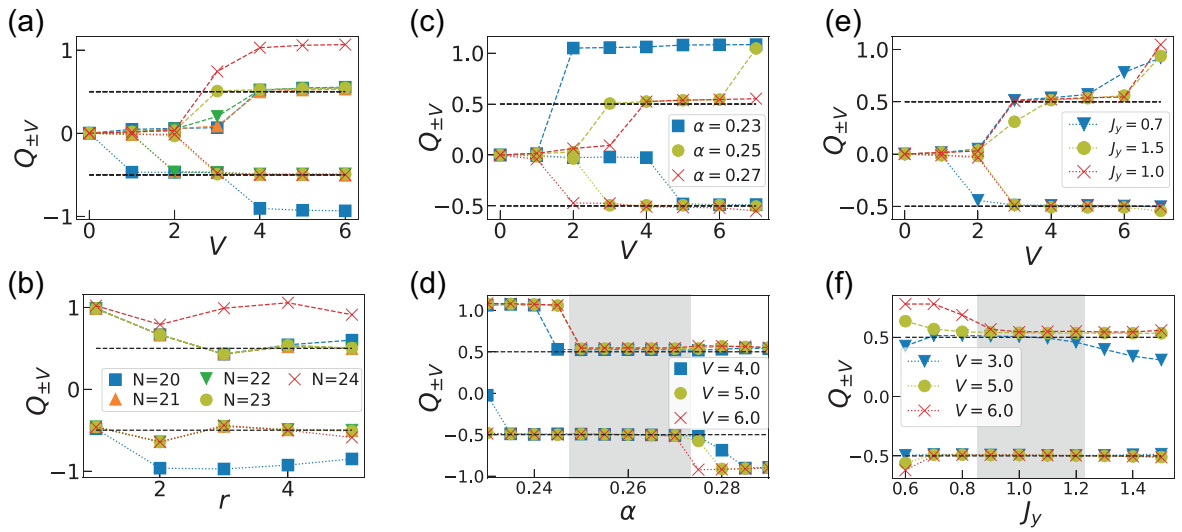

Figure 5.7: (a) Charges integrated at radius $r = 4$ as a function of pinning strength V for different particle numbers N. (b) Charges as a function of r at $V = 5$ for different N. We use the same legend in (a) and (b) and $\alpha = 1/4, J_y = 1$. (c) Charges as a function of V for different α and (d) charges as a function of α for different V with $N = 23, J_y = 1$. (e) Charges as a function of V for different J_y and (f) charges as a function of J_y for different V with $N = 23, \alpha = 1/4$. In all cases we have simultaneously applied both negative and positive four-site pinning potentials in a system of size 21×10.

The fact that the charge fractionalization expected for the FCI state breaks down when the global filling $N/N_\phi = N/[\alpha(L_x - 1)(L_y - 1)]$ deviates too much from the bulk value $\nu = 1/2$ of the FCI, can also be observed by varying the plaquette flux quantified by the number of flux quanta per plaquette α. This is investigated in Figs. 5.7(c) and (d). In panel (c) we observe that the threshold for the creation of a QH (QP) is shifted to smaller values of V, when α increases (decreases). Moreover, for the value of $\alpha = 0.23$, no QP of fractionalized charge 1/2 can be observed. In panel (d), we plot the pinned charges versus α (comparing different values of V) and find that the fractionalization of both QH and QP can be observed for α between 0.25 and 0.27. The quantization of QH (QP) alone can, moreover, be observed for values of α as small (large) as 0.24(0.29).

Finally, we investigate the effect of a tunneling anisotropy. The robustness of charge fractionalization with respect to a variation of J_y relative to $J_x = 1$ is investigated in Figs. 5.7(e) and (f) [16]. We find charge fractionalization for values of J_y between 0.7 and 1.5. All in all, we can see that signatures of charge fractionalization can be observed in an extended parameter regime,

[16] We consider values of J_y that are both smaller and larger than 1. In systems with boundaries and defect positions that are symmetric with respect to both lattice directions, it would be sufficient to increase J_y relative to $J_x = 1$. However, since we are working in a rectangular system that is elongated in x direction and possesses two defects that are separated in x direction, increasing and decreasing J_y from 1 can lead to different results.

which is good news for a possible experimental observation of charge fractionalization in small bosonic FCIs.

5.3.3 Effect of finite interactions

So far, we have focused on the hard-core limit. However, similar behaviour is found also for sufficiently strong, but finite interactions U. In order to test the robustness of charge fractionalization with respect to different interaction strengths, we have considered a system of 17×8 sites with 14 particles (like the one studied in Fig. 5.1) and calculated the response to two local defect potentials of oppositie sign [like the ones depicted in Fig. 5.4(c)]. For the calculation we truncated the maximum possible occupation of each lattice site to four particles. In Fig. 5.8, one can observe clear signatures of charge fractionalization for interaction strengths $U/J \gtrsim 15$.

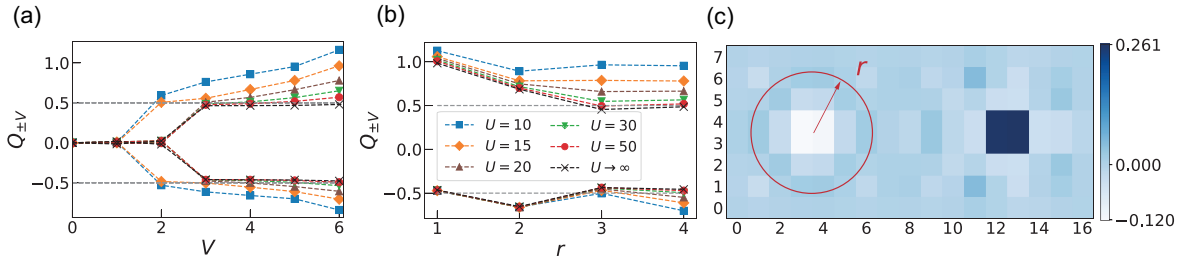

Figure 5.8: (a) Change of charge induced by a pair of 2×2 pinning potentials of opposite strength $\pm V$, measured in two circular regions of radius r centered around the pinning potentials. (b) Same as (a), but for fixed $V = 5$ and different radii r. We use the same legend for interaction U in (a) and (b). Other parameters are $L_x \times L_y = 17 \times 8$, $\alpha = 1/4$, $J_y = 1$, and $N = (L_x - 1)(L_y - 1)\alpha\nu = 14$. (c) A typical charge distributions at $V = 5$ for $U = 20$. The particle number per site was truncated to a maximum value of 4 (allowing for larger occupations did not change the results).

5.4 Fractional charge pumping

As another hallmark of quantum Hall states, quantized charge pumping can be induced by the adiabatic insertion of magnetic flux quanta [6, 166, 301]. In chapter 3, we have discussed in detail a possible protocol for the realization of the famous Laughlin Gedankenexperiment in 2D optical lattices. While its application in interacting systems of small size has also been addressed [175], in this section, we extend the study to the systems of intermediate size by using a time evolution method based on matrix product operators [236–238]. We will see that the fractional charge pumping within the bulk, as well as the edge mode population can be induced by such a local-flux insertion in a finite 2D fractional Chern insulator.

After applying additional phases $\delta\phi$ on the links between a target plaquette and the system boundary, as sketched in Fig. 5.9(a), only the flux of the target plaquette is modified to be

$\phi + \delta\phi$. After linearly ramping $\delta\phi$ from 0 to 2π within time τ, as expected, a fractional charge of $1/2$ is populated from the bulk to the edge of the system with $\nu = 1/2$ particle per flux quantum [Figs. 5.9(c,d)]. After the flux insertion, the created edge excitation follows a chiral motion, which is robust against the corner defects [Figs. 5.9(e-g)]. Note that all these signatures survive even for a system of 12×10 with 12 particles, which is a promising setup within the reach of present-day's experiments [125]. Last but not least, by modifying the fluxes of two plaquettes to be $\phi \pm \delta\phi$, as depicted in Fig. 5.9(b) and shown in Fig. 5.9(h-k), QP and QH excitations with charges $\pm 1/2$ can be created in the bulk. Interestingly, we observe fluctuating densities (like a ring structure) in the vicinity of modified plaquettes during the ramp [Fig. 5.9(j)], which is different from the quantized charge pumping in integer Chern insulators [see e.g. Fig. 3.7 in chapter 3].

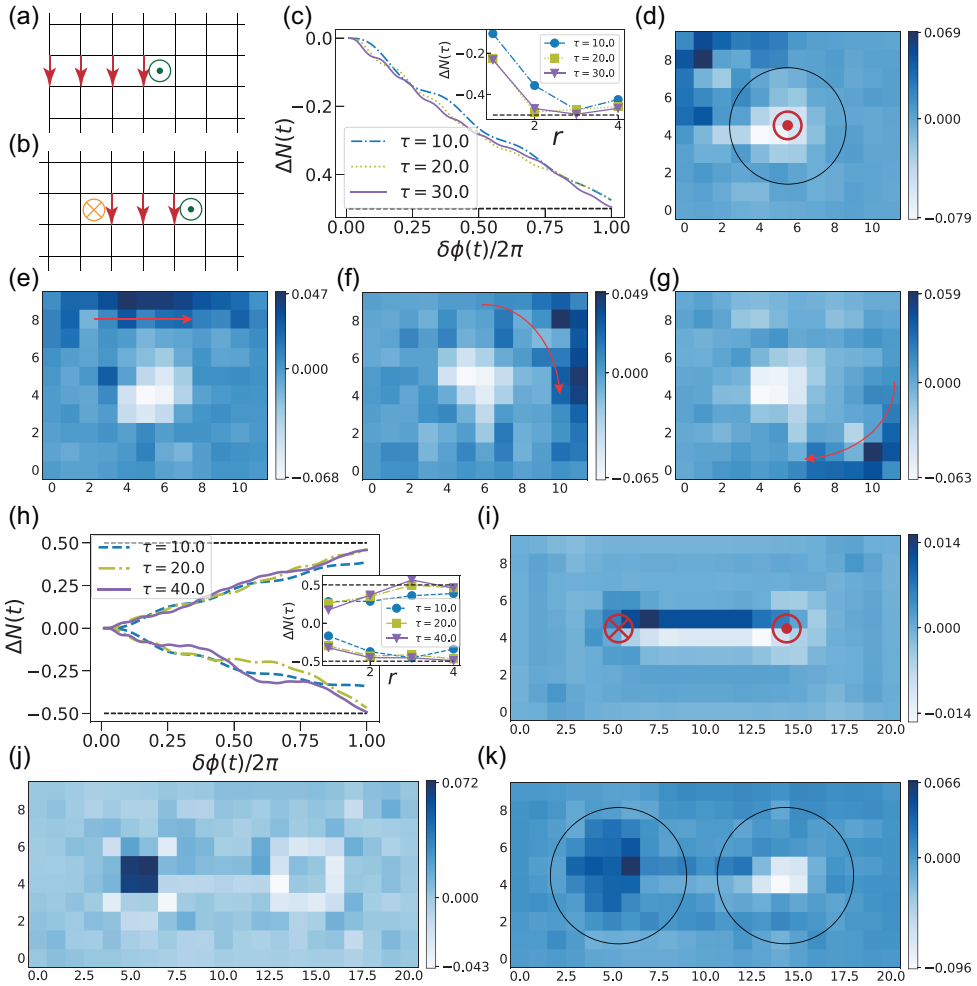

Figure 5.9: Sketch of modifying the flux in one single plaquette (a) and two plaquettes (b) in the bulk. The arrows denote additional tunnelling phases $\delta\phi$, and the fluxes of the plaquettes labelled by $\odot, \otimes$ are modified to be $\phi \pm \delta\phi$ respectively. (c) The particle number difference ('charge') $\Delta N(t) = N(t) - N(t = 0)$ integrated in the disc $r = 3$ centred at the modified plaquette as a function of $\delta\phi(t)$. The inset shows $\Delta N(\tau)$ as a function of integrated radius r. (d) Snapshots of the respective changes in spatial densities at the end of ramp with $t = \tau = 30$ (d), and after the flux insertion at (e) $t = 46$, (f) $t = 71$, (g) $t = 90$. The red arrows are used to indicate the chiral motion. Simulations of (c-g) are performed for a system of size 12×10 with $N = 12, \alpha = 1/4, J_y = 1$ and $\nu = N/N_\phi \simeq 1/2$. Tiny pinning potentials of strength $V = 1/4$ have been distributed over the four sites of the modified plaquette to prevent the bulk excitations from dispersing. (h) Particle number difference ΔN integrated in the disc with $r = 4$ centred at the modified plaquettes as a function of $\delta\phi(t)$. The dependence of charges as a function of r are shown in the inset. Snapshots of the respective density changes within the ramp at (i) $t = 4$, (j) $t = 20$, (k) $t = \tau = 40$. Simulations of (h-k) are performed for a system of size 21×10 with $N = 23, \alpha = 1/4, J_y = 1$ and $\nu = N/N_\phi \simeq 1/2$.

6 Conclusion and outlook

This thesis has been about tailoring artificial gauge fields and probing signatures of quantum Hall physics in optical lattices with ultracold atoms. By considering the paradigmatic Harper-Hofstadter model, we first introduced basic concepts (e.g. Berry phase, Chern number) that are used to describe its topological properties, followed by its experimental implementation by using Floquet engineering in chapter 2.

In chapter 3, we have proposed a scheme for the realization of tunable solenoid-type local magnetic fluxes in 2D optical lattices. Such an optical solenoid allow for quantized charge pumping in a topological Chern insulator along tailored paths. This effect can, for example, be employed for the coherent population of chiral edge modes to probe their robust chiral transport properties. Its application to a bosonic optical lattice system has also been discussed.

Motivated by the above-mentioned work, in chapter 4 we point out that the time-dependent artificial vector potentials (in the form of Peierls phases) can be designed for rapid adiabatic state preparation in optical lattice systems. This observation is based on the fact that in such systems experimentalists directly control artificial vector potentials rather than magnetic fields, in which case the flux insertion is accompanied by the creation of artificial electric fields. We demonstrated that for a ladder with flux, this approach allows for an almost immediate state preparation for non-interacting bosons. Remarkably, this can be attained with very short ramping time also for strongly interacting bosons. While the abrupt adiabatic preparation in the ladder is an extreme example, it highlights that tuning Peierls phases can be a very powerful tool for state preparation.

Last but not least, we have numerically investigated the fate of FCI states as the ground state of the strongly-interacting bosonic Harper-Hofstadter model in realistic finite system geometries with open boundary conditions, which can be realized in quantum-gas microscopes. Already for small system sizes starting from linear extents of about 6-8 lattice sites, we find robust measurable signatures that are consistent with the expected behavior of a Laughlin-like FCI state at filling $\nu = 1/2$. In particular, we find chiral edge transport, an incompressible bulk at the expected filling, as well as fractionally charged quasiparticle and quasihole excitations that can be created either by pinning potentials or via local flux insertion. These features are rather robust against modifications of system parameters. Our results provide a guide for future experiments with interacting atoms in optical lattices with artificial magnetic flux.

Outlook

While we have shown that the fractional Chern insulating states and fractionalized charges can be stabilized in a finite lattice of intermediate size with a few particles, an efficient way of preparing such exotic states is still a highly non-trivial task. There have been several proposals

for preparation protocols in lattice models, including starting from a topologically trivial Mott insulator [257, 258, 264], or coupling individual chains [265, 278]. Nevertheless, how to ramp up the desired values of flux in an efficient way is an important question. It will be interesting to see, whether the scheme for rapid state preparation via magnetic flux ramps from Chapter 4 can be extended to the preparation of (fractional) Chern insulator states in 2D. Especially, combining state preparation protocols with realistic periodic driving schemes will be of particular interest and importance.

As has been discussed in chapter 4, the chiral current in quasi-1D (two-leg ladders) is a crucial quantity to characterize the ground state phases. Its extension to 2D (fractional) Chern insulators, together with its connection to the topologically non-trivial edge modes therein, is also a very interesting direction to go. Such kind of theoretical investigations could also be addressed in future experiments by measuring the detailed current patterns based on refined quantum gas microscope techniques [68, 69, 282]. Note that although many cold atom experiments need harmonic traps, sharp boundaries are now also possible by using, for example, synthetic dimensions [91] or box trapping potentials [70], which offer ideal platforms to study edge physics.

Meanwhile, box traps provide other exciting opportunities as well [70]. For sure it is interesting to experimentally create and probe fractionalized charges in a finite lattice. Then a follow-up question would be what can we do with the created fractional excitations? One exotic phenomenon is the so-called Andreev reflection, which originally describes scattering behaviour at interfaces between a superconductor and a normal state material [302, 303]. Similarly, considering an interface between the fractional $\nu = 1/3$ and integer quantum Hall states, two incoming quasiparticles with charge $e/3$ can be reflected as a quasihole with charge $-e/3$, leaving a normal electron with charge e transmitted. Such an Andreev reflection of fractionally-charged quasiparticles has been predicted more than two decades ago [304], and has been very recently observed in a 2D electronic system [305]. Since box traps in optical lattices offer the possibilities to study interfaces between different phases of matter, it will be an exciting future task to create an interface (e.g. by using quantum gas microscopes) between a fractional Chern insulating state and a trivial one, by means of which to investigate the fate of the fractional charges by using ultracold atoms.

As Laughlin's Gedankenexperiment of flux insertion provides a powerful tool to characterize quantum Hall states, it is desirable to see the proposed protocol to be implemented in cold atom experiments. At the same time, its application in bosonic system posts an interesting question about its possible realization in other synthetic platforms, such as photonic waveguides [43–45]. As another paradigmatic Chern insulator, the Haldane model, has been implemented by using photons [306], it becomes also interesting to work out realistic driving protocols for a local flux insertion in the Haldane model.

More recently, the study of topology in quasicrystals [307] or fractals [308] is drawing more and more attentions. As a hallmark of quantum Hall state and a promising experimental probe, how to realize the above-mentioned Laughlin's gedankenexperiment of flux insertion in such systems will be also of interest. Moreover, motivated by recent experimental realization of fractal photonic lattices [309], it is interesting to investigate whether chiral edge currents show up in fractal dimension with time-reversal symmetry breaking (e.g. by applying periodic driving).

Appendix

A. Bogoliubov theory in a two-leg ladder

The Hamiltonian of the interacting two-leg ladder is rewritten as

$$\hat{H} = \hat{H}_S + \hat{H}_I, \tag{A1}$$

$$\hat{H}_S = -J\sum_r \left(e^{i\theta_1}\hat{a}^\dagger_{1,r+1}\hat{a}_{1,r} + e^{i\theta_2}\hat{a}^\dagger_{2,r+1}\hat{a}_{2,r} + h.c.\right) - J_\perp\sum_r \left(\hat{a}^\dagger_{2,r}\hat{a}_{1,r} + \hat{a}^\dagger_{1,r}\hat{a}_{2,r}\right), \tag{A2}$$

$$\hat{H}_I = \frac{U}{2}\sum_r \left(\hat{a}^\dagger_{1,r}\hat{a}^\dagger_{1,r}\hat{a}_{1,r}\hat{a}_{1,r} + \hat{a}^\dagger_{2,r}\hat{a}^\dagger_{2,r}\hat{a}_{2,r}\hat{a}_{2,r}\right). \tag{A3}$$

Here $\hat{a}^\dagger_{1,r}$ ($\hat{a}_{1,r}$) and $\hat{a}^\dagger_{2,r}$ ($\hat{a}_{2,r}$) are the creation (annihilation) operators on the rung r in the lower and upper leg respectively, J denotes the amplitude of nearest-neighbor tunneling along the legs, with $\theta_{1,2} = -\eta \pm \phi/2$ being the corresponding Peierls phases, so that the flux in each plaquette is ϕ and we consider $\phi = \pi/2$ here.

For a two-leg ladder with M rungs, under periodic boundary conditions along the legs, the quasimomentum takes discrete value $k = \frac{2\pi}{Ma}m$ with $m = -M/2, -M/2+1, \cdots, M/2-1$ (for even M) and a being the lattice constant. By performing the Fourier transformation

$$\hat{a}_{l,r} = \frac{1}{\sqrt{M}}\sum_k e^{ikar}\hat{a}_{l,k},\ l = 1, 2 \tag{A4}$$

the above Hamiltonians can be expressed in quasi-momentum representation as

$$\hat{H}_S = \sum_k \left(\epsilon_{1,k}\hat{a}^\dagger_{1,k}\hat{a}_{1,k} + \epsilon_{2,k}\hat{a}^\dagger_{2,k}\hat{a}_{2,k}\right) - J_\perp\sum_k \left(\hat{a}^\dagger_{2,k}\hat{a}_{1,k} + \hat{a}^\dagger_{1,k}\hat{a}_{2,k}\right), \tag{A5}$$

$$\hat{H}_I = \frac{U}{2M}\sum_{\{k_i\}} \left(\hat{a}^\dagger_{1,k_1}\hat{a}^\dagger_{1,k_2}\hat{a}_{1,k_3}\hat{a}_{1,k_4} + \hat{a}^\dagger_{2,k_1}\hat{a}^\dagger_{2,k_2}\hat{a}_{2,k_3}\hat{a}_{2,k_4}\right)\tilde{\delta}_{k_1+k_2,k_3+k_4}, \tag{A6}$$

with

$$\epsilon_{1,k} = -2J\cos\left(ka + \eta - \phi/2\right), \tag{A7}$$

$$\epsilon_{2,k} = -2J\cos\left(ka + \eta + \phi/2\right), \tag{A8}$$

and periodic Kronecker symbol $\tilde{\delta}_{k,q}$ vanishing unless $k = q$ modulo reciprocal lattice constants $2\pi/a$.

Diagonal basis

The single-particle Hamiltonian (A5) can be diagonalized by choosing a different basis, i.e.

$$\begin{pmatrix} \hat{a}_{1,k} \\ \hat{a}_{2,k} \end{pmatrix} = \begin{pmatrix} \zeta_k & -\eta_k \\ \eta_k & \zeta_k \end{pmatrix} \begin{pmatrix} \hat{b}_{1,k} \\ \hat{b}_{2,k} \end{pmatrix}. \tag{A9}$$

The canonical commutation $\left[\hat{b}_{i,k}, \hat{b}^\dagger_{j,k'}\right] = \delta_{i,j}\delta_{k,k'}$ requires that

$$\zeta_k^2 + \eta_k^2 = 1. \tag{A10}$$

Substituting Eq. (A9) to Eq.(A5), and imposing all the off-diagonal terms to vanish, the single particle Hamiltonian is diagonalized as

$$\hat{H}_S = E_1 \hat{b}^\dagger_{1,k}\hat{b}_{1,k} + E_2 \hat{b}^\dagger_{2,k}\hat{b}_{2,k}, \tag{A11}$$

with

$$E_1 = \frac{1}{2}\left(\epsilon_{1,k} + \epsilon_{2,k} + \sqrt{4J_\perp^2 + \left(\epsilon_{1,k} - \epsilon_{2,k}\right)^2}\right), \tag{A12}$$

$$E_2 = \frac{1}{2}\left(\epsilon_{1,k} + \epsilon_{2,k} - \sqrt{4J_\perp^2 + \left(\epsilon_{1,k} - \epsilon_{2,k}\right)^2}\right), \tag{A13}$$

$$\zeta_k^2 = \frac{1}{2}\left(1 - \frac{\epsilon_{2,k} - \epsilon_{1,k}}{\sqrt{4J_\perp^2 + \left(\epsilon_{1,k} - \epsilon_{2,k}\right)^2}}\right). \tag{A14}$$

Truncation to the lowest band

The terms related to $\hat{b}_{2,k}$ ($\hat{b}_{1,k}$) correspond to the lower (upper) band. Since the system possesses a large band gap for the parameters used ($J_\perp = 2J$), for weak interaction we are allowed to truncate our Hamiltonian to the lowest band. To do this, we plug Eq. (A9) into the Hamiltonian and neglect the $\hat{b}_{1,k}$ terms. In this case, the full Hamiltonian is truncated to the lowest band [194],

$$\hat{H} = \sum_k E(k)\,\hat{b}^\dagger_k \hat{b}_k + \frac{U}{2M}\sum_{\{k_i\}} \Gamma_{k_1,k_2,k_3,k_4}\hat{b}^\dagger_{k_1}\hat{b}^\dagger_{k_2}\hat{b}_{k_3}\hat{b}_{k_4}\tilde{\delta}_{k_1+k_2,k_3+k_4}, \tag{A15}$$

where $\hat{b}_k \equiv \hat{b}_{2,k}$, $E_k \equiv E_2(k)$ and we have defined $\Gamma_{k_1,k_2,k_3,k_4} = \zeta_{k_1}\zeta_{k_2}\zeta_{k_3}\zeta_{k_4} + \eta_{k_1}\eta_{k_2}\eta_{k_3}\eta_{k_4}$.

Bogoliubov approximation

For weak interactions and at low temperature, the number N_0 of particles occupying the single-particle ground state with quasi momentum k_0 remains of the order of total particle number N in a system of finite extent. Thus one can make the approximation

$$\hat{b}^\dagger_{k_0}\hat{b}_{k_0} = \hat{N}_0 \simeq \hat{N}_0 + 1 = \hat{b}_{k_0}\hat{b}^\dagger_{k_0}, \tag{A16}$$

which leads to

$$\hat{b}_{k_0} \simeq \hat{b}_{k_0}^\dagger = \sqrt{N_0}, \tag{A17}$$

$$\hat{b}_k = \sqrt{N_0}\delta_{k,k_0} + \hat{b}_k\left(1-\delta_{k,k_0}\right). \tag{A18}$$

Keeping all the terms up to second order in $\hat{b}_{k\neq k_0}$, the Hamiltonian (A15) becomes

$$\begin{aligned}\hat{H} =& E\left(k_0\right)N_0 + \frac{U}{2M}\Gamma_0 U N_0^2 + \sum_{k\neq 0} E\left(k+k_0\right)\hat{b}_k^\dagger \hat{b}_k \\ &+ \frac{UN_0}{2M}\sum_{k\neq 0}\left[\Gamma_1\left(\hat{b}_k\hat{b}_{-k} + \hat{b}_k^\dagger \hat{b}_{-k}^\dagger\right) + 4\Gamma_2 \hat{b}_k^\dagger \hat{b}_k\right],\end{aligned} \tag{A19}$$

with the coefficients

$$\Gamma_0 = \eta_{k_0}^4 + \zeta_{k_0}^4 = 1/2, \tag{A20}$$

$$\Gamma_1 = \left(\eta_{k+k_0}\eta_{k_0-k} + \zeta_{k+k_0}\zeta_{k_0-k}\right)/2, \tag{A21}$$

$$\Gamma_2 = \eta_{k_0}^2\eta_{k+k_0}^2 + \zeta_{k_0}^2\zeta_{k+k_0}^2 = 1/2, \tag{A22}$$

where we have used $\eta_{k_0}^2 = 1/2 = \zeta_{k_0}^2$ according to Eqs. (A7), (A8) and (A14).

Substituting $N_0 = N - \sum_{k\neq 0}\hat{b}_k^\dagger \hat{b}_k$ and keeping the terms up to second order in $\hat{b}_k$, we arrive at

$$\begin{aligned}\hat{H} =& E_0 - \sum_{k>0} C_{-k} + \sum_{k>0}\hat{H}_k \\ \hat{H}_k =& \begin{pmatrix} \hat{b}_k^\dagger & \hat{b}_{-k}\end{pmatrix}\begin{pmatrix} C_k & 2D_k \\ 2D_k & C_{-k}\end{pmatrix}\begin{pmatrix}\hat{b}_k \\ \hat{b}_{-k}^\dagger\end{pmatrix},\end{aligned} \tag{A23}$$

with

$$E_0 = \left(E\left(k_0\right) + Un\Gamma_0\right)N, \tag{A24}$$

$$C_k = E\left(k+k_0\right) - E\left(k_0\right) + Un\left(4\Gamma_2 - 2\Gamma_0\right), \tag{A25}$$

$$D_k = Un\Gamma_1 = D_{-k} \equiv D. \tag{A26}$$

Here we have introduced the total particle number per site $n = \frac{N}{2M}$, and the additional term $-\sum_{k>0} C_{-k}$ comes from the commutation relation $\hat{b}_{-k}^\dagger \hat{b}_{-k} = \hat{b}_{-k}\hat{b}_{-k}^\dagger - 1$.

Diagonalization

To diagonalize the Hamiltonian (A23), we perform the Bogoliubov transformation

$$\begin{pmatrix}\hat{b}_k \\ \hat{b}_{-k}^\dagger\end{pmatrix} = \begin{pmatrix}\mu & \nu \\ \nu & \mu\end{pmatrix}\begin{pmatrix}\hat{\rho}_k \\ \hat{\rho}_{-k}^\dagger\end{pmatrix}, \tag{A27}$$

with quasiparticle annihilation (creation) operators $\hat{\rho}_k$ ($\hat{\rho}_k^\dagger$). Requiring bosonic commutation relations for the quasiparticle operators, we have

$$\mu^2 - \nu^2 = 1. \tag{A28}$$

To get the expressions for μ, ν, we plug Eq. (A27) into Eq. (A23) and impose that

$$\hat{H}_k = \begin{pmatrix} \hat{\rho}_k^\dagger & \hat{\rho}_{-k} \end{pmatrix} \begin{pmatrix} \gamma_1 & 0 \\ 0 & \gamma_2 \end{pmatrix} \begin{pmatrix} \hat{\rho}_k \\ \hat{\rho}_{-k}^\dagger \end{pmatrix}. \tag{A29}$$

Thus we have

$$\begin{pmatrix} \gamma_1 & 0 \\ 0 & \gamma_2 \end{pmatrix} = \begin{pmatrix} \mu & \nu \\ \nu & \mu \end{pmatrix} \begin{pmatrix} C_k & 2D_k \\ 2D_k & C_{-k} \end{pmatrix} \begin{pmatrix} \mu & \nu \\ \nu & \mu \end{pmatrix} \tag{A30}$$

which leads to the solutions:

$$\gamma_1 = \frac{1}{2}\left(C_k - C_{-k} + \sqrt{(C_{-k} + C_k)^2 - 16D^2}\right), \tag{A31}$$

$$\gamma_2 = \frac{1}{2}\left(-C_k + C_{-k} + \sqrt{(C_{-k} + C_k)^2 - 16D^2}\right), \tag{A32}$$

$$\mu^2 = \frac{1}{2}\left(1 + \frac{C_{-k} + C_k}{\sqrt{(C_{-k} + C_k)^2 - 16D^2}}\right). \tag{A33}$$

Bogoliubov ground state

In the following, we follow Ref. [310] and construct the Bogoliubov ground state $\left|\Psi_0^B\right\rangle$, which is defined as the state with no quasi-particle, i.e.

$$\hat{\rho}_k \left|\Psi_0^B\right\rangle = 0, \ \forall k \neq k_0. \tag{A34}$$

As the Bogoliubov transformation (A27) connects the states with k and $-k$, the Bogoliubov ground state can be expressed as the states where n_k particles are present in k states and n_{-k} particles are in the $-k$ states [310], i.e.

$$\left|\Psi_0^B\right\rangle = \prod_k \sum_{n,n_{-k}} C^k_{n_k,n_{-k}} \frac{(\hat{b}_k^\dagger)^{n_k}}{\sqrt{n_k!}} \frac{(\hat{b}_{-k}^\dagger)^{n_{-k}}}{\sqrt{n_{-k}!}} |0\rangle, \tag{A35}$$

where $|0\rangle$ denotes the vacuum state. Substituting Eq. (A35) into Eq. (A34) and using the expression of $\hat{\rho}_k = \mu\hat{b}_k - \nu\hat{b}_{-k}^\dagger$ according to Eq. (A27), we have

$$\prod_k \sum_{n_k,n_{-k}=0}^{\infty} \left(C^k_{n_k+1,n_{-k}} \mu\sqrt{n_k+1} + C^k_{n_k,n_{-k}-1} - \nu\sqrt{n_{-k}}\,|n_k, n_{-k}\rangle\right) = 0, \tag{A36}$$

where we define $C^k_{n_k,-1} = 0$. Since the basis $\{|n_k, n_{-k}\rangle\}$ are orthogonal, we get

$$\sqrt{n_k+1}C^k_{n_k+1,n_{-k}} + \alpha_k\sqrt{n_{-k}}C^k_{n_k,n_{-k}-1} = 0 \tag{A37}$$

with $\alpha_k = -\nu/\mu$ for short.

By setting $n_{-k} = 0$ in the above equation Eq. (A37), we have $C^k_{n_k+1,0} = 0$ $(n_k \geq 0)$. A similar procedure for $\hat{b}_{1,-k}\left|\Psi^B_0\right\rangle = 0$ gives us $C^k_{0,n_{-k}+1} = 0$ $(n_{-k} \geq 0)$. Based on these observations, it turns out that all the 'off-diagonal' components vanish, i.e. $C^k_{n_k+1,n_{-k}} = 0$ $(n_{-k} \neq n_k + 1)$. In the case of $n_{-k} = n_k + 1$, Eq. (A37) gives us the following expression of the diagonal terms

$$C^k_{n_k,n_k} = (-\alpha_k)^{n_k} C^k_{0,0}, \tag{A38}$$

where $C^k_{0,0}$ is determined from the normalization of the wave-function. Therefore, the Bogoliubov ground state is a state where pairs of particles with wave vector k and $-k$ are excited.

We denote $\left|n_1,n_2,\cdots\right\rangle$ as a state with n pairs of particles with non-zero quasi-momentum k and $-k$, and $|\psi_0\rangle$ as the state with $k = 0$. In this case the Bogoliubov ground state takes the following form

$$\left|\Psi^B_0\right\rangle = Z\sum_{n_1,n_2}\left[\left(-\alpha_{k_1}\right)^{n_1}\left(-\alpha_{k_2}\right)^{n_2}\cdots\right]|n_1,n_2,\cdots\rangle\,|\psi_0\rangle\,, \tag{A39}$$

where $Z = \prod_{k>0}\sqrt{1-\alpha_k^2}$ is the normalization factor.

The state $|\psi_0\rangle$ for $k = 0$ is a coherent state $\hat{b}_0\,|\psi_0\rangle = \psi_0\,|\psi_0\rangle$ and reads

$$|\psi_0\rangle = Z_0\sum_{n_0}\frac{\psi_0^{n_0}}{\sqrt{n_0!}}\,|n_0\rangle\,, \tag{A40}$$

where we have defined the vacuum state $|\text{vac}\rangle$ for the real particles operators $\hat{b}_k$, i.e. $\hat{b}_k\,|\text{vac}\rangle = 0$. The normalization factor is $Z_0 = \exp\left(-\left|\psi_0\right|^2/2\right)$.

According to Eq. (A39) we have the overlap of two ground states

$$\mathcal{O} = \left\langle\Psi'^B_0\right|\left.\Psi^B_0\right\rangle = ZZ'\left\langle\psi'_0\right.|\psi_0\rangle\prod_{k>0}\frac{1}{1-\alpha'_k\alpha_k}. \tag{A41}$$

The overlap of coherent states $\mathcal{O}_{\text{coh}} \equiv \left\langle\psi'_0\right.|\psi_0\rangle$ is obtained by using Eq. (A40),

$$\mathcal{O}_{\text{coh}} = e^{\left(-\left|\psi'_0\right|^2-|\psi_0|^2+2\psi'_0\psi_0\right)/2}, \tag{A42}$$

which reads $\mathcal{O}_{\text{coh}} \simeq 1$ under Bogoliubov approximation $\psi'_0 = \sqrt{N'_0/2} \simeq \sqrt{N/2} \simeq \psi_0$.

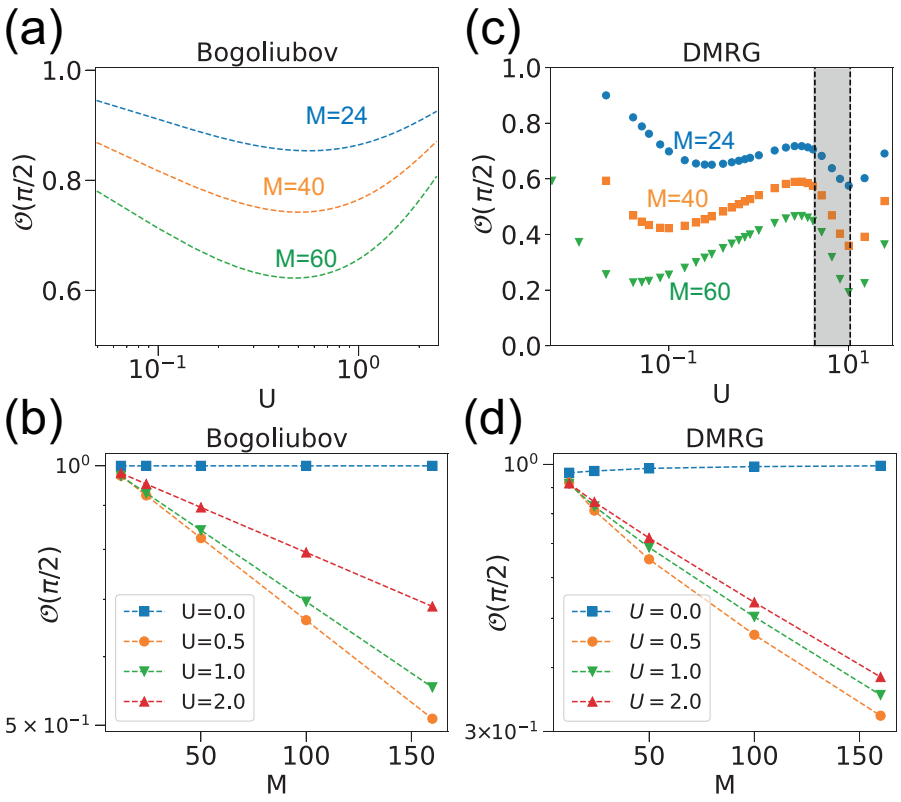

Figure A1: (a) Semi-log plot of ground state overlaps $\mathcal{O}(\pi/2)$ from Bogoliubov theory as a function of interaction U, for different number of rungs M. (b) Semi-log plot of $\mathcal{O}(\pi/2)$ as a function of M for different U. (c,d) Same plot as (a,b), but for DMRG simulations.

Occupation of finite momentum states

In the Bogoliubov ground state $\left|\Psi_0^B\right\rangle$, pairs of bosons are 'virtually' excited to states with k and $-k$. The average number of the excited bosons with wave vector k due to such quantum fluctuations is obtained from the Bogoliubov transformation (A27) and the definition of Bogoliubov ground state (A34),

$$n_k = \left\langle \Psi_0^B \right| \hat{b}_k^\dagger \hat{b}_k \left| \Psi_0^B \right\rangle = |\nu|^2 \,. \tag{A43}$$

We denote $N_{k\neq 0}$ as the number of virtually excited particles, i.e. the number of particles in the state $|k \neq 0\rangle$,

$$N_{k\neq 0} = 2\sum_{k>0} n_k = 2\sum_{k>0} |\nu|^2 \,. \tag{A44}$$

Results

Now we apply the above expressions in our ladder system at 1/2 filling with $J_\perp = 2$. We plot the analytic result for the overlap Eq. (A41) for M-rung ladder with periodic boundary condition in Fig. A1(a), which shows qualitative agreement with the dip behavior in the weakly interacting regime from the DMRG simulations of *finite* system with open boundary conditions [Fig. A1(c)]. Note that the DMRG results for the interacting regime have been divided into three regions. The beginning and the end of the grey shaded region are given by the BKT transition from a superfluid to a Mott insulator for $\phi = \pi/2$ and $\phi = 0$, respectively (similar to Fig. 4.5). Overall, both the analytic and numerical results show that the overlaps decay exponentially with the system size for finite U, and approach 1 for the non-interacting case [Fig. A1(b,d)].

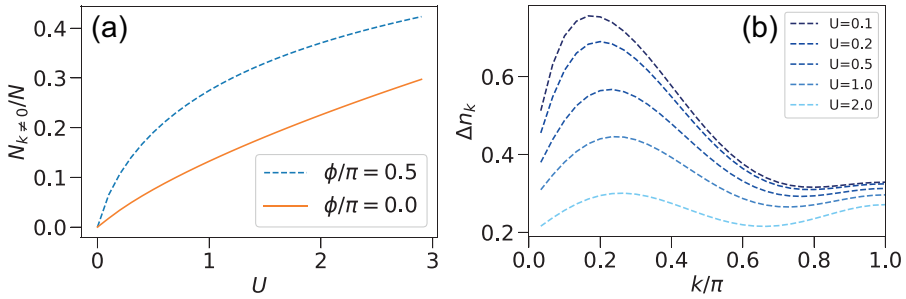

Figure A2: (a) Number of particles with non-zero quasi-momentum for $\phi = 0$ (solid line) and $\phi = \pi/2$ (dashed line), scaled with total particle number N. (b) Difference of non-zero k mode occupation between $\phi = \pi/2$ and $\phi = 0$. Here we choose the number of rungs $M = 60$, number of particles $N = 60$, and $J_\perp = 2$.

To understand the dip in the weakly interacting regime, we plot the average number of particles with non-zero quasi momentum $N_{k\neq 0}$ according to Eq. (A44), and the relative difference in the occupation of non-zero k-modes $\Delta n_k = \frac{n_k(\pi/2) - n_k(0)}{n_k(\pi/2) + n_k(0)}$ between $\phi = \pi/2$ and $\phi = 0$ in Fig. A2(a) and (b), respectively. We can observe that when switching on the interactions, the excited quasi momentum modes become occupied much faster in the presence of magnetic flux. This is related to the fact that the single-particle dispersion relation $E_-(k)$ acquires a larger effective mass with increasing flux. This is a consequence of a frustration induced into the kinetics by the magnetic flux. As a result, the momentum modes become occupied rather differently for both fluxes when U is switched on, as can be seen from Fig. A2(b). The slight increase of the overlap for even larger U can then be explained by the fact that the relative differences in the momentum distributions for both fluxes become smaller again.

Bibliography

1. Anderson, P. W. More Is Different. *Science* **177,** 393–396. ISSN: 0036-8075. https://science.sciencemag.org/content/177/4047/393 (1972) (cit. on p. 1).
2. Landau, L. D. On the theory of phase transitions. *Zh. Eksp. Teor. Fiz.* **7,** 19–32 (1937) (cit. on p. 1).
3. Ginzburg, V. L. & Landau, L. D. On the Theory of superconductivity. *Zh. Eksp. Teor. Fiz.* **20,** 1064–1082 (1950) (cit. on p. 1).
4. Klitzing, K. v., Dorda, G. & Pepper, M. New Method for High-Accuracy Determination of the Fine-Structure Constant Based on Quantized Hall Resistance. *Phys. Rev. Lett.* **45,** 494–497. https://link.aps.org/doi/10.1103/PhysRevLett.45.494 (6 1980) (cit. on p. 1).
5. Tsui, D. C., Stormer, H. L. & Gossard, A. C. Two-Dimensional Magnetotransport in the Extreme Quantum Limit. *Phys. Rev. Lett.* **48,** 1559–1562. https://link.aps.org/doi/10.1103/PhysRevLett.48.1559 (22 1982) (cit. on pp. 1, 91).
6. Laughlin, R. B. Quantized Hall conductivity in two dimensions. *Phys. Rev. B* **23,** 5632–5633. https://link.aps.org/doi/10.1103/PhysRevB.23.5632 (10 1981) (cit. on pp. 2, 45, 46, 105).
7. Thouless, D. J., Kohmoto, M., Nightingale, M. P. & den Nijs, M. Quantized Hall Conductance in a Two-Dimensional Periodic Potential. *Phys. Rev. Lett.* **49,** 405–408. https://link.aps.org/doi/10.1103/PhysRevLett.49.405 (6 1982) (cit. on pp. 2, 18).
8. Simon, B. Holonomy, the Quantum Adiabatic Theorem, and Berry's Phase. *Phys. Rev. Lett.* **51,** 2167–2170. https://link.aps.org/doi/10.1103/PhysRevLett.51.2167 (24 1983) (cit. on pp. 2, 13, 18).
9. Berry, M. V. Quantal phase factors accompanying adiabatic changes. *Proceedings of the Royal Society of London. A. Mathematical and Physical Sciences* **392,** 45–57. https://royalsocietypublishing.org/doi/abs/10.1098/rspa.1984.0023 (1984) (cit. on pp. 2, 9, 11, 12, 16).
10. Laughlin, R. B. Anomalous Quantum Hall Effect: An Incompressible Quantum Fluid with Fractionally Charged Excitations. *Phys. Rev. Lett.* **50,** 1395–1398. https://link.aps.org/doi/10.1103/PhysRevLett.50.1395 (18 1983) (cit. on pp. 2, 91).
11. Von Klitzing, K., Chakraborty, T., Kim, P., Madhavan, V., Dai, X., McIver, J., Tokura, Y., Savary, L., Smirnova, D., Rey, A. M., *et al.* 40 years of the quantum Hall effect. *Nature Reviews Physics* **2,** 397–401. https://www.nature.com/articles/s42254-020-0209-1 (2020) (cit. on p. 2).

12. Wen, X.-G. Colloquium: Zoo of quantum-topological phases of matter. *Rev. Mod. Phys.* **89,** 041004. https://link.aps.org/doi/10.1103/RevModPhys.89.041004 (4 2017) (cit. on pp. 2, 3, 91).

13. Wen, X.-G. Choreographed entanglement dances: Topological states of quantum matter. *Science* **363.** ISSN: 0036-8075. https://science.sciencemag.org/content/363/6429/eaal3099 (2019) (cit. on pp. 2, 3).

14. Bednorz, J. G. & Müller, K. A. Possible high T c superconductivity in the Ba- La- Cu- O system. *Zeitschrift für Physik B Condensed Matter* **64,** 189–193. https://link.springer.com/article/10.1007/BF01303701 (1986) (cit. on p. 2).

15. Kalmeyer, V. & Laughlin, R. B. Equivalence of the resonating-valence-bond and fractional quantum Hall states. *Phys. Rev. Lett.* **59,** 2095–2098. https://link.aps.org/doi/10.1103/PhysRevLett.59.2095 (18 1987) (cit. on p. 2).

16. Wen, X. G. Vacuum degeneracy of chiral spin states in compactified space. *Phys. Rev. B* **40,** 7387–7390. https://link.aps.org/doi/10.1103/PhysRevB.40.7387 (10 1989) (cit. on p. 2).

17. Wen, X. G. & Niu, Q. Ground-state degeneracy of the fractional quantum Hall states in the presence of a random potential and on high-genus Riemann surfaces. *Phys. Rev. B* **41,** 9377–9396. https://link.aps.org/doi/10.1103/PhysRevB.41.9377 (13 1990) (cit. on p. 2).

18. Zeng, B., Chen, X., Zhou, D.-L. & Wen, X.-G. *Quantum information meets quantum matter: From quantum entanglement to topological phases of many-body systems* https://link.springer.com/book/10.1007%2F978-1-4939-9084-9#about (Springer, 2019) (cit. on p. 2).

19. WEN, X. G. TOPOLOGICAL ORDERS IN RIGID STATES. *International Journal of Modern Physics B* **04,** 239–271. https://doi.org/10.1142/S0217979290000139 (1990) (cit. on p. 2).

20. Halperin, B. I. Quantized Hall conductance, current-carrying edge states, and the existence of extended states in a two-dimensional disordered potential. *Phys. Rev. B* **25,** 2185–2190. https://link.aps.org/doi/10.1103/PhysRevB.25.2185 (4 1982) (cit. on p. 2).

21. Wen, X. G. Chiral Luttinger liquid and the edge excitations in the fractional quantum Hall states. *Phys. Rev. B* **41,** 12838–12844. https://link.aps.org/doi/10.1103/PhysRevB.41.12838 (18 1990) (cit. on p. 2).

22. Kitaev, A. & Preskill, J. Topological Entanglement Entropy. *Phys. Rev. Lett.* **96,** 110404. https://link.aps.org/doi/10.1103/PhysRevLett.96.110404 (11 2006) (cit. on pp. 3, 91).

23. Levin, M. & Wen, X.-G. Detecting Topological Order in a Ground State Wave Function. *Phys. Rev. Lett.* **96,** 110405. https://link.aps.org/doi/10.1103/PhysRevLett.96.110405 (11 2006) (cit. on pp. 3, 91).

24. Chen, X., Gu, Z.-C. & Wen, X.-G. Local unitary transformation, long-range quantum entanglement, wave function renormalization, and topological order. *Phys. Rev. B* **82,** 155138. https://link.aps.org/doi/10.1103/PhysRevB.82.155138 (15 2010) (cit. on pp. 3, 74, 83).

25. Kane, C. L. & Mele, E. J. Quantum Spin Hall Effect in Graphene. *Phys. Rev. Lett.* **95,** 226801. https://link.aps.org/doi/10.1103/PhysRevLett.95.226801 (22 2005) (cit. on p. 3).

26. Kane, C. L. & Mele, E. J. Z_2 Topological Order and the Quantum Spin Hall Effect. *Phys. Rev. Lett.* **95,** 146802. https://link.aps.org/doi/10.1103/PhysRevLett.95.146802 (14 2005) (cit. on p. 3).

27. Bernevig, B. A. & Zhang, S.-C. Quantum Spin Hall Effect. *Phys. Rev. Lett.* **96,** 106802. https://link.aps.org/doi/10.1103/PhysRevLett.96.106802 (10 2006) (cit. on p. 3).

28. Hasan, M. Z. & Kane, C. L. Colloquium: Topological insulators. *Rev. Mod. Phys.* **82,** 3045–3067. https://link.aps.org/doi/10.1103/RevModPhys.82.3045 (4 2010) (cit. on p. 3).

29. Qi, X.-L. & Zhang, S.-C. Topological insulators and superconductors. *Rev. Mod. Phys.* **83,** 1057–1110. https://link.aps.org/doi/10.1103/RevModPhys.83.1057 (4 2011) (cit. on p. 3).

30. Kitaev, A. Y. Fault-tolerant quantum computation by anyons. *Annals of Physics* **303,** 2–30. https://doi.org/10.1016/S0003-4916(02)00018-0 (2003) (cit. on p. 3).

31. Nayak, C., Simon, S. H., Stern, A., Freedman, M. & Das Sarma, S. Non-Abelian anyons and topological quantum computation. *Rev. Mod. Phys.* **80,** 1083–1159. https://link.aps.org/doi/10.1103/RevModPhys.80.1083 (3 2008) (cit. on pp. 3, 91).

32. Arovas, D., Schrieffer, J. R. & Wilczek, F. Fractional Statistics and the Quantum Hall Effect. *Phys. Rev. Lett.* **53,** 722–723. https://link.aps.org/doi/10.1103/PhysRevLett.53.722 (7 1984) (cit. on p. 3).

33. Halperin, B. I. Statistics of Quasiparticles and the Hierarchy of Fractional Quantized Hall States. *Phys. Rev. Lett.* **52,** 1583–1586. https://link.aps.org/doi/10.1103/PhysRevLett.52.1583 (18 1984) (cit. on p. 3).

34. Moore, G. & Read, N. Nonabelions in the fractional quantum hall effect. *Nuclear Physics B* **360,** 362–396. ISSN: 0550-3213. https://www.sciencedirect.com/science/article/pii/0550321391904070 (1991) (cit. on p. 3).

35. Wen, X. G. Non-Abelian statistics in the fractional quantum Hall states. *Phys. Rev. Lett.* **66,** 802–805. https://link.aps.org/doi/10.1103/PhysRevLett.66.802 (6 1991) (cit. on p. 3).

36. Goldman, N, Budich, J. & Zoller, P. Topological quantum matter with ultracold gases in optical lattices. *Nat. Phys.* **12,** 639–645. https://www.nature.com/articles/nphys3803 (2016) (cit. on pp. 3, 5, 74, 91).

37. Gross, C. & Bloch, I. Quantum simulations with ultracold atoms in optical lattices. *Science* **357,** 995–1001. ISSN: 0036-8075. http://science.sciencemag.org/content/357/6355/995 (2017) (cit. on pp. 3, 5).

38. Cooper, N. R., Dalibard, J. & Spielman, I. B. Topological bands for ultracold atoms. *Rev. Mod. Phys.* **91,** 015005. https://link.aps.org/doi/10.1103/RevModPhys.91.015005 (1 2019) (cit. on pp. 3, 5, 38, 74, 91, 93).

39. Zhang, D.-W., Zhu, Y.-Q., Zhao, Y. X., Yan, H. & Zhu, S.-L. Topological quantum matter with cold atoms. *Advances in Physics* **67,** 253–402. https://doi.org/10.1080/00018732.2019.1594094 (2018) (cit. on pp. 3, 5, 38, 91).

40. Bloch, I. Quantum simulations come of age. *Nature Physics* **14,** 1159–1161. https://www.nature.com/articles/s41567-018-0371-x (2018) (cit. on pp. 3–5).

41. Schäfer, F., Fukuhara, T., Sugawa, S., Takasu, Y. & Takahashi, Y. Tools for quantum simulation with ultracold atoms in optical lattices. *Nature Reviews Physics* **2,** 411–425. https://www.nature.com/articles/s42254-020-0195-3 (2020) (cit. on pp. 3–5).

42. Feynman, R. P. Simulating physics with computers. *International journal of theoretical physics* **21,** 467–488. https://link.springer.com/article/10.1007%2FBF02650179?LI=true (1982) (cit. on p. 4).

43. Ozawa, T., Price, H. M., Amo, A., Goldman, N., Hafezi, M., Lu, L., Rechtsman, M. C., Schuster, D., Simon, J., Zilberberg, O. & Carusotto, I. Topological photonics. *Rev. Mod. Phys.* **91,** 015006. https://link.aps.org/doi/10.1103/RevModPhys.91.015006 (1 2019) (cit. on pp. 4, 73, 109).

44. Carusotto, I., Houck, A. A., Kollár, A. J., Roushan, P., Schuster, D. I. & Simon, J. Photonic materials in circuit quantum electrodynamics. *Nature Physics* **16,** 268–279. https://www.nature.com/articles/s41567-020-0815-y (2020) (cit. on pp. 4, 109).

45. Kremer, M., Maczewsky, L. J., Heinrich, M. & Szameit, A. Topological effects in integrated photonic waveguide structures. *Opt. Mater. Express* **11,** 1014–1036. http://www.osapublishing.org/ome/abstract.cfm?URI=ome-11-4-1014 (2021) (cit. on pp. 4, 109).

46. Kjaergaard, M., Schwartz, M. E., Braumüller, J., Krantz, P., Wang, J. I.-J., Gustavsson, S. & Oliver, W. D. Superconducting Qubits: Current State of Play. *Annual Review of Condensed Matter Physics* **11,** 369–395. https://doi.org/10.1146/annurev-conmatphys-031119-050605 (2020) (cit. on p. 4).

47. Monroe, C., Campbell, W. C., Duan, L.-M., Gong, Z.-X., Gorshkov, A. V., Hess, P. W., Islam, R., Kim, K., Linke, N. M., Pagano, G., Richerme, P., Senko, C. & Yao, N. Y. Programmable quantum simulations of spin systems with trapped ions. *Rev. Mod. Phys.* **93,** 025001. https://link.aps.org/doi/10.1103/RevModPhys.93.025001 (2 2021) (cit. on p. 4).

48. Blatt, R. & Roos, C. F. Quantum simulations with trapped ions. *Nature Physics* **8,** 277–284 (2012) (cit. on p. 4).

49. Bose, S. Planck's law and the light quantum hypothesis. *Journal of Astrophysics and Astronomy* **15,** 3–7. https://link.springer.com/article/10.1007/BF03010400 (1994) (cit. on p. 4).

50. Anderson, M. H., Ensher, J. R., Matthews, M. R., Wieman, C. E. & Cornell, E. A. Observation of Bose-Einstein Condensation in a Dilute Atomic Vapor. *Science* **269,** 198–201. ISSN: 0036-8075. https://science.sciencemag.org/content/269/5221/198 (1995) (cit. on p. 4).

51. Davis, K. B., Mewes, M. O., Andrews, M. R., van Druten, N. J., Durfee, D. S., Kurn, D. M. & Ketterle, W. Bose-Einstein Condensation in a Gas of Sodium Atoms. *Phys. Rev. Lett.* **75,** 3969–3973. https://link.aps.org/doi/10.1103/PhysRevLett.75.3969 (22 1995) (cit. on p. 4).

52. Bradley, C. C., Sackett, C. A., Tollett, J. J. & Hulet, R. G. Evidence of Bose-Einstein Condensation in an Atomic Gas with Attractive Interactions. *Phys. Rev. Lett.* **75,** 1687–1690. https://link.aps.org/doi/10.1103/PhysRevLett.75.1687 (9 1995) (cit. on p. 4).

53. Pitaevskii, L. & Stringari, S. *Bose-Einstein condensation and superfluidity* (Oxford University Press, 2016) (cit. on p. 4).

54. Grimm, R., Weidemüller, M. & Ovchinnikov, Y. B. Optical dipole traps for neutral atoms. *Advances in atomic, molecular, and optical physics* **42,** 95–170. https://www.sciencedirect.com/science/article/abs/pii/S1049250X0860186X (2000) (cit. on p. 4).

55. Bloch, I., Dalibard, J. & Zwerger, W. Many-body physics with ultracold gases. *Rev. Mod. Phys.* **80,** 885–964. https://link.aps.org/doi/10.1103/RevModPhys.80.885 (3 2008) (cit. on pp. 4, 5, 21).

56. Jaksch, D., Bruder, C., Cirac, J. I., Gardiner, C. W. & Zoller, P. Cold Bosonic Atoms in Optical Lattices. *Phys. Rev. Lett.* **81,** 3108–3111. https://link.aps.org/doi/10.1103/PhysRevLett.81.3108 (15 1998) (cit. on p. 4).

57. Fisher, M. P. A., Weichman, P. B., Grinstein, G. & Fisher, D. S. Boson localization and the superfluid-insulator transition. *Phys. Rev. B* **40,** 546–570. https://link.aps.org/doi/10.1103/PhysRevB.40.546 (1 1989) (cit. on p. 4).

58. Greiner, M., Mandel, O., Esslinger, T., Hänsch, T. W. & Bloch, I. Quantum phase transition from a superfluid to a Mott insulator in a gas of ultracold atoms. *nature* **415,** 39–44. https://www.nature.com/articles/415039a (2002) (cit. on p. 4).

59. Chin, C., Grimm, R., Julienne, P. & Tiesinga, E. Feshbach resonances in ultracold gases. *Rev. Mod. Phys.* **82,** 1225–1286. https://link.aps.org/doi/10.1103/RevModPhys.82.1225 (2 2010) (cit. on p. 5).

60. Lahaye, T, Menotti, C, Santos, L, Lewenstein, M & Pfau, T. The physics of dipolar bosonic quantum gases. *Reports on Progress in Physics* **72,** 126401. https://doi.org/10.1088/0034-4885/72/12/126401 (2009) (cit. on p. 5).

61. Baranov, M. A., Dalmonte, M., Pupillo, G. & Zoller, P. Condensed Matter Theory of Dipolar Quantum Gases. *Chemical Reviews* **112,** 5012–5061. https://doi.org/10.1021/cr2003568 (2012) (cit. on p. 5).

62. Gadway, B. & Yan, B. Strongly interacting ultracold polar molecules. *Journal of Physics B: Atomic, Molecular and Optical Physics* **49,** 152002. https://doi.org/10.1088/0953-4075/49/15/152002 (2016) (cit. on p. 5).

63. Moses, S. A., Covey, J. P., Miecnikowski, M. T., Jin, D. S. & Ye, J. New frontiers for quantum gases of polar molecules. *Nature Physics* **13,** 13–20. https://www.nature.com/articles/nphys3985 (2017) (cit. on p. 5).

64. Browaeys, A. & Lahaye, T. Many-body physics with individually controlled Rydberg atoms. *Nature Physics* **16,** 132–142. https://www.nature.com/articles/s41567-019-0733-z (2020) (cit. on pp. 5, 91).

65. Bakr, W. S., Gillen, J. I., Peng, A., Fölling, S. & Greiner, M. A quantum gas microscope for detecting single atoms in a Hubbard-regime optical lattice. *Nature* **462,** 74–77. https://www.nature.com/articles/nature08482 (2009) (cit. on pp. 5, 74, 91).

66. Sherson, J. F., Weitenberg, C., Endres, M., Cheneau, M., Bloch, I. & Kuhr, S. Single-atom-resolved fluorescence imaging of an atomic Mott insulator. *Nature* **467,** 68–72. https://www.nature.com/articles/nature09378 (2010) (cit. on pp. 5, 91).

67. Weitenberg, C., Endres, M., Sherson, J. F., Cheneau, M., Schauss, P., Fukuhara, T., Bloch, I. & Kuhr, S. Single-spin addressing in an atomic Mott insulator. *Nature* **471,** 319–324. https://www.nature.com/articles/nature09827 (2011) (cit. on p. 5).

68. Ott, H. Single atom detection in ultracold quantum gases: a review of current progress. *Rep. Prog. Phys.* **79,** 054401. http://stacks.iop.org/0034-4885/79/i=5/a=054401 (2016) (cit. on pp. 5, 74, 91, 109).

69. Kuhr, S. Quantum-gas microscopes: a new tool for cold-atom quantum simulators. *Natl. Sci. Rev* **3,** 170–172. http://dx.doi.org/10.1093/nsr/nww023 (2016) (cit. on pp. 5, 74, 109).

70. Navon, N., Smith, R. P. & Hadzibabic, Z. Quantum Gases in Optical Boxes. *arXiv:2106.09716* (2021) (cit. on pp. 5, 109).

71. Eckardt, A. Colloquium: Atomic quantum gases in periodically driven optical lattices. *Rev. Mod. Phys.* **89,** 011004. https://journals.aps.org/rmp/abstract/10.1103/RevModPhys.89.011004 (2017) (cit. on pp. 5–7, 29, 38, 40, 67, 74, 92).

72. Tomita, T., Nakajima, S., Danshita, I., Takasu, Y. & Takahashi, Y. Observation of the Mott insulator to superfluid crossover of a driven-dissipative Bose-Hubbard system. *Science Advances* **3.** https://advances.sciencemag.org/content/3/12/e1701513 (2017) (cit. on p. 5).

73. Sponselee, K, Freystatzky, L, Abeln, B, Diem, M, Hundt, B, Kochanke, A, Ponath, T, Santra, B, Mathey, L, Sengstock, K & Becker, C. Dynamics of ultracold quantum gases in the dissipative Fermi–Hubbard model. *Quantum Science and Technology* **4,** 014002. https://doi.org/10.1088/2058-9565/aadccd (2018) (cit. on p. 5).

74. Nakagawa, M., Tsuji, N., Kawakami, N. & Ueda, M. Dynamical Sign Reversal of Magnetic Correlations in Dissipative Hubbard Models. *Phys. Rev. Lett.* **124,** 147203. https://link.aps.org/doi/10.1103/PhysRevLett.124.147203 (14 2020) (cit. on p. 5).

75. Bouganne, R., Aguilera, M. B., Ghermaoui, A., Beugnon, J. & Gerbier, F. Anomalous decay of coherence in a dissipative many-body system. *Nature Physics* **16,** 21–25. https://www.nature.com/articles/s41567-019-0678-2 (2020) (cit. on p. 5).

76. Galitski, V. & Spielman, I. B. Spin-orbit coupling in quantum gases. *Nature* **494,** 49–54. https://www.nature.com/articles/nature11841 (2013) (cit. on pp. 5, 74, 91).

77. Zhai, H. Degenerate quantum gases with spin–orbit coupling: a review. *Rep. Prog. Phys.* **78,** 026001. http://stacks.iop.org/0034-4885/78/i=2/a=026001 (2015) (cit. on pp. 5, 91).

78. Zhang, W., Yi, W. & Melo, C. A. R. S. M. *Synthetic Spin-Orbit Coupling in Cold Atoms* https://www.worldscientific.com/doi/abs/10.1142/11050 (WORLD SCIENTIFIC, 2018) (cit. on p. 5).

79. Dalibard, J., Gerbier, F., Juzeliūnas, G. & Öhberg, P. Colloquium: Artificial gauge potentials for neutral atoms. *Rev. Mod. Phys.* **83,** 1523–1543. https://link.aps.org/doi/10.1103/RevModPhys.83.1523 (4 2011) (cit. on pp. 5, 38, 74, 91).

80. Goldman, N, Juzeliūnas, G, Öhberg, P & Spielman, I. B. Light-induced gauge fields for ultracold atoms. *Rep. Prog. Phys.* **77,** 126401. http://stacks.iop.org/0034-4885/77/i=12/a=126401 (2014) (cit. on pp. 5, 6, 38, 74, 91).

81. Aidelsburger, M., Nascimbene, S. & Goldman, N. Artificial gauge fields in materials and engineered systems. *Comptes Rendus Physique* **19.** Quantum simulation / Simulation quantique, 394–432. ISSN: 1631-0705. https://www.sciencedirect.com/science/article/pii/S1631070518300318 (2018) (cit. on pp. 5, 38, 91).

82. Cooper, N. Rapidly rotating atomic gases. *Advances in Physics* **57,** 539–616. https://doi.org/10.1080/00018730802564122 (2008) (cit. on p. 5).

83. Fetter, A. L. Rotating trapped Bose-Einstein condensates. *Rev. Mod. Phys.* **81,** 647–691. https://link.aps.org/doi/10.1103/RevModPhys.81.647 (2 2009) (cit. on p. 5).

84. Lin, Y.-J., Compton, R. L., Jimenez-Garcia, K, Porto, J. V. & Spielman, I. B. Synthetic magnetic fields for ultracold neutral atoms. *Nature* **462,** 628–632 (2009) (cit. on p. 5).

85. Cooper, N. R. Optical Flux Lattices for Ultracold Atomic Gases. *Phys. Rev. Lett.* **106,** 175301. https://link.aps.org/doi/10.1103/PhysRevLett.106.175301 (17 2011) (cit. on p. 5).

86. Cooper, N. R. & Dalibard, J. Optical flux lattices for two-photon dressed states. *Europhysics Letters* **95,** 66004. https://doi.org/10.1209/0295-5075/95/66004 (2011) (cit. on p. 5).

87. Juzeliūnas, G & Spielman, I. B. Flux lattices reformulated. *New Journal of Physics* **14,** 123022. https://doi.org/10.1088/1367-2630/14/12/123022 (2012) (cit. on p. 5).

88. Cooper, N. R. & Moessner, R. Designing Topological Bands in Reciprocal Space. *Phys. Rev. Lett.* **109,** 215302. https://link.aps.org/doi/10.1103/PhysRevLett.109.215302 (21 2012) (cit. on p. 6).

89. Boada, O., Celi, A., Latorre, J. I. & Lewenstein, M. Quantum Simulation of an Extra Dimension. *Phys. Rev. Lett.* **108,** 133001. https://link.aps.org/doi/10.1103/PhysRevLett.108.133001 (13 2012) (cit. on p. 6).

90. Celi, A., Massignan, P., Ruseckas, J., Goldman, N., Spielman, I. B., Juzeliūnas, G. & Lewenstein, M. Synthetic Gauge Fields in Synthetic Dimensions. *Phys. Rev. Lett.* **112,** 043001. https://link.aps.org/doi/10.1103/PhysRevLett.112.043001 (4 2014) (cit. on p. 6).

91. Ozawa, T. & Price, H. M. Topological quantum matter in synthetic dimensions. *Nature Reviews Physics* **1,** 349–357 (2019) (cit. on pp. 6, 38, 91, 109).

92. Mancini, M., Pagano, G., Cappellini, G., Livi, L., Rider, M., Catani, J., Sias, C., Zoller, P., Inguscio, M., Dalmonte, M. & Fallani, L. Observation of chiral edge states with neutral fermions in synthetic Hall ribbons. *Science* **349,** 1510–1513 (2015) (cit. on pp. 6, 74, 80, 91, 97).

93. Stuhl, B. K., Lu, H.-I., Aycock, L. M., Genkina, D. & Spielman, I. B. Visualizing edge states with an atomic Bose gas in the quantum Hall regime. *Science* **349,** 1514–1518 (2015) (cit. on pp. 6, 74, 80, 91, 97).

94. Genkina, D., Aycock, L. M., Lu, H.-I., Lu, M., Pineiro, A. M. & Spielman, I. Imaging topology of Hofstadter ribbons. *New journal of physics* **21,** 053021. https://iopscience.iop.org/article/10.1088/1367-2630/ab165b (2019) (cit. on pp. 6, 91, 97).

95. Chalopin, T., Satoor, T., Evrard, A., Makhalov, V., Dalibard, J., Lopes, R. & Nascimbene, S. Probing chiral edge dynamics and bulk topology of a synthetic Hall system. *Nature Physics,* 1–5. https://www.nature.com/articles/s41567-020-0942-5 (2020) (cit. on pp. 6, 91, 97).

96. An, F. A., Meier, E. J. & Gadway, B. Direct observation of chiral currents and magnetic reflection in atomic flux lattices. *Sci. Adv.* **3.** http://advances.sciencemag.org/content/3/4/e1602685 (2017) (cit. on pp. 6, 74, 91, 97).

97. An, F. A., Meier, E. J. & Gadway, B. Engineering a Flux-Dependent Mobility Edge in Disordered Zigzag Chains. *Phys. Rev. X* **8,** 031045. https://link.aps.org/doi/10.1103/PhysRevX.8.031045 (3 2018) (cit. on p. 6).

98. An, F. A., Sundar, B., Hou, J., Luo, X.-W., Meier, E. J., Zhang, C., Hazzard, K. R. & Gadway, B. Nonlinear dynamics in a synthetic momentum state lattice. *arXiv preprint arXiv:2105.04429*. https://arxiv.org/abs/2105.04429 (2021) (cit. on p. 6).

99. Thouless, D. J. Quantization of particle transport. *Phys. Rev. B* **27,** 6083–6087. https://link.aps.org/doi/10.1103/PhysRevB.27.6083 (10 1983) (cit. on p. 6).

100. Wang, L., Troyer, M. & Dai, X. Topological Charge Pumping in a One-Dimensional Optical Lattice. *Phys. Rev. Lett.* **111,** 026802. https://link.aps.org/doi/10.1103/PhysRevLett.111.026802 (2 2013) (cit. on p. 6).

101. Lohse, M., Schweizer, C., Zilberberg, O., Aidelsburger, M. & Bloch, I. A Thouless quantum pump with ultracold bosonic atoms in an optical superlattice. *Nat. Phys.* **12,** 350–354. https://www.nature.com/articles/nphys3584 (2016) (cit. on p. 6).

102. Nakajima, S., Tomita, T., Taie, S., Ichinose, T., Ozawa, H., Wang, L., Troyer, M. & Takahashi, Y. Topological Thouless pumping of ultracold fermions. *Nat. Phys.* **12,** 296–300. https://www.nature.com/articles/nphys3622 (2016) (cit. on p. 6).

103. Schweizer, C., Lohse, M., Citro, R. & Bloch, I. Spin Pumping and Measurement of Spin Currents in Optical Superlattices. *Phys. Rev. Lett.* **117,** 170405. https://link.aps.org/doi/10.1103/PhysRevLett.117.170405 (17 2016) (cit. on p. 6).

104. Lu, H.-I, Schemmer, M., Aycock, L. M., Genkina, D., Sugawa, S. & Spielman, I. B. Geometrical Pumping with a Bose-Einstein Condensate. *Phys. Rev. Lett.* **116,** 200402. https://link.aps.org/doi/10.1103/PhysRevLett.116.200402 (20 2016) (cit. on p. 6).

105. Lohse, M., Schweizer, C., Price, H. M., Zilberberg, O. & Bloch, I. Exploring 4D quantum Hall physics with a 2D topological charge pump. *Nature* **553,** 55–58. https://www.nature.com/articles/nature25000 (2018) (cit. on p. 6).

106. Bukov, M., D'Alessio, L. & Polkovnikov, A. Universal high-frequency behavior of periodically driven systems: from dynamical stabilization to Floquet engineering. *Advances in Physics* **64,** 139–226. https://doi.org/10.1080/00018732.2015.1055918 (2015) (cit. on p. 6).

107. Hauke, P., Tieleman, O., Celi, A., Ölschläger, C., Simonet, J., Struck, J., Weinberg, M., Windpassinger, P., Sengstock, K., Lewenstein, M. & Eckardt, A. Non-Abelian Gauge Fields and Topological Insulators in Shaken Optical Lattices. *Phys. Rev. Lett.* **109,** 145301. https://link.aps.org/doi/10.1103/PhysRevLett.109.145301 (14 2012) (cit. on p. 6).

108. Struck, J., Ölschläger, C., Weinberg, M., Hauke, P., Simonet, J., Eckardt, A., Lewenstein, M., Sengstock, K. & Windpassinger, P. Tunable Gauge Potential for Neutral and Spinless Particles in Driven Optical Lattices. *Phys. Rev. Lett.* **108,** 225304. https://link.aps.org/doi/10.1103/PhysRevLett.108.225304 (22 2012) (cit. on pp. 6, 74).

109. Struck, J., Weinberg, M., Ölschläger, C., Windpassinger, P., Simonet, J., Sengstock, K., Höppner, R., Hauke, P., Eckardt, A., Lewenstein, M., *et al.* Engineering Ising-XY spin-models in a triangular lattice using tunable artificial gauge fields. *Nature Physics* **9,** 738–743 (2013) (cit. on p. 6).

110. Oka, T. & Aoki, H. Photovoltaic Hall effect in graphene. *Phys. Rev. B* **79,** 081406. https://link.aps.org/doi/10.1103/PhysRevB.79.081406 (8 2009) (cit. on p. 6).

111. Haldane, F. D. M. Model for a Quantum Hall Effect without Landau Levels: Condensed-Matter Realization of the "Parity Anomaly". *Phys. Rev. Lett.* **61,** 2015–2018. https://link.aps.org/doi/10.1103/PhysRevLett.61.2015 (18 1988) (cit. on p. 6).

112. Jotzu, G., Messer, M., Desbuquois, R., Lebrat, M., Uehlinger, T., Greif, D. & Esslinger, T. Experimental realization of the topological Haldane model with ultracold fermions. *Nature* **515,** 237–240. https://www.nature.com/articles/nature13915 (2014) (cit. on pp. 6, 29, 68, 91).

113. Tarnowski, M., Ünal, F. N., Fläschner, N., Rem, B. S., Eckardt, A., Sengstock, K. & Weitenberg, C. Measuring topology from dynamics by obtaining the Chern number from a linking number. *Nature communications* **10,** 1–13. https://doi.org/10.1038/s41467-019-09668-y (2019) (cit. on pp. 6, 29, 91).

114. Asteria, L., Tran, D. T., Ozawa, T., Tarnowski, M., Rem, B. S., Fläschner, N., Sengstock, K., Goldman, N. & Weitenberg, C. Measuring quantized circular dichroism in ultracold topological matter. *Nature physics* **15,** 449–454. https://www.nature.com/articles/s41567-019-0417-8 (2019) (cit. on pp. 6, 29, 91).

115. Jaksch, D & Zoller, P. Creation of effective magnetic fields in optical lattices: the Hofstadter butterfly for cold neutral atoms. *New J. Phys.* **5,** 56. http://stacks.iop.org/1367-2630/5/i=1/a=356 (2003) (cit. on pp. 6, 42).

116. Gerbier, F. & Dalibard, J. Gauge fields for ultracold atoms in optical superlattices. *New J. Phys.* **12,** 033007. http://stacks.iop.org/1367-2630/12/i=3/a=033007 (2010) (cit. on pp. 6, 42).

117. Kolovsky, A. R. Creating artificial magnetic fields for cold atoms by photon-assisted tunneling. *Europhys. Lett.* **93,** 20003. http://stacks.iop.org/0295-5075/93/i=2/a=20003 (2011) (cit. on pp. 6, 44).

118. Harper, P. G. Single Band Motion of Conduction Electrons in a Uniform Magnetic Field. *Proceedings of the Physical Society. Section A* **68,** 874. http://stacks.iop.org/0370-1298/68/i=10/a=304 (1955) (cit. on pp. 6, 21, 22, 91).

119. Hofstadter, D. R. Energy levels and wave functions of Bloch electrons in rational and irrational magnetic fields. *Phys. Rev. B* **14,** 2239–2249. https://link.aps.org/doi/10.1103/PhysRevB.14.2239 (6 1976) (cit. on pp. 6, 21, 22, 91).

120. Miyake, H., Siviloglou, G. A., Kennedy, C. J., Burton, W. C. & Ketterle, W. Realizing the Harper Hamiltonian with Laser-Assisted Tunneling in Optical Lattices. *Phys. Rev. Lett.* **111,** 185302. https://link.aps.org/doi/10.1103/PhysRevLett.111.185302 (18 2013) (cit. on pp. 6, 29, 44, 54, 92).

121. Aidelsburger, M., Atala, M., Lohse, M., Barreiro, J. T., Paredes, B. & Bloch, I. Realization of the Hofstadter Hamiltonian with Ultracold Atoms in Optical Lattices. *Phys. Rev. Lett.* **111,** 185301. https://link.aps.org/doi/10.1103/PhysRevLett.111.185301 (18 2013) (cit. on pp. 6, 29, 44, 54, 92).

122. Atala, M. *Measuring topological invariants and chiral Meissner currents with ultracold bosonic atoms* (2014). http://nbn-resolving.de/urn:nbn:de:bvb:19-177350 (cit. on pp. 6, 20, 44, 74, 77–80, 91, 92, 95).

123. Kennedy, C. J., Burton, W. C., Chung, W. C. & Ketterle, W. Observation of Bose-Einstein condensation in a strong synthetic magnetic field. *Nature Physics* **11,** 859–864. https://www.nature.com/articles/nphys3421?cacheBust=1507839649762 (2015) (cit. on pp. 6, 54, 74).

124. Aidelsburger, M., Lohse, M., Schweizer, C, Atala, M., Barreiro, J. T., Nascimbene, S, Cooper, N., Bloch, I. & Goldman, N. Measuring the Chern number of Hofstadter bands with ultracold bosonic atoms. *Nat. Phys.* https://www.nature.com/articles/nphys3171 (2015) (cit. on pp. 6, 29, 44, 54, 63, 71, 73, 91, 92).

125. Tai, M. E., Lukin, A., Rispoli, M., Schittko, R., Menke, T., Borgnia, D., Preiss, P. M., Grusdt, F., Kaufman, A. M. & Greiner, M. Microscopy of the interacting Harper–Hofstadter model in the two-body limit. *Nature* **546,** 519–523. https://www.nature.com/articles/nature22811 (2017) (cit. on pp. 6, 44, 54, 74, 91, 92, 97, 106).

126. Eckardt, A., Weiss, C. & Holthaus, M. Superfluid-Insulator Transition in a Periodically Driven Optical Lattice. *Phys. Rev. Lett.* **95,** 260404. https://link.aps.org/doi/10.1103/PhysRevLett.95.260404 (26 2005) (cit. on p. 7).

127. Zenesini, A., Lignier, H., Ciampini, D., Morsch, O. & Arimondo, E. Coherent Control of Dressed Matter Waves. *Phys. Rev. Lett.* **102,** 100403. https://link.aps.org/doi/10.1103/PhysRevLett.102.100403 (10 2009) (cit. on p. 7).

128. Clark, L. W., Anderson, B. M., Feng, L., Gaj, A., Levin, K. & Chin, C. Observation of Density-Dependent Gauge Fields in a Bose-Einstein Condensate Based on Micromotion Control in a Shaken Two-Dimensional Lattice. *Phys. Rev. Lett.* **121,** 030402. https://link.aps.org/doi/10.1103/PhysRevLett.121.030402 (3 2018) (cit. on p. 7).

129. Görg, F., Sandholzer, K., Minguzzi, J., Desbuquois, R., Messer, M. & Esslinger, T. Realization of density-dependent Peierls phases to engineer quantized gauge fields coupled to ultracold matter. *Nature Physics* **15,** 1161–1167. https://www.nature.com/articles/s41567-019-0615-4 (2019) (cit. on p. 7).

130. Schweizer, C., Grusdt, F., Berngruber, M., Barbiero, L., Demler, E., Goldman, N., Bloch, I. & Aidelsburger, M. Floquet approach to Z2 lattice gauge theories with ultracold atoms in optical lattices. *Nature Physics* **15,** 1168–1173. https://www.nature.com/articles/s41567-019-0649-7 (2019) (cit. on p. 7).

131. Mil, A., Zache, T. V., Hegde, A., Xia, A., Bhatt, R. P., Oberthaler, M. K., Hauke, P., Berges, J. & Jendrzejewski, F. A scalable realization of local U(1) gauge invariance in cold atomic mixtures. *Science* **367,** 1128–1130. ISSN: 0036-8075. https://science.sciencemag.org/content/367/6482/1128 (2020) (cit. on p. 7).

132. Aidelsburger, M., Barbiero, L., Bermudez, A., Chanda, T., Dauphin, A., González-Cuadra, D., Grzybowski, P. R., Hands, S., Jendrzejewski, F., Jünemann, J., *et al.* Cold atoms meet lattice gauge theory. *arXiv preprint arXiv:2106.03063.* https://arxiv.org/abs/2106.03063 (2021) (cit. on p. 7).

133. BERGHOLTZ, E. J. & LIU, Z. TOPOLOGICAL FLAT BAND MODELS AND FRACTIONAL CHERN INSULATORS. *International Journal of Modern Physics B* **27,** 1330017. https://doi.org/10.1142/S021797921330017X (2013) (cit. on pp. 7, 91).

134. Parameswaran, S. A., Roy, R. & Sondhi, S. L. Fractional quantum Hall physics in topological flat bands. *Comptes Rendus Physique* **14.** Topological insulators / Isolants topologiques, 816–839. ISSN: 1631-0705. https://www.sciencedirect.com/science/article/pii/S163107051300073X (2013) (cit. on pp. 7, 91).

135. Anandan, J. The geometric phase. *Nature* **360,** 307–313. https://www.nature.com/articles/360307a0 (1992) (cit. on pp. 9, 14, 16).

136. Wilczek, F. & Shapere, A. *Geometric phases in physics* https://www.worldscientific.com/worldscibooks/10.1142/0613 (World Scientific, 1989) (cit. on pp. 9, 13).

137. Xiao, D., Chang, M.-C. & Niu, Q. Berry phase effects on electronic properties. *Rev. Mod. Phys.* **82,** 1959–2007. https://link.aps.org/doi/10.1103/RevModPhys.82.1959 (3 2010) (cit. on pp. 10–12, 18–20).

138. Resta, R. The insulating state of matter: a geometrical theory. *The European Physical Journal B* **79,** 121–137. https://link.springer.com/article/10.1140/epjb/e2010-10874-4#Abs1 (2011) (cit. on pp. 11, 13, 14).

139. Wilczek, F. & Zee, A. Appearance of Gauge Structure in Simple Dynamical Systems. *Phys. Rev. Lett.* **52,** 2111–2114. https://link.aps.org/doi/10.1103/PhysRevLett.52.2111 (24 1984) (cit. on p. 13).

140. Aharonov, Y. & Anandan, J. Phase change during a cyclic quantum evolution. *Phys. Rev. Lett.* **58,** 1593–1596. https://link.aps.org/doi/10.1103/PhysRevLett.58.1593 (16 1987) (cit. on p. 13).

141. Anandan, J. & Aharonov, Y. Geometric quantum phase and angles. *Phys. Rev. D* **38,** 1863–1870. https://link.aps.org/doi/10.1103/PhysRevD.38.1863 (6 1988) (cit. on p. 13).

142. Batelaan, H. & Tonomura, A. The Aharonov–Bohm effects: Variations on a subtle theme. *Phys. Today* **62,** 38. https://physicstoday.scitation.org/doi/10.1063/1.3226854 (2009) (cit. on pp. 15, 16).

143. Ehrenberg, W & Siday, R. E. The Refractive Index in Electron Optics and the Principles of Dynamics. *Proceedings of the Physical Society. Section B* **62,** 8–21. https://doi.org/10.1088/0370-1301/62/1/303 (1949) (cit. on p. 15).

144. Aharonov, Y. & Bohm, D. Further Considerations on Electromagnetic Potentials in the Quantum Theory. *Phys. Rev.* **123,** 1511–1524. https://link.aps.org/doi/10.1103/PhysRev.123.1511 (4 1961) (cit. on p. 16).

145. Aharonov, Y. & Bohm, D. Significance of Electromagnetic Potentials in the Quantum Theory. *Phys. Rev.* **115,** 485–491. https://link.aps.org/doi/10.1103/PhysRev.115.485 (3 1959) (cit. on p. 16).

146. Chambers, R. G. Shift of an Electron Interference Pattern by Enclosed Magnetic Flux. *Phys. Rev. Lett.* **5,** 3–5. https://link.aps.org/doi/10.1103/PhysRevLett.5.3 (1 1960) (cit. on p. 16).

147. Tonomura, A., Osakabe, N., Matsuda, T., Kawasaki, T., Endo, J., Yano, S. & Yamada, H. Evidence for Aharonov-Bohm effect with magnetic field completely shielded from electron wave. *Phys. Rev. Lett.* **56,** 792–795. https://link.aps.org/doi/10.1103/PhysRevLett.56.792 (8 1986) (cit. on p. 16).

148. Sakurai, J. J. & Napolitano, J. Modern quantum mechanics, 145 (2011) (cit. on p. 17).

149. Zak, J. Berry's phase for energy bands in solids. *Phys. Rev. Lett.* **62,** 2747–2750. https://link.aps.org/doi/10.1103/PhysRevLett.62.2747 (23 1989) (cit. on p. 20).

150. Roberts, B. W. *Time Reversal* Prepared for the Routledge Handbook of Philosophy of Physics, Eleanor Knox and Alistair Wilson (Eds). 2019. http://philsci-archive.pitt.edu/15033/ (cit. on p. 20).

151. Krutitsky, K. V. Ultracold bosons with short-range interaction in regular optical lattices. *Physics Reports* **607.** Ultracold bosons with short-range interaction in regular optical lattices, 1–101. ISSN: 0370-1573. https://www.sciencedirect.com/science/article/pii/S0370157315004366 (2016) (cit. on p. 21).

152. Peierls, R. Zur Theorie des Diamagnetismus von Leitungselektronen. *Zeitschrift fur Physik* **80,** 763–791 (Nov. 1933) (cit. on p. 21).

153. Wannier, G. H. Dynamics of Band Electrons in Electric and Magnetic Fields. *Rev. Mod. Phys.* **34,** 645–655. https://link.aps.org/doi/10.1103/RevModPhys.34.645 (4 1962) (cit. on p. 21).

154. Bernevig, B. A. & Hughes, T. L. *Topological insulators and topological superconductors* (Princeton University Press, 2013) (cit. on p. 23).

155. Aidelsburger, M. *Artificial gauge fields with ultracold atoms in optical lattices* https://www.springer.com/gp/book/9783319258270 (Springer, 2016) (cit. on pp. 23, 28, 55, 57).

156. Satija, I. I. *Butterfly in the Quantum World* ISBN: 978-1-6817-4117-8. http://dx.doi.org/10.1088/978-1-6817-4117-8 (Morgan and Claypool Publishers, 2016) (cit. on p. 26).

157. MacDonald, A. H. Landau-level subband structure of electrons on a square lattice. *Phys. Rev. B* **28,** 6713–6717. https://link.aps.org/doi/10.1103/PhysRevB.28.6713 (12 1983) (cit. on p. 28).

158. Fukui, T., Hatsugai, Y. & Suzuki, H. Chern numbers in discretized Brillouin zone: efficient method of computing (spin) Hall conductances. *Journal of the Physical Society of Japan* **74,** 1674–1677 (2005) (cit. on p. 28).

159. Eckardt, A. & Anisimovas, E. High-frequency approximation for periodically driven quantum systems from a Floquet-space perspective. *New Journal of Physics* **17,** 093039. http://stacks.iop.org/1367-2630/17/i=9/a=093039 (2015) (cit. on pp. 29, 34, 37, 38).

160. Goldman, N. & Dalibard, J. Periodically Driven Quantum Systems: Effective Hamiltonians and Engineered Gauge Fields. *Phys. Rev. X* **4,** 031027. https://link.aps.org/doi/10.1103/PhysRevX.4.031027 (3 2014) (cit. on p. 37).

161. Mueller, E. J. Artificial electromagnetism for neutral atoms: Escher staircase and Laughlin liquids. *Phys. Rev. A* **70,** 041603. https://link.aps.org/doi/10.1103/PhysRevA.70.041603 (4 2004) (cit. on p. 42).

162. Osterloh, K., Baig, M., Santos, L., Zoller, P. & Lewenstein, M. Cold Atoms in Non-Abelian Gauge Potentials: From the Hofstadter "Moth" to Lattice Gauge Theory. *Phys. Rev. Lett.* **95,** 010403. https://link.aps.org/doi/10.1103/PhysRevLett.95.010403 (1 2005) (cit. on p. 42).

163. Creffield, C. E. & Sols, F. Comment on "Creating artificial magnetic fields for cold atoms by photon-assisted tunneling" by Kolovsky A. R. *EPL (Europhysics Letters)* **101,** 40001. https://doi.org/10.1209/0295-5075/101/40001 (2013) (cit. on p. 44).

164. Bermudez, A., Schaetz, T. & Porras, D. Synthetic Gauge Fields for Vibrational Excitations of Trapped Ions. *Phys. Rev. Lett.* **107,** 150501. https://link.aps.org/doi/10.1103/PhysRevLett.107.150501 (15 2011) (cit. on p. 44).

165. Aidelsburger, M., Atala, M., Nascimbène, S., Trotzky, S., Chen, Y.-A. & Bloch, I. Experimental Realization of Strong Effective Magnetic Fields in an Optical Lattice. *Phys. Rev. Lett.* **107,** 255301. https://link.aps.org/doi/10.1103/PhysRevLett.107.255301 (25 2011) (cit. on p. 44).

166. Wang, B., Ünal, F. N. & Eckardt, A. Floquet Engineering of Optical Solenoids and Quantized Charge Pumping along Tailored Paths in Two-Dimensional Chern Insulators. *Phys. Rev. Lett.* **120,** 243602. https://link.aps.org/doi/10.1103/PhysRevLett.120.243602 (24 2018) (cit. on pp. 45, 74, 105).

167. Yoshioka, D. *The Quantum Hall Effect* https://link.springer.com/book/10.1007%2F978-3-662-05016-3#toc (Springer, Berlin, 2002) (cit. on pp. 46, 47).

168. Jeanneret, B., Hall, B. D., Bühlmann, H.-J., Houdré, R., Ilegems, M., Jeckelmann, B. & Feller, U. Observation of the integer quantum Hall effect by magnetic coupling to a Corbino ring. *Phys. Rev. B* **51,** 9752–9756. https://link.aps.org/doi/10.1103/PhysRevB.51.9752 (15 1995) (cit. on p. 47).

169. Liu, Z., Bhatt, R. N. & Regnault, N. Characterization of quasiholes in fractional Chern insulators. *Phys. Rev. B* **91,** 045126. https://link.aps.org/doi/10.1103/PhysRevB.91.045126 (4 2015) (cit. on pp. 52, 99).

170. Bilitewski, T. & Cooper, N. R. Population dynamics in a Floquet realization of the Harper-Hofstadter Hamiltonian. *Phys. Rev. A* **91,** 063611. https://link.aps.org/doi/10.1103/PhysRevA.91.063611 (6 2015) (cit. on p. 67).

171. Lin, Y.-J., Compton, R. L., Jimenez-Garcia, K., Phillips, W. D., Porto, J. V. & Spielman, I. B. A synthetic electric force acting on neutral atoms. *Nature Physics* **7,** 531. https://www.nature.com/articles/nphys1954 (2011) (cit. on p. 74).

172. Beeler, M. C., Williams, R. A., Jimenez-Garcia, K., LeBlanc, L. J., Perry, A. R. & Spielman, I. B. The spin Hall effect in a quantum gas. *Nature* **498,** 201. https://www.nature.com/articles/nature12185 (2013) (cit. on p. 74).

173. LeBlanc, L. J., Jiménez-García, K, Williams, R. A., Beeler, M. C., Phillips, W. D. & Spielman, I. B. Gauge matters: Observing the vortex-nucleation transition in a Bose condensate. *New Journal of Physics* **17,** 065016. http://stacks.iop.org/1367-2630/17/i=6/a=065016 (2015) (cit. on p. 74).

174. Möller, G. & Cooper, N. R. Condensed ground states of frustrated Bose-Hubbard models. *Phys. Rev. A* **82,** 063625. https://link.aps.org/doi/10.1103/PhysRevA.82.063625 (6 2010) (cit. on p. 74).

175. Račiūnas, M., Ünal, F. N., Anisimovas, E. & Eckardt, A. Creating, probing, and manipulating fractionally charged excitations of fractional Chern insulators in optical lattices. *Phys. Rev. A* **98,** 063621. https://link.aps.org/doi/10.1103/PhysRevA.98.063621 (6 2018) (cit. on pp. 74, 91, 93, 99, 102, 105).

176. Wang, B., Dong, X.-Y. & Eckardt, A. Measurable signatures of bosonic fractional Chern insulator states and their fractional excitations in a quantum-gas microscope. *arXiv:2111.01110.* https://arxiv.org/abs/2111.01110 (2021) (cit. on p. 74).

177. Yılmaz, F & Oktel, M. Artificial magnetic-field quenches in synthetic dimensions. *Phys. Rev. A* **97,** 023612. https://link.aps.org/doi/10.1103/PhysRevA.97.023612 (2 2018) (cit. on p. 74).

178. Lelas, K., Čelan, O., Prelogović, D., Buljan, H. & Jukić, D. Modulation instability in the nonlinear Schrödinger equation with a synthetic magnetic field: Gauge matters. *Phys. Rev. A* **103,** 013309. https://link.aps.org/doi/10.1103/PhysRevA.103.013309 (1 2021) (cit. on p. 74).

179. Yamamoto, R., Kobayashi, J., Kuno, T., Kato, K. & Takahashi, Y. An ytterbium quantum gas microscope with narrow-line laser cooling. *New J. Phys.* **18,** 023016. http://stacks.iop.org/1367-2630/18/i=2/a=023016 (2016) (cit. on p. 74).

180. Zupancic, P., Preiss, P. M., Ma, R., Lukin, A., Tai, M. E., Rispoli, M., Islam, R. & Greiner, M. Ultra-precise holographic beam shaping for microscopic quantum control. *Opt. Express* **24,** 13881–13893. http://www.opticsexpress.org/abstract.cfm?URI=oe-24-13-13881 (2016) (cit. on p. 74).

181. Cocchi, E., Miller, L. A., Drewes, J. H., Koschorreck, M., Pertot, D., Brennecke, F. & Köhl, M. Equation of State of the Two-Dimensional Hubbard Model. *Phys. Rev. Lett.* **116,** 175301. https://link.aps.org/doi/10.1103/PhysRevLett.116.175301 (17 2016) (cit. on p. 74).

182. Drewes, J. H., Miller, L. A., Cocchi, E., Chan, C. F., Wurz, N., Gall, M., Pertot, D., Brennecke, F. & Köhl, M. Antiferromagnetic Correlations in Two-Dimensional Fermionic Mott-Insulating and Metallic Phases. *Phys. Rev. Lett.* **118,** 170401. https://link.aps.org/doi/10.1103/PhysRevLett.118.170401 (17 2017) (cit. on p. 74).

183. Livi, L. F., Cappellini, G., Diem, M., Franchi, L., Clivati, C., Frittelli, M., Levi, F., Calonico, D., Catani, J., Inguscio, M. & Fallani, L. Synthetic Dimensions and Spin-Orbit Coupling with an Optical Clock Transition. *Phys. Rev. Lett.* **117,** 220401. https://link.aps.org/doi/10.1103/PhysRevLett.117.220401 (22 2016) (cit. on pp. 74, 91, 97).

184. Orignac, E. & Giamarchi, T. Meissner effect in a bosonic ladder. *Phys. Rev. B* **64,** 144515. https://link.aps.org/doi/10.1103/PhysRevB.64.144515 (14 2001) (cit. on p. 74).

185. Granato, E. Field-induced superconductor-to-insulator transition in Josephson-junction ladders. *Phys. Rev. B* **72,** 104521. https://link.aps.org/doi/10.1103/PhysRevB.72.104521 (10 2005) (cit. on p. 74).

186. Dhar, A., Maji, M., Mishra, T., Pai, R. V., Mukerjee, S. & Paramekanti, A. Bose-Hubbard model in a strong effective magnetic field: Emergence of a chiral Mott insulator ground state. *Phys. Rev. A* **85,** 041602. https://link.aps.org/doi/10.1103/PhysRevA.85.041602 (4 2012) (cit. on pp. 74, 86).

187. Dhar, A., Mishra, T., Maji, M., Pai, R. V., Mukerjee, S. & Paramekanti, A. Chiral Mott insulator with staggered loop currents in the fully frustrated Bose-Hubbard model. *Phys. Rev. B* **87,** 174501. https://link.aps.org/doi/10.1103/PhysRevB.87.174501 (17 2013) (cit. on p. 74).

188. Petrescu, A. & Le Hur, K. Bosonic Mott Insulator with Meissner Currents. *Phys. Rev. Lett.* **111,** 150601. https://link.aps.org/doi/10.1103/PhysRevLett.111.150601 (15 2013) (cit. on p. 74).

189. Hügel, D. & Paredes, B. Chiral ladders and the edges of quantum Hall insulators. *Phys. Rev. A* **89,** 023619. https://link.aps.org/doi/10.1103/PhysRevA.89.023619 (2 2014) (cit. on pp. 74, 77).

190. Greschner, S., Piraud, M., Heidrich-Meisner, F., McCulloch, I. P., Schollwöck, U. & Vekua, T. Spontaneous Increase of Magnetic Flux and Chiral-Current Reversal in Bosonic Ladders: Swimming against the Tide. *Phys. Rev. Lett.* **115,** 190402. https://link.aps.org/doi/10.1103/PhysRevLett.115.190402 (19 2015) (cit. on pp. 74, 89).

191. Bilitewski, T. & Cooper, N. R. Synthetic dimensions in the strong-coupling limit: Supersolids and pair superfluids. *Phys. Rev. A* **94,** 023630. https://link.aps.org/doi/10.1103/PhysRevA.94.023630 (2 2016) (cit. on p. 74).

192. Greschner, S., Piraud, M., Heidrich-Meisner, F., McCulloch, I. P., Schollwöck, U. & Vekua, T. Symmetry-broken states in a system of interacting bosons on a two-leg ladder with a uniform Abelian gauge field. *Phys. Rev. A* **94,** 063628. https://link.aps.org/doi/10.1103/PhysRevA.94.063628 (6 2016) (cit. on pp. 74, 77, 86, 87, 89).

193. Buser, M., Hubig, C., Schollwöck, U., Tarruell, L. & Heidrich-Meisner, F. Interacting bosonic flux ladders with a synthetic dimension: Ground-state phases and quantum quench dynamics. *Phys. Rev. A* **102,** 053314. https://link.aps.org/doi/10.1103/PhysRevA.102.053314 (5 2020) (cit. on pp. 74, 89).

194. Wei, R. & Mueller, E. J. Theory of bosons in two-leg ladders with large magnetic fields. *Phys. Rev. A* **89,** 063617. https://link.aps.org/doi/10.1103/PhysRevA.89.063617 (6 2014) (cit. on pp. 74, 78, 89, 111).

195. Uchino, S. & Tokuno, A. Population-imbalance instability in a Bose-Hubbard ladder in the presence of a magnetic flux. *Phys. Rev. A* **92,** 013625. https://link.aps.org/doi/10.1103/PhysRevA.92.013625 (1 2015) (cit. on pp. 74, 89).

196. Uchino, S. Analytical approach to a bosonic ladder subject to a magnetic field. *Phys. Rev. A* **93,** 053629. https://link.aps.org/doi/10.1103/PhysRevA.93.053629 (5 2016) (cit. on pp. 74, 89).

197. Piraud, M., Heidrich-Meisner, F., McCulloch, I. P., Greschner, S., Vekua, T. & Schollwöck, U. Vortex and Meissner phases of strongly interacting bosons on a two-leg ladder. *Phys. Rev. B* **91,** 140406. https://link.aps.org/doi/10.1103/PhysRevB.91.140406 (14 2015) (cit. on pp. 74, 89).

198. Tokuno, A. & Georges, A. Ground states of a Bose-Hubbard ladder in an artificial magnetic field: field-theoretical approach. *New Journal of Physics* **16,** 073005. https://doi.org/10.1088%2F1367-2630%2F16%2F7%2F073005 (2014) (cit. on p. 74).

199. Keleş, A. & Oktel, M. Mott transition in a two-leg Bose-Hubbard ladder under an artificial magnetic field. *Phys. Rev. A* **91,** 013629. https://link.aps.org/doi/10.1103/PhysRevA.91.013629 (1 2015) (cit. on p. 74).

200. Di Dio, M, Citro, R, De Palo, S, Orignac, E & Chiofalo, M.-L. Meissner to vortex phase transition in a two-leg ladder in artificial gauge field. *The European Physical Journal Special Topics* **224,** 525–531. https://link.springer.com/article/10.1140%2Fepjst%2Fe2015-02382-2#citeas (2015) (cit. on p. 74).

201. Di Dio, M., De Palo, S., Orignac, E., Citro, R. & Chiofalo, M.-L. Persisting Meissner state and incommensurate phases of hard-core boson ladders in a flux. *Phys. Rev. B* **92,** 060506. https://link.aps.org/doi/10.1103/PhysRevB.92.060506 (6 2015) (cit. on p. 74).

202. Natu, S. S. Bosons with long-range interactions on two-leg ladders in artificial magnetic fields. *Phys. Rev. A* **92,** 053623. https://link.aps.org/doi/10.1103/PhysRevA.92.053623 (5 2015) (cit. on p. 74).

203. Orignac, E, Citro, R, Dio, M. D., Palo, S. D. & Chiofalo, M.-L. Incommensurate phases of a bosonic two-leg ladder under a flux. *New Journal of Physics* **18,** 055017. https://doi.org/10.1088%2F1367-2630%2F18%2F5%2F055017 (2016) (cit. on p. 74).

204. Orignac, E., Citro, R., Di Dio, M. & De Palo, S. Vortex lattice melting in a boson ladder in an artificial gauge field. *Phys. Rev. B* **96,** 014518. https://link.aps.org/doi/10.1103/PhysRevB.96.014518 (1 2017) (cit. on p. 74).

205. Sachdeva, R., Singh, M. & Busch, T. Extended Bose-Hubbard model for two-leg ladder systems in artificial magnetic fields. *Phys. Rev. A* **95,** 063601. https://link.aps.org/doi/10.1103/PhysRevA.95.063601 (6 2017) (cit. on p. 74).

206. Citro, R., De Palo, S., Di Dio, M. & Orignac, E. Quantum phase transitions of a two-leg bosonic ladder in an artificial gauge field. *Phys. Rev. B* **97,** 174523. https://link.aps.org/doi/10.1103/PhysRevB.97.174523 (17 2018) (cit. on p. 74).

207. Romen, C. & Läuchli, A. M. Chiral Mott insulators in frustrated Bose-Hubbard models on ladders and two-dimensional lattices: A combined perturbative and density matrix renormalization group study. *Phys. Rev. B* **98,** 054519. https://link.aps.org/doi/10.1103/PhysRevB.98.054519 (5 2018) (cit. on p. 74).

208. Grusdt, F., Letscher, F., Hafezi, M. & Fleischhauer, M. Topological Growing of Laughlin States in Synthetic Gauge Fields. *Phys. Rev. Lett.* **113,** 155301. https://link.aps.org/doi/10.1103/PhysRevLett.113.155301 (15 2014) (cit. on pp. 74, 92, 97).

209. Petrescu, A. & Le Hur, K. Chiral Mott insulators, Meissner effect, and Laughlin states in quantum ladders. *Phys. Rev. B* **91,** 054520. https://link.aps.org/doi/10.1103/PhysRevB.91.054520 (5 2015) (cit. on p. 74).

210. Cornfeld, E. & Sela, E. Chiral currents in one-dimensional fractional quantum Hall states. *Phys. Rev. B* **92,** 115446. https://link.aps.org/doi/10.1103/PhysRevB.92.115446 (11 2015) (cit. on p. 74).

211. Greschner, S. & Vekua, T. Vortex-Hole Duality: A Unified Picture of Weak- and Strong-Coupling Regimes of Bosonic Ladders with Flux. *Phys. Rev. Lett.* **119,** 073401. https://link.aps.org/doi/10.1103/PhysRevLett.119.073401 (7 2017) (cit. on p. 74).

212. Calvanese Strinati, M., Cornfeld, E., Rossini, D., Barbarino, S., Dalmonte, M., Fazio, R., Sela, E. & Mazza, L. Laughlin-like States in Bosonic and Fermionic Atomic Synthetic Ladders. *Phys. Rev. X* **7,** 021033. https://link.aps.org/doi/10.1103/PhysRevX.7.021033 (2 2017) (cit. on p. 74).

213. Calvanese Strinati, M., Sahoo, S., Shtengel, K. & Sela, E. Pretopological fractional excitations in the two-leg flux ladder. *Phys. Rev. B* **99,** 245101. https://link.aps.org/doi/10.1103/PhysRevB.99.245101 (24 2019) (cit. on p. 74).

214. Prelovšek, P, Long, M., Markež, T & Zotos, X. Hall Constant of Strongly Correlated Electrons on a Ladder. *Phys. Rev. Lett.* **83,** 2785–2788. https://link.aps.org/doi/10.1103/PhysRevLett.83.2785 (14 1999) (cit. on p. 74).

215. Zotos, X, Naef, F, Long, M. & Prelovšek, P. Reactive Hall Response. *Phys. Rev. Lett.* **85,** 377–380. https://link.aps.org/doi/10.1103/PhysRevLett.85.377 (2 2000) (cit. on p. 74).

216. Greschner, S., Filippone, M. & Giamarchi, T. Universal Hall Response in Interacting Quantum Systems. *Phys. Rev. Lett.* **122,** 083402. https://link.aps.org/doi/10.1103/PhysRevLett.122.083402 (8 2019) (cit. on p. 74).

217. Filippone, M., Bardyn, C.-E., Greschner, S. & Giamarchi, T. Vanishing Hall Response of Charged Fermions in a Transverse Magnetic Field. *Phys. Rev. Lett.* **123,** 086803. https://link.aps.org/doi/10.1103/PhysRevLett.123.086803 (8 2019) (cit. on p. 74).

218. Buser, M., Schollwöck, U. & Grusdt, F. Snapshot based characterization of particle currents and the Hall response in synthetic flux lattices. https://arxiv.org/abs/2110.14952 (cit. on pp. 74, 95).

219. Wu, S., Qin, X., Xu, J. & Lee, C. Universal spatiotemporal dynamics of spontaneous superfluidity breakdown in the presence of synthetic gauge fields. *Phys. Rev. A* **94,** 043606. https://link.aps.org/doi/10.1103/PhysRevA.94.043606 (4 2016) (cit. on p. 74).

220. Kolovsky, A. R. Bogoliubov depletion of the fragmented condensate in the bosonic flux ladder. *Phys. Rev. A* **95,** 033622. https://link.aps.org/doi/10.1103/PhysRevA.95.033622 (3 2017) (cit. on p. 74).

221. Zheng, Y., Feng, S. & Yang, S.-J. Chiral Bloch oscillation and nontrivial topology in a ladder lattice with magnetic flux. *Phys. Rev. A* **96,** 063613. https://link.aps.org/doi/10.1103/PhysRevA.96.063613 (6 2017) (cit. on p. 74).

222. Filippone, M., Bardyn, C.-E. & Giamarchi, T. Controlled parity switch of persistent currents in quantum ladders. *Phys. Rev. B* **97,** 201408. https://link.aps.org/doi/10.1103/PhysRevB.97.201408 (20 2018) (cit. on p. 74).

223. Strinati, M. C., Gerbier, F. & Mazza, L. Spin-gap spectroscopy in a bosonic flux ladder. *New Journal of Physics* **20,** 015004. https://doi.org/10.1088%2F1367-2630%2Faa9ca2 (2018) (cit. on p. 74).

224. Kamar, N. A., Kantian, A. & Giamarchi, T. Dynamics of a Mobile Impurity in a Two Leg Bosonic Ladder. *arXiv:1901.04091.* https://arxiv.org/abs/1901.04091 (2019) (cit. on p. 74).

225. Buser, M., Heidrich-Meisner, F. & Schollwöck, U. Finite-temperature properties of interacting bosons on a two-leg flux ladder. *Phys. Rev. A* **99,** 053601. https://link.aps.org/doi/10.1103/PhysRevA.99.053601 (5 2019) (cit. on p. 74).

226. Demirplak, M. & Rice, S. A. Adiabatic Population Transfer with Control Fields. *The Journal of Physical Chemistry A* **107,** 9937–9945. https://doi.org/10.1021/jp030708a (2003) (cit. on pp. 74, 83).

227. Demirplak, M. & Rice, S. A. Assisted Adiabatic Passage Revisited. *The Journal of Physical Chemistry B* **109.** PMID: 16851769, 6838–6844. https://doi.org/10.1021/jp040647w (2005) (cit. on pp. 74, 83).

228. Berry, M. V. Transitionless quantum driving. *Journal of Physics A: Mathematical and Theoretical* **42,** 365303. https://doi.org/10.1088%2F1751-8113%2F42%2F36%2F365303 (2009) (cit. on pp. 74, 83).

229. Torrontegui, E., Ibáñez, S., Martínez-Garaot, S., Modugno, M., del Campo, A., Guéry-Odelin, D., Ruschhaupt, A., Chen, X. & Muga, J. G. in *Advances in Atomic, Molecular, and Optical Physics* (eds Arimondo, E., Berman, P. R. & Lin, C. C.) 117–169 (Academic Press, 2013). https://www.sciencedirect.com/science/article/pii/B9780124080904000025 (cit. on p. 74).

230. Guéry-Odelin, D., Ruschhaupt, A., Kiely, A., Torrontegui, E., Martínez-Garaot, S. & Muga, J. G. Shortcuts to adiabaticity: Concepts, methods, and applications. *Rev. Mod. Phys.* **91,** 045001. https://link.aps.org/doi/10.1103/RevModPhys.91.045001 (4 2019) (cit. on pp. 74, 83, 84).

231. Wang, B., Dong, X.-Y., Ünal, F. N. & Eckardt, A. Robust and ultrafast state preparation by ramping artificial gauge potentials. *New Journal of Physics* **23,** 063017. https://doi.org/10.1088/1367-2630/abf9b2 (2021) (cit. on p. 75).

232. De Andrada e Silva, E. A. Probability current in the tight-binding model. *American Journal of Physics* **60,** 753–754. https://doi.org/10.1119/1.17084 (1992) (cit. on pp. 77, 94).

233. White, S. R. Density matrix formulation for quantum renormalization groups. *Phys. Rev. Lett.* **69,** 2863–2866. https://link.aps.org/doi/10.1103/PhysRevLett.69.2863 (19 1992) (cit. on pp. 85, 92).

234. Schollwöck, U. The density-matrix renormalization group. *Rev. Mod. Phys.* **77,** 259–315. https://link.aps.org/doi/10.1103/RevModPhys.77.259 (1 2005) (cit. on pp. 85, 92).

235. Kjäll, J. A., Zaletel, M. P., Mong, R. S. K., Bardarson, J. H. & Pollmann, F. Phase diagram of the anisotropic spin-2 XXZ model: Infinite-system density matrix renormalization group study. *Phys. Rev. B* **87,** 235106. https://link.aps.org/doi/10.1103/PhysRevB.87.235106 (23 2013) (cit. on p. 85).

236. Hauschild, J. & Pollmann, F. Efficient numerical simulations with Tensor Networks: Tensor Network Python (TeNPy). *SciPost Phys. Lect. Notes,* 5. https://scipost.org/10.21468/SciPostPhysLectNotes.5 (2018) (cit. on pp. 85, 92, 93, 99, 105).

237. Zaletel, M. P., Mong, R. S. K., Karrasch, C., Moore, J. E. & Pollmann, F. Time-evolving a matrix product state with long-ranged interactions. *Phys. Rev. B* **91,** 165112. https://link.aps.org/doi/10.1103/PhysRevB.91.165112 (16 2015) (cit. on pp. 85, 92, 99, 105).

238. Gohlke, M., Verresen, R., Moessner, R. & Pollmann, F. Dynamics of the Kitaev-Heisenberg Model. *Phys. Rev. Lett.* **119,** 157203. https://link.aps.org/doi/10.1103/PhysRevLett.119.157203 (15 2017) (cit. on pp. 85, 92, 99, 105).

239. Kosterlitz, J. M. & Thouless, D. J. Ordering, metastability and phase transitions in two-dimensional systems. *Journal of Physics C: Solid State Physics* **6,** 1181–1203. https://doi.org/10.1088%2F0022-3719%2F6%2F7%2F010 (1973) (cit. on p. 86).

240. Halperin, B. I. & Jain, J. K. *Fractional Quantum Hall Effects* https://www.worldscientific.com/doi/abs/10.1142/11751 (WORLD SCIENTIFIC, 2020) (cit. on p. 91).

241. Wilczek, F. Quantum Mechanics of Fractional-Spin Particles. *Phys. Rev. Lett.* **49,** 957–959. https://link.aps.org/doi/10.1103/PhysRevLett.49.957 (14 1982) (cit. on p. 91).

242. Stern, A. Anyons and the quantum Hall effect—A pedagogical review. *Annals of Physics* **323.** January Special Issue 2008, 204–249. ISSN: 0003-4916. https://www.sciencedirect.com/science/article/pii/S0003491607001674 (2008) (cit. on p. 91).

243. Zhang, S.-L. & Zhou, Q. Manipulating novel quantum phenomena using synthetic gauge fields. *Journal of Physics B: Atomic, Molecular and Optical Physics* **50,** 222001. http://stacks.iop.org/0953-4075/50/i=22/a=222001 (2017) (cit. on p. 91).

244. Wu, Z., Zhang, L., Sun, W., Xu, X.-T., Wang, B.-Z., Ji, S.-C., Deng, Y., Chen, S., Liu, X.-J. & Pan, J.-W. Realization of two-dimensional spin-orbit coupling for Bose-Einstein condensates. *Science* **354,** 83–88. ISSN: 0036-8075. http://science.sciencemag.org/content/354/6308/83 (2016) (cit. on p. 91).

245. Mittal, S., Ganeshan, S., Fan, J., Vaezi, A. & Hafezi, M. Measurement of topological invariants in a 2D photonic system. *Nature Photonics* **10,** 180–183. https://www.nature.com/articles/nphoton.2016.10 (2016) (cit. on p. 91).

246. Sugawa, S., Salces-Carcoba, F., Perry, A. R., Yue, Y. & Spielman, I. B. Second Chern number of a quantum-simulated non-Abelian Yang monopole. *Science* **360,** 1429–1434. ISSN: 0036-8075. https://science.sciencemag.org/content/360/6396/1429 (2018) (cit. on p. 91).

247. Sun, W., Yi, C.-R., Wang, B.-Z., Zhang, W.-W., Sanders, B. C., Xu, X.-T., Wang, Z.-Y., Schmiedmayer, J., Deng, Y., Liu, X.-J., Chen, S. & Pan, J.-W. Uncover Topology by Quantum Quench Dynamics. *Phys. Rev. Lett.* **121,** 250403. https://link.aps.org/doi/10.1103/PhysRevLett.121.250403 (25 2018) (cit. on p. 91).

248. Kolkowitz, S, Bromley, S., Bothwell, T, Wall, M., Marti, G., Koller, A., Zhang, X, Rey, A. & Ye, J. Spin–orbit-coupled fermions in an optical lattice clock. *Nature* **542,** 66–70. https://www.nature.com/articles/nature20811 (2017) (cit. on pp. 91, 97).

249. Lustig, E., Weimann, S., Plotnik, Y., Lumer, Y., Bandres, M. A., Szameit, A. & Segev, M. Photonic topological insulator in synthetic dimensions. *Nature* **567,** 356–360. https://www.nature.com/articles/s41586-019-0943-7 (2019) (cit. on pp. 91, 97).

250. McDonald, M., Trisnadi, J., Yao, K.-X. & Chin, C. Superresolution Microscopy of Cold Atoms in an Optical Lattice. *Phys. Rev. X* **9,** 021001. https://link.aps.org/doi/10.1103/PhysRevX.9.021001 (2 2019) (cit. on p. 91).

251. Wang, B., Dong, X.-Y. & Eckardt, A. Measurable signatures of bosonic fractional Chern insulator states and their fractional excitations in a quantum-gas microscope. *arXiv:2111.01110* (2021) (cit. on p. 91).

252. Sørensen, A. S., Demler, E. & Lukin, M. D. Fractional Quantum Hall States of Atoms in Optical Lattices. *Phys. Rev. Lett.* **94,** 086803. https://link.aps.org/doi/10.1103/PhysRevLett.94.086803 (8 2005) (cit. on pp. 91, 93).

253. Palmer, R. N. & Jaksch, D. High-Field Fractional Quantum Hall Effect in Optical Lattices. *Phys. Rev. Lett.* **96,** 180407. https://link.aps.org/doi/10.1103/PhysRevLett.96.180407 (18 2006) (cit. on pp. 91, 93).

254. Wu, Y.-H., Jain, J. K. & Sun, K. Adiabatic continuity between Hofstadter and Chern insulator states. *Phys. Rev. B* **86,** 165129. https://link.aps.org/doi/10.1103/PhysRevB.86.165129 (16 2012) (cit. on pp. 91, 93).

255. Gerster, M., Rizzi, M., Silvi, P., Dalmonte, M. & Montangero, S. Fractional quantum Hall effect in the interacting Hofstadter model via tensor networks. *Phys. Rev. B* **96,** 195123. https://link.aps.org/doi/10.1103/PhysRevB.96.195123 (19 2017) (cit. on pp. 91, 93).

256. Niu, Q., Thouless, D. J. & Wu, Y.-S. Quantized Hall conductance as a topological invariant. *Phys. Rev. B* **31,** 3372–3377. https://link.aps.org/doi/10.1103/PhysRevB.31.3372 (6 1985) (cit. on p. 91).

257. Hafezi, M., Sørensen, A. S., Demler, E. & Lukin, M. D. Fractional quantum Hall effect in optical lattices. *Phys. Rev. A* **76,** 023613. https://link.aps.org/doi/10.1103/PhysRevA.76.023613 (2 2007) (cit. on pp. 91, 93, 109).

258. Cian, Z.-P., Dehghani, H., Elben, A., Vermersch, B., Zhu, G., Barkeshli, M., Zoller, P. & Hafezi, M. Many-Body Chern Number from Statistical Correlations of Randomized Measurements. *Phys. Rev. Lett.* **126,** 050501. https://link.aps.org/doi/10.1103/PhysRevLett.126.050501 (5 2021) (cit. on pp. 91–93, 109).

259. Sterdyniak, A., Regnault, N. & Bernevig, B. A. Extracting Excitations from Model State Entanglement. *Phys. Rev. Lett.* **106,** 100405. https://link.aps.org/doi/10.1103/PhysRevLett.106.100405 (10 2011) (cit. on p. 91).

260. Sterdyniak, A., Regnault, N. & Möller, G. Particle entanglement spectra for quantum Hall states on lattices. *Phys. Rev. B* **86,** 165314. https://link.aps.org/doi/10.1103/PhysRevB.86.165314 (16 2012) (cit. on p. 91).

261. Kjäll, J. A. & Moore, J. E. Edge excitations of bosonic fractional quantum Hall phases in optical lattices. *Phys. Rev. B* **85,** 235137. https://link.aps.org/doi/10.1103/PhysRevB.85.235137 (23 2012) (cit. on p. 91).

262. Dong, X.-Y., Grushin, A. G., Motruk, J. & Pollmann, F. Charge Excitation Dynamics in Bosonic Fractional Chern Insulators. *Phys. Rev. Lett.* **121,** 086401. https://link.aps.org/doi/10.1103/PhysRevLett.121.086401 (8 2018) (cit. on pp. 91, 93, 95).

263. Grusdt, F., Yao, N. Y., Abanin, D, Fleischhauer, M. & Demler, E. Interferometric measurements of many-body topological invariants using mobile impurities. *Nature communications* **7,** 1–9 (2016) (cit. on p. 91).

264. Motruk, J. & Pollmann, F. Phase transitions and adiabatic preparation of a fractional Chern insulator in a boson cold-atom model. *Phys. Rev. B* **96,** 165107. https://link.aps.org/doi/10.1103/PhysRevB.96.165107 (16 2017) (cit. on pp. 91–93, 97, 109).

265. He, Y.-C., Grusdt, F., Kaufman, A., Greiner, M. & Vishwanath, A. Realizing and adiabatically preparing bosonic integer and fractional quantum Hall states in optical lattices. *Phys. Rev. B* **96,** 201103. https://link.aps.org/doi/10.1103/PhysRevB.96.201103 (20 2017) (cit. on pp. 91–93, 97, 109).

266. Umucalılar, R. O., Macaluso, E., Comparin, T. & Carusotto, I. Time-of-Flight Measurements as a Possible Method to Observe Anyonic Statistics. *Phys. Rev. Lett.* **120,** 230403. https://link.aps.org/doi/10.1103/PhysRevLett.120.230403 (23 2018) (cit. on pp. 91, 93).

267. Macaluso, E., Comparin, T., Umucalılar, R. O., Gerster, M., Montangero, S., Rizzi, M. & Carusotto, I. Charge and statistics of lattice quasiholes from density measurements: A tree tensor network study. *Phys. Rev. Research* **2,** 013145. https://link.aps.org/doi/10.1103/PhysRevResearch.2.013145 (1 2020) (cit. on pp. 91, 93, 99).

268. Tran, D. T., Dauphin, A., Grushin, A. G., Zoller, P. & Goldman, N. Probing topology by heating: Quantized circular dichroism in ultracold atoms. *Science Advances* **3.** https://advances.sciencemag.org/content/3/8/e1701207 (2017) (cit. on p. 91).

269. Repellin, C. & Goldman, N. Detecting Fractional Chern Insulators through Circular Dichroism. *Phys. Rev. Lett.* **122,** 166801. https://link.aps.org/doi/10.1103/PhysRevLett.122.166801 (16 2019) (cit. on pp. 91, 93).

270. Motruk, J. & Na, I. Detecting Fractional Chern Insulators in Optical Lattices through Quantized Displacement. *Phys. Rev. Lett.* **125,** 236401. https://link.aps.org/doi/10.1103/PhysRevLett.125.236401 (23 2020) (cit. on pp. 92, 93).

271. Repellin, C., Léonard, J. & Goldman, N. Fractional Chern insulators of few bosons in a box: Hall plateaus from center-of-mass drifts and density profiles. *Phys. Rev. A* **102,** 063316. https://link.aps.org/doi/10.1103/PhysRevA.102.063316 (6 2020) (cit. on pp. 92, 93).

272. Popp, M., Paredes, B. & Cirac, J. I. Adiabatic path to fractional quantum Hall states of a few bosonic atoms. *Phys. Rev. A* **70,** 053612. https://link.aps.org/doi/10.1103/PhysRevA.70.053612 (5 2004) (cit. on p. 92).

273. Cooper, N. R. & Dalibard, J. Reaching Fractional Quantum Hall States with Optical Flux Lattices. *Phys. Rev. Lett.* **110,** 185301. https://link.aps.org/doi/10.1103/PhysRevLett.110.185301 (18 2013) (cit. on p. 92).

274. Yao, N. Y., Gorshkov, A. V., Laumann, C. R., Läuchli, A. M., Ye, J. & Lukin, M. D. Realizing Fractional Chern Insulators in Dipolar Spin Systems. *Phys. Rev. Lett.* **110,** 185302. https://link.aps.org/doi/10.1103/PhysRevLett.110.185302 (18 2013) (cit. on p. 92).

275. Kapit, E., Hafezi, M. & Simon, S. H. Induced Self-Stabilization in Fractional Quantum Hall States of Light. *Phys. Rev. X* **4,** 031039. https://link.aps.org/doi/10.1103/PhysRevX.4.031039 (3 2014) (cit. on p. 92).

276. Barkeshli, M., Yao, N. Y. & Laumann, C. R. Continuous Preparation of a Fractional Chern Insulator. *Phys. Rev. Lett.* **115,** 026802. https://link.aps.org/doi/10.1103/PhysRevLett.115.026802 (2 2015) (cit. on p. 92).

277. Repellin, C., Yefsah, T. & Sterdyniak, A. Creating a bosonic fractional quantum Hall state by pairing fermions. *Phys. Rev. B* **96,** 161111. https://link.aps.org/doi/10.1103/PhysRevB.96.161111 (16 2017) (cit. on p. 92).

278. Hudomal, A., Regnault, N. & Vasić, I. Bosonic fractional quantum Hall states in driven optical lattices. *Phys. Rev. A* **100,** 053624. https://link.aps.org/doi/10.1103/PhysRevA.100.053624 (5 2019) (cit. on pp. 92, 109).

279. Andrade, B., Kasper, V., Lewenstein, M., Weitenberg, C. & Graß, T. Preparation of the 1/2-Laughlin state with atoms in a rotating trap. *arXiv:2009.08943.* https://arxiv.org/abs/2009.08943 (2020) (cit. on p. 92).

280. Rosson, P., Lubasch, M., Kiffner, M. & Jaksch, D. Bosonic fractional quantum Hall states on a finite cylinder. *Phys. Rev. A* **99,** 033603. https://link.aps.org/doi/10.1103/PhysRevA.99.033603 (3 2019) (cit. on p. 93).

281. Killi, M., Trotzky, S. & Paramekanti, A. Anisotropic quantum quench in the presence of frustration or background gauge fields: A probe of bulk currents and topological chiral edge modes. *Phys. Rev. A* **86,** 063632. https://link.aps.org/doi/10.1103/PhysRevA.86.063632 (6 2012) (cit. on p. 95).

282. Keßler, S. & Marquardt, F. Single-site-resolved measurement of the current statistics in optical lattices. *Phys. Rev. A* **89,** 061601. https://link.aps.org/doi/10.1103/PhysRevA.89.061601 (6 2014) (cit. on pp. 95, 109).

283. Trotzky, S., Cheinet, P., Fölling, S., Feld, M., Schnorrberger, U., Rey, A. M., Polkovnikov, A., Demler, E. A., Lukin, M. D. & Bloch, I. Time-resolved observation and control of superexchange interactions with ultracold atoms in optical lattices. *Science* **319,** 295–299. https://www.science.org/doi/abs/10.1126/science.1150841 (2008) (cit. on p. 95).

284. Trotzky, S., Chen, Y.-A., Flesch, A., McCulloch, I. P., Schollwöck, U., Eisert, J. & Bloch, I. Probing the relaxation towards equilibrium in an isolated strongly correlated one-dimensional Bose gas. *Nature physics* **8,** 325–330. https://www.nature.com/articles/nphys2232 (2012) (cit. on p. 95).

285. Nascimbene, S., Chen, Y.-A., Atala, M., Aidelsburger, M., Trotzky, S., Paredes, B. & Bloch, I. Experimental Realization of Plaquette Resonating Valence-Bond States with Ultracold Atoms in Optical Superlattices. *Phys. Rev. Lett.* **108,** 205301. https://link.aps.org/doi/10.1103/PhysRevLett.108.205301 (20 2012) (cit. on p. 95).

286. Greif, D., Uehlinger, T., Jotzu, G., Tarruell, L. & Esslinger, T. Short-range quantum magnetism of ultracold fermions in an optical lattice. *Science* **340,** 1307–1310. https://www.science.org/doi/abs/10.1126/science.1236362 (2013) (cit. on p. 95).

287. Ardila, L. A. P., Heyl, M. & Eckardt, A. Measuring the Single-Particle Density Matrix for Fermions and Hard-Core Bosons in an Optical Lattice. *Phys. Rev. Lett.* **121,** 260401. https://link.aps.org/doi/10.1103/PhysRevLett.121.260401 (26 2018) (cit. on p. 95).

288. Palm, F. A., Buser, M., Léonard, J., Aidelsburger, M., Schollwöck, U. & Grusdt, F. Bosonic Pfaffian state in the Hofstadter-Bose-Hubbard model. *Phys. Rev. B* **103,** L161101. https://link.aps.org/doi/10.1103/PhysRevB.103.L161101 (16 2021) (cit. on p. 97).

289. Rezayi, E. H. & Haldane, F. D. M. Laughlin state on stretched and squeezed cylinders and edge excitations in the quantum Hall effect. *Phys. Rev. B* **50,** 17199–17207. https://link.aps.org/doi/10.1103/PhysRevB.50.17199 (23 1994) (cit. on p. 97).

290. Seidel, A., Fu, H., Lee, D.-H., Leinaas, J. M. & Moore, J. Incompressible Quantum Liquids and New Conservation Laws. *Phys. Rev. Lett.* **95,** 266405. https://link.aps.org/doi/10.1103/PhysRevLett.95.266405 (26 2005) (cit. on p. 97).

291. Bergholtz, E. J. & Karlhede, A. Half-Filled Lowest Landau Level on a Thin Torus. *Phys. Rev. Lett.* **94,** 026802. https://link.aps.org/doi/10.1103/PhysRevLett.94.026802 (2 2005) (cit. on p. 97).

292. Bergholtz, E. J. & Karlhede, A. 'One-dimensional'theory of the quantum Hall system. *Journal of Statistical Mechanics: Theory and Experiment* **2006,** L04001. https://iopscience.iop.org/article/10.1088/1742-5468/2006/04/L04001 (2006) (cit. on p. 97).

293. Seidel, A. & Lee, D.-H. Abelian and Non-Abelian Hall Liquids and Charge-Density Wave: Quantum Number Fractionalization in One and Two Dimensions. *Phys. Rev. Lett.* **97,** 056804. https://link.aps.org/doi/10.1103/PhysRevLett.97.056804 (5 2006) (cit. on p. 97).

294. Umucalılar, R. O. Real-space probe for lattice quasiholes. *Phys. Rev. A* **98,** 063629. https://link.aps.org/doi/10.1103/PhysRevA.98.063629 (6 2018) (cit. on p. 99).

295. Jaworowski, B. d. z., Regnault, N. & Liu, Z. Characterization of quasiholes in two-component fractional quantum Hall states and fractional Chern insulators in $|C|$=2 flat bands. *Phys. Rev. B* **99,** 045136. https://link.aps.org/doi/10.1103/PhysRevB.99.045136 (4 2019) (cit. on p. 99).

296. Macaluso, E., Comparin, T., Mazza, L. & Carusotto, I. Fusion Channels of Non-Abelian Anyons from Angular-Momentum and Density-Profile Measurements. *Phys. Rev. Lett.* **123,** 266801. https://link.aps.org/doi/10.1103/PhysRevLett.123.266801 (26 2019) (cit. on p. 99).

297. Kapit, E., Ginsparg, P. & Mueller, E. Non-Abelian Braiding of Lattice Bosons. *Phys. Rev. Lett.* **108,** 066802. https://link.aps.org/doi/10.1103/PhysRevLett.108.066802 (6 2012) (cit. on p. 99).

298. Graß, T., Juliá-Díaz, B. & Lewenstein, M. Topological phases in small quantum Hall samples. *Phys. Rev. A* **89,** 013623. https://link.aps.org/doi/10.1103/PhysRevA.89.013623 (1 2014) (cit. on p. 99).

299. Nielsen, A. E., Glasser, I. & Rodríguez, I. D. Quasielectrons as inverse quasiholes in lattice fractional quantum Hall models. *New Journal of Physics* **20,** 033029. https://iopscience.iop.org/article/10.1088/1367-2630/aab5d0/meta (2018) (cit. on p. 99).

300. Srivatsa, N. S., Li, X. & Nielsen, A. E. B. Squeezing anyons for braiding on small lattices. *Phys. Rev. Research* **3,** 033044. https://link.aps.org/doi/10.1103/PhysRevResearch.3.033044 (3 2021) (cit. on p. 99).

301. Fabre, A., Bouhiron, J.-B., Satoor, T., Lopes, R. & Nascimbene, S. Laughlin's topological charge pump in an atomic Hall cylinder. https://arxiv.org/abs/2110.12971 (cit. on p. 105).

302. Andreev, A. The thermal conductivity of the intermediate state in superconductors. *Soviet Physics-JETP* **19,** 1228–1231 (1964) (cit. on p. 109).

303. Tinkham, M. *Introduction to superconductivity* (Courier Corporation, 2004) (cit. on p. 109).

304. Sandler, N. P., Chamon, C. d. C. & Fradkin, E. Andreev reflection in the fractional quantum Hall effect. *Phys. Rev. B* **57,** 12324–12332. https://link.aps.org/doi/10.1103/PhysRevB.57.12324 (19 1998) (cit. on p. 109).

305. Hashisaka, M., Jonckheere, T., Akiho, T., Sasaki, S., Rech, J., Martin, T. & Muraki, K. Andreev reflection of fractional quantum Hall quasiparticles. *Nature communications* **12,** 1–7. https://www.nature.com/articles/s41467-021-23160-6 (2021) (cit. on p. 109).

306. Rechtsman, M. C., Zeuner, J. M., Plotnik, Y., Lumer, Y., Podolsky, D., Dreisow, F., Nolte, S., Segev, M. & Szameit, A. Photonic Floquet topological insulators. *Nature* **496,** 196–200. https://www.nature.com/articles/nature12066 (2013) (cit. on p. 109).

307. Zilberberg, O. Topology in quasicrystals. *Opt. Mater. Express* **11,** 1143–1157. http://www.osapublishing.org/ome/abstract.cfm?URI=ome-11-4-1143 (2021) (cit. on p. 109).

308. Manna, S., Duncan, C. W., Weidner, C. A., Sherson, J. F. & Nielsen, A. E. Laughlin-Type Topological Order on a Fractal Lattice with a Local Hamiltonian. *arXiv:2106.13816* (2021) (cit. on p. 109).

309. Xu, X.-Y., Wang, X.-W., Chen, D.-Y., Smith, C. M. & Jin, X.-M. Quantum transport in fractal networks. *Nature Photonics* **15,** 703–710. https://www.nature.com/articles/s41566-021-00845-4 (2021) (cit. on p. 109).

310. Ueda, M. *Fundamentals and new frontiers of Bose-Einstein condensation* https://www.worldscientific.com/worldscibooks/10.1142/7216 (World Scientific, 2010) (cit. on p. 113).

Acknowledgments

First of all, I would like to express my immense gratitude to my supervisor Prof. Dr. André Eckardt. I admire all the wonderful projects that he has suggested, as well as all those insightful discussions. It has been a great pleasure and luck to be part of his group. His strong intuition and taste in interesting topics, his nice and diligent personality, together with his humour and optimism, will definitely affect me in the very long run. Meanwhile, I want to thank André for giving me also plenty of freedom, which helps me to become more and more independent. I also highly appreciated all the nice conferences that he has suggested and supported. They have been excellent opportunities not only for meeting people and broadening horizon, but also for improving my presentation skills. Last but not least, I am grateful to André for the careful reading of my dissertation. All his comments and suggestions absolutely help to largely improve the quality of this work.

I am greatly indebted to my collaborators, F. Nur Ünal and Xiaoyu Dong, without whom there would be no such a dissertation. Especially, I would like to thank Nur for co-supervising me at the initial stage of my PhD. All those fruitful discussions quickly brought me into our projects. I would like to thank Xiaoyu for introducing me the DMRG simulation, which plays an important role in my scientific research even until today. Meanwhile, I would like to express my gratitude to Egidijus Anisimovas, Mantas Račiūnas, Monika Aidelsburger, Maximilian Buser, Andrew Hayward, Julian Léonard, Fabian Heidrich-Meisner, Anne E. B. Nielsen, Frank Pollmann, Hong-Hao Tu, Xikun Li, Wei Wang, Yi-Ping Huang, Jhihshih You, Chuan Chen, Guoyi Zhu, Yanliang Guo, and Hepeng Yao for a lot of insightful discussions.

I do not want to miss this chance to thank all the great colleagues in our group. In particular, I would like to thank Prof. Dr. Roland Ketzmerick for being my official supervisor at Technische Universität Dresden during my staying at Max Planck Institute for the Physics of Complex Systems. I would like to thank Prof. Dr. Arnd Bäcker, Alexander Schnell, Daniel Vorberg, Christoph Sträter, Alexander Leymann, Ling-Na Wu, Francesco Petiziol, Tobias Becker, Manuel L. Alamo Ulloa, Martina Vlaho, Arko Roy, Swetamber Das, Sanku Paul, Konstantin Clauß, Felix Fritzsch, Isaac Liben Iskel Tesfaye, Sebastian Nagies, Wenhua Zhao, for all the wonderful time and experience that we have shared. Thank you for the various group activities, including hiking, barbecue, boat trip, bars and restaurants, as well as the lunch table conversation. All the valuable moments will never fade away with time.

I am grateful to the support from DFG Research Unit FOR 2414, and IMPRS-MPSSE hosted by MPIPKS as well. I would like to thank Monika Aidelsburger, Immanuel Bloch, Fabian Grusdt,

Fabian Heidrich-Meisner, Walter Hofstetter, Stefan Kehrein, Karyn Le Hur, Belen Paredes, Ulrich Schneider, Ulrich Schollwöck, Klaus Sengstock, Leticia Tarruell, Christof Weitenberg, César Cabrera, Christian Schweizer, Karen Wintersperger, Tridev Akshaya Mishra, Andrew Hayward, Eric Bertok, Luca Asteria, Maximilian Buser, Leo Stenzel, Niklas Käming, Ephraim Bernhardt, Kirill Plekhanov, Philipp W. Klein, Fan Yang, Tao Qin, Jun-Hui Zheng, Bernhard Irsigler, Ana Hudomal, Ivana Vasić, Mohsen Hafez-Torbati and many other great people from this research unit. All the lectures, talks and discussions that we have together surely enriched my PhD life. Meanwhile, I am grateful to Prof. Dr. Walter Strunz, Prof. Dr. Carsten Timm, and Prof. Dr. Jan Carl Budich for those excellent lectures at TU Dresden. I would like to thank Paul McClarty, Heike Walther, Roderich Moessner, Markus Heyl, David Luitz, Francesco Piazza, Alex Eisfeld, Alberto Corticelli, Robin Schäfer, Sebastián Felipe Mantilla Serrano, Daniele Trapin, Luis Colmenarez, Oles Matsyshyn, Soumi Dutta, Huang-Hsiang Lin, Tsai-Jung Liu and many other members from IMPRS and MPIPKS, for the valuable experience.

I also want to take this opportunity to thank all the friends that I met in both Dresden and Berlin. I would like to thank my nice office mates Onur Erten, Shashi C. L. Srivastava, and Lars Hubatsch. I am also indebted to Wen-Wen Huang, Hong-Cheng Ni, Qi-Cheng Ning, Yong-Chang Zhang, Xing Gao, Xue-Feng Zhang, Zeng-Zhao Li, Gao-Yong Sun, Jin-Lei Liu, Jian-Da Wu, Fulu Zheng, Laoshi Cui, Peng Rao, Wei-Chen Tang, Hui Liu, Xue-Ping Zhao, Xiao-Xiao Sun, Xin-Jia Hu, Ji-Hang Zhu, Misha Chai, Yu Meng, Yu-Long Qiao, Hong-Zheng Zhao, Zhen-Jiu Wang, Po-Yao Chang, Chi-Nan Wu, Chi-Hui Chou, Hui-Shun Kuan, Chengli Wu, Fu Wang, Jingbei Wang, Fubo Dai, Ziyi Qiu, Kai Ma, Wang-Wang Tan, Ya-Qiong Wang, Hao-Tian Shen, Yukai Sun, Sida Zhuang, and many other wonderful colleagues and partners, for all the joyful time that we spent together.

Special thanks go to Michael Genkin, Katrin Lantsch, Maria Voigt, Mandy Lochar, Claudia Domaschke from the Visitors Program at MPIPKS for all the very kind help. I am greatly indebted to Hubert Scherrer-Paulus, Steffen Peters, Thomas Müller and many other IT staff for the technical support. I am grateful to Elise Voigt, Christina Matthes and Luise Reinhardt, for all the kind assistance in dealing with various documents including contract and travelling forms. I am grateful Irena Koschinski, Andrea Schulze, Peter Orlowski, Norbert Paschedag, and other colleagues from TU Berlin, for all the kind help, especially for the efforts that have enabled a quite fluent transfer from Dresden to TU Berlin even in the COVID-19 situation. I would like to thank Prof. Dr. Nathan Goldman for agreeing to be part of the doctoral committee and for reviewing my dissertation. I am also grateful to Prof. Dr. Stephan Reitzenstein for being the chairman of my defense, and particularly to Lara Schäfer for taking care of all those document work.

Last, but crucially, endless thanks go to my great family. I am extremely grateful to my beloved parents, my beautiful sisters, my adorable nieces and nephews, for everything! Without you I would not be the person I am today.